

Compressive Sensing Based Single-Pixel Imaging Systems



Universidade do Porto
Faculdade de Engenharia
FEUP

Filipe Tiago Alves de Magalhães

Thesis submitted to the Faculty of Engineering in partial fulfillment of the requirements
for the degree of Doctor of Philosophy in Electrical and Computer Engineering

Work supervised by

Miguel Fernando Paiva Velhote Correia, PhD

Assistant Professor at the Department of Electrical and Computer Engineering
Faculdade de Engenharia da Universidade do Porto

and by

Francisco Manuel da Moita Araújo, PhD

Senior Researcher at the Optoelectronics and Electronic Systems Unit – UOSE
INESC TEC

January 2013

The candidate has been financially supported by the FCT - Fundação para a Ciência e a Tecnologia (Portuguese Foundation for Science and Technology) through a Ph.D. grant.

(Grant ID - SFRH / BD / 45380 / 2008)

FCT Fundação para a Ciência e a Tecnologia
MINISTÉRIO DA EDUCAÇÃO E CIÊNCIA

“Estudar é uma coisa em que está indistinta
A distinção entre nada e coisa nenhuma.”

in Liberdade, Fernando Pessoa

“Study's the thing where the distinction
Is unclear between nothing and nothing at all.”

in Liberty, Fernando Pessoa

Acknowledgements

I would like to address my special thanks to Prof. Miguel Velhote for having accepted this challenge and for all the guidance provided and availability demonstrated in all our interactions. I am sure this relationship has just been the start of something even greater.

I would like to express my very great appreciation to Dr. Francisco Araújo who since the beginning of this thesis showed an impressive encompassing perspective. After so many years of collaboration, it was extremely fulfilling to reach this point with him by my side.

I am also particularly grateful to Prof. Faramarz Farahi for welcoming me in his lab and even at his home and for providing me the opportunity to work and learn on such a friendly, creative and enthusiastic environment. It has been a pleasure to become a link of the already existing chain, between these two sides of the Atlantic, which spreads far beyond science and technology.

To Mehrdad Abolbashari I must say that his patience and never ending availability have been much esteemed. Thank you for all the interesting and productive discussions we had and for all the contributions. I really enjoyed the time we spent together, not only on a scientific perspective but also on a personal level. I hope we can continue to collaborate in the future.

Thank you to all those that have helped me to solve those “little big” issues, in particular to Nuno Sousa and Eduardo Marques, for the help with the electronics and with the C++ programming for the LightCommander, respectively.

To Dr. Rui Martins from the Centre of Molecular and Environmental Biology at the University of Minho I would like to say that I much appreciated the enthusiasm with which he got involved with my work and the help he gave me in finding applications for it.

To Ricardo Sousa I would like to acknowledge the cooperation we established and the help provided with the machine learning mechanisms.

I am thankful to Rita Pacheco for the help provided in clarifying the doubts related with the English language.

I would like to recognize the encouragement and support provided by Prof. Aurélio Campilho to the creation and establishment of the BioStar group.

I have to say to Helder Oliveira that it has been a pleasure to be his partner during these last four years and that the BioStar has been a very enjoyable adventure.

To Marco Scipioni I would like to say thank you for sharing with me his keen curiosity and for bringing up many meaningful “small” questions. I must also recognize that the occasions we spent together, be it talking about Physics, doing sports or just having a laugh, surely were pleasant.

Many thanks to the UOSE team at INESC TEC for granting me with the adequate conditions and resources despite the setbacks we found along the way. Thank you for believing in me and for the excellent working atmosphere.

I would like to acknowledge the Fundação para a Ciência e a Tecnologia (FCT) for the financial support given through the form of a PhD grant. I also kindly thank the Fundação Luso-Americana para o Desenvolvimento (FLAD) and the Fundação Calouste Gulbenkian for the funding provided for travelling expenses.

I was also very fortunate to have my friends and family always caring about me.

To my aunt Alice, for all her love and dedication, I would like to say that she will be forever in my heart.

To my parents, for being a source of endless love and support, I would like to express my deepest gratitude. Without them I would surely not be who and where I am today.

Domo arigatō gozaimashita Joana for all your love and all the good things we have together. I will always be by your side...

It would be unfair trying to refer all those that have made a difference throughout these years because they were so many and I would end up forgetting someone, but as “no man is an island”, here I leave a word of recognition for them.

Abstract

Compressive sensing has recently emerged and is now a subject of increasing research and discussion, undergoing significant advances at an incredible pace. The novel theory of compressive sensing provides a fundamentally new approach to data acquisition which overcomes the common wisdom of information theory, specifically that provided by the Shannon-Nyquist sampling theorem. Perhaps surprisingly, it predicts that certain signals or images can be accurately, and sometimes even exactly, recovered from what was previously believed to be highly incomplete data.

In 2006, the Digital Signal Processing group at Rice University created a single-pixel camera, which fused an innovative camera hardware architecture with the mathematical theory and algorithms of compressive sensing. This work constituted the start sparkle for the development of many enthusiastic and impressive compressive imaging systems, which now define state-of-the-art solutions in many imaging applications.

In this thesis, initially, a comprehensive review of the current state-of-the-art of compressive imaging systems with particular emphasis in single-pixel architectures is presented. Afterwards, the main subject of this thesis is explored and the single-pixel imaging systems which were developed for various imaging modalities are exposed, namely for monochrome, color, multispectral, hyperspectral and high dynamic range imaging. For each of these modalities a configuration that operated with passive illumination and another that operated with active illumination has been implemented. This allowed a thorough comparative analysis to be made. An algorithm was also developed and demonstrated for the generation of compressive random binary codes to be used by a CMOS imager and enrich it with a compressive imaging mode of operation.

There was still the opportunity to explore the developed compressive single-pixel imaging systems in three different applications. In one of those applications, a passive illumination single-pixel monochrome imaging system has been mounted on a microscope and has been used to acquire images with very fine spatial resolution. In another application, the theory of compressive sensing has been combined with machine learning and pattern recognition mechanisms to detect faces without explicit image reconstruction. Within this context, the passive illumination single-pixel monochrome imaging system has also been used to acquire real-world data and test this innovative concept. The third application used a passive illumination single-pixel hyperspectral imaging system to derive spectroscopic information of grapes from hyperspectral images. This information may be used to analyze and assess the physicochemical properties of the grapes.

Before the concluding remarks, a tangible idea is presented for future consideration. It is related with the development of a compressive single-pixel imaging LIDAR system for the aerospace industry.

Resumo

A sensorização compressiva surgiu recentemente e constitui hoje um assunto de grande investigação e discussão, manifestando avanços significativos com uma cadência impressionante. A inovadora teoria de sensorização compressiva fornece-nos uma abordagem fundamentalmente nova ao tema da aquisição de dados que ultrapassa o conhecimento comum providenciado pela teoria da informação, em particular aquele estabelecido pelo teorema da amostragem de Shannon-Nyquist. Talvez surpreendentemente, ela prevê que certos sinais ou imagens podem ser recuperados com precisão, e por vezes de um modo exacto, a partir do que anteriormente se acreditava serem dados altamente incompletos.

Em 2006, o *Digital Signal Processing Group* da Universidade de Rice criou uma câmara com um único pixel, que fundiu uma arquitectura inovadora de hardware com a teoria matemática e os algoritmos da sensorização compressiva. Este trabalho foi determinante para o desenvolvimento entusiástico e impressionante de muitos sistemas de imagiologia compressiva que definem actualmente soluções ao nível do estado-da-arte em diversas aplicações.

Nesta tese, inicialmente, é apresentada uma revisão extensa do estado-da-arte actual no que respeita a sistemas de imagiologia compressivos com particular ênfase nas arquitecturas que empregam um único pixel. Depois, o tema principal desta tese é explorado e são expostos os sistemas de imagiologia com um único pixel que foram desenvolvidos para diferentes modalidades, nomeadamente para aquisição de imagens monocromáticas, a cores, multiespectrais, hiperespectrais e de gama dinâmica alargada. Para cada uma das modalidades foi implementada uma configuração que operava com iluminação passiva e outra que operava com iluminação activa. Isto permitiu realizar uma análise comparativa minuciosa dos sistemas em causa. Foi também desenvolvido e demonstrado um algoritmo de geração dos códigos compressivos para ser usado por um sensor de imagem CMOS e enriquecê-lo com um modo compressivo de aquisição de imagens.

Houve ainda a oportunidade de explorar os sistemas desenvolvidos em três aplicações. Numa dessas aplicações, um sistema de iluminação passiva para aquisição de imagens monocromáticas com um único pixel foi montado num microscópio e foram obtidas imagens com uma resolução espacial muito fina. Noutra aplicação, a teoria de sensorização compressiva foi combinada com mecanismos de aprendizagem computacional para detecção de faces sem a reconstrução explícita das imagens. Neste contexto, o sistema de iluminação passiva para aquisição de imagens monocromáticas com um único pixel foi usado para adquirir dados reais e testar este conceito inovador. A terceira aplicação usou um sistema de iluminação passiva para aquisição de imagens hiperespectrais com um único pixel para derivar informação espectroscópica de uvas. Esta informação pode ser usada para analisar e avaliar as suas propriedades físico-químicas. Antes das notas finais, é apresentada uma ideia para prossecução futura relacionada com o desenvolvimento de um sistema LIDAR de imagiologia com um único pixel para a indústria aeroespacial.

Contents

Acknowledgements	IX
Abstract	XI
Resumo.....	XIII
List of Figures	XVII
List of Tables.....	XXXIII
List of Acronyms	XXXV
Chapter 1. Introduction.....	1
1.1 Thesis structure.....	3
1.2 Motivation	3
1.3 Contributions	4
1.4 Publications	6
Chapter 2. The Theory of Compressive Sensing – An Overview.....	7
2.1 K -sparse and compressible signals.....	7
2.2 Recovering K -sparse signals.....	8
2.3 Incoherence.....	8
2.4 How compressive sensing works.....	9
2.5 Robustness of compressive sensing.....	12
Chapter 3. Compressive Imaging Systems – A Review	15
3.1 The single-pixel camera.....	15
3.2 Feature-specific structured imaging system	17
3.3 Random projections based feature-specific structured imaging	18
3.4 Compressed sensing magnetic resonance imaging.....	19
3.5 Single-pixel terahertz imager	22
3.6 Compressive structured light for recovering inhomogeneous participating media.....	26
3.7 Compressive spectral imagers	27
3.8 Compressive ghost imaging system	34
3.9 CMOS compressive sensing imager.....	36
3.10 Compressive microscopy imaging systems	38
3.11 Compressive optical coherence tomography	41
3.12 Photon-counting compressive sensing laser radar for 3D imaging.....	45
3.13 Millimeter-wave imaging with compressive sensing	47
3.14 Compressive polarimetric imaging.....	50
Chapter 4. Compressive Sensing Based Single-Pixel Imaging Systems	53
4.1 Monochrome Imaging Systems	53
4.1.1 <i>Active illumination single-pixel monochrome imaging system</i>	53
4.1.2 <i>Passive illumination single-pixel monochrome imaging systems</i>	69

4.1.3	<i>Transmissive single-pixel imaging system</i>	79
4.1.4	<i>Concluding remarks</i>	85
4.2	Color Imaging Systems.....	87
4.2.1	<i>Active illumination single-pixel color imaging systems</i>	87
4.2.2	<i>Passive illumination single-pixel color imaging systems</i>	97
4.2.3	<i>Concluding remarks</i>	101
4.3	Multispectral Imaging Systems.....	103
4.3.1	<i>Active illumination single-pixel multispectral imaging system</i>	103
4.3.2	<i>Passive illumination multispectral single-pixel imaging system</i>	109
4.3.3	<i>Concluding remarks</i>	112
4.4	Hyperspectral Imaging Systems.....	113
4.4.1	<i>Active illumination single-pixel hyperspectral imaging system</i>	114
4.4.2	<i>Passive illumination single-pixel hyperspectral imaging system</i>	119
4.4.3	<i>Concluding remarks</i>	132
4.5	High Dynamic Range Compressive Imaging Systems.....	133
4.5.1	<i>Active illumination high dynamic range compressive imaging system</i>	142
4.5.2	<i>Passive illumination high dynamic range compressive imaging system</i>	149
4.5.3	<i>Concluding remarks</i>	156
4.6	CMOS Based Compressive Imaging Sensor	157
4.6.1	<i>Overall architecture and operation</i>	157
4.6.2	<i>Compressive sensing based mode of operation</i>	159
4.6.3	<i>Concluding remarks</i>	161
Chapter 5.	Applications	163
5.1	Microscopic imaging using a passive illumination single-pixel monochrome imaging system	163
5.2	Face detection without explicit image reconstruction	164
5.3	Physicochemical analysis of grapes based on hyperspectral images.....	173
Chapter 6.	Future Work	181
6.1	Single-Pixel Imaging LIDAR System Based on Compressive Sensing.....	181
Chapter 7.	General Conclusions	185
References	189

List of Figures

- Figure 1 – Example of a simple recovery problem. (a) The Logan–Shepp phantom test image. (b) Sampling domain in the frequency plane; Fourier coefficients are sampled along 22 approximately radial lines. (c) Minimum energy reconstruction obtained by setting unobserved Fourier coefficients to zero. (d) Compressive sensing based reconstruction. This reconstruction is an exact replica of the original image in (a) [5].....2
- Figure 2 – Geometry of ℓ_1 recovery. (a) Visualization of the ℓ_2 minimization that finds the non-sparse point of contact \hat{s} between the ℓ_2 ball (hypersphere, in red) and the translated measurement matrix null space (in green). (b) Visualization of the ℓ_1 minimization solution that finds the sparse point of contact \hat{s} with high probability thanks to the pointiness of the ℓ_1 ball. Picture adapted from [19].....11
- Figure 3 – Single-Pixel Camera block-diagram. Incident light field (corresponding to the desired image x) is reflected off a DMD array whose mirror orientations are modulated by a pseudorandom pattern. Each different mirror pattern produces a voltage at the single photodiode that corresponds to one measurement $y[m]$. From M measurements a sparse approximation to the desired image x using CS techniques can be obtained. Picture reproduced from [15].....15
- Figure 4 – Optical setup of the single-pixel camera developed at the Rice University. Picture reproduced from [15].16
- Figure 5 – Flow diagram for the Feature-Specific Structured Imaging (FSSI) system. Picture reproduced from [31].17
- Figure 6 – Flow diagram for the binary Random Projections FSSI (RPFSSI) system. Picture reproduced from [32].19
- Figure 7 – Scheme of a CS based MRI system. The user controls the gradient waveforms and RF pulses (block (a)) that, in turn, control the phase of the pixels/voxels (block (b)) in the image. An RF coil receives the signal in an encoded form (block (c)). The incoherent measurements result from the control of the gradient waveforms (block (d)). An image can then be reconstructed with an appropriate nonlinear reconstruction enforcing sparsity (block (e)). Picture reproduced from [36].....20

Figure 8 – 3D contrast enhanced angiography. Even acquiring only 10% of the samples, CS could recover most of the blood vessel information revealed by Nyquist sampling and significantly reduce the artifacts when compared to the linear reconstruction. Images taken from [36].	21
Figure 9 – Brain scanning using MRI. The results obtained with CS, using fewer sampling trajectories, were comparable to those obtained with the full Nyquist-sampled set. CS was also more successful than linear reconstruction from incoherent sampling in suppressing aliasing artifacts and exhibited improved resolution over a low-resolution acquisition with the same scan time. Picture reproduced from [36].	22
Figure 10 – CS-based THz Fourier imaging setup. Picture reproduced from [37].	23
Figure 11 – Compressive sensing imaging results. (a) Magnitude of image reconstructed by inverse Fourier transform using the full dataset (4096 uniformly sampled measurements) and (d) its phase. Note the phase distortion inherent in the THz beam in (d). Compressed sensing reconstruction result using 500 measurements (12%) from the full dataset: (b) magnitude and (e) phase. Compressed sensing with phase correction improves image quality (c) and eliminates phase distortion (f). All figures show a zoom-in view on a 40×40 grid centered on the object. Picture reproduced from [37].	24
Figure 12 – Diagram of the CS-based THz imaging system discarding the need for raster scanning. Picture reproduced from [38].	25
Figure 13 – Compressive structured light for recovering inhomogeneous participating media. (a) Coded light is emitted along the z-axis to the volume while the camera acquires images as line-integrated measurements of the volume density along the x-axis. The light is coded in either the spatial domain or temporal domain with a predetermined sequence. (b) Image formation model for participating medium under single scattering. The image irradiance at one pixel, $I(y, z)$, depends on the integral along the x-axis of the projector's light, $L(x, y)$, and the medium density, $\rho(x, y, z)$, along a ray through the camera center. (c) Experimental setup. The volume density is reconstructed from the measurements by the use of compressive sensing techniques. Picture reproduced from [39].	26
Figure 14 – Reconstruction results of milk drops dissolving in water. 24 images were used to reconstruct the volume at $128 \times 128 \times 250$ at 15fps. The reconstructed volumes are shown in three different views and the image in the leftmost column shows the corresponding photograph (taken with all projector pixels emitting white) of the dynamic process). Picture reproduced from [39].	27
Figure 15 – Schematic drawing of the single-shot CS-based spectral imager. Picture reproduced from [40].	27

Figure 16 – Experimental prototype of the proposed architecture. Picture reproduced from [40]...	28
Figure 17 – Experimental results from simple targets with narrow-band illumination. (a) Detector image recorded for illumination with a 10 nm full width at half maximum (FWHM) bandpass filter centered at 560 nm – note the modulation introduced by the coding aperture. (b) Intensity image generated by summing the spectral information in the reconstruction for the 560 nm bandpass filter. (c) Spectral reconstruction at a particular spatial location for the 560 nm bandpass filter. (d) Spectral reconstruction at a particular spatial location for the 580 nm bandpass filter. The small peak near 520 nm is due to spectral aliasing. Picture and info reproduced from [40].....	29
Figure 18 – Schematic drawing of the SD-CASSI system. Picture reproduced from [41].	30
Figure 19 – Top view of the SD-CASSI experimental setup. Picture reproduced from [41].	30
Figure 20 – Scene consisting of a ping-pong ball illuminated by a 543 nm green laser and a white light source filtered by a 560 nm narrowband filter (left), and a red ping-pong ball illuminated by a white light source (right). Picture reproduced from [41].....	31
Figure 21 – Spatial content of the scene of Figure 20 in each of 28 spectral channels between 540 and 640 nm. The green ball can be seen in channels 3 to 8; the red ball can be seen in channels 23 to 25. Picture reproduced from [41].	31
Figure 22 – (left) Spectral intensity through a point on the ping-pong ball illuminated by a 543 nm green laser and a white light source filtered by a 560 nm narrowband filter. (right) Spectral intensity through a point on the red ping-pong ball illuminated by a white light source. Spectra from an Ocean Optics non-imaging reference spectrometer are shown for comparison. Picture reproduced from [41].	32
Figure 23 – (a) Mosaic of hyperspectral images with a lateral resolution of 256 x 256 pixels and a spectrum resolution of 4 nm (averaged over several channels). (b) Reconstructed image after summing all the bands. (c) Image taken with a conventional camera. Images reproduced from [42].	33
Figure 24 – 256 x 256 pixels images for two spectral bands obtained via raster scan (left column) and compressive sensing (right column). Images reproduced from [42].	34
Figure 25 – Scheme of a standard setup for pseudothermal ghost imaging with two detectors. Picture reproduced from [43].....	35
Figure 26 – Scheme of the compressive ghost imaging setup with a single detector. Picture reproduced from [43].	35

Figure 27 – Ghost imaging results for the reconstruction of images of a double-slit transmission plate. Top row: Conventional ghost imaging with: (a) 256 realizations; (b) 512 realizations; Bottom row: Compressive ghost imaging reconstruction using the same experimental data as in (a) and (b). Picture reproduced from [43].	36
Figure 28 – Scheme of the CMOS CS-imager. Picture reproduced from [45].	38
Figure 29 – Schematic drawing of the compressive confocal microscope along with its principle of operation. Picture reproduced from [48].	39
Figure 30 – Diagram of the experimental off-axis, frequency-shifting digital holography setup. Picture reproduced from [51].	40
Figure 31 – (a) Results obtained with standard holography. (b) CS reconstruction, using 7% of the Fresnel coefficients. Images reproduced from [51].	41
Figure 32 – Scheme of the common path spectral domain OCT setup. Picture reproduced from [53].	42
Figure 33 – OCT image of onion cells: (a) obtained using complete spectral data; (b), (c), and (d) obtained by sampling 62.5%, 50%, 37.5% of the pixels and pursuing sparsity in pixel domain; (e), (f), and (g) obtained by sampling 62.5%, 50%, 37.5% of the pixels and pursuing sparsity in wavelet domain. Picture reproduced from [53].	43
Figure 34 – Setup of the swept-source OCT system constructed with a 1060 nm source and a standard Michelson interferometer. The regular raster scan pattern was modified to acquire randomly spaced horizontal B-scans. The full volume was generated through CS-recovery in post processing. Picture reproduced from [54].	44
Figure 35 – Results recovered with CS. The top row shows the position of the frames that were acquired, the second row shows the CS reconstructed summed voxel projection, the third and fourth row show a selected B-scan and slow scan from the CS-recovered info, respectively. Picture reproduced from [54].	45
Figure 36 – Experimental setup of the photon-counting compressive sensing laser radar system for 3D imaging. Picture reproduced from [13].	46
Figure 37 – Results obtained with the photon-counting compressive sensing laser radar system for 3D imaging. Reconstructions for objects ‘U’ and ‘R’ at depths 1.75 m and 2.10 m. (a) and (b) consider only ‘U’ and ‘R’, respectively, while (c) considers a range including both. Timing histogram (d) peaks represent, from left to right, ‘U’, ‘R’, and the room wall. Picture reproduced from [13].	46

Figure 38 – Example of an extended Hadamard mask with 81×85 pixels. The colored boxes represent two different sub-masks (41×43 pixels) that are used in two different acquisitions. Picture reproduced from [62].	48
Figure 39 – Diagram of the compressive sensing based passive mm-wave imaging setup. Picture reproduced from [63].	49
Figure 40 – 41×43 pixels images of the incandescent bulb acquired with the CS based PMMW system with: (a) 100% and (b) 11% of the samples. Picture reproduced from [63].	49
Figure 41 – Setup for single-pixel imaging polarimetry. An example of a binary intensity pattern displayed by the SLM is also shown. Picture reproduced from [64].	50
Figure 42 – (a) 1024×1024 pixels image of the object used in the experiment, which consists of an amplitude mask with a cellophane film covering the zone colored in yellow. (b), (c) and (d) represent 64×64 pixels pseudo-color images for the Stokes parameters. Picture reproduced from [64].	51
Figure 43 – Active illumination single-pixel-camera experimental setup. Following the red arrows, it can be seen that the image projected by the video projector is reflected on the wall and by means of a lens is focused on the photodiode active area. The output of the photodiode amplifier circuit is connected to a data acquisition board.	54
Figure 44 – (a) Compact active illumination single-pixel camera setup. (b) Detailed photo of the assembly comprising the lens and the photodiode circuit.	55
Figure 45 – Schematics of the photodiode amplifier circuit.	55
Figure 46 – Example of one of the projected images, representing the product between a random measurement pattern and the image to be reconstructed.	56
Figure 47 – (a) Reference image. First results obtained (32×32 pixels $\Rightarrow N = 1024$) with the active illumination single-pixel camera using: (b) 205 measurements \Rightarrow 20% (PSNR = 11.08 dB); (c) 410 measurements \Rightarrow 40% (PSNR = 12.30 dB); (d) 717 measurements \Rightarrow 70% (PSNR = 13.21 dB). All the PSNR were calculated using the reference image and the respective reconstructed image.	56
Figure 48 – (a) Original scene; Image reconstruction using: (b) 20% of the measurements (PSNR = 69.74 dB); (c) 40% of the measurements (PSNR = 75.60 dB); (d) 60% of the measurements. All the reconstructions are images with 64×64 pixels ($N = 4096$). All the PSNR values were obtained comparing the respective image with the image reconstructed using 60% of the measurements.	57

Figure 49 – Reconstruction of the image of Figure 47 c) after the addition of uniformly distributed noise with maximum amplitude of: (a) 10% of the maximum amplitude of the measured signal (SNR = 20.63 dB) – PSNR = 26.62 dB; (b) 20% of the maximum amplitude of the measured signal (SNR = 14.54 dB) – PSNR = 25.03 dB; (c) 30% of the maximum amplitude of the measured signal (SNR = 11.41 dB) – PSNR = 20.17 dB; (d) 40% of the maximum amplitude of the measured signal (SNR = 8.48 dB) – PSNR = 13.87 dB. All the PSNR values were calculated comparing the respective image with the image of Figure 47 c).....	58
Figure 50 – Spectral responsivity of the Thorlabs PDA100A-EC amplified Silicon photodiode. Picture reproduced from the manual, available at http://thorlabs.com/Thorcat/13000/PDA100A-Manual.pdf	59
Figure 51 – Scheme of the compressive active illumination single-pixel imaging system.....	61
Figure 52 – Photo of the compressive active illumination single-pixel imaging system.....	61
Figure 53 – Photo of the black and white wood object with character “A” taken with a conventional camera.....	62
Figure 54 – Several images of the black and white wood object containing the character “A”. Image resolution (in pixels) from top to bottom: 32×32 ; 64×64 ; 128×128 ; 512×512 . Left column contains the images acquired with the active illumination single-pixel monochrome imaging system. Center column contains the images represented in left column after median filtering and contrast adjustment. Right column contains the images acquired with a conventional camera downsized for comparison purposes.	63
Figure 55 – Plot of the voltage signal on the output of the amplified photodiode circuit. It is clearly seen the effect of the variable modulation and ripple of the light.....	64
Figure 56 – Five-pointed black star filled with three different gray levels.....	67
Figure 57 – Several images of the grayscale five-pointed star. Image resolution (in pixels) from top to bottom: 32×32 ; 64×64 ; 128×128 . Left column contains the images obtained with the active illumination single-pixel monochrome imaging system. Center column contains the images represented in left column after median filtering and contrast adjustment. Right column contains the images acquired with a conventional camera downsized for comparison purposes.....	68
Figure 58 – Photos of the LightCommander™ development kit from Logic PD.....	70
Figure 59 – LightCommander’s optical schematics. (Kindly provided by LogicPD)	71

Figure 60 – Photo of a DMD chip from Texas Instruments next to a 1 cent coin for size comparison. Picture reproduced from http://de.academic.ru/pictures/dewiki/68/DLP_Chip.jpg .	71
Figure 61 – (a) Schematic of two mirrors from a digital micromirror device (DMD), illustrating its principle of operation. (b) A portion of an actual DMD array with an ant leg for scale. Picture reproduced from [23].	72
Figure 62 – Scheme of the passive illumination single-pixel monochrome imaging system.	73
Figure 63 – Photo of the passive illumination single-pixel monochrome imaging system illuminating the black and white wood object of Figure 53.	73
Figure 64 – (left) Several images of the black and white wood object containing the character “A” acquired with the passive illumination single-pixel monochrome imaging system. (right) Images acquired with a conventional camera downsized for comparison purposes.	74
Figure 65 – (left) Several images of the grayscale five-pointed star acquired with the passive illumination single-pixel monochrome imaging system. (right) Images acquired with a conventional camera downsized for comparison purposes.	76
Figure 66 – Illustration for the definition of a projector’s throw ratio.	79
Figure 67 – Scheme of the transmissive single-pixel imaging system.	80
Figure 68 – Transmissive single-pixel camera mounted on a microscope, placed on the vertical optical path. Note the conventional camera (in blue) mounted on the other optical path.	81
Figure 69 – Photo of the LCD module taken from the Epson® PowerLite S5 projector that has been used in the transmissive single-pixel camera (active area: 11.2 mm × 8.4 mm).	81
Figure 70 – Thorlabs FDS series photodiode responsivity curves. The yellow curve relates to the photodiode (FDS1010) used on the transmissive single-pixel camera setup. Picture reproduced from http://www.thorlabs.de/Thorcat/2700/2739-s01.pdf .	82
Figure 71 – Image of one of the acquired scenes. This image was obtained from the stitching of 4 separate pictures taken with the conventional camera due to its sensor size (1/2-inch CCD) when compared to the size of the LCD active region. The red inset indicates the region acquired with our single-pixel camera.	82
Figure 72 – Reconstruction of an image with 32×32 pixels ($N = 1024$) from: (a) 25% ($K = 256$); (b) 50% ($K = 512$); (c) 75% ($K = 768$); (d) 100% ($K = 1024$) measurements. For each reconstructed image, the PSNR has been calculated relatively to the image reconstructed using 100% ($K = 1024$) of the measurements: (a) PSNR = 12.85 dB; (b) PSNR = 14.34 dB; (c) PSNR = 25.89 dB.	83

Figure 73 – Reconstruction of an image with 64×64 pixels ($N = 4096$) from: (a) 25% ($K = 1024$); (b) 50% ($K = 2048$); (c) 75% ($K = 3072$); (d) 100% ($K = 4096$) measurements. For each reconstructed image, the PSNR has been calculated relatively to the image reconstructed using 100% ($K = 4096$) of the measurements: (a) PSNR = 20.27 dB; (b) PSNR = 22.63 dB; (c) PSNR = 32.44 dB.....	83
Figure 74 – Halogen lamp emission spectrum, obtained with a commercial spectrometer.....	85
Figure 75 – (a) Piece of paper with the painted red contour and green background (the coin is present only for size comparison). (b) Color image of the painted area in (a), reconstructed with 32×32 pixels (410 measurements were acquired for each of the RGB channels).	88
Figure 76 – Color reconstruction of a 64×64 pixels image of the real scene depicted in Figure 48 (a). 40% of the measurements were used to reconstruct each image associated with the RGB channels.	88
Figure 77 – Photo of the colored wood object with character “B”.....	89
Figure 78 – Photo with detail of the colored wood object being illuminated with a green and black random binary compressive measurement code with 32×32 pixels.	89
Figure 79 – Spectra of the RGB components used for illumination along with the spectrum of the “white” light resulting from their combinations.....	90
Figure 80 – Illustrative examples of the application of the post-processing algorithm (selective local median filter) and median filtering to filter noisy points. The white portion of the matrix with a thicker black border represents the 3×3 neighborhood under analysis.	91
Figure 81 – Images of the colored wood object containing the character “B” acquired with the active illumination color imaging system with spectral filtering on the illumination end. Image resolution (in pixels) from top to bottom: 32×32 ; 64×64 ; 128×128 . (left) Color images filtered with the selective local median filter. (center) Color images after median filtering. (right) Images acquired with a conventional camera downsized for comparison purposes.	92
Figure 82 – Spectra of the RGB components resulting from filtering the “white” light emitted by the projector.	94

Figure 83 – Images of the colored wood object containing the character “B” acquired with the active illumination color imaging system with spectral filtering on the detection end. Image resolution (in pixels) from top to bottom: 32×32 ; 64×64 ; 128×128 . (left) Color images filtered with the selective local median filter. (center) Color images after median filtering. (right) Images acquired with a conventional camera downsized for comparison purposes.	95
Figure 84 – 128×128 pixels image obtained after median filtering the raw images representative of the RGB channels.	95
Figure 85 – From left to right, images representative of the Red, Green and Blue components with 128×128 pixels.	96
Figure 86 – Images of the colored wood object containing the character “B” acquired with the passive illumination color imaging system with spectral filtering on the illumination end. Image resolution (in pixels) from top to bottom: 32×32 ; 64×64 ; 128×128 . (left) Color images filtered with the selective local median filter. (center) Color images after median filtering. (right) Images acquired with a conventional camera downsized for comparison purposes.	98
Figure 87 – Images of the colored wood object containing the character “B” acquired with the passive illumination color imaging system with spectral filtering on the detection end. Image resolution (in pixels) from top to bottom: 32×32 ; 64×64 ; 128×128 . (left) Color images filtered with the selective local median filter. (center) Color images after median filtering. (right) Images acquired with a conventional camera downsized for comparison purposes.	100
Figure 88 – Scheme of the setup for the active illumination single-pixel multispectral imaging system.	103
Figure 89 – Normalized emission spectra of the red, green and blue LED light bulbs used for illumination in the active illumination single-pixel multispectral imaging system.	104
Figure 90 – Photos of the active illumination single-pixel multispectral imaging system. Left: Light from the blue LED light bulb is being launched into the Lightcommander’s tunnel. The LightCommander’s illumination module and respective power unit have been removed. Right: Detailed photo of the amplified photodiode and of the scene being illuminated with a binary random code.	104
Figure 91 – RGB scene composed to be used on the performance evaluation of the active illumination single-pixel multispectral imaging system.	105

Figure 92 – From top to bottom: 32×32 ; 64×64 ; 128×128 ; pixels images captured with the active illumination single-pixel multispectral imaging system. The RGB images resulting from the combination of the raw images after selective local median filtering can be seen on the left column, while the center column contains the RGB images resulting from the combination of the raw images after median filtering. On the right column, it can be seen the images acquired with a conventional camera downsized for comparison purposes.	106
Figure 93 – 128×128 pixels images acquired to evaluate the reflectance of the printed scene of Figure 91. On the top row it can be seen the images acquired with the active illumination single-pixel multispectral imaging system after median filtering. The photos acquired with a conventional camera are displayed on the bottom row. The images represented from left to right, illustrate the acquisitions made when the scene was being independently illuminated with the red, green, and blue LED bulb, respectively.	108
Figure 94 – Plot of the normalized voltage on the output of the amplified photodiode circuit when one LED light bulb was being used for illumination of the scene being acquired.	109
Figure 95 – Scheme of the setup for the passive illumination single-pixel multispectral imaging system.	110
Figure 96 – Photo of the passive illumination single-pixel multispectral imaging system during operation.	110
Figure 97 – From top to bottom: 32×32 , 64×64 and 128×128 pixels images captured with the passive illumination single-pixel multispectral imaging system. On the left column are the RGB images obtained after filtering each color channel raw image with the selective local median filter. The center column contains the RGB images obtained after median filtering each color channel raw image. On the right column, it can be seen images acquired with a conventional camera downsized for comparison purposes.	111
Figure 98 – Setup of the active illumination single-pixel hyperspectral imaging system.	115
Figure 99 – Photo of the active illumination single-pixel hyperspectral imaging system.	115
Figure 100 – Paper with “V” and “E” characters printed in black in a red and green background, respectively.	116
Figure 101 – Images with different resolutions obtained with the active illumination single-pixel hyperspectral imaging system for the paper object with the characters “V” and “E” printed in black in a red and green background, respectively (see Figure 100). The images on the left column were obtained when the He-Ne laser (red) was on and the images on the right column were obtained when the Nd:YAG laser (green) was on.	117

Figure 102 – 128×75 pixels images, from Figure 101, converted to RGB images.....	118
Figure 103 – Red (left) and Green (right) channels of the RGB photos taken with a conventional camera when the scene was being illuminated with the He-Ne laser (on the left) or with the Nd:YAG laser (on the right). These photos have been resized to 128×60 pixels for comparison with the images displayed in Figure 102.....	118
Figure 104 – RGB image resulting from the addition of the images of Figure 102.	118
Figure 105 – Reflectance spectra of the red and green regions of the scene presented in Figure 100. In black it is also presented the emission spectrum of the halogen bulb that was used for illumination.....	119
Figure 106 – Photo of the Infocus LP120 video projector.	120
Figure 107 – Scheme depicting the principle of operation of the Zollner-Thurnar's type monochromator of the ANDO AQ6317B optical spectrum analyser (OSA).....	121
Figure 108 – Scheme depicting the principle of operation of the passive illumination single-pixel hyperspectral imaging system.....	122
Figure 109 – Optical engine of the Infocus LP120 projector.	123
Figure 110 – Detailed photo of the Infocus LP120 with the 10x microscope objective launching the light into the 50/125 μm multi-mode optical fiber.	123
Figure 111 – Normalized reconstructed spectrum obtained along the reconstructed datacube in a fixed spatial position where the laser line was imaged (black trace). The red trace represents the normalized spectrum of the He-Ne source measured with the OSA. ..	124
Figure 112 – Rows (a) and (c) represent the images reconstructed at 632.800 nm with 32×32 and 64×64 pixels, respectively, along with a 3-D representation of their normalized intensities. Rows (b) and (d) represent the images reconstructed at 632.790 nm with 32×32 and 64×64 pixels, respectively, along with a 3-D representation of their normalized intensities.....	125
Figure 113 – Detailed photo of the assembly used for launching light coming from LightCommander's light tunnel into the optical fiber.	126
Figure 114 – 512×512 pixels photo of the lit LED lamp acquired with: (a) conventional camera; (b) with passive illumination single-pixel hyperspectral camera, at 630.900 nm.	126
Figure 115 – PSNR versus the percentage of measurements used to reconstruct the 512×512 pixels images of the lit LED bulb with respect to their full dimensionality. All the PSNR values were calculated relatively to the 512×512 pixels image reconstructed using 100% of the measurements [see Figure 114 (b)].....	127

Figure 116 – Photo of an Ocean Optics USB 2000 miniature fiber optic spectrometer. Image reproduced from http://www.oceanoptics.com/Products/usb2000.asp	129
Figure 117 – (left) Ocean Optics USB 2000 miniature fiber optic spectrometer without the cover. (right) Scheme of the light path through the optical arrangement of the USB2000. The photo on left was reproduced from http://www.biophotonicsworld.org/system/uploads/0000/0037/IMG_9538.JPG ...	129
Figure 118 – Conventional camera photo of the composed scene of a red LED bulb being hit by a spot of a laser emitting at 654 nm.....	131
Figure 119 – Spectrum of the scene composed by a red LED bulb and by a laser spot at 654 nm. The spectrum directly measured with the USB 2000 spectrometer is represented in black while the spectrum obtained along the reconstructed datacube is represented in red.....	131
Figure 120 – 128×128 pixels images reconstructed at 630.88 nm and 654.03 nm, representing the red LED bulb and the laser spot, respectively.....	132
Figure 121 – Picture of a hemispherical surface.....	135
Figure 122 – Example of a sinusoidal fringe pattern used for the extraction of 3D information about the object into which it is projected.	135
Figure 123 – Photos of the hemispherical object from Figure 121 with a sinusoidal pattern projected on its surface, acquired with a conventional camera using different exposure times and gains: (a) exposure time: 31 ms, gain: 14; (b) exposure time: 230 ms, gain: 81.	136
Figure 124 – Scheme of the experimental setup used for high dynamic range imaging with adaptive intensity control.	137
Figure 125 – Photo of the experimental setup used for high dynamic range imaging with adaptive intensity control.	137
Figure 126 – Flowchart of the application developed for adaptive intensity control.	138
Figure 127 – Results obtained with the adaptive intensity control imaging system for the acquisition of high dynamic range images of a hemispherical surface (top row) and of a metallic and highly reflective object (bottom row): (a) and (d) initial image; (b) and (e) final image; (c) and (f) mask applied to the LCD that provided the acquisition of the final image.	139
Figure 128 – Synthetic scene created to evaluate the performance of the HDRCI system.	140
Figure 129 – Photos of the scene depicted in Figure 128, acquired with a conventional camera, using different exposure times: (a) 1/320 s; (b) 1/25 s.	141

Figure 130 – 128×128 pixels high dynamic range image resulting from the combination of the photos from Figure 129 captured with different exposure times.	141
Figure 131 – Flowchart describing the procedure for HDRCI by means of acquiring images with different equivalent exposure times.	143
Figure 132 – Photo of the active illumination HDRCI system under operation.	143
Figure 133 – 128×128 pixels image initially obtained with low equivalent exposure time and without mask, using the active illumination HDRCI system.	144
Figure 134 – 128×128 pixels image obtained with equivalent long exposure time and with a mask totally blocking the right half part, using the active illumination HDRCI system.	144
Figure 135 – 128×128 pixels high dynamic range image resulting from the combination of the images acquired with different equivalent exposure times of Figure 133 and Figure 134. Tone mapping has been used to display the image with 8 bits.	145
Figure 136 – Flowchart of the algorithm implemented for HDRCI by means of intensity control.	146
Figure 137 – (a) 128×128 pixels image reconstructed with the active illumination HDRCI system when the mask displayed in (b) was used. The mask reduced 60% the radiance of the right half of scene.	147
Figure 138 – 128×128 pixels high dynamic range image resulting from the division of the image in Figure 137 (a) by the mask displayed in Figure 137 (b). Tone mapping has been used to display the image with 8 bits.	148
Figure 139 – Normalized intensity measured by the photodiode as a function of the gray level [0, 255] of the image projected with the Epson® video projector.	149
Figure 140 – Scheme of the passive illumination HDRCI system.	149
Figure 141 – Top view photo of the passive illumination HDRCI system.	150
Figure 142 – General view of the passive illumination HDRCI system during operation. Next to the lower right corner of the photo, it is possible to see the amplified photodiode mounted in front of the LightCommander light tunnel.	151
Figure 143 – 128×128 pixels image initially obtained with low equivalent exposure time and without mask, using the passive illumination HDRCI system.	151
Figure 144 – 128×128 pixels image obtained with equivalent long exposure time and with a mask totally blocking the right half part, using the passive illumination HDRCI system.	152

Figure 145 – 128×128 pixels high dynamic range image resulting from the combination of the images acquired with different equivalent exposure times of Figure 143 and Figure 144. Tone mapping has been used to display the image with 8 bits.	152
Figure 146 – (a) 128×128 pixels image reconstructed with the passive illumination HDRCI system when the mask displayed in (b) was used. The mask reduced 50% the radiance of the right half of scene.	153
Figure 147 – 128×128 pixels high dynamic range image resulting from the division of the image in Figure 146 (a) by the mask displayed in Figure 146 (b). Tone mapping has been used to display the image with 8 bits.	153
Figure 148 – Binary PWM sequence pattern with two examples of how intensity values are generated with 5 bits.	154
Figure 149 – Plots of the measured PWM signals when different gray levels were being assigned to the DMD pixels.	155
Figure 150 – Normalized intensity measured by the photodiode as a function of the gray level [0, 255] of the image projected with the LightCommander.	156
Figure 151 – Architecture of the CMOS based imaging sensor.	158
Figure 152 – Layout of the integrated circuit of the imaging sensor.	159
Figure 153 – 32×32 pixels image with several geometric shapes and different gray levels used in the simulations performed to study the feasibility of the algorithm created to generate binary random compressive codes to be used by the CMOS based imaging sensor.	161
Figure 154 – 32×32 pixels reconstructions of the image in Figure 153. The reconstructions were performed using: (a) 10% (PSNR = 5.32 dB); (b) 50% (PSNR = 12.51 dB), of the total number of measurements (1024). The PSNR were calculated relatively to the image of Figure 153.	161
Figure 155 – Photo of the LightCommander with the photodiode in front of the light tunnel assembled on a Leica microscope.	164
Figure 156 – 128×128 pixels result images acquired with: (left) the compressive single-pixel imaging system; (right) a conventional camera; assembled on the microscope, for a scene consisting of the characters “ste” printed in black on standard white paper.	164
Figure 157 – Examples of images belonging to the created sets. (Top) Images of faces of three persons in upright frontal positions, with two examples for the same person. (Bottom) Images of three different objects/animals, with two examples for the same object.	165

Figure 158 – Plot of vectors with the 1024 incoherent measurements obtained with an image of a face and with an image of an object/animal.....	166
Figure 159 – Three different standard approaches for feature selection: (left) depicts the filter feature selection (FS) approach done before the model design (MD); (center) the wrapper consists on an iterative approach where features are removed step by step until a desirable performance of the model is achieved; and (right) embedded method is designed jointly with the learning model algorithm.	167
Figure 160 – Performance of the SVM classifier trained with different amounts of data and with random feature selection.....	167
Figure 161 – Performance of the SVM classifier trained with different amounts of data and with optimized feature selection.....	168
Figure 162 – Examples of images belonging to the created sets with over imposed blobs representing the SIFT descriptors.....	169
Figure 163 – Photo of the arrangement used to acquire the measurements for face detection with the passive illumination single-pixel imaging system.	170
Figure 164 – Images of a face (128×128 pixels) and of an object (256×256 pixels) that have been used to assess the performance of the face detection system under real-world conditions with the passive illumination single-pixel monochrome imaging system.	170
Figure 165 – Images of Figure 164 resized to 32×32 pixels.	171
Figure 166 – Images of a face (PSNR = 12.41 dB) and of an object (PSNR = 9.86 dB) with 32×32 pixels reconstructed using 1024 measurements acquired with the passive illumination single-pixel monochrome imaging system. The PSNR values were calculated using the homologous images of Figure 165 as references.	171
Figure 167 – Images of a face (PSNR = 24.84 dB) and of an object (PSNR = 22.93 dB) with 32×32 pixels reconstructed using 1024 measurements obtained multiplying the image to be reconstructed by the Hadamard random binary codes. The PSNR values were calculated using the homologous images of Figure 165 as references.....	172
Figure 168 – Setup used to acquire hyperspectral images of grapes with the passive illumination single-pixel hyperspectral imaging system.	174
Figure 169 – Photos of the three grapes with different maturation levels illuminated in transmission. These photos were acquired with a conventional camera. From left to right, the grapes had 13.7 %Bx, 16.8 %Bx and 20.8 %Bx.	174

Figure 170 – (left) 32×32 pixels image of the grape with 20.8 %Bx acquired at 671.02 nm with the passive illumination hyperspectral imaging system. (right) The seeds observable in the image on the left were highlighted with a red contour.	175
Figure 171 – 32×32 pixels image of the halogen bulb behind the opening on the black plastic piece at 645.10 nm acquired with the passive illumination hyperspectral imaging system.	175
Figure 172 – 32×32 pixels image of the halogen bulb with three points marked in red, green and blue to indicate the positions where the spectra were obtained along the datacube.	176
Figure 173 – Spectra obtained along the halogen bulb datacube in the positions marked by the red, green and blue pixels in the image of Figure 172.	176
Figure 174 – Spectra of the halogen bulb. The normalized real spectrum is represented with a thick black trace while the normalized integrated spectrum, obtained from the reconstructed datacube, is represented with a thin red trace.	177
Figure 175 – Transmission spectra obtained from the datacube of the grape with 20.8 %Bx in the positions marked by the red, green and blue pixels in the image of Figure 172.	178
Figure 176 – Transmission spectra of the grape with 20.8 %Bx. The normalized real spectrum is represented with a thick black trace while the normalized integrated spectrum, obtained from the reconstructed datacube, is represented with a thin red trace.	179
Figure 177 – Normalized integrated transmission spectra of the three grapes, obtained from each of the respective datacubes.	179
Figure 178 – Scheme illustrating the principle of operation of the single-pixel imaging LIDAR system based on compressive sensing.	182

List of Tables

Table 1 – Comparison between the number of measurements required by the RPFSSI and FSSI systems to achieve the same RMSE-based performance.....	19
Table 2 – Comparison of the main aspects of DD-CASSI and SD-CASSI.	32
Table 3 – Equipment for the active illumination single-pixel imaging system.	60
Table 4 – PSNR values obtained for the reconstructed images of Figure 54 relatively to the images acquired with the conventional camera.	65
Table 5 – Maximum values of the normalized cross-correlation obtained for the reconstructed images of Figure 54 relatively to the images acquired with the conventional camera.	66
Table 6 – Time taken to perform 100% of the measurements needed to reconstruct the images with different resolutions, using the Epson® video projector to project the compressive codes.	67
Table 7 – Time consumed during reconstruction for different compression levels and different resolutions.	67
Table 8 – PSNR values obtained for the reconstructed images of Figure 57 relatively to the images acquired with the conventional camera.	69
Table 9 – Maximum values of the normalized cross-correlation obtained for the reconstructed images of Figure 57 relatively to the images acquired with the conventional camera.	69
Table 10 – Main specifications of the Nikon lens that accompanies the LightCommander.	71
Table 11 – PSNR values obtained for the reconstructed images of Figure 64 relatively to the images acquired with the conventional camera.	75
Table 12 – Maximum values of the normalized cross-correlation obtained for the reconstructed images of Figure 64 relatively to the images acquired with the conventional camera.	75
Table 13 – PSNR values obtained for the reconstructed images of Figure 65 relatively to the images acquired with the conventional camera.	76
Table 14 – Maximum values of the normalized cross-correlation obtained for the reconstructed images of Figure 65 relatively to the images acquired with the conventional camera.	77
Table 15 – Time taken to perform 100% of the measurements needed to reconstruct the images with different resolutions, using the Lightcommander's to project the compressive codes.	78

Table 16 – PSNR values obtained for the reconstructed images of Figure 81 relatively to the images acquired with the conventional camera.....	93
Table 17 – Maximum values of the normalized cross-correlation obtained for the reconstructed images of Figure 81 relatively to the images acquired with the conventional camera.....	93
Table 18 – PSNR values obtained for the reconstructed images of Figure 83 relatively to the images acquired with the conventional camera.....	96
Table 19 – Maximum values of the normalized cross-correlation obtained for the reconstructed images of Figure 83 relatively to the images acquired with the conventional camera.....	96
Table 20 – PSNR values obtained for the reconstructed images of Figure 86 relatively to the images acquired with the conventional camera.....	99
Table 21 – Maximum values of the normalized cross-correlation obtained for the reconstructed images of Figure 86 relatively to the images acquired with the conventional camera.....	99
Table 22 – PSNR values obtained for the reconstructed images of Figure 87 relatively to the images acquired with the conventional camera.....	101
Table 23 – Maximum values of the normalized cross-correlation obtained for the reconstructed images of Figure 87 relatively to the images acquired with the conventional camera.....	101
Table 24 – PSNR values obtained for the reconstructed images of Figure 92 relatively to the images acquired with the conventional camera.....	107
Table 25 – Maximum values of the normalized cross-correlation obtained for the reconstructed images of Figure 92 relatively to the images acquired with the conventional camera.....	107
Table 26 – PSNR values obtained for the reconstructed images of Figure 97 relatively to the images acquired with the conventional camera.....	112
Table 27 – Maximum values of the normalized cross-correlation obtained for the reconstructed images of Figure 97 relatively to the images acquired with the conventional camera.....	112
Table 28 – Noise equivalent power and maximum noise current for the PDA100A amplified photodiode when the gain of 50 dB or 60 dB was chosen.....	147

List of Acronyms

1D	– One-Dimensional
2D	– Two-Dimensional
3D	– Three-Dimensional
APD	– Avalanche PhotoDiode
CCD	– Charge-Coupled Device
CI	– Computational Imaging
CMOS	– Complementary Metal Oxide Semiconductor
CS	– Compressive Sensing
DLP	– Digital Light Processing
DMD	– Digital Micromirror Device
DWT	– Discrete Wavelet Transform
FOV	– Field Of View
FWHM	– Full Width at Half Maximum
HDR	– High Dynamic Range
HDRI	– High Dynamic Range Imaging
HDRCI	– High Dynamic Range Compressive Imaging
He-Ne	– Helium-Neon
HSI	– HyperSpectral Imaging
ILS	– Imaging LIDAR System
JPEG	– Joint Picture Experts Group
LCD	– Liquid Crystal Display
LC-SLM	– Liquid Crystal Spatial Light Modulator
LED	– Light Emitting Diode
LIDAR	– LIght Detection And Ranging
MOEMS	– Micro-Opto-Electro-Mechanical Systems
MP3	– Moving Picture Experts Group Layer-3 Audio
MRI	– Magnetic Resonance Imaging

MSE – Mean-Square-Error

Nd:YAG – Neodymium Yttrium Aluminum Garnet

OCT – Optical Coherence Tomography

Pixel – Picture (Pix) + Element

PMMW – Passive MilliMeter-Wave

PSNR – Peak Signal-to-Noise Ratio

PWM – Pulse-Width Modulation

QE – Quantum Efficiency

RGB – Red – Green – Blue color space

RIP – Restricted Isometry Principle

RMSE – Root-Mean-Square Error

SLM – Spatial Light Modulator

SNR – Signal-to-Noise Ratio

SVM – Support Vector Machine

THz – TeraHertz

Chapter 1. Introduction

It is clear that the Nyquist-Shannon sampling theorem has been a fundamental rule of signal processing for many years and can be found in nearly all signal acquisition protocols, being extensively used from consumer video and audio electronics to medical imaging devices or communication systems. Basically, it states that a band-limited input signal can be recovered without distortion if it is sampled at a rate of at least twice the bandwidth of the signal. For some signals, such as images that are not naturally band limited, the sampling rate is dictated not by the Nyquist-Shannon theorem but by the desired temporal or spatial resolution. However, it is common in such systems to use an anti-aliasing low-pass filter to band limit the signal before sampling it, and so the Nyquist-Shannon theorem plays an implicit role [1].

In the last few years, an alternative theory has emerged, showing that super-resolved signals and images can be reconstructed from far fewer data or measurements than what is usually considered necessary. This is the main concept of compressive sensing (CS), also known as compressed sensing, compressive sampling and sparse sampling. In fact, “the theory was so revolutionary when it was created a few years ago that an early paper outlining it was initially rejected on the basis that its claims appeared impossible to substantiate [2].”

CS relies on the empirical observation that many types of signals or images can be well approximated by a sparse expansion in terms of a suitable basis, that is, by only a small number of non-zero coefficients. This is the key aspect of many lossy compression techniques such as JPEG (Joint Picture Experts Group) and MP3 (Moving Picture Experts Group Layer-3 Audio), where compression is achieved by simply storing only the largest basis coefficients of a sparsifying transform.

In CS, since the number of samples taken is smaller than the number of coefficients in the full image or signal, converting the information back to the intended domain would involve solving an underdetermined matrix equation. Thus, there would be a huge number of candidate solutions and, as a result, a strategy to select the “best” solution must be found.

Different approaches to recover information from incomplete data sets have existed for several decades. One of its earliest applications was related with reflection seismology, in which a sparse reflection function (indicating meaningful changes between surface layers) was sought from band limited data [1, 3, 4]. It was, however, very recently, that the field has gained increasing attention, when Emmanuel J. Candès, Justin Romberg and Terence Tao [5], discovered that it was possible to reconstruct Magnetic Resonance Imaging (MRI) images from what appeared to be highly incomplete data sets in face of the Nyquist-Shannon criterion (see Figure 1). Following Candès *et al.* work, this decoding or reconstruction problem can be seen as an optimization problem and be efficiently solved using the ℓ_1 -norm [6] or the total-variation [7, 8].

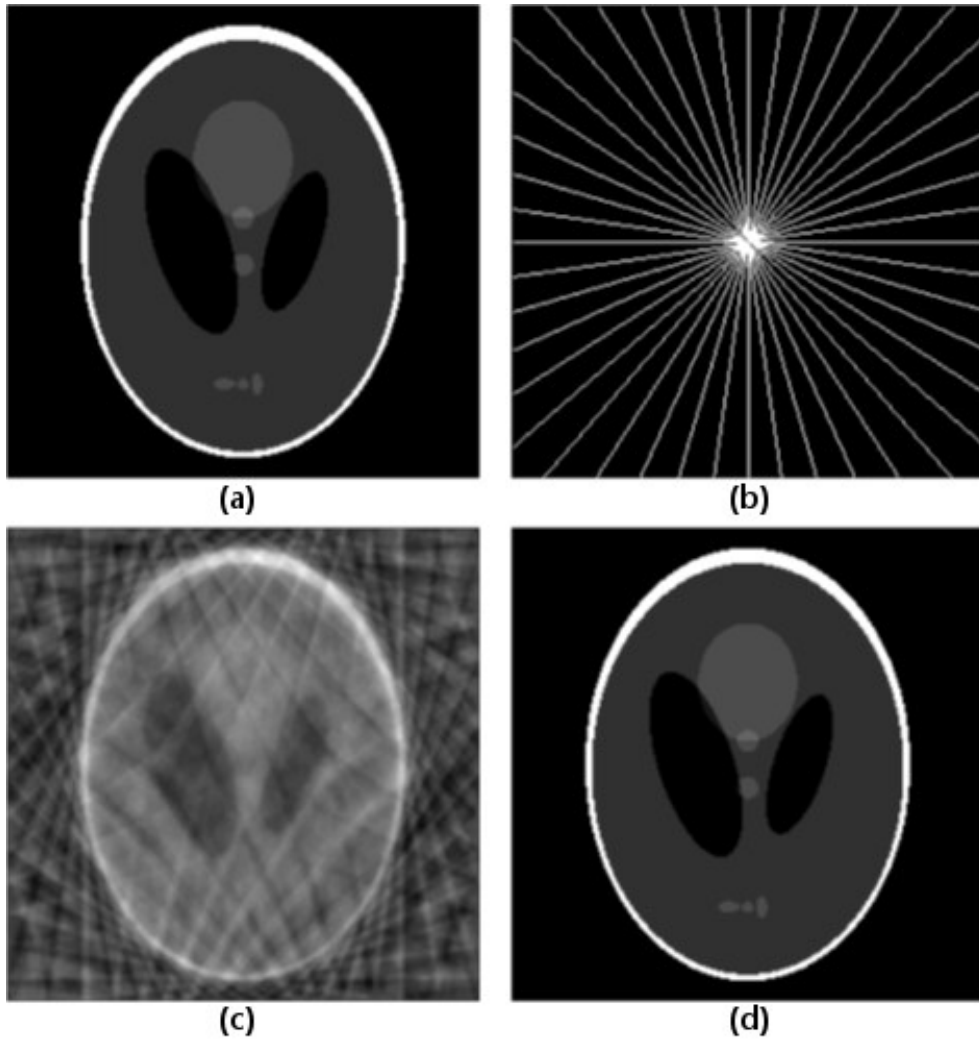


Figure 1 – Example of a simple recovery problem. (a) The Logan–Shepp phantom test image. (b) Sampling domain in the frequency plane; Fourier coefficients are sampled along 22 approximately radial lines. (c) Minimum energy reconstruction obtained by setting unobserved Fourier coefficients to zero. (d) Compressive sensing based reconstruction. This reconstruction is an exact replica of the original image in (a) [5].

As a result, CS has become a kind of revolutionary research topic that draws from diverse fields, such as mathematics, engineering, signal processing, probability and statistics, convex optimization, random matrix theory and computer science.

Undergoing significant advances, CS has proved to be far reaching and has enabled several applications in many fields, such as: distributed source coding in sensor networks [9, 10], coding, analog–digital (A/D) conversion, remote wireless sensing [1, 11], 3D LIDAR [12, 13] and inverse problems, such as those presented by MRI [14].

One application with particular interest within the aim of the work presented here, is the ground-breaking single-pixel imaging setup developed by D. Takhar *et al.* at the Rice University [15]. This camera represented a simple, compact and low cost solution that could operate efficiently across a much broader spectral range than conventional silicon based cameras.

1.1 Thesis structure

This thesis is divided in seven chapters as follows:

- **Chapter 1** presents the motivation and structure of the thesis. The main contributions and a record of publications are also enumerated.
- **Chapter 2** describes the mathematical background of compressive sensing theory along with its main properties;
- **Chapter 3** reviews the evolution of compressive sensing based imaging systems;
- **Chapter 4** expounds the core work of this thesis. It describes the experimental work and results associated with the development of compressive single-pixel imaging systems for different imaging modalities. An algorithm that can concede a compressive sensing based operation mode to a CMOS imager is also presented.
- **Chapter 5** exemplifies distinct applications for two of the compressive single-pixel imaging systems described in Chapter 4.
- **Chapter 6** exposes one prospective idea for future pursuance aiming the reinforcement and exploitation of the competencies inherited from the work presented in this thesis.
- **Chapter 7** closes the thesis with some concluding remarks.

1.2 Motivation

In a technological era where commercial cameras have reached tens of Megapixels, the theory of compressive sensing has emerged as a new paradigm which has been particularly materialized in the form of single-pixel cameras that operate, at least on a first look, in a counter intuitive manner.

Based on compressive sensing, single-pixel cameras can reconstruct images from fewer data than what is usually considered necessary. This creates the potential to perform faster still ensuring the quality of the results. Additionally, with these cameras, the information is gathered in an encrypted form right from the moment it is acquired, therefore bringing advantages in terms of storage/transmission and security. Their principle of operation places most of the complexity on the decoding end, which typically possesses more resources and can be improved disregarding the subtleties of the data acquired and provide even better reconstruction results with the same data.

Because of their versatility different light detection devices may be used, which brings benefits in terms of sensitivity and signal quality. Furthermore, these cameras created opportunities to operate with increased spectral resolution in wavelengths that were practically impossible or very expensive before.

For certain applications these cameras may even represent the only available solution.

From a personal point of view, despite the particularly exploratory nature of the subject, it was with great pleasure and enthusiasm that I have embraced it. It constituted an opportunity to further extend my knowledge and to work in such a revolutionary and novel theme as that of compressive sensing. Having in mind the risks and implications of such decision, the initially posed challenge has been turned into an extremely rewarding experience that will certainly contribute to my personal and professional future as well as to the future of the research group.

1.3 Contributions

At an institutional level it should be said that the work presented in this thesis stimulated the establishment of a new research and actuation area inside the Optoelectronics and Electronic Systems Unit at INESC TEC. Besides the direct benefits this aspect raised in terms of innovation and creation of knowledge, it also helped to reinforce the privileged position INESC TEC has been setting for long in the scientific community. In concrete terms, new cooperation opportunities have been initiated with the European Space Agency; with universities from different countries, namely, the University of North Carolina at Charlotte (USA); the University of Minho (Portugal); the University Jaume I (Spain), and with industrial partners, to explore applications of the knowledge gathered with this work.

Concerning the theme of this thesis the following main contributions can be enumerated. Several different compressive single-pixel imaging systems have been developed, methodically characterized and compared. These systems were capable of acquiring monochrome, color, multispectral, hyperspectral and high dynamic range images, operating either in a passive or in an active illumination mode.

Emphasis should be directed towards the implemented active illumination single-pixel monochrome imaging system, which was the first to present a compressive sensing based principle of operation and that enabled the subsequent development of active illumination compressive single-pixel imaging systems for different modalities (color, multispectral, hyperspectral and high dynamic range).

A high dynamic range imaging system using an LCD for the spatial control of the image intensity was implemented. The knowledge gathered with this system would later be used for the development of an innovative high dynamic range compressive imaging technique, as will be exposed further below in this text.

A transmissive compressive single-pixel imaging system has also been developed and used to acquire microscopic images. To the extent of our knowledge, we were the first to present an imaging system that used an LCD to incorporate the compressive random binary codes into the system and produce the incoherent projections characteristic of compressive imaging. The development of this system has given us an adequate insight to compare LCD with DMD as spatial light modulators for compressive single-pixel cameras.

Even though we have not been the first to implement a passive illumination compressive sensing based monochrome single-pixel imaging system, we have explored it and improved it to work for the acquisition of color, multispectral, hyperspectral and high dynamic range images.

Perhaps, both the passive and the active illumination compressive single-pixel hyperspectral imaging systems may be considered the major contributions resulting from this work in the sense that they allow the acquisition of high spectral resolution hyperspectral images to be performed in a simple manner and empower the development of fast hyperspectral cameras that do not require any scanning. In particular, it has been demonstrated a hyperspectral compressive single-pixel imaging system with a spectral resolution of 10 nm, which represents an improvement of two orders of magnitude relatively to the best systems available on the market. Such a camera may find applications in different fields and enable its users to acquire images that were before practically impossible or very difficult or expensive to obtain.

High dynamic range imaging and compressive imaging have been combined for the first time, with the combination benefitting from the advantages of both techniques. Both in active and in passive illumination mode, it was demonstrated that the new imaging modality could successfully reconstruct images with increased dynamic range disregarding the need for any geometrical calibration. Two different techniques have been presented and demonstrated for this purpose.

We have also developed and demonstrated an algorithm for the generation of compressive codes, which has been particularly addressed to take benefit of the hardware configuration of a CMOS imager and provide it with a compressive imaging mode of operation. Based in this work a Provisional Patent Request has been submitted.

The gathered knowledge and some of the developed compressive single-pixel imaging systems have also been explored in three different applications. The passive illumination monochrome single-pixel imaging system has been used to acquire microscopic images. Its potential has been demonstrated with the acquisition of 128×128 pixels images which yielded a spatial resolution of 42.19 $\mu\text{m}/\text{pixel}$.

A preliminary feasibility analysis of a face detection system without explicit image reconstruction, that combined compressive sensing with machine learning and pattern recognition tools, was also conducted. The detection results yielded a detection error rate as low as 3% with less than 3% of the compressive measurements and were better than those obtained with a state-of-the-art feature detector and descriptor. The passive illumination single-pixel monochrome imaging system has been used in this context to acquire real world data and evaluate the potential of this innovative framework.

The passive illumination single-pixel hyperspectral imaging system has been used to gather spectroscopic data of grapes derived from hyperspectral images. These data can be used for the analysis and assessment of the physicochemical properties of the grapes.

Some prospects were also provided for the future development of a single-pixel imaging LIDAR system based on compressive sensing to be used by the European Space Agency.

1.4 Publications

Next, it is presented a record of the publications deriving from the work presented in this thesis. These have been divided into journal and conference publications and are listed in reverse chronological order.

Journal

- F. Magalhães, M. Abolbashari, F. M. Araújo, M. V. Correia, F. Faramarz, *High-resolution hyperspectral single-pixel imaging system based on compressive sensing*, in Optical Engineering, 2012. 51(7): p. 071406, DOI: 10.1117/1.OE.51.7.071406.
- M. Abolbashari, F. Magalhães, F. M. Araújo, M. V. Correia, F. Faramarz, *High dynamic range compressive imaging: a programmable imaging system*, in Optical Engineering, 2012. 51(7): p. 071407, DOI: 10.1117/1.OE.51.7.071407.
- F. Magalhães, M. Abolbashari, F. M. Araújo, M. V. Correia, F. Faramarz, *Active Illumination Single-Pixel Camera Based on Compressive Sensing*, in Applied Optics, 2011. 50(4): pp. 405-414, DOI: 10.1364/AO.50.000405.

Conference

- F. Magalhães, R. Sousa, F. M. Araújo, M. V. Correia, *Compressive Sensing based Face Detection without Explicit Image Reconstruction using Support Vector Machines*, in ICIAR 2013: X International Conference on Image Analysis and Recognition, 26-28 June, 2013, Póvoa de Varzim, Portugal.
- F. Magalhães, M. Abolbashari, F. M. Araújo, F. Farahi, M. V. Correia, *Single-pixel hyperspectral camera based on compressive sensing*, StudECE-1st PhD Students Conference in Electrical and Computer Engineering, Porto, Portugal, 28-29 June, 2012.
- F. Magalhães, H. Gonçalves, F. M. Araújo, V. G. Tavares, M. V. Correia, *MicroEye - Imager with compressive sensing capability*, StudECE-1st PhD Students Conference in Electrical and Computer Engineering, Porto, Portugal, 28 - 29 June, 2012.
- M. Abolbashari, G. Babaie, F. Magalhães, M. V. Correia, F. M. Araújo, A. S. Gerges, F. Farahi, *Biological imaging with high dynamic range using compressive imaging technique*, in Photonics West 2012, BIOS 8225-71, 21-26/January, 2012, San Francisco, USA, DOI: 10.1117/12.907365.
- F. Magalhães, M. Abolbashari, F. Faramarz, F. M. Araújo, M. V. Correia, *A compressive sensing based transmissive single-pixel camera*, in AOP 2011 - International Conference on Applications of Optics and Photonics, 3-7/May , 2011, Braga, Portugal, DOI: 10.1117/12.891940.
- F. Magalhães, F. M. Araújo, M. V. Correia, *An active illumination single-pixel camera based on compressive sensing*, in Ciência 2010 - Encontro com a Ciência e a Tecnologia em Portugal. 4-7/July/2010. Lisbon - Portugal. (poster)

Chapter 2. The Theory of Compressive Sensing – An Overview

In order to become possible, CS is built upon two principles: sparsity, related with the signals of interest, and incoherence, related with the sensing modality. In the following sub-sections, these two subjects are presented and analyzed in detail. Then, the principles behind CS are presented along with its main properties. In the end, the robustness of compressive sensing to measurement errors and noise is analyzed.

2.1 K -sparse and compressible signals

Let's consider a real-valued, finite-length, one dimensional, discrete-time signal x , which can be viewed as a $N \times 1$ column vector in \Re^N with elements $x[n]$, where $n=1,2,\dots,N$. Any signal in \Re^N can be represented in terms of a basis of $N \times 1$ vectors $\{\psi_i\}_{i=1}^N$. For simplicity, let's assume that the basis is orthonormal. Using the $N \times N$ basis matrix $\Psi = \{\psi_1, \psi_2, \dots, \psi_N\}$ with the vectors $\{\psi_i\}$ as columns, a signal x can be expressed as:

$$x = \sum_{i=1}^N s_i \psi_i \text{ or } x = \Psi s, \quad (1)$$

where s is the $N \times 1$ column vector of weighting coefficients $s_i = \langle x, \psi_i \rangle = \psi_i^T x$. s and x are equivalent representations of the signal with x in time or space domain and s in Ψ domain.

The signal x is K -sparse if it is a linear combination of only K basis vectors, which means that only K of the s_i coefficients in equation (1) are nonzero, while the remaining $(N-K)$ coefficients are null. In addition, the signal x is compressible if the representation in Eq. (1) has just a few large coefficients and many small coefficients, setting the basis of transform coding. Therefore, we can say that a signal x is sparse in the Ψ domain if the coefficient sequence is supported on a small set, and compressible if the sequence is concentrated near a small set.

In face of the typical data acquisition paradigm, huge amounts of data are collected only to be in large part discarded at the compression stage to facilitate storage and transmission. Imagine, for example, a digital camera that captures images with millions of sensors (pixels) but eventually encodes the image in just a few hundred kilobytes. Clearly, this is a tremendously wasteful process and suffers from three principal drawbacks. First, the initial number of samples N may be large, even if the desired K is small. Second, the set of all N transform coefficients $\{s_i\}$ must be computed even though all but K of them will be discarded. Third, there is an overhead that is introduced by the encoding of the large coefficients locations.

2.2 Recovering K -sparse signals

Following the work presented in [16], Candès and Tao developed a refined version of the *Uniform Uncertainty Principle* (UUP) [17], which has proved to be essential to the study of the general robustness of CS. This key notion was then named *Restricted Isometry Property* (RIP) and can be defined as follows:

For each integer $K=1,2,\dots$, define the isometry constant δ_K of a measurement matrix A as the smallest number such that

$$(1-\delta_K)\|x\|_{\ell_2}^2 \leq \|Ax\|_{\ell_2}^2 \leq (1+\delta_K)\|x\|_{\ell_2}^2 \quad (2)$$

holds for all K -sparse vectors x . Therefore, we can say that a matrix A obeys the RIP of order K if δ_K differs enough from one. When this condition is verified, A approximately preserves the Euclidean length of K -sparse signals, which in turn implies that K -sparse vectors cannot be in the null space of A . An alternative description of this property is to say that all subsets of K columns taken from A are in fact nearly orthogonal (they cannot be exactly orthogonal since we have more columns than rows).

Let's imagine we want to acquire K -sparse signals making use of matrix A . Suppose that δ_{2K} is sufficiently smaller than one. This indicates that all pair-wise distances between K -sparse signals must be well preserved in the measurement space, which means that

$$(1-\delta_{2K})\|x_1 - x_2\|_{\ell_2}^2 \leq \|Ax_1 - Ax_2\|_{\ell_2}^2 \leq (1+\delta_{2K})\|x_1 - x_2\|_{\ell_2}^2 \quad (3)$$

is true for all K -sparse vectors x_1, x_2 [1, 18].

2.3 Incoherence

Let's now consider $M < N$ linear measurements of x and a collection of test functions $\{\varphi_m\}_{m=1}^M$ such that $y[m] = \langle x, \varphi_m \rangle$. By stacking the measurements $y[m]$ into the $M \times 1$ vector y and the test functions φ_m^T as rows into an $M \times N$ sensing matrix Φ we can write

$$y = \Phi x = \Phi \Psi s = \Theta s \quad (4)$$

A condition related with RIP is incoherence, which requires that the rows of Φ (the measurement or sensing matrix) cannot represent the columns of Ψ in a sparse way (and vice-versa).

Incoherence extends the duality between time and frequency and expresses the idea that an object having a sparse representation in Ψ must be spread out in the domain in which it was acquired. This incoherence property is verified for many pairs of bases, including, for instance, delta spikes and sine waves of the Fourier basis, or the Fourier basis and noiselets.

The coherence between the sensing basis Φ and the representation basis Ψ can be given by the following equation:

$$\mu(\Phi, \Psi) = \sqrt{n} \cdot \max_{1 \leq k, j \leq n} \left| \langle \phi_k, \psi_j \rangle \right|, \quad (5)$$

which, in simple words, is measuring the largest correlation between any two elements of Φ and Ψ . CS is essentially interested in low coherence pairs. For instance, for the previously referred delta spikes and sine waves (time-frequency) pair, $\mu(\Phi, \Psi) = 1$, therefore, indicating maximal incoherence [1, 19].

A particular aspect of interest is that random matrices are largely incoherent with any fixed basis Ψ . This enables the use of known fast transforms such as a Walsh, Hadamard, or Noiselet transform [20].

Furthermore, what is most remarkable about this concept is that it allows capturing information contained in a sparse signal in a very efficient way without trying to understand that signal. In other words, it is not required to know about the details of the signal being acquired.

2.4 How compressive sensing works

Compressive sensing addresses the inefficiencies presented by the *sample-then-compress* framework by directly acquiring a compressed signal representation, avoiding the intermediate stage of acquiring N samples [5]. CS bypasses the sampling process and directly acquires a condensed representation y consisting of M linear measurements. Furthermore, the measurement process is nonadaptive in that Φ does not depend in any way on the signal x .

The transformation from x to y is a dimensionality reduction and so implies the loss of information in general. In particular, since $M < N$, for a given y , there is an infinite number of x' such that $\Phi x' = y$, if there is no restriction on x' . The overwhelming capacity of CS is that Φ can be designed such that sparse/compressible x can be recovered exactly/approximately from measurements of y .

To recover the signal \mathbf{x} from the random measurements of \mathbf{y} , the traditional preferred method of least squares has been shown to fail with high probability. Instead, it has been demonstrated that minimizing the ℓ_1 -norm [16]:

$$\hat{\mathbf{s}} = \arg \min \|\mathbf{s}'\|_{\ell_1} \text{ such that } \Theta \mathbf{s}' = \mathbf{y} \quad (6)$$

$$\text{given that } \|\mathbf{s}'\|_{\ell_1} := \sum_i |s'_i| \quad , \quad (7)$$

it is possible to exactly reconstruct K -sparse vectors and closely approximate compressible vectors stably with high probability using just $M \geq O(K \cdot \log(N/K))$ random measurements [5, 6]. Minimizing the ℓ_1 -norm subject to linear equality constraints can easily be recast as a linear program, also known as basis pursuit, which can find several alternative reconstruction techniques based on greedy, stochastic and variational algorithms [5, 11, 21, 22].

As it has been referred, in compressive sensing, since we are in the presence of an underdetermined equation system, simply invert a transform is not enough. In the particular context of compressive imaging, there are many configurations of pixels that could explain what have been measured. However, very few of these exhibit the structure expected in a real-world image. Fortunately, there are various popular models to quantify this structure. One model, motivated by the achievements in image compression, is, for instance, sparsity in the wavelet domain. Next, from a geometric standpoint, it will be illustrated why ℓ_2 reconstruction fails to find the sparse solution that can be identified by ℓ_1 reconstruction. Figure 2 presents significant information to this subject. Part (a) illustrates the ℓ_2 ball in \mathfrak{R}^3 with a certain radius. It must be emphasized that this ball is isotropic. Part (b) represents the ℓ_1 ball in \mathfrak{R}^3 , which is anisotropic (“pointy” along the axes).

The ℓ_2 minimizer $\hat{\mathbf{s}}$ is the point from \mathbf{H} closest to the origin. This point can be found by blowing the ℓ_2 ball until it bumps into \mathbf{H} . Due to the random orientation of \mathbf{H} (imposed by the randomness in matrix Θ), the closest point $\hat{\mathbf{s}}$ will be away from the coordinate axes with high probability and, therefore, will not be sparse and will be far from the sparsest answer \mathbf{s} (only one of its components is non-zero). In higher dimensions, this difference becomes even more significant. Paying attention to the part (b) of Figure 2, it can be seen that the point of intersection $\hat{\mathbf{s}}$ is now defined by the vector that solves equation (6).

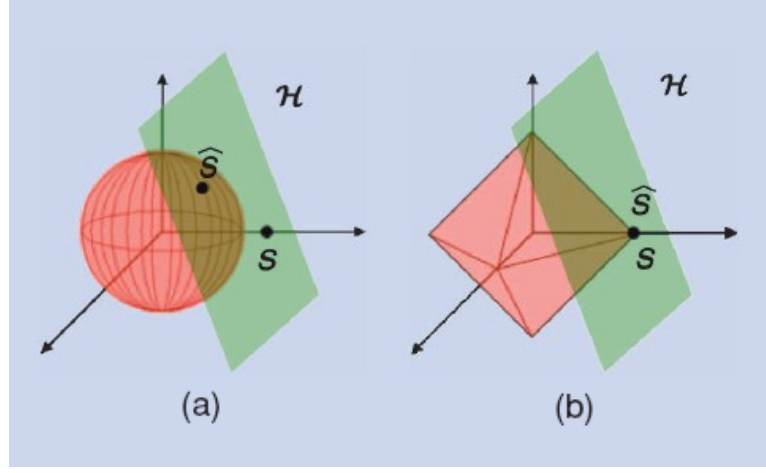


Figure 2 – Geometry of ℓ_1 recovery. (a) Visualization of the ℓ_2 minimization that finds the non-sparse point of contact $\hat{\mathbf{s}}$ between the ℓ_2 ball (hypersphere, in red) and the translated measurement matrix null space (in green). (b) Visualization of the ℓ_1 minimization solution that finds the sparse point of contact $\hat{\mathbf{s}}$ with high probability thanks to the pointiness of the ℓ_1 ball. Picture adapted from [19].

Another model, and one which tends to produce slightly better results in practice, assumes that typical images tend to have small total-variation (TV) compared to their energy [7, 8]. The total-variation of an $N \times N$ pixels image \mathbf{x} is given by:

$$TV(\mathbf{x}) = \sum_{i,j=1}^N \sqrt{(x_{i+1,j} - x_{i,j})^2 + (x_{i,j+1} - x_{i,j})^2} \quad (8)$$

The recovery procedure then searches for the image with smallest total-variation which explains the observed values.

In addition to enabling sub-Nyquist sampling, CS exhibits a number of attractive properties.

- **Universality:** Φ can be considered a universal encoding strategy, as it does not need to be designed with regards to the structure of Ψ . This allows exactly the same encoding strategy to be applied in a variety of different sensing environments; no knowledge is required about the subtleties of the data being acquired. Random measurements are also future proof – i.e., if new research yields a better sparsity inducing basis, then the same set of random measurements can be used to reconstruct data with even better quality –.
- **Encryption:** A pseudorandom basis can be generated using a simple algorithm according to a random seed. Such encoding effectively implements a form of

encryption: randomized measurements will themselves resemble noise and be meaningless to an observer without knowledge of the associated seed.

- **Robustness and progressivity:** Random coding is robust in that the randomized measurements have equal priority, unlike the Fourier or wavelet coefficients in current transform coders. Thus, this enables progressively better data reconstruction as more measurements are obtained. Besides this, one or more measurements can also be lost without corrupting the entire reconstruction. Oppositely, since the bits in JPEG 2000 do not have all the same value, if important bits are missing – e.g., because of packet loss –, then it is impossible to retrieve the information accurately.
- **Scalability:** the number of measurements to compute can be adaptively selected in order to trade off the amount of compression of the acquired image versus acquisition time. In contrast, conventional cameras trade off resolution versus the number of pixel sensors.
- **Computational asymmetry:** CS places most of its computational complexity in the recovery system (decoder), which will often have more substantial computational resources than the encoder. The encoder is very simple since it merely computes incoherent projections and makes no decisions [15].

2.5 Robustness of compressive sensing

In any realistic application, we cannot expect to measure Φx without any error. Therefore, now, it is important to analyze the robustness of compressive sampling in face of measurement errors. This is a critical topic since any real-world sensor is subject to noise. For that reason, one immediately understands that to be widely applicable, the methodology needs to be stable. Small perturbations in the observed data should, then, induce only small perturbations in the reconstruction. Fortunately, the recovery procedures may be adapted to be surprisingly stable and robust in the presence of arbitrary perturbations.

Let's suppose the measurements are affected by noise and define the following model:

$$y = \Phi x + e, \tag{9}$$

where e is a stochastic or deterministic error term with bounded energy $\|e\|_{\ell_2} \leq \varepsilon$, being ε an upper bound on the noise magnitude.

Because of the measurement inaccuracies, a modification has been introduced to equation (6) to make it noise-aware. In this way, the reconstruction proposal has the following form:

$$\hat{s} = \arg \min \|s\|_{\ell_1} \text{ such that } \|y - \Phi \Psi s\|_{\ell_2} < \varepsilon, \quad (10)$$

which satisfies $\|\hat{s} - s\|_{\ell_2} < C_N \varepsilon + C_K \sigma_K(x)$ with overwhelming probability. C_N and C_K are the noise and approximation error amplification constants, respectively, and $\sigma_K(x)$ is the ℓ_2 error incurred by approximating s using its largest K terms. Once again, this problem is convex and can be solved using standard convex programming algorithms [18, 23].

Chapter 3. Compressive Imaging Systems – A Review

In this chapter, a chronologically ordered review of the main contributions to the subject of compressive imaging is presented along with their key features and outcomes.

Recent work in the emerging field of compressive sensing indicates that, when feasible, well-judged selection of the type of distortion induced by measurement systems may dramatically improve reconstruction results. The basic idea of this theory is that when the signal of interest is very sparse or compressible, relatively few incoherent observations are necessary to reconstruct the most significant non-zero signal components. However, applying this theory to practical imaging systems is very challenging in face of several requirements and measurement constraints. Therefore, in the following sub-sections several systems that can be seen as the state-of-the-art in the field of compressive sensing imagers are described and analyzed along with the strategies implemented to overcome these challenges.

The first work here presented corresponds to the breakthrough single-pixel camera from Rice University which was in the base of the foreseen developments in this area of research and application.

3.1 The single-pixel camera

The single-pixel camera, developed originally at the Rice University [15], is one of the most paramount examples of CS. It can be seen as an optical computer comprising a digital micro-mirror device (DMD) with an array of 1024×768 micromirrors, two lenses, a single photodiode and an analog-to-digital (A/D) converter. Basically, this configuration computes random linear measurements of the scene under view. The image is then reconstructed from these measurements by a digital computer. A block-diagram depicting the single-pixel camera setup can be seen in Figure 3.

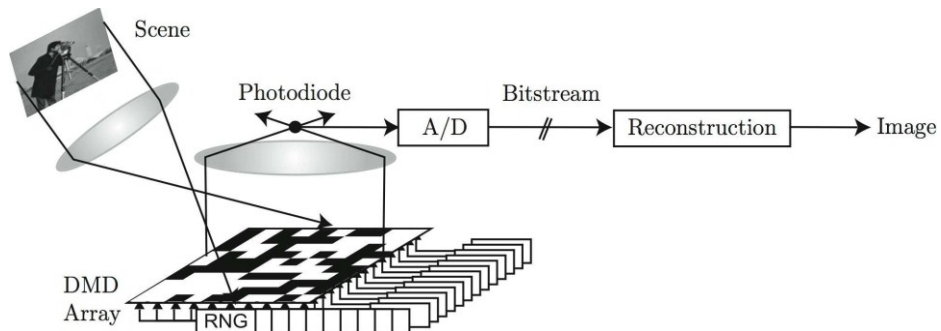


Figure 3 – Single-Pixel Camera block-diagram. Incident light field (corresponding to the desired image \mathbf{x}) is reflected off a DMD array whose mirror orientations are modulated by a pseudorandom pattern. Each different mirror pattern produces a voltage at the single photodiode that corresponds to one measurement $y[m]$. From M measurements a sparse approximation to the desired image \mathbf{x} using CS techniques can be obtained. Picture reproduced from [15].

This time-multiplexing technique enables the use of a single and yet more efficient photon detector in contrast with the individual pixel in the array counterpart. This is particularly important when the detector is expensive, making an N-pixel array/matrix prohibitive. Furthermore, sometimes these N-pixel arrays/matrices are simply not available due to technological constraints. A single-pixel camera can also be adapted to acquire images at wavelengths that are currently impossible with conventional digital cameras.

Figure 4 presents the experimental setup comprising the optical hardware of the single-pixel camera previously described. Following the red arrows in Figure 4, it can be seen that a light source is used to illuminate the object (in this case, a black and white printout of an “R” character). Then, the object’s image is formed by means of Lens 1 on the DMD that adequately reflects or not the light incident on each of its pixels towards the detector, depending on the imposed spatial modulation pattern. The light collected by Lens 2 will finally be concentrated on the single light detector that will integrate it, thus, yielding an output voltage that depends on the used DMD modulation pattern. This voltage is amplified through an operational amplifier circuit to be finally digitized by an A/D converter. This process is repeated until M values are acquired so that we can, finally, use them to reconstruct the imaged object. Each of these values (output voltage of the photodiode) can be interpreted as the inner product of the desired image x with a two-dimensional measurement basis $\Phi(m), m=1,2,\dots,M$.

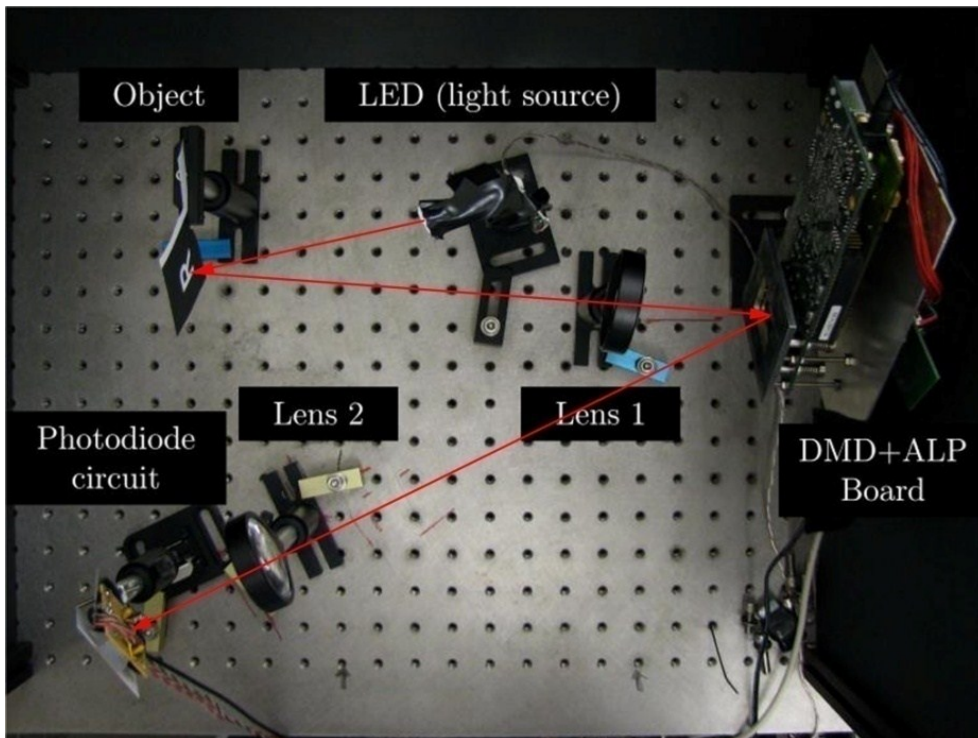


Figure 4 – Optical setup of the single-pixel camera developed at the Rice University. Picture reproduced from [15].

With this arrangement the resolution of the reconstructed image is defined by the resolution of the random binary codes applied to the DMD.

3.2 Feature-specific structured imaging system

The physical measurements that are obtained by a computational imaging (CI) system can often be interpreted as projections or features of the object space. The overall CI system may therefore be viewed as an optical feature extraction module followed by a module for the computational feature exploitation.

Several features have been used in the past, such as: random projections [24], discrete cosine projections [25] and principal and independent components [26, 27].

Deriving from CI paradigm several benefits have been quantified, namely, reduced hardware complexity, improved signal-to-noise ratio (SNR), faster frame rates and higher feature fidelity resulting in improvements of the reconstruction quality and/or task performance (e.g., recognition rate) compared to conventional imagers.

Often, this previous work on feature-specific CI relied on passive illumination imaging modalities, rather than those making use of active illumination. Passive illumination imaging modalities rely on ambient illumination, while the active illumination ones use structured illumination that can be either temporally structured (e.g., pulses and/or coded waveforms) [28, 29] or spatially structured (e.g., depth map extraction for 3D imaging) [30].

Following this approach, Baheti and Neifeld presented a feature-specific imaging system based on the use of structured light [31]. The illumination patterns used in their system are based on principal component features and the features' measurements they obtain correspond to the light reflected from an object over which the spatially structured illumination has been projected. The reflected light is then gathered by a single photodetector. The system flow diagram can be seen on Figure 5.

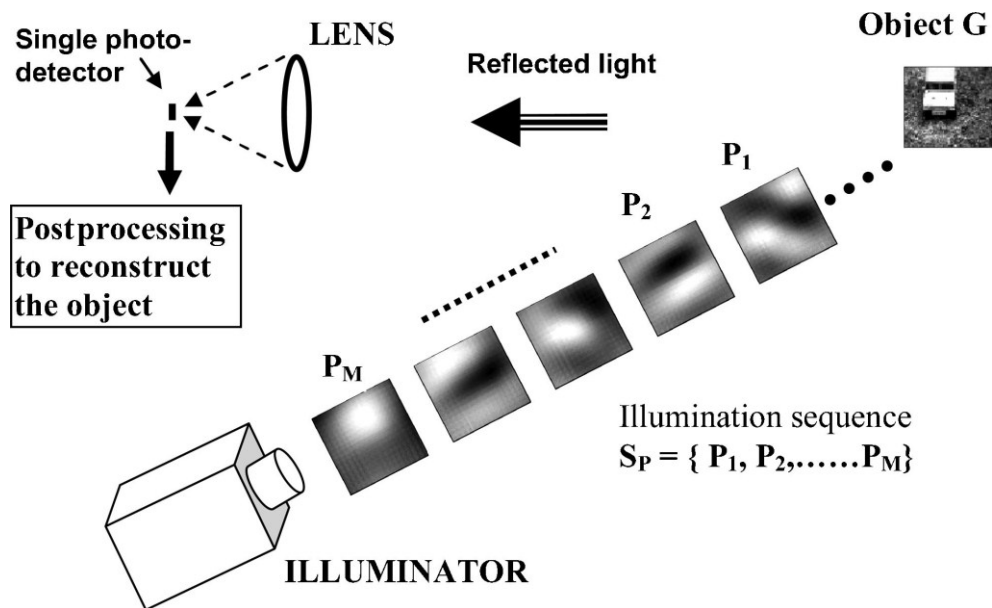


Figure 5 – Flow diagram for the Feature-Specific Structured Imaging (FSSI) system. Picture reproduced from [31].

As shown in Figure 5, after the projection and measurement steps, there is a post-processing phase, whose goal is to provide an estimate of the object reflectance function that is quantified by its Mean-Square-Error (MSE).

When compared to conventional imagers this system yielded far better results, with potential benefits in terms of hardware complexity, costs, SNR, frame rate and/or bandwidth. In particular, the feature-specific structured imaging (FSSI) system is capable of providing significant Root-Mean-Square Error (RMSE) reduction within a high-noise environment, providing a 38% RMSE reduction and requiring 400 times fewer measurements (for a noise standard deviation of 0.002), when compared to the optimal Linear Minimum MSE (LMMSE) post-processing of a conventional image.

3.3 Random projections based feature-specific structured imaging

Following the work presented in Section 3.2, shortly after, Baheti and Neifield presented a FSSI system whose illumination patterns were defined using random binary patterns [32]. In this case, following more closely the style of compressive sensing, the illumination system does not require prior knowledge about the object being imaged and the object estimates are generated using ℓ_1 -norm minimization and gradient-projection sparse reconstruction algorithms [33]. In particular, their experiments have shown the feasibility of the proposed approach by using 42% fewer measurements than the object dimensionality.

The benefits of this system over the passive compressive single-pixel imaging architecture presented by the Rice University [15] are twofold: first, the active modality enables imaging with zero ambient light levels, and, second, the active modality reduces the complexity of the light-collection hardware.

The advantage of this work compared to the FSSI system presented in Section 3.2 is that the measurement mechanism uses a Random Projections (RP) basis and so does not depend on the object. However, as presented in detail in Section 2.3, in the light of compressive sensing theory, the reconstruction fidelity is dependent on the incoherence between the RP basis and the basis in which the object is sparse [6, 20].

Figure 6 depicts the approach previously described. The main differences between this and the FSSI are the active illumination patterns and the reconstruction phase, which in the latter case relies on non-linear methods.

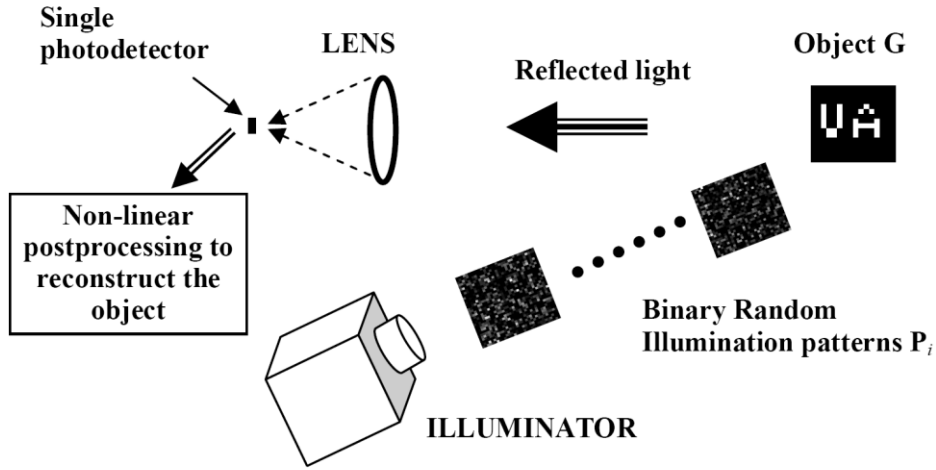


Figure 6 – Flow diagram for the binary Random Projections FSSI (RPFSSI) system. Picture reproduced from [32].

Since no prior knowledge about the object reflectance profile is used, the cost of this “ignorance” is reflected by the increased number of measurements that the RPFSSI requires to outcome with the same RMSE of the FSSI system, as can be found on Table 1.

Table 1 – Comparison between the number of measurements required by the RPFSSI and FSSI systems to achieve the same RMSE-based performance.

RMSE	Number of measurements	
	RPFSSI	FSSI
0.212	150	1
0.204	200	2
0.192	300	4
0.173	400	6
0.168	500	7
0.163	600	9

3.4 Compressed sensing magnetic resonance imaging

Imaging speed has always been a critical issue in Magnetic Resonance Imaging (MRI) and the development of methods to reduce the amount of acquired data without degrading the image quality has always been desired. This quest turns this problem particularly attractive for compressive sensing and as a result, in 2007, Lustig, Donoho and Pauly [34] combined CS with MRI, exploiting the implicit sparsity of this type of images. The transform sparsity of MR images can be demonstrated by applying a sparsifying transform, such as the discrete wavelet transform (DWT) [35], to a fully sampled image and reconstructing an approximation to the image from a

subset of the largest transform coefficients. The sparsity of the image then corresponds to the percentage of transform coefficients that are sufficient for a reconstruction that has enough quality for diagnostic purposes.

MRI and CS tend to naturally fit since the transform sparsity of MR images and the coded acquisition process used in MRI match with two fundamental properties of CS. As it has already been explained in this thesis, in CS one measures a relatively small number of random linear combinations of the signal values, but as the underlying signal is sparse/compressible it can be reconstructed with good accuracy from relatively few measurements by a nonlinear procedure. In CS-MRI, we are in the presence of a special case of CS where the sampled linear combinations are simply individual Fourier coefficients. The work of Candès, Romberg, and Tao [5] was motivated in large part by MRI since it looked at random undersampling of Fourier coefficients.

Designing a CS scheme for MRI can now be viewed as selecting a subset of the frequency domain that can be efficiently sampled and is incoherent with respect to the sparsifying transform. Figure 7 depicts a scheme of a compressive sensing based MRI system. There it can be seen that incoherent measurements in the frequency domain can be obtained from the control of the gradient waveforms and RF pulses of the MRI system. Those measurements can then be used to reconstruct an image using an appropriate nonlinear reconstruction method with sparsity constraints.

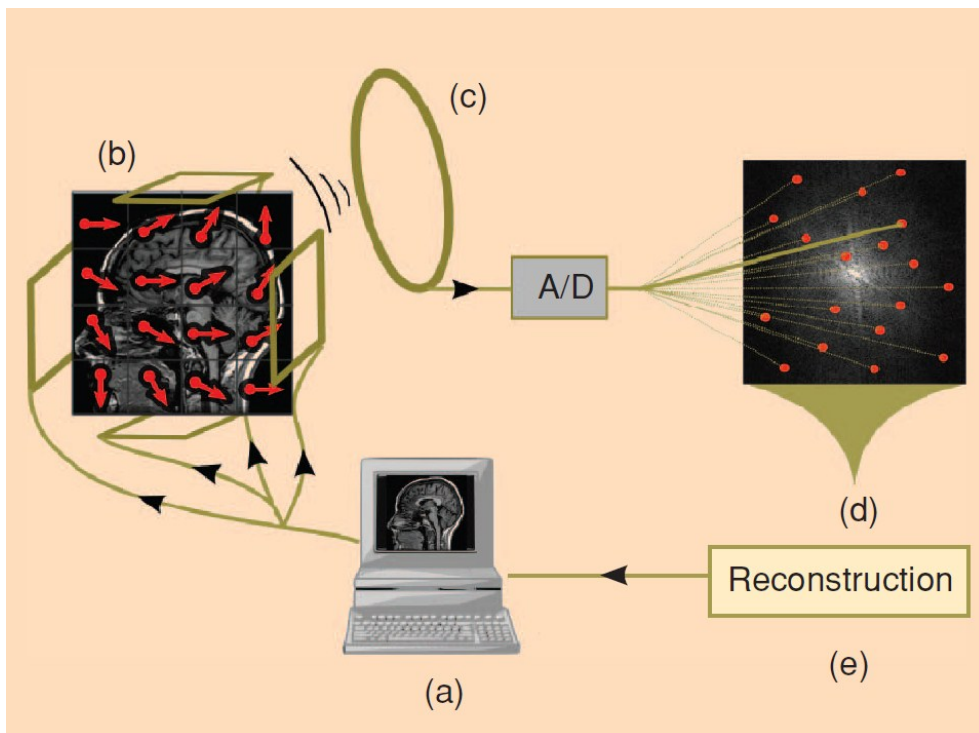


Figure 7 – Scheme of a CS based MRI system. The user controls the gradient waveforms and RF pulses (block (a)) that, in turn, control the phase of the pixels/voxels (block (b)) in the image. An RF coil receives the signal in an encoded form (block (c)). The incoherent measurements result from the control of the gradient waveforms (block (d)). An image can then be reconstructed with an appropriate nonlinear reconstruction enforcing sparsity (block (e)). Picture reproduced from [36].

The authors have explored this concept in four applications (rapid 3D angiography; whole-heart coronary imaging; brain imaging and dynamic heart imaging) and have highlighted the way in which different applications face different constraints, imposed either by MRI scanning hardware or by patient considerations, and how the inherent freedom of CS to choose the trajectories for sampling and sparsifying transforms plays a crucial role in matching those constraints [34, 36].

Next, the results obtained for two of those applications are displayed and discussed.

Angiograms are inherently sparse in the pixel representation and also if they are target of spatial finite differencing. The need for high temporal and spatial resolution strongly encourages undersampling. CS was able to improve current strategies by significantly reducing the artifacts that result from undersampling. In the example shown in Figure 8, the authors have applied CS to 3D Cartesian contrast enhanced angiography. Selecting a pseudorandom subset they have combined undersampling (10-fold) with low coherence. CS was able to significantly accelerate MR angiography, enabling better temporal resolution or alternatively improving the resolution of current imagery without compromising scan time. Additionally, most of the artifacts that appeared in the linear reconstruction from undersampled data were not present in the CS nonlinear reconstruction [34, 36].

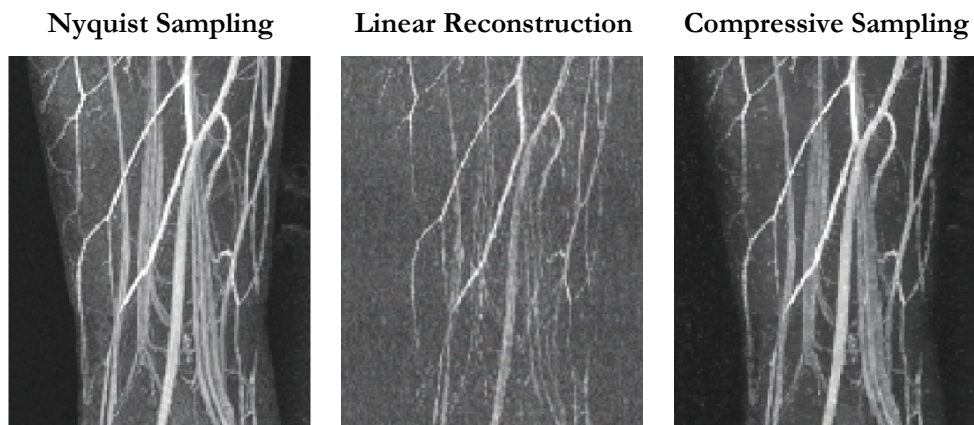


Figure 8 – 3D contrast enhanced angiography. Even acquiring only 10% of the samples, CS could recover most of the blood vessel information revealed by Nyquist sampling and significantly reduce the artifacts when compared to the linear reconstruction. Images taken from [36].

Brain scanning is the most common clinical application of MRI. Most brain scans use 2D Cartesian multislice acquisitions and it has been shown that brain images are sparse in the wavelet domain [34, 36].

Lustig *et al.* tested the application of CS to brain imaging by acquiring a full Nyquist-sampled data set which was, after, retrospectively undersampled. The 2-D Cartesian multislice sampling trajectories are illustrated in Figure 9. For each slice, a different random subset of 80 trajectories from 192 possible trajectories, which represented an increase of speed by a factor of 2.4, has been

selected. The authors also made use of the fact that undersampling each slice differently increased incoherence compared to sampling all the slices in the same way [34, 36].

In Figure 9 it is also visible an axial slice of the multislice CS reconstruction that has been compared to full Nyquist sampling, linear reconstruction from the undersampled data, and linear reconstruction from a low resolution (LR) acquisition taking the same amount of scan time.

CS was able to reconstruct images with a quality similar to that obtained with the full Nyquist-sampled set. CS also exhibited better suppression of aliasing artifacts when compared to linear reconstruction from incoherent sampling and improved resolution over a low-resolution acquisition with the same scan time.

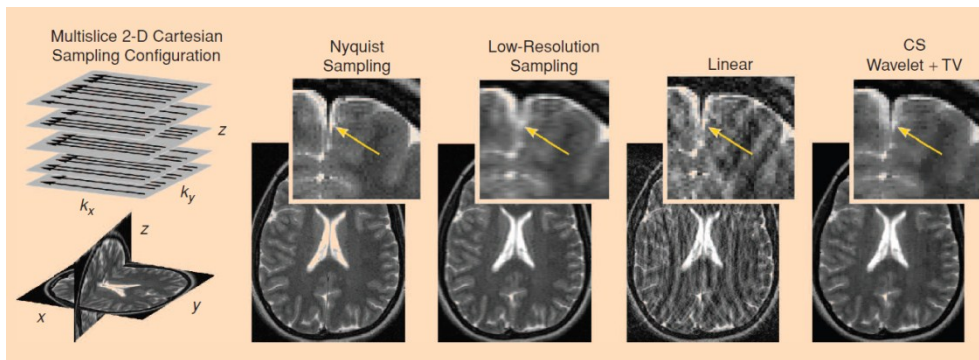


Figure 9 – Brain scanning using MRI. The results obtained with CS, using fewer sampling trajectories, were comparable to those obtained with the full Nyquist-sampled set. CS was also more successful than linear reconstruction from incoherent sampling in suppressing aliasing artifacts and exhibited improved resolution over a low-resolution acquisition with the same scan time. Picture reproduced from [36].

In sum, the authors proved that applying CS to MRI can potentially reduce significantly the scan times without compromising the quality of the results, raising benefits for patients and health care economics.

Despite the impressive good results the authors have obtained, many crucial issues have been enumerated, namely: optimizing sampling trajectories; developing improved sparse transforms that are incoherent to the sampling operator; studying reconstruction quality in terms of clinical significance; and improving the speed of reconstruction algorithms [34, 36].

3.5 Single-pixel terahertz imager

Another very interesting system was again developed by the Rice University and this time the first example of a CS-based terahertz (THz) imaging system was presented [37]. Within this work, a successful reconstruction of a target's image with a randomly chosen subset of samples from the Fourier plane was demonstrated. It combined CS with traditional phase retrieval (PR) algorithms for image reconstruction with only a random subset of the Fourier amplitude image.

The setup that was developed is shown in Figure 10.

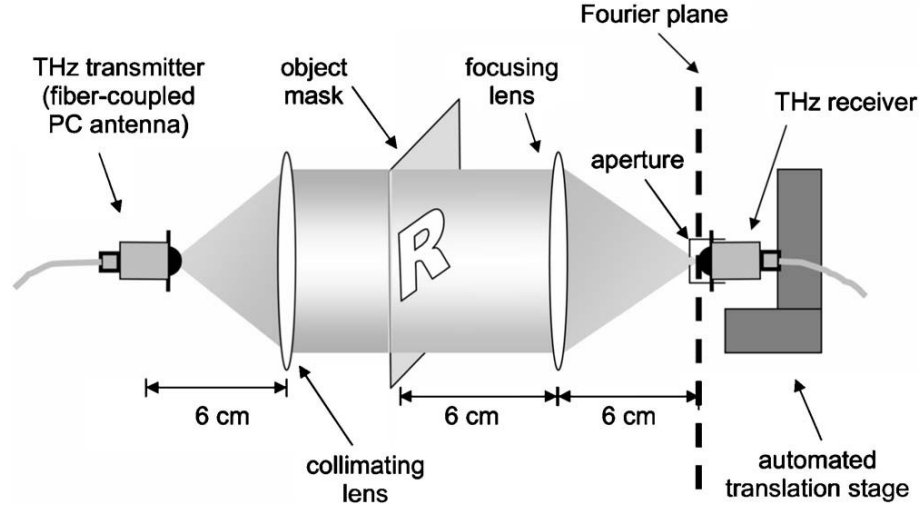


Figure 10 – CS-based THz Fourier imaging setup. Picture reproduced from [37].

Supported by Figure 10, the principle of operation can be explained as follows.

The imaging system consists of a pulsed THz transmitter and receiver and two lenses, one of which collimates the THz beam, while the other focuses the beam. The object mask, placed in the optical path between the two lenses, scatters the THz waves. The focusing lens forms the Fourier transform of the object mask at its focal plane and the receiver, mounted on a translation stage, performs a raster scan in the focal plane, over an area of 64×64 mm, at 1 mm intervals. The authors have placed a circular aperture (1 mm diameter) in front of the receiver antenna in order to sample only a small area of the Fourier pattern, rather than relying on the ~ 6 mm receiver aperture. The object mask was made of opaque copper tape on a transparent plastic plate and it consisted of an R-shaped hole with 34×31 mm dimensions.

At each detector position, an entire time-domain THz waveform is measured and the power spectrum of each waveform is computed. After that, the spectral amplitude and phase at a particular wavelength is selected ($\lambda = 1.5$ mm) to obtain a (complex) pixel value. In this manner, a 64×64 Fourier image is assembled.

It was stated that the system is able to reconstruct images with a resolution of 1.40 mm/pixel and that, using CS, it was capable of reducing the number of measurements required for image reconstruction by more than a factor of 8.

The authors also concluded that the reconstruction result could be improved by removing the background profile of the phase, which is not caused by the object but is inherent in the spherical wavefront curvature of the Gaussian beam that illuminates the object. As a result, the phase in the Fourier plane is distorted by the superposition of a spherically varying background. Then, the object mask was initially removed from the setup and a 64×64 pixels image of the background phase of the beam was obtained through 2D Fourier inversion. As a result, it was concluded that the phase-correction procedure not only removes the spherically varying phase profile in the reconstruction but also improves the quality of the reconstruction. This is supported by the results exhibited in Figure 11.

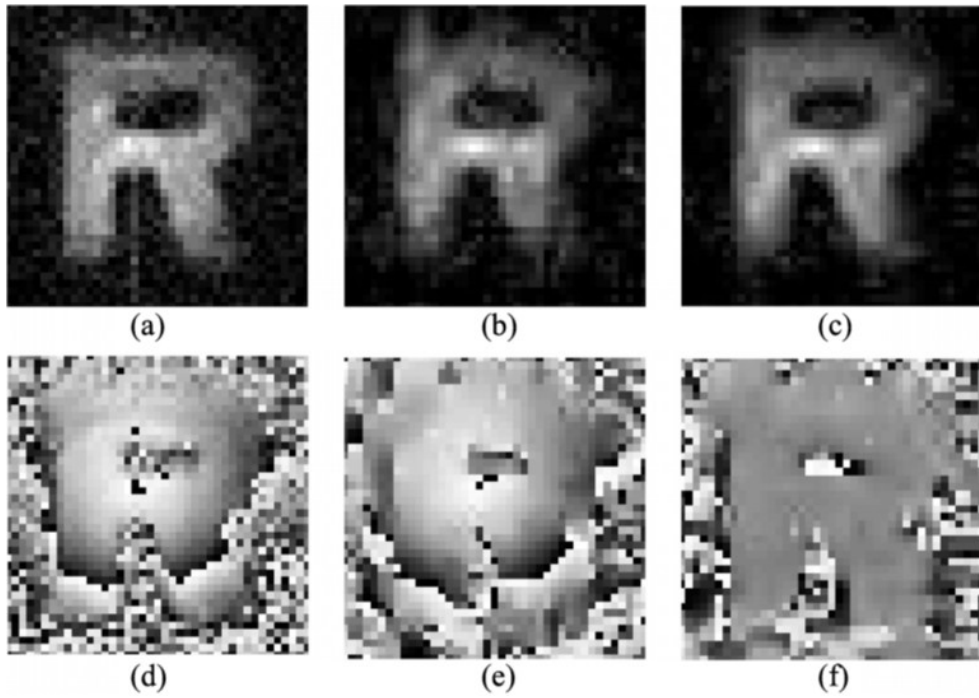


Figure 11 – Compressive sensing imaging results. (a) Magnitude of image reconstructed by inverse Fourier transform using the full dataset (4096 uniformly sampled measurements) and (d) its phase. Note the phase distortion inherent in the THz beam in (d). Compressed sensing reconstruction result using 500 measurements (12%) from the full dataset: (b) magnitude and (e) phase. Compressed sensing with phase correction improves image quality (c) and eliminates phase distortion (f). All figures show a zoom-in view on a 40×40 grid centered on the object. Picture reproduced from [37].

Therefore, in this work the authors have shown that the incorporation of CS into THz imaging designs can significantly reduce the image acquisition time, since fewer measurements are required. In particular, they have shown to be able to successfully recover the test object using only 12% of the dimensionality. They claim that their transmission configuration can be useful for quality control applications, such as detection of point impurities in manufactured products, because Fourier-domain measurements are particularly sensitive to sharp point-like features.

Following this work, Chan *et al.* [38] presented another single-pixel terahertz imaging system based on compressive sensing.

For practical, time-critical applications, a terahertz imaging system should not require raster scanning of the object or the terahertz beam. In addition, one would like to preserve the superior detection sensitivity of a single-point detector such as photoconductive antennas (rather than the lower sensitivity provided by existing multipixel arrays) and the simplicity and spatial coherence of a point-source transmitter. As a result, the authors have devised a system that enables both of these goals.

The speed of most existing terahertz imaging systems is limited by the need to mechanically raster scan the object (or the terahertz beam) and, therefore, in contrast to their previous work, this system replaced the mechanical scanning with the spatial modulation of the free-space terahertz beam, which can in principle be much faster.

Furthermore, supported by CS theory, this system requires fewer measurements than the total number of image pixels to fully reconstruct an image, thus, speeding up the acquisition process.

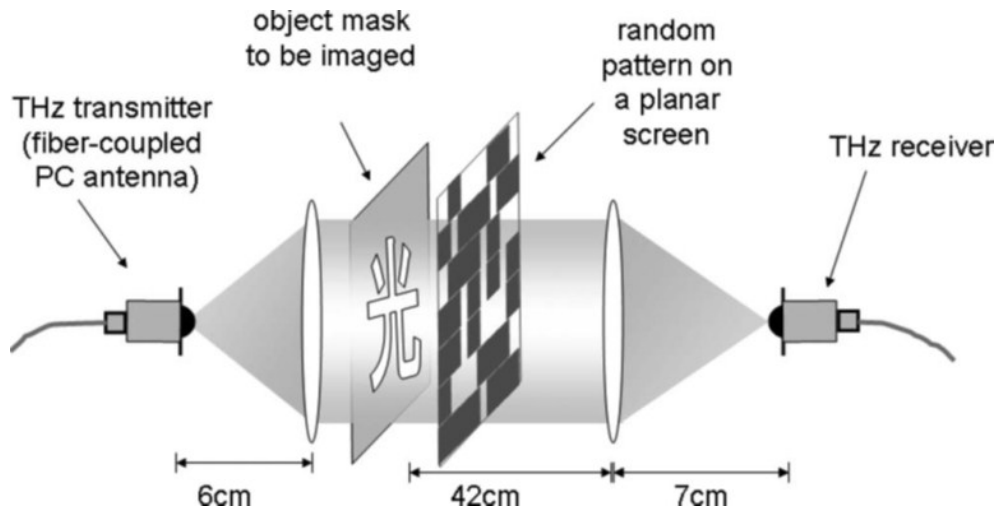


Figure 12 – Diagram of the CS-based THz imaging system discarding the need for raster scanning. Picture reproduced from [38].

Observing Figure 12 it is possible to see that an approximately collimated beam from the terahertz transmitter illuminates an object mask and is partially ($\sim 50\%$) transmitted through a random pattern of opaque pixels. The random patterns, the focusing lens and the receiver are placed in order to most efficiently focus the terahertz beam onto the receiver antenna. To ensure accurate alignment when changing from one random pattern to another, an automatic translation stage was used. The reconstruction process takes less than 10 seconds to be computed in MATLAB® on a standard personal computer.

The authors state that reconstruction using more measurements yields a sharper image but also adds some artifacts. Main sources of noise include laser power fluctuation and alignment errors between patterns.

In sum, this time, the authors have eliminated the need for raster scanning of the object or the terahertz beam, while maintaining the high sensitivity of a single-element detector. Based on the theory of CS, the system is capable of recovering a 32×32 pixels image of a rather complicated object with only 300 measurements ($\sim 30\%$), a fact that significantly increases the acquisition speed comparatively to traditional raster scan systems. The major limitation of the system is related to the transition from one random pattern to another. The authors also indicate the possibility of the system being used in spectroscopy applications.

3.6 Compressive structured light for recovering inhomogeneous participating media

Another impressive work was presented by Gu *et al.* [39], in which structured light was used, not for the conventional idea of establishing correspondence for triangulation, but for the purpose of obtaining volumetric information of participating mediums, such as translucent objects, smoke, clouds, mixing fluids, and biological tissues. Therefore, the new called, compressive structured light projects patterns into a volume of participating medium to produce images which are integral measurements of the volume density along the line of sight. For a typical participating medium encountered in the real world, the integral nature of the acquired images enables the use of compressive sensing techniques that can recover the entire volume density from only a few measurements. This makes the acquisition process more efficient and enables reconstruction of dynamic volumetric phenomena. An iterative algorithm was also proposed to correct for the attenuation of the participating medium during the reconstruction process.

This system principle of operation can be seen in Figure 13.

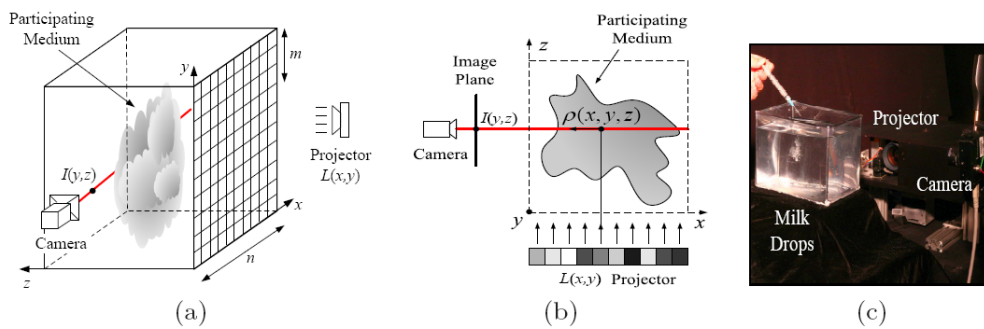


Figure 13 – Compressive structured light for recovering inhomogeneous participating media. (a) Coded light is emitted along the z -axis to the volume while the camera acquires images as line-integrated measurements of the volume density along the x -axis. The light is coded in either the spatial domain or temporal domain with a predetermined sequence. (b) Image formation model for participating medium under single scattering. The image irradiance at one pixel, $I(y, z)$, depends on the integral along the x -axis of the projector's light, $L(x, y)$, and the medium density, $\rho(x, y, z)$, along a ray through the camera center. (c) Experimental setup. The volume density is reconstructed from the measurements by the use of compressive sensing techniques. Picture reproduced from [39].

Observing Figure 13, it can be seen that for participating media, each camera pixel receives light from all points along the line of sight within the volume. Thus, each camera pixel is an integral measurement of one row of the volume density. Whereas conventional structured light range finding methods seek to triangulate the position of a single point, compressed structured light seeks to reconstruct the unidimensional (1D) density “signal” from a few measured integrals of this signal.

The authors stated that compressive structured light codes yield high efficiency both in acquisition time and illumination power, at the expense of a more sophisticated reconstruction process.

Figure 14 presents some of the reconstruction results of milk drops dissolving in water.

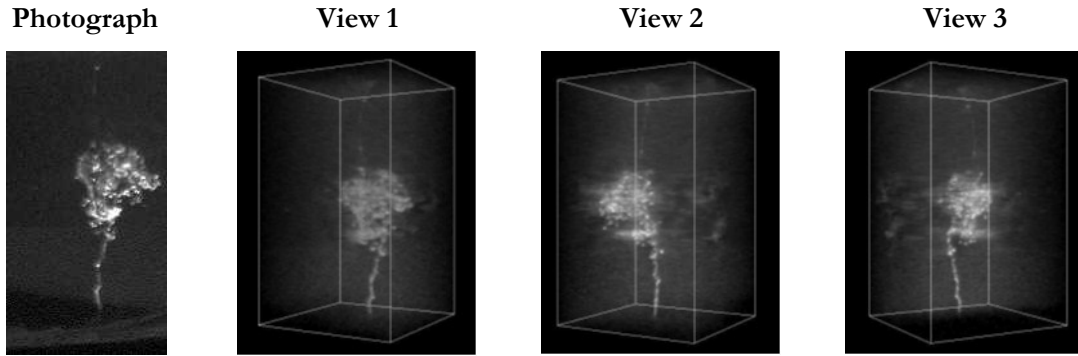


Figure 14 – Reconstruction results of milk drops dissolving in water. 24 images were used to reconstruct the volume at $128 \times 128 \times 250$ at 15fps. The reconstructed volumes are shown in three different views and the image in the leftmost column shows the corresponding photograph (taken with all projector pixels emitting white) of the dynamic process). Picture reproduced from [39].

The authors point as future direction the possibility of designing more complex coding strategies to improve the performance or to apply the method to new problems.

3.7 Compressive spectral imagers

In 2007, Gehm *et al.* [40] presented a single-shot CS-based spectral imaging system. The primary features of the system design are two dispersive elements, arranged in opposition and surrounding a binary-valued aperture code. The schematic drawing of the proposed system is presented in Figure 15.

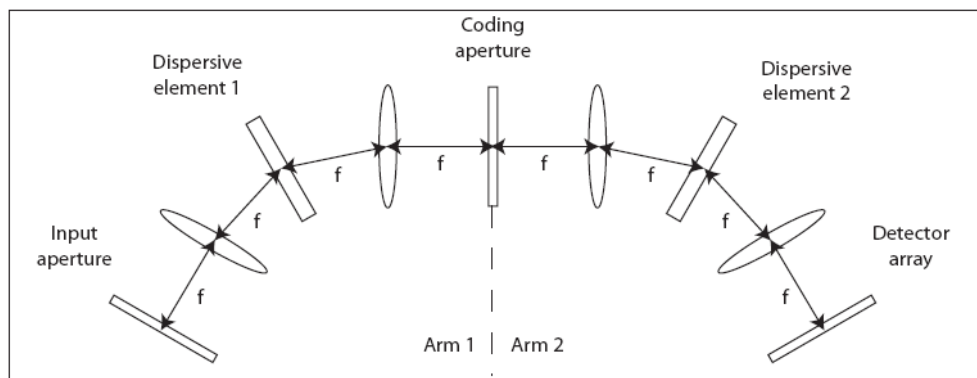


Figure 15 – Schematic drawing of the single-shot CS-based spectral imager. Picture reproduced from [40].

Even though it is not shown in Figure 15, an image of a remote scene is formed on the plane of the input aperture, which is then imaged through the first arm onto the plane containing the

coding aperture. However, due to the employed dispersive element, multiple images are formed at wavelength-dependent locations.

At this point, both the spatial and spectral information about the scene are mixed on the spatial structure of the coding aperture plane. After, passing through the coding aperture, this information is modulated by the coding pattern. The second arm, then, unmixes the spatial and spectral information introduced by the first arm and forms an image of the scene on the detector array. In other words, the two arms are arranged in opposition so that the second arm exactly cancels the dispersion introduced by the first arm, leaving only the spatial spectral modulation introduced by the coding aperture.

In Figure 16, a photograph of the experimental prototype can be seen.

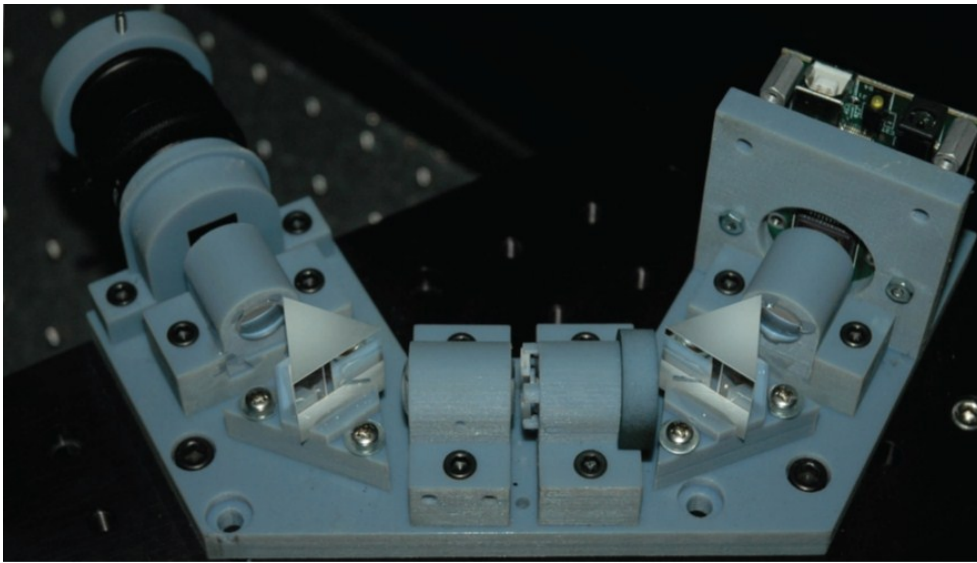


Figure 16 – Experimental prototype of the proposed architecture. Picture reproduced from [40].

This new class of imagers was named by the group as coded aperture snapshot spectral imager (CASSI), and in this particular case as dual disperser CASSI (DD-CASSI).

The reconstruction phase relies on a unique multiscale method. This reconstruction method combines a maximum likelihood estimator with a penalty-based multiscale denoising technique that utilizes spatio-spectral correlations in the scene to improve the reconstruction quality. Figure 17 shows some of the results obtained with the described imaging system.

To sum up, the authors have presented a single-shot spectral imager that, for the first time, mitigated the trade-offs between spatial resolution, spectral resolution, light collection, and measurement acquisition time. Despite the acceptable performance of the system for a first proof-of-concept, it was stated that the results were limited by the stock optics used to create the present prototype and that could be further improved.

A useful property of this design is that the measurement resembles the scene, making it easy to focus the camera on objects in the scene. This also makes it possible to perform local block processing of the detector data to generate smaller data cubes of subsets of the entire scene.

Following the DD-CASSI system, in 2008, Wagadarikar *et al.* [41] reported a new CASSI system, this time called a single disperser CASSI (SD-CASSI). Like the DD-CASSI, the SD-CASSI does not directly measure each voxel in the desired three-dimensional data cube. It collects a small number (relatively to the size of the data cube) of coded measurements and a sparse reconstruction method is used to estimate the data cube from the noisy projections. The instrument disperses spectral information from each spatial location in the scene over a large area across the detector.

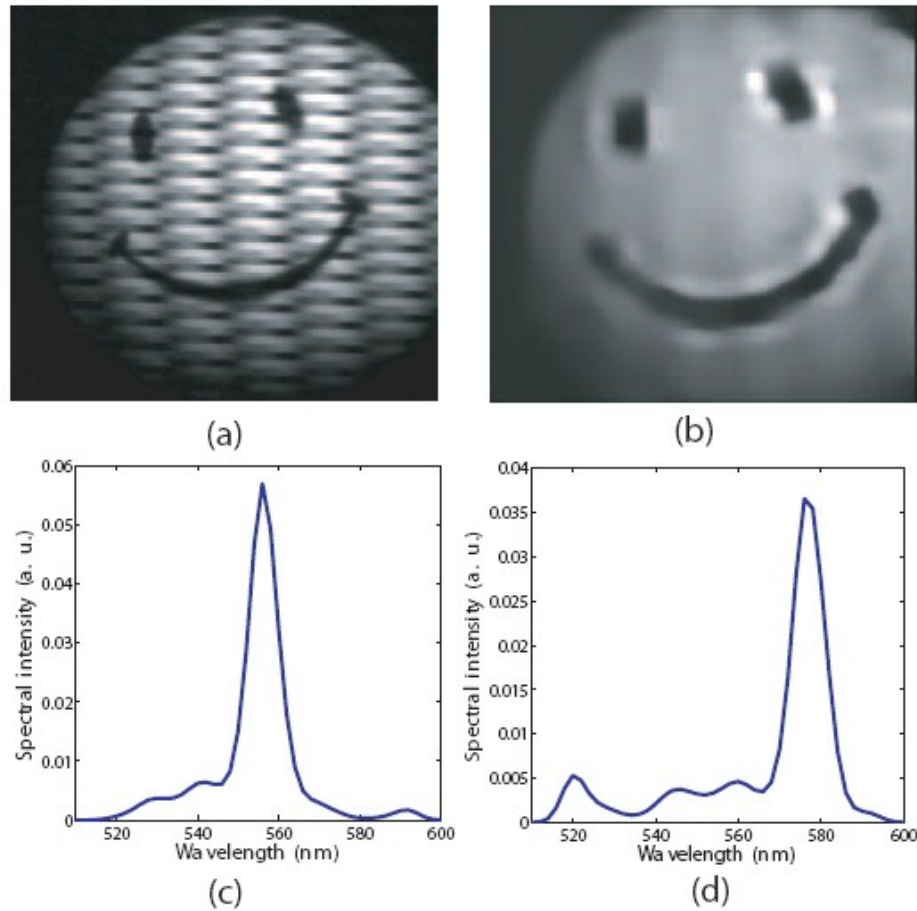


Figure 17 – Experimental results from simple targets with narrow-band illumination. (a) Detector image recorded for illumination with a 10 nm full width at half maximum (FWHM) bandpass filter centered at 560 nm – note the modulation introduced by the coding aperture. (b) Intensity image generated by summing the spectral information in the reconstruction for the 560 nm bandpass filter. (c) Spectral reconstruction at a particular spatial location for the 560 nm bandpass filter. (d) Spectral reconstruction at a particular spatial location for the 580 nm bandpass filter. The small peak near 520 nm is due to spectral aliasing. Picture and info reproduced from [40].

Thus, spatial and spectral information from the scene is multiplexed on the detector, implying that the null space of the sensing operation of the SD-CASSI differs from that of the DD-CASSI. Furthermore, with SD-CASSI, a raw measurement of a scene on the detector rarely reveals the spatial structure of the scene and makes block processing more challenging.

In Figure 18 a schematic drawing of the SD-CASSI system is presented.

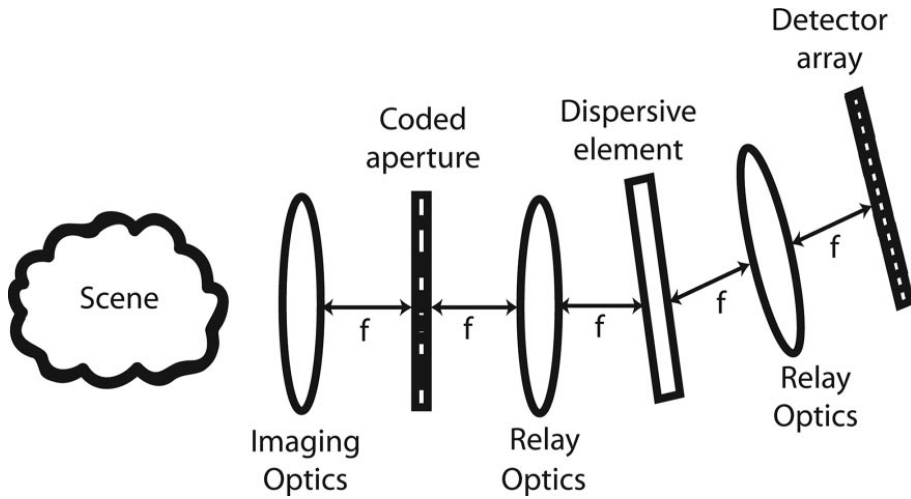


Figure 18 – Schematic drawing of the SD-CASSI system. Picture reproduced from [41].

In this system, standard optics are used to form an image of a scene on the coded aperture plane, which modulates the spatial information over all wavelengths in the spectral cube with the coded pattern. Imaging the data cube from this plane through the dispersive element results in multiple images of the code-modulated scene at wavelength-dependent locations in the plane of the detector array. The spatial intensity pattern in this plane contains a coded mixture of spatial and spectral information about the scene.

Figure 19 shows the experimental setup of the SD-CASSI.

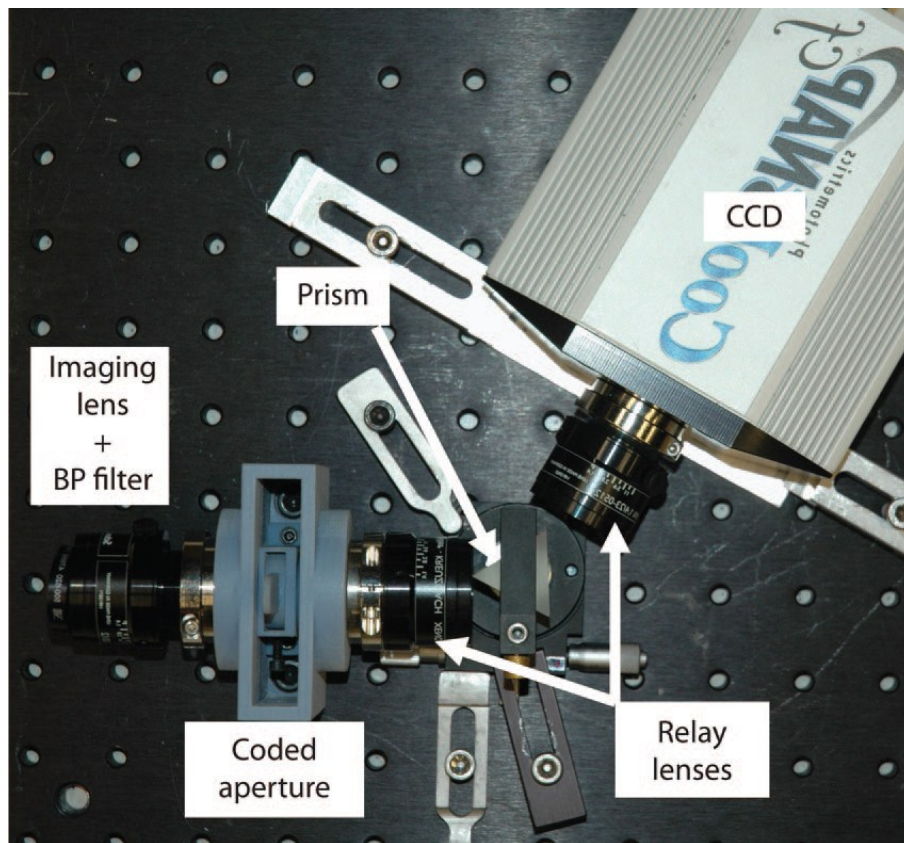


Figure 19 – Top view of the SD-CASSI experimental setup. Picture reproduced from [41].



Figure 20 – Scene consisting of a ping-pong ball illuminated by a 543 nm green laser and a white light source filtered by a 560 nm narrowband filter (left), and a red ping-pong ball illuminated by a white light source (right). Picture reproduced from [41].

In Figure 21 it can be seen the results obtained with the SD-CASSI system for the scene represented in Figure 20.

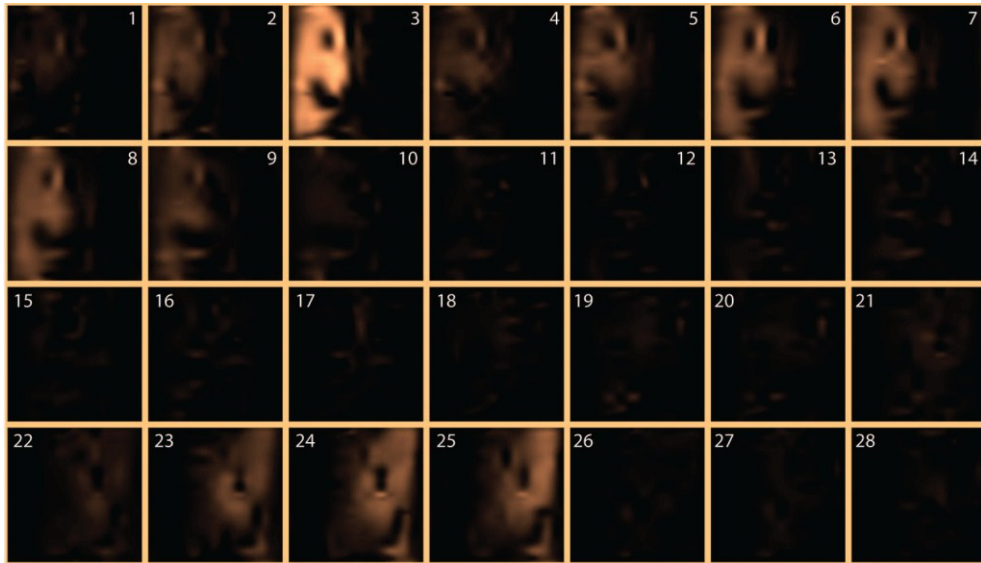


Figure 21 – Spatial content of the scene of Figure 20 in each of 28 spectral channels between 540 and 640 nm. The green ball can be seen in channels 3 to 8; the red ball can be seen in channels 23 to 25. Picture reproduced from [41].

To evaluate the ability of the SD-CASSI to reconstruct the spectral signature of objects in the scene, the authors measured the spectral signatures of each ping-pong ball using a commercial spectrometer from Ocean Optics. These results are presented in Figure 22.

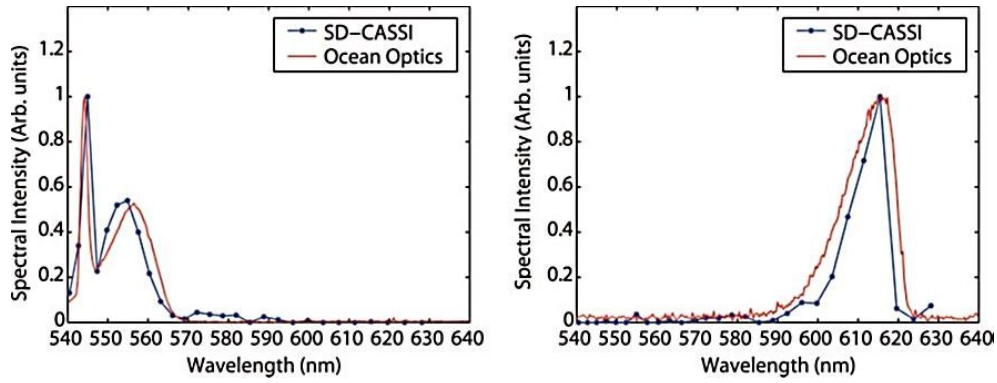


Figure 22 – (left) Spectral intensity through a point on the ping-pong ball illuminated by a 543 nm green laser and a white light source filtered by a 560 nm narrowband filter. (right) Spectral intensity through a point on the red ping-pong ball illuminated by a white light source. Spectra from an Ocean Optics non-imaging reference spectrometer are shown for comparison. Picture reproduced from [41].

From the previous results, it is possible to observe that the SD-CASSI reconstructed spectra closely follow those measured by the non-imaging reference spectrometer.

An important characteristic of any spectrometer or spectral imager is the spectral resolution. As the authors reported, if the optical distortions such as the blurring and the smile distortion were ignored, the spectral resolution of the SD-CASSI would then be determined by the width of the smallest code feature.

The authors have also stated that the system exhibits an average spectral resolution of 3.6 nm/spectral channel.

The reconstruction phase relied on the application of the Gradient Projection for Sparse Reconstruction (GPSR) method [33] so that the data cube could be estimated from the SD-CASSI measurements. For that purpose, spatial sparsity of the scene in the wavelet basis was assumed.

In a concluding manner, the main differences between the DD-CASSI and SD-CASSI are presented in Table 2.

Table 2 – Comparison of the main aspects of DD-CASSI and SD-CASSI.

DD-CASSI	SD-CASSI
Uses 9 optical elements	Uses 6 optical elements
Only spectral multiplexing	Spatial and spectral multiplexing, less compressive measurement
Cannot spectrally resolve point sources	May spatially resolve point sources
Block processing possible	Block processing challenging
Instrument of choice for high spatial resolution but lesser spectral resolution	Instrument of choice for high spectral resolution but lesser spatial resolution

In 2009, Sun and Kelly, from the Rice University, presented a CS-based hyperspectral imager capable of reconstructing images with 0.8 nm of spectral resolution [42]. This work represents a clear extension of the work presented in 2006 by Takhar *et al.* [15] and instead of a photodetector, this time, a spectrometer (Ocean Optics QE65000) was used as the light detection device. Unfortunately, no details were provided regarding the optical and mechanical arrangement of the system. In Figure 23 some of the results obtained with this system are presented.

The authors also applied a pixel-by-pixel raster scan pattern and acquired the measurements under the same illumination and spectrometer integration conditions as in the compressive results, for comparison purposes. In Figure 24 it can be seen the raster scan results and the compressive results for the same scene for two spectral bands. Supported by these results, one can say that the quality of the compressive results is higher. This can be justified by the fact that CS measurement always captures approximately half of the total light from the scene instead of $1/N^2$ with raster scan. Therefore, the signal-to-noise ratio (SNR) is much higher in the compressive approach. The authors also stated that besides bringing better image quality, CS saves 90% of acquisition time and data storage volume.

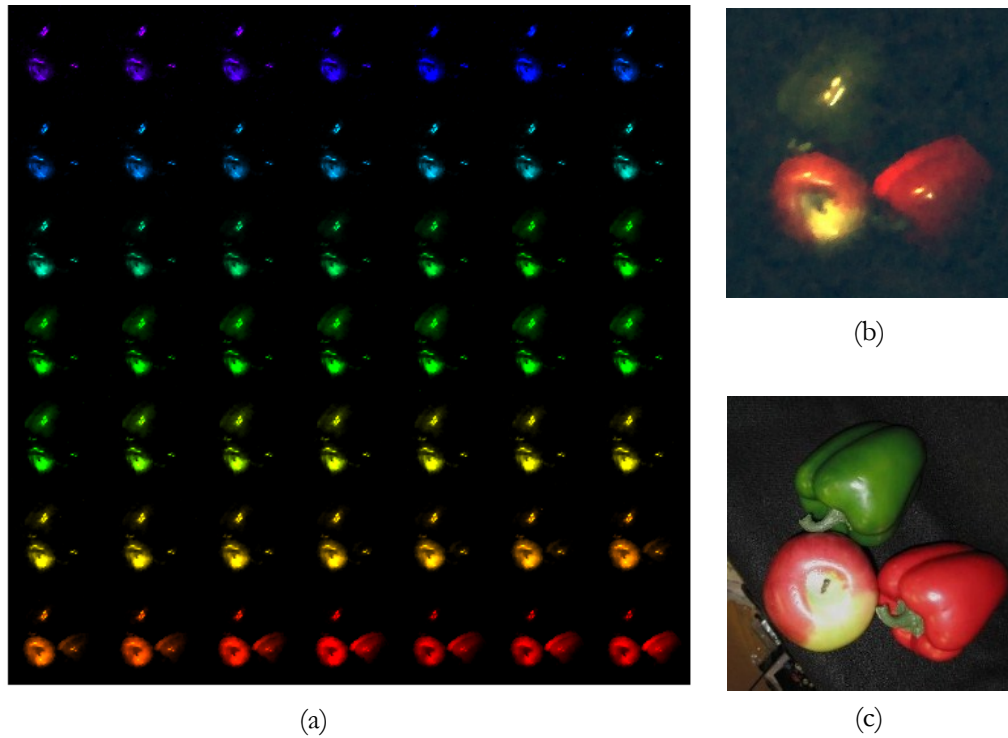


Figure 23 – (a) Mosaic of hyperspectral images with a lateral resolution of 256 x 256 pixels and a spectrum resolution of 4 nm (averaged over several channels). (b) Reconstructed image after summing all the bands. (c) Image taken with a conventional camera. Images reproduced from [42].

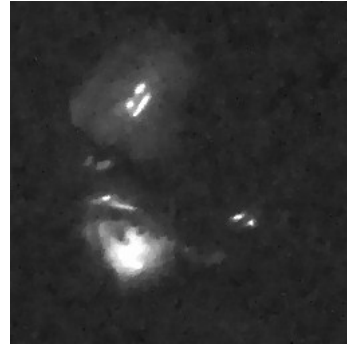
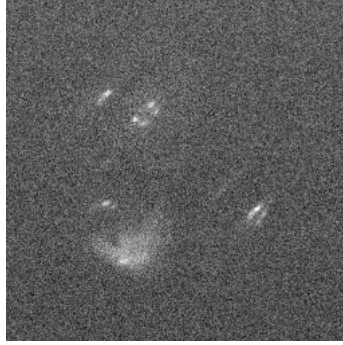
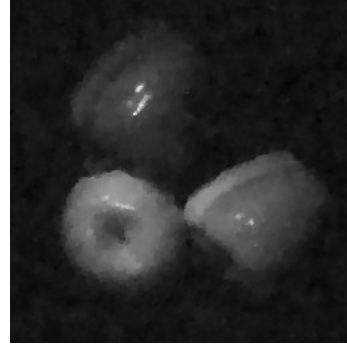
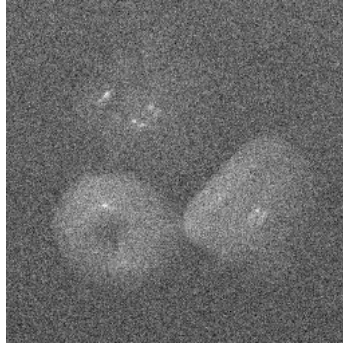
Band 1**Band 2**

Figure 24 – 256 x 256 pixels images for two spectral bands obtained via raster scan (left column) and compressive sensing (right column). Images reproduced from [42].

3.8 Compressive ghost imaging system

In 2009, Katz *et al.* presented an algorithm based on compressive sensing for ghost imaging (GI) and proved a substantial increase in the signal-to-noise ratio of the reconstructed images [43]. Succinctly, ghost imaging establishes quantum correlations between photon pairs to build up an image of an unseen object as follows: while one of the photons strikes the object, the other follows a different path to the camera's lens. If the camera is constructed to only record pixels from photons that hit simultaneously the object and the camera's image plane, an image of the object can be reconstructed. Figure 25 shows a scheme of the experimental setup used for standard ghost imaging. In conventional GI, the object is illuminated by a speckle field generated by passing a laser beam through a rotating diffuser. For each phase realization of the diffuser, the speckle field which impinges on the object is imaged. This is done by splitting the beam before the object to an object arm and a reference arm, and placing a CCD camera at the reference arm. At the object arm, a bucket detector measures the total intensity which is transmitted through the object. To reconstruct the transmission function of the object, the bucket detector measurements are cross-correlated with the intensities measured at the reference arm. Each bucket measurement consists in the overlap between the object and the illumination pattern. Thus, the GI measurement process is in essence a vector projection of the object transmission function over M different random vectors, and the GI reconstruction is a linear superposition of these vectors determined by the measured projections.

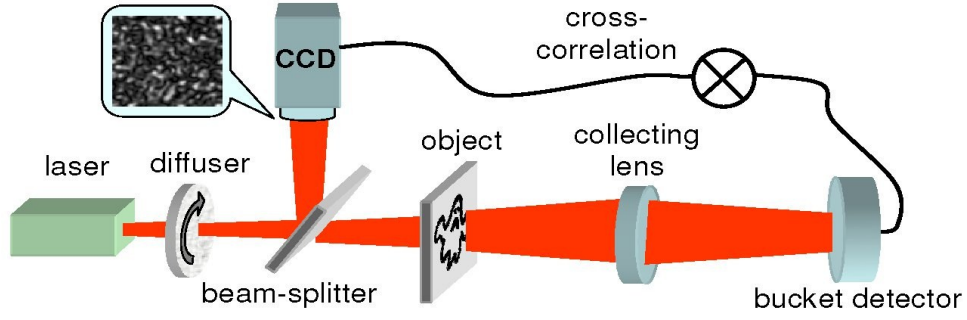


Figure 25 – Scheme of a standard setup for pseudothermal ghost imaging with two detectors. Picture reproduced from [43].

The GI linear reconstruction process has no assumptions on the object to be resolved. Thus, if the number of speckles that cover the object is N , one needs at least $M = N$ different intensity patterns in order to reconstruct the object. In fact, since the different intensity patterns overlap, $M \gg N$ measurements are needed to meet $SNR \gg 1$ [44]. However, any prior information on the structure of the object could significantly reduce the number of measurements required for a faithful reconstruction. As we have already seen, most natural images are sparse in an appropriate basis and CS exploits that fact to reduce the number of measurements needed for faithful image recovery. Katz *et al.* applied this knowledge to GI and experimentally demonstrated CS reconstruction in GI. For that they have used the setup depicted in Figure 26. This implementation is a variation of the standard GI with two detectors, where the rotating diffuser has been replaced with a computer controlled spatial light modulator (SLM). Knowing the applied SLM phase mask for each realization, the field intensity in the reference arm was computed using the Fresnel-Huygens principle of propagation, instead of measuring it as in conventional GI.

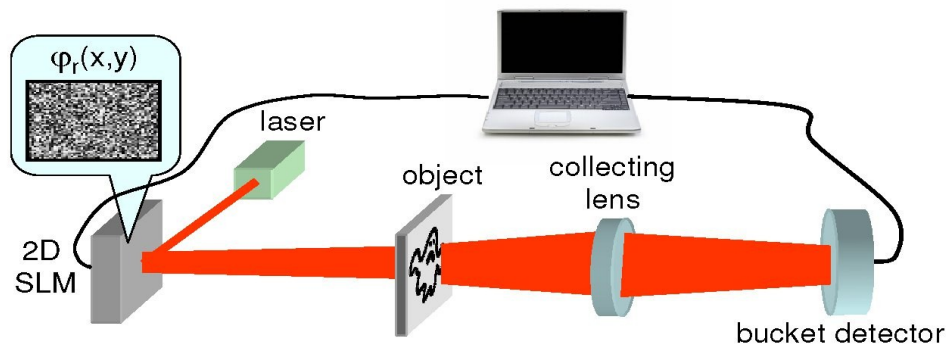


Figure 26 – Scheme of the compressive ghost imaging setup with a single detector. Picture reproduced from [43].

The authors have used reference data for 64×64 pixels and reconstructed images of a double slit transmission plate (width $220 \mu\text{m}$, separation $500 \mu\text{m}$), using 256 and 512 realizations. The corresponding results for conventional GI reconstruction are shown in Figure 27 a-b, while the CS reconstruction results using the same set of measured data are presented in Figure 27 c-d.

It can be seen that the main features of the object were recovered with standard GI but with a poor SNR, justified by the common speckle features of GI. The CS results, on the other hand, exhibit a noticeable higher SNR and a more accurate reconstruction. To quantify the improvement gained by utilizing CS reconstruction, the calculated SNR for the CS reconstruction using 256 realizations is 2.1 times higher than the standard GI reconstruction, and is 3.5 times higher for the 512 realizations case. For the CS reconstruction they have utilized the gradient projection for sparse reconstruction (GPSR) algorithm [33], minimizing the ℓ_1 -norm in the 2D-DCT domain.

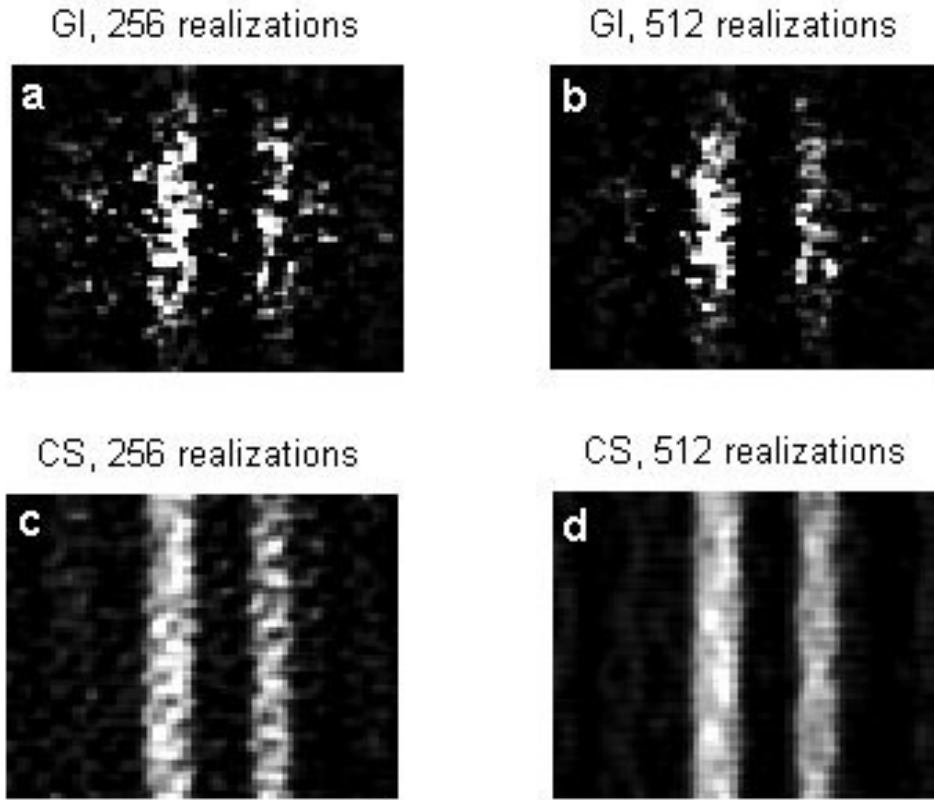


Figure 27 – Ghost imaging results for the reconstruction of images of a double-slit transmission plate. Top row: Conventional ghost imaging with: (a) 256 realizations; (b) 512 realizations; Bottom row: Compressive ghost imaging reconstruction using the same experimental data as in (a) and (b). Picture reproduced from [43].

3.9 CMOS compressive sensing imager

Jacques, Majidzadeh *et al.* presented a Complementary Metal Oxide Semiconductor (CMOS) imager with built-in capability to perform Compressed Sensing coding by Random Convolution [45-47]. The CMOS CS-imager scheme with N^2 pixels is depicted in Figure 28. This device relies on a Linear Feedback Shift Register (LFSR) initiated in a pseudo-random sequence \mathbf{a} , following a Rademacher distribution (equal probability of occurrence for -1 and $+1$). It acts as a convolutive filter on the imager focal plane and the output current in each pixel is proportional to the light intensity. The sign of this current is adjusted by the 1-bit value (a_i) of the pseudo-random

sequence stored in the memory and, conforming Kirchhoff's Law, the current of all the pixels along each column is combined. Each column is connected to the input of one Operational Amplifier (Op-Amp) and its output voltage is subsequently digitized by an Analog to Digital converter (ADC), in a time-multiplexed manner. Finally, the output of the ADC is integrated to represent that specific compressed image measurement.

For the realization of the next measurements, the content of the shift-registers (SR) grid has to be adapted. This is achieved by pushing the last 1-bit value of the sequence, i.e. a_{N^2} , into the first pixel memory, therefore causing all the remaining bits to update their positions. However, to fit the random convolution model, a random activation of the Op-Amps/ADC blocks must be applied. This is achieved by logically combining several LFSR, producing a certain activation probability. If this triggering is off, a new shift is produced by the SR and no reading is performed. Otherwise, a measurement is acquired and quantized by the Op-Amps/ADC blocks following the scheme initially described.

It is claimed that the system enables an image acquisition rate of 60 frames-per-second (fps) with a 4MHz sampling clock, thanks to the reduced number of measurements required in compressive sensing. If the oversampling, introduced to reduce the effect of the circuit thermal noise, is not conducted, the image acquisition rate can be increased up to 180 fps [46].

The reconstruction burden is all supported by a computer system which does it by means of Nesterov iterative boosting inside a convex minimization algorithm based on operator splitting and proximal methods.

Analyzing the key principles of CS and the conclusions drawn by the authors, it can be said that such a camera would be perfect for devices with low CPU power and targeting low energy consumption. The authors also said that they plan to adapt the same technology to 2D grids of biosensors for analyzing the electrical activity of a group of connected neural cells. The produced biosignal is indeed sparse both in the spatial and in the time domains, corroborating the applicability of CS.

Comparatively to the Rice University single-pixel camera [15], the authors referred that the DMD-photodiode pair is subject to various nonlinearities (e.g. non-uniform reflectance of the mirrors through the focusing lens, non-uniform mirror positions, photo-electric conversion) and, in principle, the proposed imager suffers less from these imperfections since it relies on an homogeneous analog processing in the electric domain and uses a mature CMOS technology. Furthermore, errors and nonlinearities induced by all the micro-electronic modules can be reduced, modeled and on-chip calibrated to oppose their effects.

Despite exhibiting some similarities with the work of Robucci *et al.* [8], this system is optimized for CS-based imaging, while the other is a more general architecture intended to perform alternative analog signal processing tasks (e.g. DCT or wavelet transform).

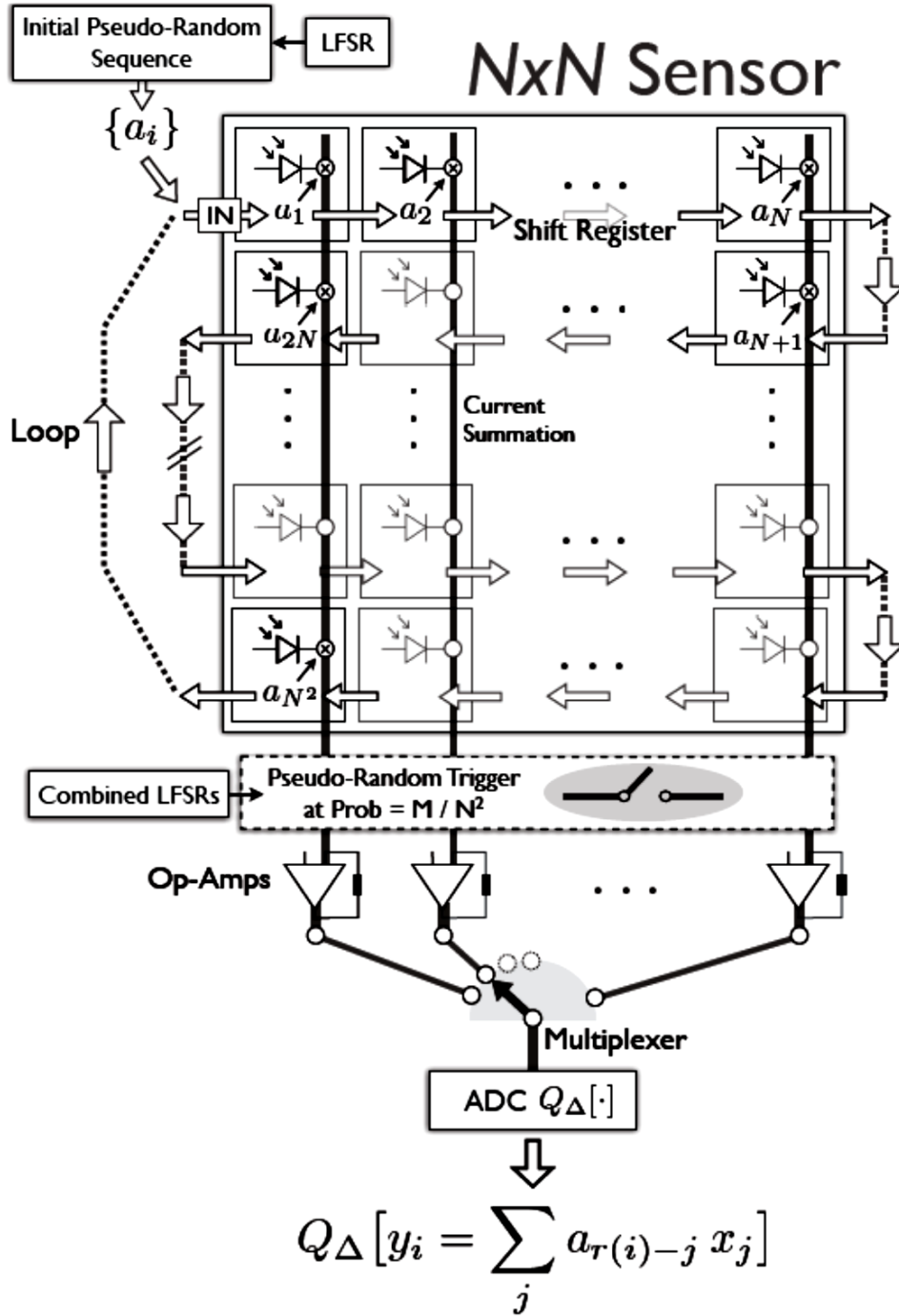


Figure 28 – Scheme of the CMOS CS-imager. Picture reproduced from [45].

3.10 Compressive microscopy imaging systems

Some groups have also dedicated themselves to the application of compressive sensing theory to microscopy systems, in particular, confocal microscopy systems [48-50]. Analyzing their research, it is possible to conclude that the proposed compressive confocal microscopy system acts in a kind of a parallel beam confocal imaging system which uses a single pixel detector and a digital micromirror device (DMD) to capture linear projections of the in-focus image.

Compressive confocal microscopy has emerged as a new framework offering the potential advantage of lowering costs by reducing the hardware and optical complexity. This is achieved because most of the burden is moved from data acquisition to image reconstruction, which is performed digitally in a standard computer. Another advantage comes from the fact that there is no need for any scanning scheme or mechanical scanning device, which is translated on faster operation times. Figure 29 shows the schematic drawing of the compressive confocal microscope along with its principle of operation.

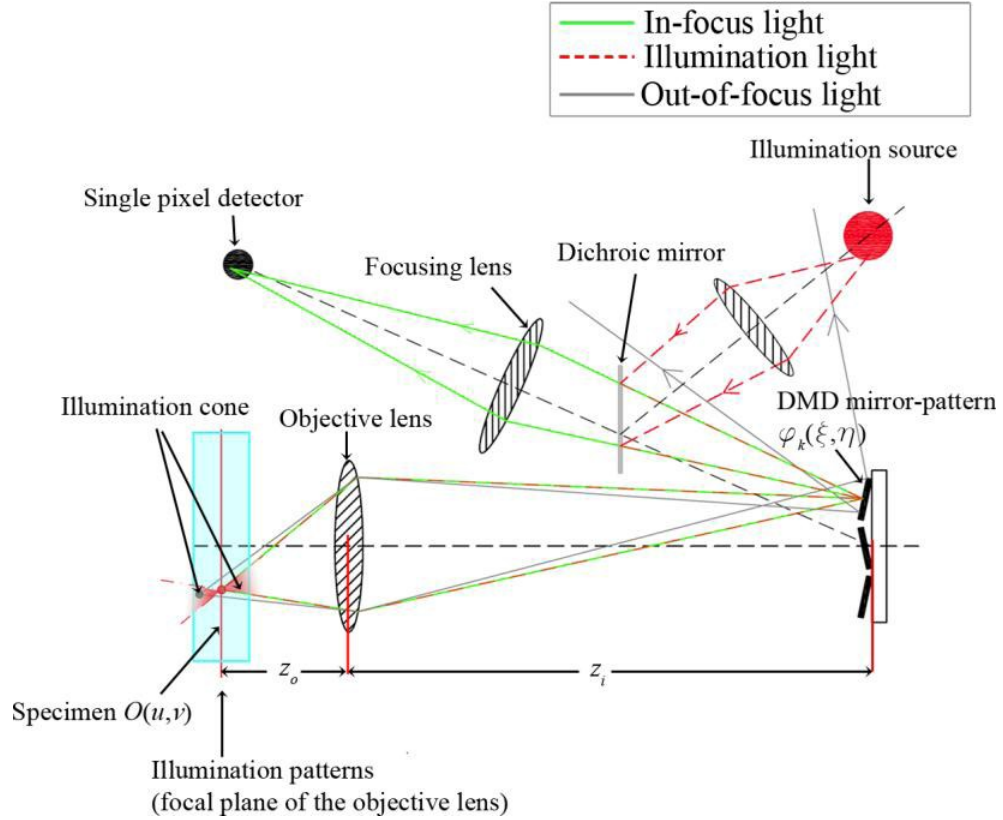


Figure 29 – Schematic drawing of the compressive confocal microscope along with its principle of operation. Picture reproduced from [48].

Observing Figure 29, it is perceptible that only the light coming from the in-focus plane will be measured by the single-pixel detector. The measured light then contains the spatial information compressed by the used DMD coding patterns.

The authors stated that, in some cases, up to 90% reduction of scan effort and 50% light efficiency are feasible. It is also referred that, in the future, it is possible to consider the use of faster DMD or other spatial light modulating devices to improve the image acquisition speed/quality of the system. Besides, the use of more efficient CS coding patterns, such that fewer measurements could be used to reconstruct an image, was also among the authors' intentions.

In 2010, Marim *et al.* [51] presented a microscopy acquisition scheme successfully combining compressive sensing and digital holography in off-axis and frequency-shifting conditions. Their imaging scheme works for sparse gradient images, acquiring a diffraction map of the optical field with holographic microscopy and recovering the signal from as little as 7% of random

measurements. The reconstruction process is based on an iterative approach that, given a partial knowledge of the Fresnel coefficients, seeks for a solution with maximum sparsity and whose Fresnel coefficients match the observed subset.

The experimental setup diagram can be found in Figure 30.

The principle of operation of the system depicted in Figure 30 can be explained as follows: initially, the monochromatic optical field from a diode laser dynamically backscattered by an intralipid emulsion illuminates an United States Air Force (USAF) resolution target; then, it beats against a separate local oscillator field detuned by $\Delta\omega/(2\pi) = 200\text{Hz}$ and finally it creates a time-fluctuating interference pattern measured with a $N = 1024 \times 1024$ array detector. The diffracted object field map in the detector plane, resolved in quadrature (in amplitude and phase) is calculated from a four-phase measurement. The frequency detuning $\Delta\omega$ enables rejection of non-fluctuating light components reflected by the target as well as speckle reduction through signal accumulation.

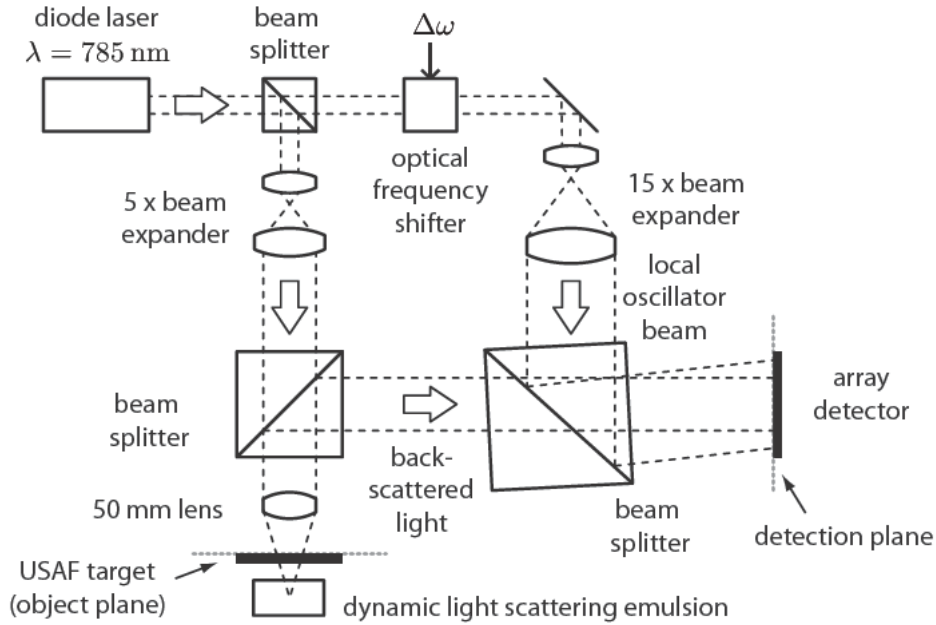


Figure 30 – Diagram of the experimental off-axis, frequency-shifting digital holography setup. Picture reproduced from [51].

In Figure 31 comparative images of the results obtained with standard holography and those obtained with the reported system are presented and are a good evidence of the reconstruction quality.

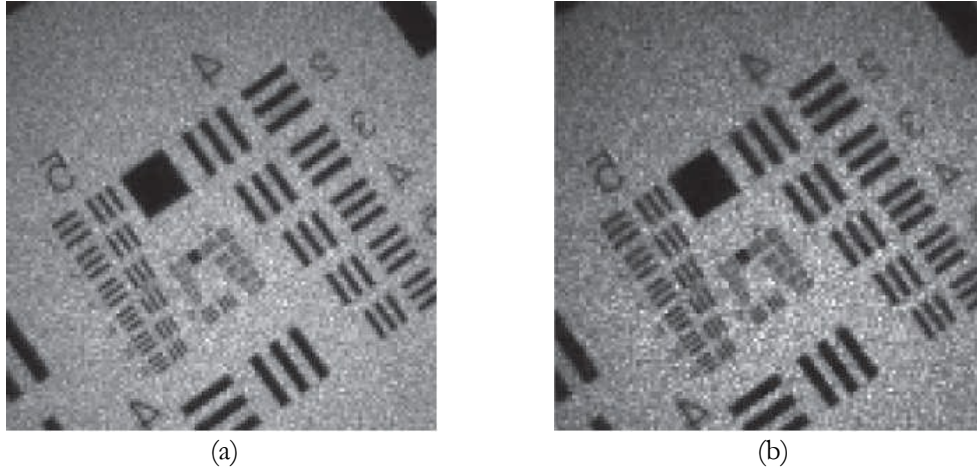


Figure 31 – (a) Results obtained with standard holography. (b) CS reconstruction, using 7% of the Fresnel coefficients. Images reproduced from [51].

3.11 Compressive optical coherence tomography

Optical coherence tomography (OCT) is a non-invasive, depth resolved, imaging modality, which has been widely used in medical diagnosis and research. Spectral domain OCT (SD-OCT) uses an array detector such as a CCD or CMOS camera to sample and digitize the spectral interferograms. Due to the Fourier domain detection configuration, SD-OCT has superior sensitivity and imaging speed compared with time domain OCT (TD-OCT) and, therefore, has supplanted conventional TD-OCT in many applications [52]. However, the advantages come at the charge of an expensive, large array, and high-speed camera. Moreover, when large imaging depth as well as high axial resolution is required, the camera has to capture spectra at a large sampling rate, because conventional image reconstruction algorithms for SD-OCT require spectral domain sampling beyond Nyquist rate to achieve a certain imaging depth. In other words, the camera has to have enough pixels to guarantee that at least two data points are sampled within one period of the spectral interferogram. Such CCD or CMOS cameras and associated electronics are usually expensive and limit the imaging speed. Besides, it is challenging to transfer and process the large amounts of data acquired [53].

In 2010, Liu and Kang presented a study where they have explored the potential of using compressed sensing for SD-OCT (CS-SD-OCT) [53]. Their intent was to reduce the need for a large pixel array camera and enable the reconstruction of high-resolution images with less data and processing. So, the authors used a common path SD-OCT (CP-SD-OCT) as illustrated in Figure 32. There, it can be seen the broadband light source used to illuminate the common path interferometer which consisted of a 50/50 fiber optic coupler and a single mode fiber probe serving as both sample and reference arm. The probe was scanned laterally to obtain B-mode images. The partial reflection at the distal end of the probe arm has been assumed to represent the reference signal. After being coupled back to the probe arm, the sample signal interfered with the reference

signal and was detected by the spectrometer, which used a CCD camera with 2048 pixels to discretize and digitize the spectral interferograms. The broadband source consisted of three superluminescent emission diodes resulting in an emission spectrum with a bandwidth of ~ 100 nm full width at half maximum (FWHM) centered at 800 nm. The axial resolution was measured to be $3.2 \mu\text{m}$.

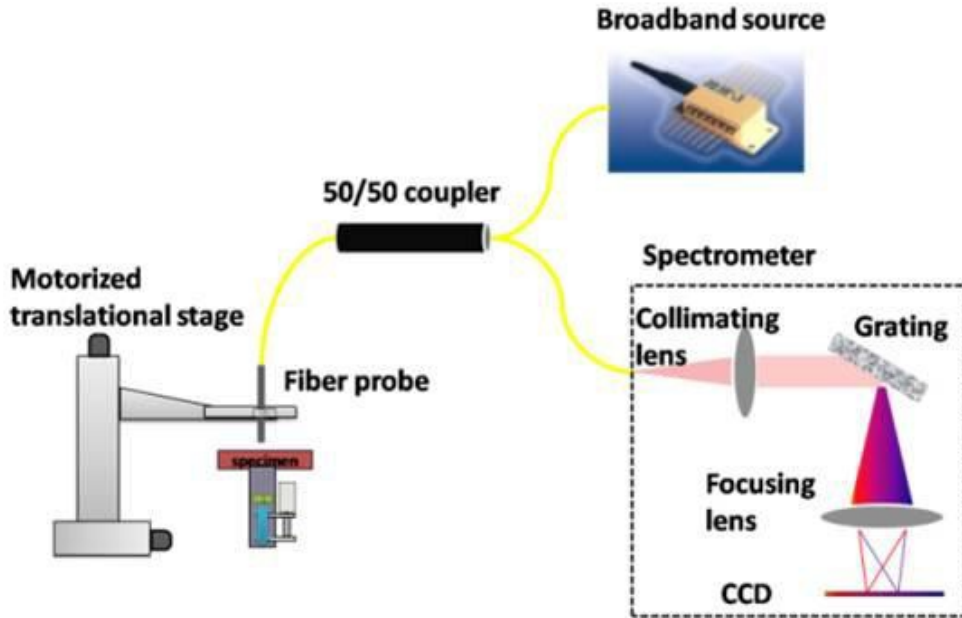


Figure 32 – Scheme of the common path spectral domain OCT setup. Picture reproduced from [53].

So with this setup, they randomly undersampled the spectra by applying known random masks to the full pixel array to demonstrate the concept of compressed sensing in OCT. These random masks have been used to sample 62.5%, 50%, and 37.5% of the CCD camera pixels. OCT images have been reconstructed by minimizing the ℓ_1 -norm of a transformed image to enforce sparsity, subject to data consistency constraints, and the results showed great potential for this technique. Some of the results obtained are shown in Figure 33.

Despite the demonstrated good performance, the authors stated that it could be possible to increase the acquisition speed with more appropriate hardware, such as that provided by a high-speed camera capable of randomly sample the pixels of interest. Even though a high-speed camera with random access to the pixels would be more expensive than a standard high-speed camera it would effectively improve the imaging speed. The authors also expressed the future intention of taking full advantage of signal compressibility in both axial and lateral directions, which would allow high fidelity reconstruction with even fewer sampling points.

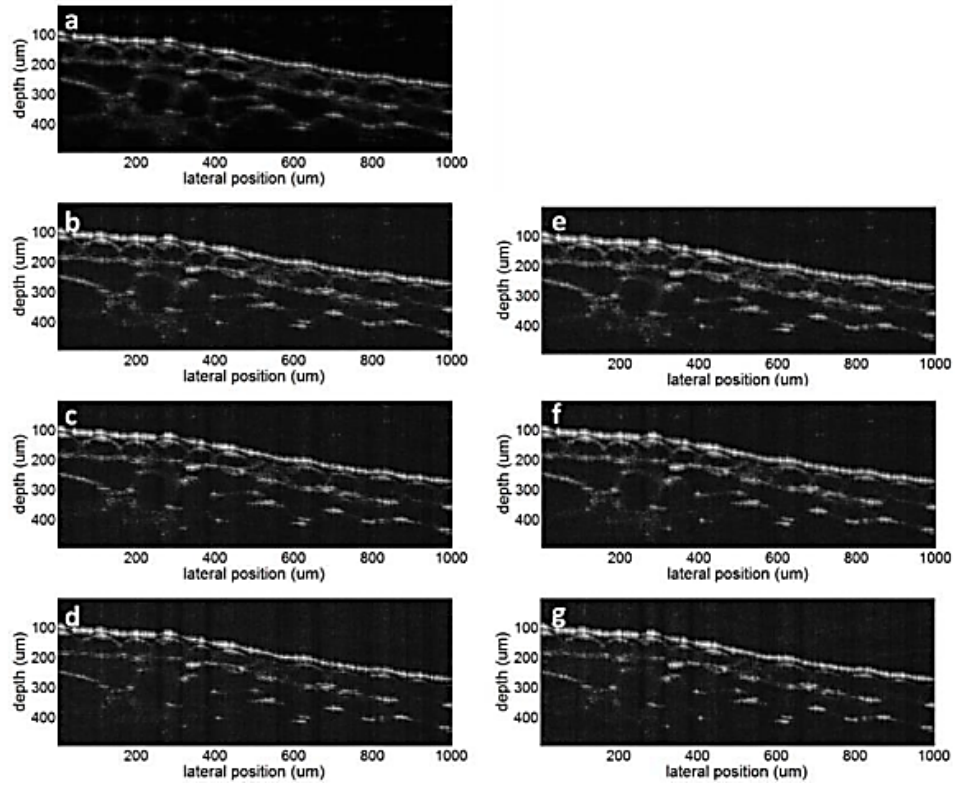


Figure 33 – OCT image of onion cells: (a) obtained using complete spectral data; (b), (c), and (d) obtained by sampling 62.5%, 50%, 37.5% of the pixels and pursuing sparsity in pixel domain; (e), (f), and (g) obtained by sampling 62.5%, 50%, 37.5% of the pixels and pursuing sparsity in wavelet domain. Picture reproduced from [53].

In 2011, Young *et al.* [54] demonstrated real-time CS-OCT for volumetric imaging of the Optic Nerve Head (ONH) using a 1060 nm Swept-Source OCT prototype. A common problem faced in ophthalmic imaging is motion artifact due to eye movements, such as subconscious microsaccades, which occur approximately once a second [54], therefore, it is of utmost importance the capability of acquiring images at fast rates (real-time) in this type of applications. By the time Young *et al.* presented this work, compressive sensing had already been demonstrated as a novel method for rapid image acquisition of OCT volumes [55], and it has been showed that OCT images of the Optic Nerve Head (ONH) reconstructed with CS had better recovery of anatomical features than that achieved with basic interpolation schemes. This was mainly due to the minimization of motion artifacts from rapid acquisition and from registering and averaging OCT volumes, which have different speckle characteristics due to CS reconstruction, thus yielding images with higher quality and higher SNR [54]. So, in their work, Young *et al.* used X-Y galvanometer mounted mirrors to scan the beam across the sample. The used source was a commercial swept-source with an effective 3dB bandwidth of 61.5 nm, corresponding to an axial resolution of $\sim 6 \mu\text{m}$ in tissue. The optical system used a standard fiber coupler Michelson interferometer topology, and the sample arm optics delivered a spot size at the cornea and at the retina of 1.3 mm and $17 \mu\text{m}$ (assuming a 25 mm axial eye length), respectively [54]. The CS-OCT volumes were acquired using a modified raster scan pattern consisting of randomly spaced horizontal scans, as depicted in Figure 34.

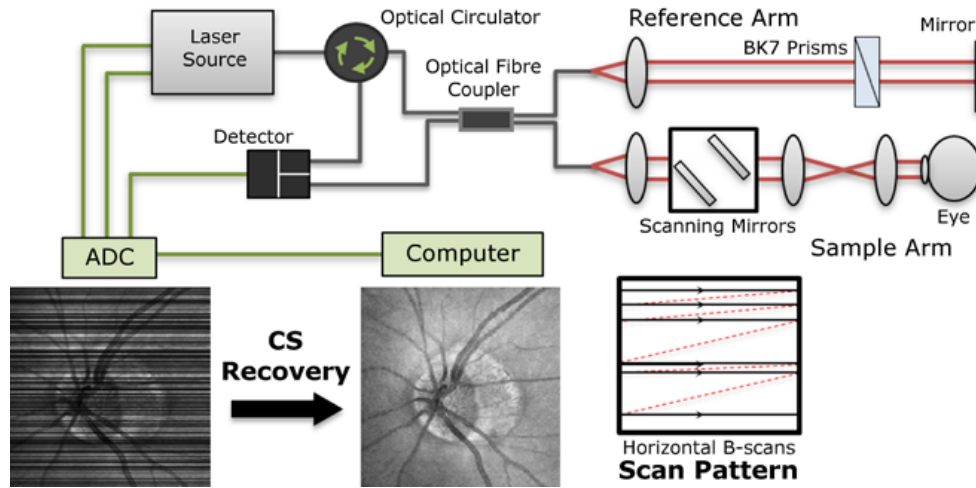


Figure 34 – Setup of the swept-source OCT system constructed with a 1060 nm source and a standard Michelson interferometer. The regular raster scan pattern was modified to acquire randomly spaced horizontal B-scans. The full volume was generated through CS-recovery in post processing. Picture reproduced from [54].

In their experiments, they have fully acquired a volume and partially acquired volumes with 36, 48 and 65 percent of missing data at a similar location. The fully sampled volume required 1.6 s for acquisition, while the partial volumes with 36, 48 and 65 percent of missing data required 1.02 s, 0.83 s and 0.56 s, respectively. The acquired B-scans from the volumes for different percentages of missing data were axially cropped and constructed into a data volume consisting of 512 (axial), 400 and 400 (lateral) voxels. The acquired frames were inserted into the volumes at their corresponding frame positions and missing frames were filled with zeros. The sparsely sampled data volume for each percentage of missing data acquired was recovered in MATLAB® using the Iterative Soft-Thresholding (IST) algorithm [56], following the processing details previously presented in [55]. For a volume with the dimensions of $512 \times 400 \times 400$ voxels, the CS-recovery process took approximately two hours on a computer with an i7 Intel CPU running at 2.67 GHz and 20 GB of memory. The authors stated that the speed of CS-recovery algorithm could be improved using C++ implementations or by using a general purpose Graphics Processing Unit (GPU). The top row of Figure 35 contains the reconstructions obtained after acquiring the data and that have been placed in the corresponding positions in the volume. The CS-recovered summed voxel images are shown in the second row of Figure 35. In the third and fourth row of Figure 35, it can be seen frames reconstructed from each CS-recovered volume in the fast (B-scan) and in the slow scan directions, respectively. Qualitatively, it can be said that CS interpolation preserved the main structures of the eye. However, a modest degradation of image quality was evidenced in the images recovered from summing the data with 65% of missing data. In the slow scan images, the 65% missing CS-recovered volume preserved more of the physiological curvature of the retina compared to that of the fully-acquired data, or CS with 36% and 48% of missing data, because of the shorter acquisition time.

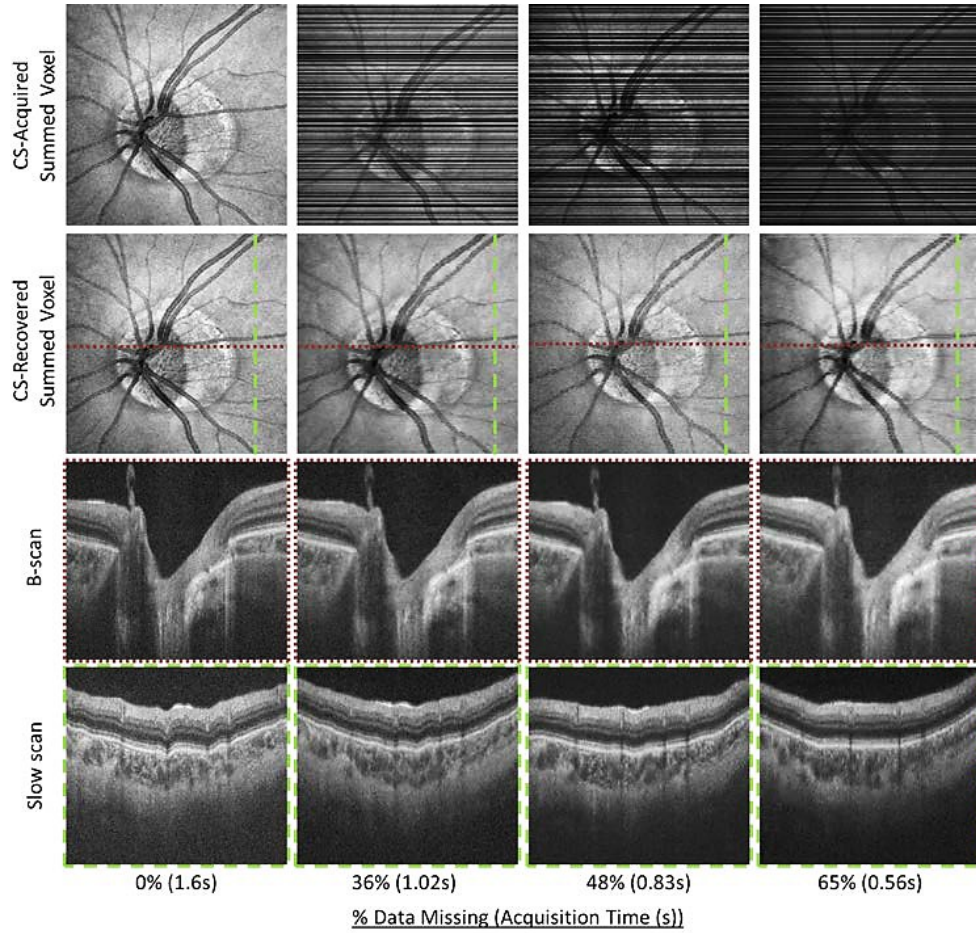


Figure 35 – Results recovered with CS. The top row shows the position of the frames that were acquired, the second row shows the CS reconstructed summed voxel projection, the third and fourth row show a selected B-scan and slow scan from the CS-recovered info, respectively. Picture reproduced from [54].

So, with this work CS-OCT has been validated as a promising novel method for increasing volumetric acquisition speed for new and existing OCT systems without sacrificing image quality. This can be easily achieved as it only requires changes in the scanning protocol and in the post-processing of acquired data. The CS acquisition scan pattern can be easily modified for different percentages of missing data, thus corresponding to different durations for volume acquisition.

3.12 Photon-counting compressive sensing laser radar for 3D imaging

In 2011, Rowland *et al.* [12, 13] demonstrated a photon-counting, single-pixel, laser radar – also known as LIDAR (LIght Detection And Ranging) – camera for 3D imaging where spatial resolution is obtained through compressive sensing. Their implementation does not rely on scanning and represents an improvement upon pixel-array based designs in the sense that it is compact and resource-efficient. It can easily be scaled to higher resolutions and to operate at any wavelength with an adequate single photon detection device. In Figure 36 it is presented a picture of the experimental setup of the implemented imaging LIDAR system (ILS). There it can be seen the pulsed light source used to illuminate the scene and the DMD array where an image of the

scene is formed. The spatial compression takes place on the DMD where the random compressive codes are applied and the reflected light is collected by the avalanche photodiode (APD). The output of the APD, obtained for each compressive code, is correlated with the original pulse signal to produce a histogram of single photon arrival times, thus compressing the range information. Peaks in the timing histogram indicate objects at different distances. Figure 37 contains results obtained with this system for objects placed at different depths.

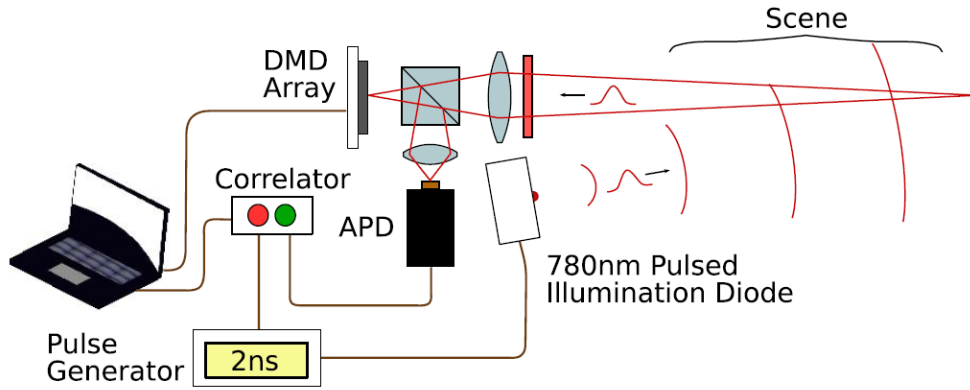


Figure 36 – Experimental setup of the photon-counting compressive sensing laser radar system for 3D imaging. Picture reproduced from [13].

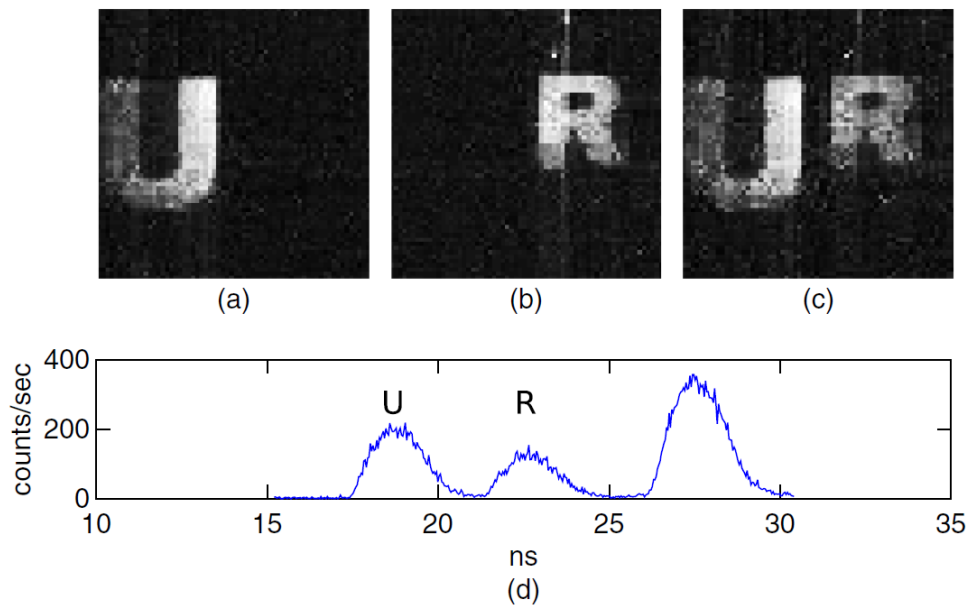


Figure 37 – Results obtained with the photon-counting compressive sensing laser radar system for 3D imaging. Reconstructions for objects 'U' and 'R' at depths 1.75 m and 2.10 m. (a) and (b) consider only 'U' and 'R', respectively, while (c) considers a range including both. Timing histogram (d) peaks represent, from left to right, 'U', 'R', and the room wall. Picture reproduced from [13].

Within this context, it is opportune to contextualize this system and present its main advantages when compared to other imaging LIDAR systems. ILS based on Time-of-Flight (TOF) are the preferred ones, thanks to their ability to accurately range-find over large ranges. Pulsed

direct detection probably offers the best performance since it is less constrained by range limitations, exhibits higher SNR and offers greater scope for imaging through the use of Focal Plane Array (FPA) detectors. Therefore, the biggest interest falls within the development of fast high resolution detectors with high sensitivity. For that, arrays of APD operated in Geiger-mode have proved to be the most successful approach, since these sub-ns timing detectors have single-photon precision and sensitivity close to shot-noise limit. However, it is still hard to increase their pixel density. The highest resolution commercially available array sensor is only 32×32 pixels, being under development arrays with 32×128 [57, 58] and 64×256 pixels [59, 60]. The Jigsaw system [61] has proved its performance and relies on prism-based scanning to improve its resolution and field of view (FOV). Despite this, the spectral range of the currently available array sensors is limited due to peak quantum efficiency (QE) in the mid-visible spectrum. For resolved targets, the amount of light returning to the receiver drops inversely with the range squared. In a pulsed ILS this energy is even more divided, among multiple detectors, causing shot-noise to become significant. With CS approximately 50% of the DMD pixels are “ON” for each measurement code, thus causing the system to gather about $N/2$ times more photons than an average pixel sensor ($1/N$), which significantly reduces image distortion from dark noise and read-out noise. The advantages of the single-pixel design include the fact that the QE of a photodiode is higher than that of the sensors in a typical CCD/CMOS array. More, the fill factor of a DMD can reach 90% whereas that of a CCD/CMOS array is only $\sim 50\%$. Unlike Fourier or Wavelet coefficients, for instance, random coding is robust because equal priority is credited to all the measurements. Consequently, as more measurements are gathered progressively better reconstructions can be obtained.

3.13 Millimeter-wave imaging with compressive sensing

Earlier in 2011 and later in 2012, Gopalsami *et al.* [62, 63] presented a millimeter-wave imaging system which benefited from compressive sensing theory.

Passive millimeter-wave (PMMW) imagers using a single radiometer, called single-pixel imagers, employ raster scanning to produce images. A serious disadvantage of such imaging systems is the long acquisition time needed to produce a high-fidelity image. This aspect originates from two factors, namely, the time to scan the whole scene pixel by pixel and the integration time for each pixel to achieve adequate SNR. As it has already been evinced in this document, compressive sensing (CS) can significantly reduce the imaging time and at the same time generate high-fidelity images by exploiting the sparsity of the data in some transform domain. While the efficiency of CS has been recognized for single-pixel optical systems, its application to PMMW imaging is not direct due to its longer wavelength by three to four orders of magnitude, which causes high diffraction losses and due to the weaker intensity of the radiation, which can be eight orders of magnitude less than that of infrared, for example. The authors have then developed and implemented a CS technique for PMMW imagers which improved the imaging speed by a factor of ten.

The main advantage of PMMW imaging is the robustness under all weather conditions, unlike visible and infrared optical systems, which require clear atmospheric conditions. It finds applications in remote sensing for polar ice mapping, terrain mapping and meteorology, for instance. It can also be applied to aircraft navigation for landing in optically obscure weather, and to security and defense scenarios for the detection of concealed weapons, for example. [63]

So, for the development of the compressive sensing based PMMW imaging system, the authors took advantage of the cyclic nature of the Hadamard basis and relied on the use of a single extended 2D Hadamard mask of size $(2p-1) \times (2q-1)$ to expose a different $p \times q$ sub-mask for each acquisition, translating the extended 2D mask one pixel at a time. This represented an enormous contribution comparatively to the manual introduction of the masks verified in the aim of the single-pixel THz imaging system presented in section 3.5 (see reference [38]). Figure 38 shows an image of an extended Hadamard mask with two highlighted examples of sub-masks. The mask was fabricated using chrome coating on a millimeter-wave transparent quartz plate. [62]

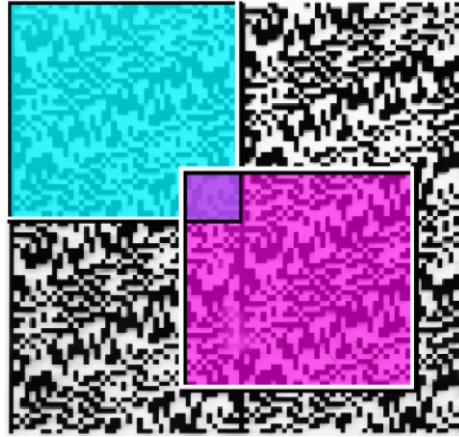


Figure 38 – Example of an extended Hadamard mask with 81×85 pixels. The colored boxes represent two different sub-masks (41×43 pixels) that are used in two different acquisitions. Picture reproduced from [62].

Figure 39 shows a diagram of the compressive sensing based PMMW imaging system that has been developed. There, it can be seen that the extended Hadamard mask is placed at the image plane of a 6 inches diameter lens, where the image of a distant target is formed. The exposure window is defined by a metal plate with a hole of size $p \times q$ that is placed in front of the extended mask. For each compressive measurement, the extended mask is controlled by a two-axis translation stage to expose different sub-mask patterns. A second lens of 1 inch diameter collects the modulated radiation field through the Hadamard mask and focuses it onto the multichannel radiometer. The positions of the lenses and the mask are governed by the lens equation $1/f_r = 1/d_i + 1/d_o$, where f_r is the focal length of either of the lenses, and d_i and d_o are the image and object distances, respectively. As the targets used in their experiments did not have spectral features, the authors averaged all 16 spectral channels, thus increasing the SNR by a factor of four.

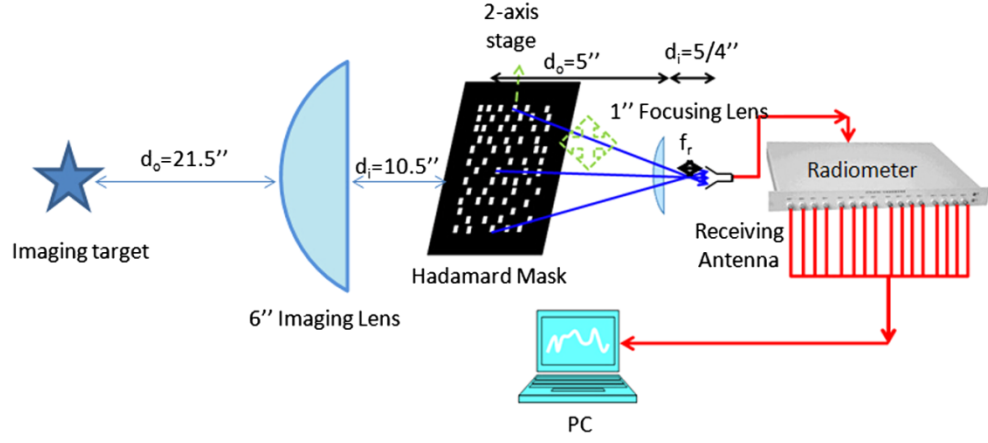


Figure 39 – Diagram of the compressive sensing based passive mm-wave imaging setup. Picture reproduced from [63].

This setup has been used for the acquisition of images of a 60 W incandescent bulb (thermal source). Figure 40 contains the results of those acquisitions when different amounts of samples for the reconstruction have been used. It can be said that the images reconstructed with 11% of the samples compare well with those reconstructed with 100% of the samples. The slight distortion in the object geometry can be justified by the smoothing nature of the reconstruction algorithm around sharp edges.

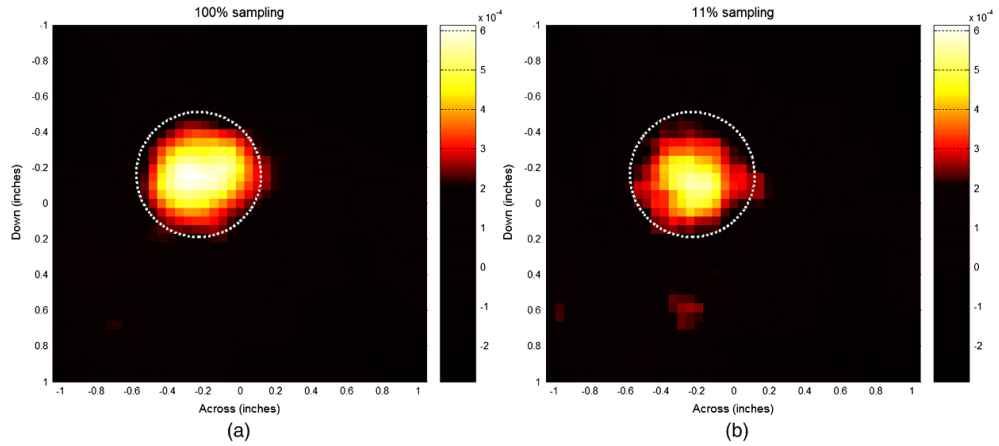


Figure 40 – 41×43 pixels images of the incandescent bulb acquired with the CS based PMMW system with: (a) 100% and (b) 11% of the samples. Picture reproduced from [63].

The possibility to reconstruct images with good quality from approximately 10% of the samples offered a ten-fold increase in imaging speed. The system also enabled the reconstruction of images with 41×43 pixels with pixel size of 1.24 mm, which is about half of the wavelength of the used radiometer (146 to 154 GHz), with better SNR than that of raster scanning systems.

3.14 Compressive polarimetric imaging

In early 2012, Durán *et al.* presented a CS-based optical system capable of performing spatially resolved polarimetric imaging with a single-pixel detector [64, 65]. A scheme of the implemented setup is shown in Figure 41. The principle of operation of the single-pixel polarimetric imager can be described as follows.

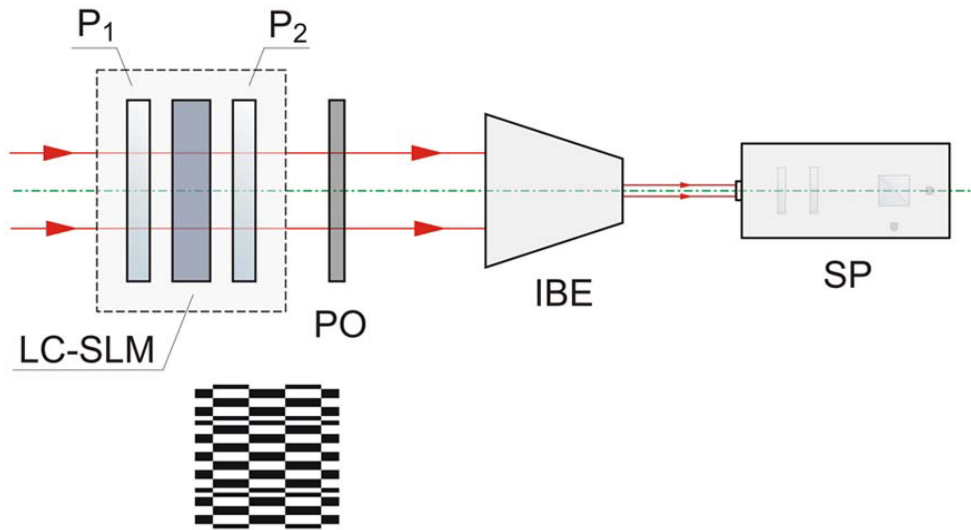


Figure 41 – Setup for single-pixel imaging polarimetry. An example of a binary intensity pattern displayed by the SLM is also shown. Picture reproduced from [64].

A collimated (unpolarized) laser beam passes through a liquid crystal spatial light modulator (LC-SLM), which is used to apply the compressive measurement binary patterns. Next, the light goes through a polarization object (PO) that is placed right after the LC-SLM to produce a space-variant polarimetric vector. In order to illuminate the PO with linearly polarized light the LC-SLM had to be enclosed by properly oriented linear polarizers (P1 and P2). After passing through the PO, the light is guided to a commercial Stokes polarimeter (SP) by means of an inverted beam expander (IBE). This element adequately shapes the beam width to the reduced entrance window of the SP, being crucial to ensure that all the light emerging from the object is collected by the SP and to keep the normal incidence. For this experiment, a He-Ne laser emitting at 632.8 nm and a transmissive twisted nematic LCD with 800×600 pixels were used. The Walsh-Hadamard basis was chosen as the measurement basis and the corresponding binary patterns had 64×64 pixels. The compression level was approximately 70% (1225 measurements were performed). For this polarimetric imager, the problem of measuring a spatial-dependent Stokes vector is equivalent to solve three times the CS algorithm for single-pixel imaging, one for each Stokes parameter. Figure 42 contains some results obtained with this system. The imaged object consisted of an amplitude mask with the characters “UJI”, being the character “J” covered with a cellophane film to act as an inhomogeneous polarization distributor.

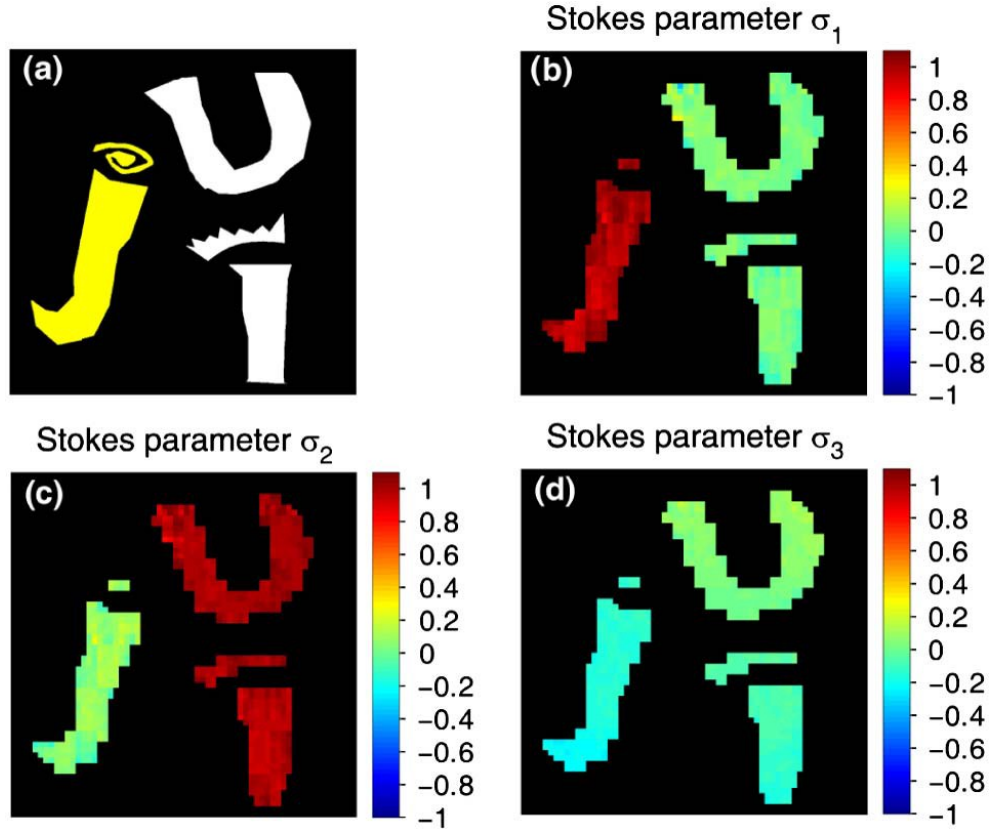


Figure 42 – (a) 1024×1024 pixels image of the object used in the experiment, which consists of an amplitude mask with a cellophane film covering the zone colored in yellow. (b), (c) and (d) represent 64×64 pixels pseudo-color images for the Stokes parameters. Picture reproduced from [64].

Chapter 4. Compressive Sensing Based Single-Pixel Imaging Systems

This chapter expounds the core subject of this dissertation, which is focused on the study and development of single-pixel imaging systems based on compressive sensing. Its content is distributed along six sections. The first five are related with the compressive sensing based acquisition of monochrome, color, multispectral, hyperspectral and high dynamic range images. In the last section, an algorithm that has been developed to include compressive sensing based imaging capabilities into a CMOS imager is presented. Illustrative results are provided for all the systems and for all the experiments that were conducted.

For the sake of clarity and simplification, there are some considerations that have been assumed for all the conducted experimental procedures, unless stated otherwise, that will now be presented. To acquire the data used to reconstruct the images, the sampling frequency was 250 kSamples/s. For each measurement, 10000 samples were acquired and averaged. The random binary codes used for spatial compression were permuted Hadamard codes. The NESTA software package [66] has been used for image reconstruction, in particular, using the TV minimization option. The images were reconstructed using 100% of the measurements and have been normalized to [0, 255] using 8 bits. Whenever used, the connection that enabled the transmission of the video signal, containing the images to be projected, between the computer and the Epson® projector has been established via a D-sub 15 pin interface. For the case of the LightCommander it was connected to the computer via an HDMI (High-Definition Multimedia Interface) interface.

More details will be provided throughout the dissertation as necessary.

4.1 Monochrome Imaging Systems

In this section we present the work related with the implementation of compressive sensing based single-pixel imaging systems capable of acquiring monochrome images. Monochrome images instead of recording the color of a scene, only register a single sample for each pixel, that is, they only preserve intensity information. The single-pixel monochrome imaging systems here presented compress the spatial information by incorporating the random measurement codes, either into the light used to illuminate the scene being acquired, here designated as active illumination systems, or into the light field coming from the same scene, here designated passive illumination systems.

4.1.1 Active illumination single-pixel monochrome imaging system

Following the work of the Rice and Arizona groups [15, 23, 32], in a preliminary manner, we have developed an innovative active illumination single-pixel imaging system. This system's setup

employed a video projector to incorporate the random binary measurement matrix and the proposed experimental setup is presented in Figure 43.

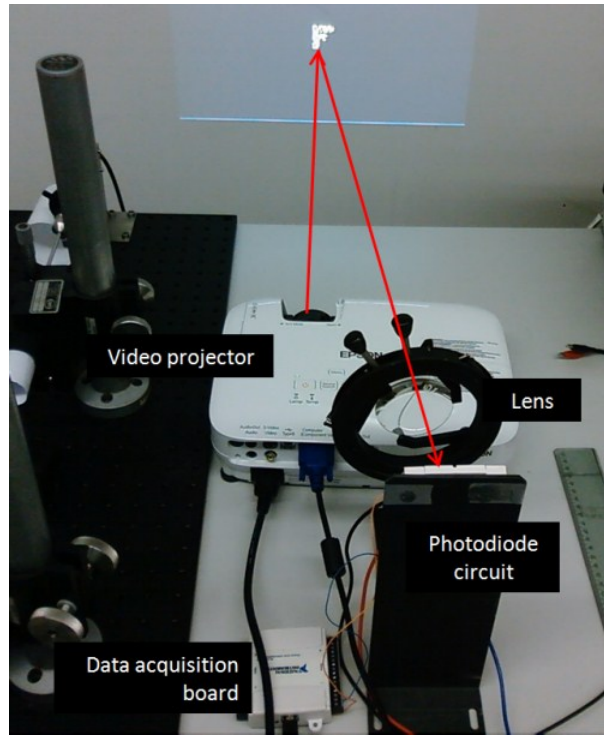


Figure 43 – Active illumination single-pixel-camera experimental setup. Following the red arrows, it can be seen that the image projected by the video projector is reflected on the wall and by means of a lens is focused on the photodiode active area. The output of the photodiode amplifier circuit is connected to a data acquisition board.

Figure 44 shows an integrated version of the proposed single-pixel imaging system in a much smaller assembly comprising the same configuration of Figure 43. This integrated setup has been developed to comprise the lens and the photodiode circuit in a single integrated module (see Figure 44 (b)), therefore, it is considerably more compact. A large area (1 cm²) silicon photodiode (RS 303-674) was used in order to facilitate the optical alignment and maximize the integration of light over the objective's field of view. The schematics of the photodiode amplifier circuit are shown in Figure 45. In this circuit, the output voltage is proportional to the current drawn by the photodiode (I) and is given by the following expression: $V_{out} = (R1 + R2) \times I$. The experimental setup also included a video projector with 1280×800 (WXGA) maximum resolution (Epson® model EB W7), a 12 bits resolution analog-to-digital (A/D) data acquisition board with a maximum sampling frequency of 10 kSamples/s and maximum voltage range [-10 V; 10 V] (National Instruments™ USB-6008), and a 8 mm focal length Computar® lens with focus distance ranging from 30 cm to infinity.

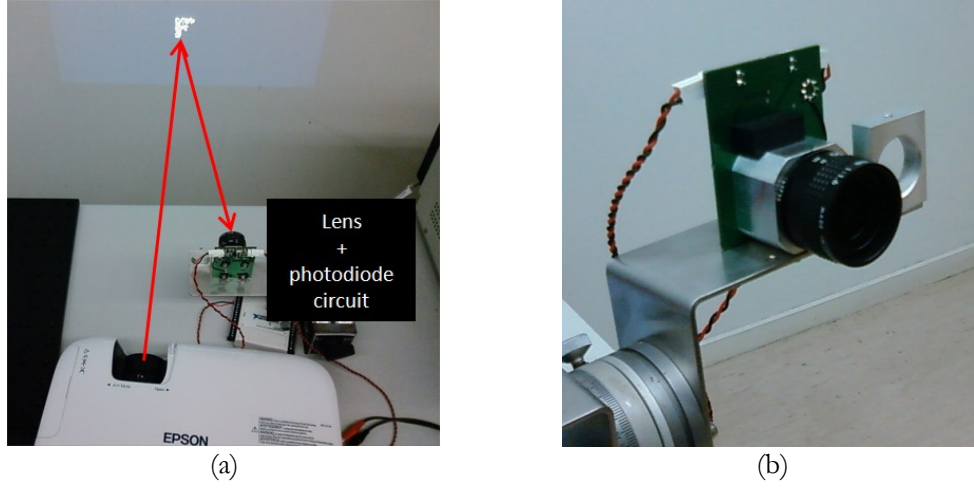


Figure 44 – (a) Compact active illumination single-pixel camera setup. (b) Detailed photo of the assembly comprising the lens and the photodiode circuit.

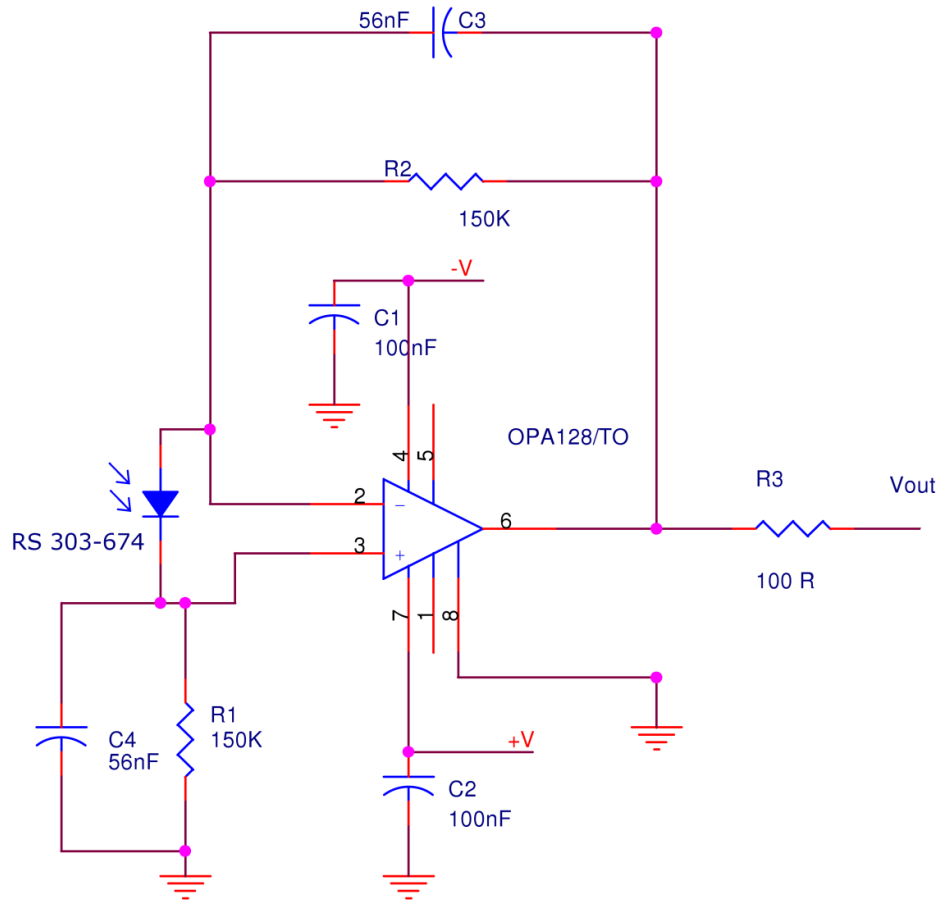


Figure 45 – Schematics of the photodiode amplifier circuit.

Regarding the proposed configuration, the video projector was used to project the result of the product between the image to be reconstructed and the random measurement patterns (see Figure 46). Therefore, each of the output voltages of the photodiode amplifier circuit was representative of the inner product between the used pattern for that measurement and the image to be reconstructed.

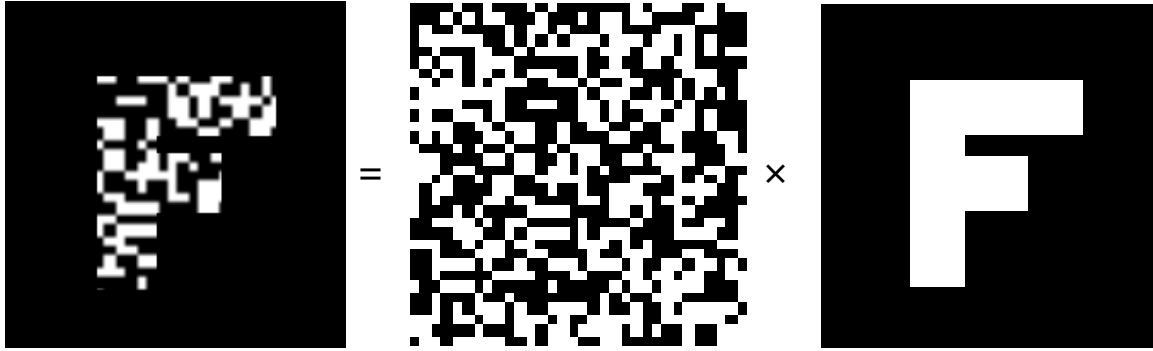


Figure 46 – Example of one of the projected images, representing the product between a random measurement pattern and the image to be reconstructed.

Initial results obtained with the active illumination system for an image containing sharp edges are presented in Figure 47. The reconstructed images have 32×32 pixels, in order to speed up the reconstruction and testing procedures during this experimental phase.

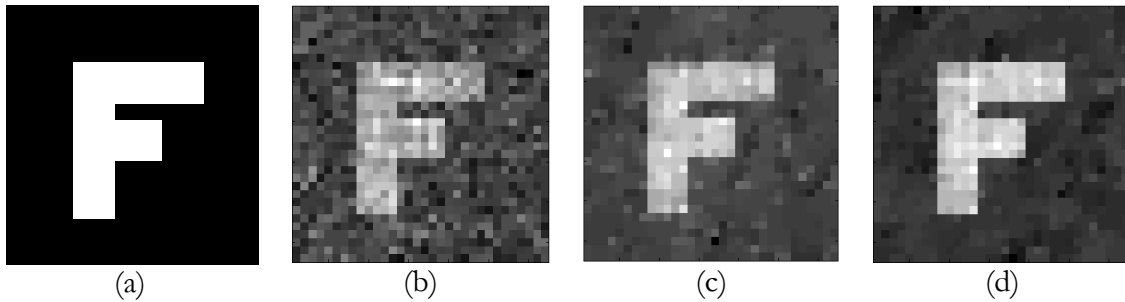


Figure 47 – (a) Reference image. First results obtained (32×32 pixels $\Rightarrow N = 1024$) with the active illumination single-pixel camera using: (b) 205 measurements \Rightarrow 20% (PSNR = 11.08 dB); (c) 410 measurements \Rightarrow 40% (PSNR = 12.30 dB); (d) 717 measurements \Rightarrow 70% (PSNR = 13.21 dB). All the PSNR were calculated using the reference image and the respective reconstructed image.

The data management and all the measurement steps, related with image projection and data sampling, were controlled and synchronized with MATLAB® software that was specifically developed for this purpose. The sampling frequency used for these experiments was 10 kSamples/s and 1000 samples were acquired and averaged for each measurement.

The reconstructions were obtained with the ℓ_1 -Magic software package [67] finding the solution with minimum total-variation. ℓ_1 -Magic is a collection of MATLAB® routines for solving the convex optimization programs central to compressive sampling. The results were obtained with MATLAB® on Microsoft Windows 7 with an Intel® Core™2 Duo CPU @ 2.50GHz and 3 GB of RAM. The average processing time to reconstruct a 32×32 pixels image from 410 measurements was approximately 10 seconds and the average processing time to reconstruct a 64×64 pixels image from 1640 measurements was approximately 400 seconds. In addition, it should be taken into account the approximate 420 ms consumed to project each code and perform the associated measurement. Therefore, bigger images could have been reconstructed at the expense of more time.

From the results shown in Figure 47, based on the PSNR values, it is clear that with an increasing number of measurements, the overall quality of the reconstructed images is also increased. The size of the “F” character on the wall was 4 cm \times 3 cm, thus resulting on a spatial resolution of approximately 2 mm per pixel, for the 32 \times 32 pixels image.

The Peak Signal-to-Noise Ratio (PSNR) values were calculated according to the formula presented in equation (11). In equation (11), MAX is the maximum possible pixel value of the image and MSE is the Mean-Squared-Error (see equation (12)) for two monochromatic images, I and K , with sizes $m \times n$.

$$PSNR = 20 \log_{10} \left(\frac{MAX}{\sqrt{MSE}} \right) \quad (11)$$

$$MSE = \frac{1}{mn} \sum_{i=0}^{m-1} \sum_{j=0}^{n-1} [I(i, j) - K(i, j)]^2 \quad (12)$$

Figure 48 depicts the results obtained when the active illumination system was used for imaging of a more complex scene. In this case, only the random patterns were projected as the scene was composed of real objects.

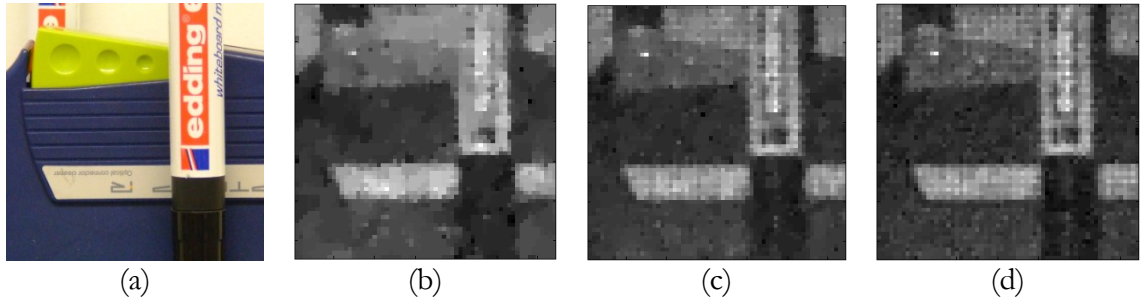


Figure 48 – (a) Original scene; Image reconstruction using: (b) 20% of the measurements (PSNR = 69.74 dB); (c) 40% of the measurements (PSNR = 75.60 dB); (d) 60% of the measurements. All the reconstructions are images with 64 \times 64 pixels (N = 4096). All the PSNR values were obtained comparing the respective image with the image reconstructed using 60% of the measurements.

Experiments were also conducted in order to test the robustness of the system in the presence of noise. Based on the PSNR values, it was possible to conclude that the system was able to reconstruct images of similar quality when the amplitude of the added noise was below 20% of the maximum amplitude of the signal (SNR = 14.54 dB). The results of the conducted experiments are depicted on Figure 49.

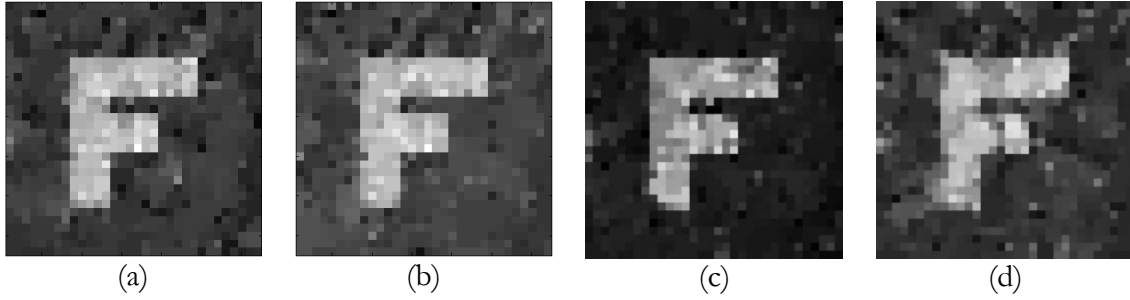


Figure 49 – Reconstruction of the image of Figure 47 c) after the addition of uniformly distributed noise with maximum amplitude of: (a) 10% of the maximum amplitude of the measured signal (SNR = 20.63 dB) – PSNR = 26.62 dB; (b) 20% of the maximum amplitude of the measured signal (SNR = 14.54 dB) – PSNR = 25.03 dB; (c) 30% of the maximum amplitude of the measured signal (SNR = 11.41 dB) – PSNR = 20.17 dB; (d) 40% of the maximum amplitude of the measured signal (SNR = 8.48 dB) – PSNR = 13.87 dB. All the PSNR values were calculated comparing the respective image with the image of Figure 47 c).

Besides the time taken to perform all the desired measurements and to reconstruct an image, some limitations concerning memory usage, which limited the number of acquired measurements, were also experienced. These arose from the fact that the pseudo-random measurement or sensing matrices (generated with uniform distribution) were being stored for the reconstruction phase as they were being used. The preliminary algorithms were not optimized in the sense that the measurement and reconstruction phases have been condensed into the same execution. Therefore, if one wanted to reconstruct an image using two different amounts of measurements, the complete algorithm had to be run twice.

As stated before in section 2.3, random matrices are largely incoherent with any fixed basis. So, afterwards, we compared the performance obtained with pseudo-random measurement matrices to that obtained with permuted Hadamard measurement matrices, having both given similar results. The major advantage in using Hadamard based measurement matrices relied on the fact that they could be built on-the-run during the measurement and reconstruction phases, avoiding the memory usage that otherwise is required to save all the matrices. As will be attested, this was an important aspect taken into consideration for the development of a system with improved performance.

Even though the projector's resolution limit was not fully exploited in the current work, it must be emphasized that super-resolution images could have been obtained either by using multiple sub-pixel shifted images of the same scene [68] or by exploring the fact that patches in a natural image tend to redundantly recur many times inside the image, both within the same scale, as well as across different scales [69].

This preliminary work was very important to get acquainted with the subject of single-pixel imaging. Moreover, it was also possible to obtain interesting experimental results for a flexible single-pixel CS imaging architecture based on active illumination.

However, the performance of this system could benefit from:

- the use of a photodiode amplifier circuit with better signal conditioning and variable gain – to provide improved immunity against electrical noise and scale the signal in order to make use of all the dynamic range.
- the use of an A/D signal acquisition board with better resolution – to reduce the quantization error;
- the use of an A/D signal acquisition board with higher sampling frequency – to speed up the measurement process;
- the use of a faster image reconstruction software;
- the use of optimized and more flexible optical components – to maximize the amount of collected light and to ease the optical alignment;
- the use of Hadamard based measurement matrices - to avoid the memory usage that otherwise is required to save all the matrices containing the random codes;
- the development and implementation of optimized software for data management and measurement control.

In order to overcome these limitations, an improved active illumination single-pixel imaging system, whose scheme is presented in Figure 51, has been implemented (see Figure 52) with the equipment listed in Table 3.

The spectral responsivity of the amplified Silicon photodiode can be found in Figure 50.

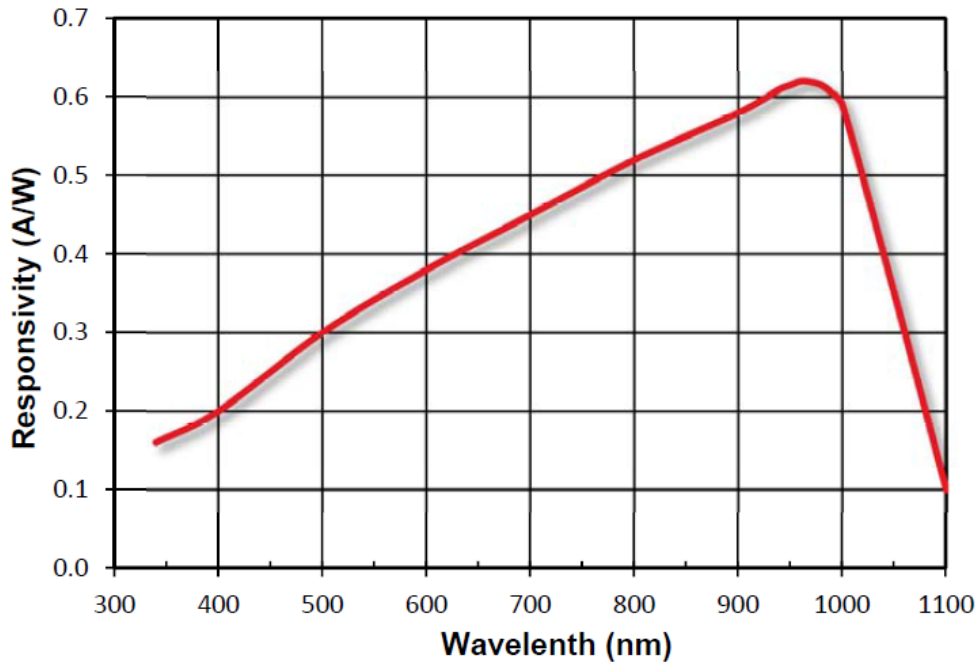





Figure 50 – Spectral responsivity of the Thorlabs PDA100A-EC amplified Silicon photodiode. Picture reproduced from the manual, available at <http://thorlabs.com/Thorcat/13000/PDA100A-Manual.pdf>.

Table 3 – Equipment for the active illumination single-pixel imaging system.

	LCD video projector Epson® - model EB W7 <ul style="list-style-type: none"> • 1280 × 800 (WXGA) maximum resolution.
	Analog-to-Digital converter National Instruments™ DAQ board - model PCI-6221 <ul style="list-style-type: none"> • maximum sampling rate – 250 kSamples/s; • resolution – 16 bits; • maximum voltage range – [-10 V, 10 V].
	Amplified Silicon photodiode Thorlabs – model PDA100A-EC <ul style="list-style-type: none"> • output voltage range [0 V, 10 V]; • switchable gain adjustment over a 70 dB range; • active area - Ø9.8 mm; • wavelength range [400 nm, 1100 nm].

In the photo of Figure 52, in the closest plane to the observer, one can see the Epson® projector. In the background, from left to right, one can observe the object being acquired with the random binary measurement codes projected on it, the amplified photodiode with the lens and the BNC connector block (National Instruments™ - BNC-2110) that was connected to the DAQ board.

The NESTA software package [66], available in MATLAB®, was used for image reconstruction and proved to be much faster than the ℓ_1 -Magic. For example, on the same computer of the preliminary system, for a 32×32 pixels image from 410 measurements the average reconstruction processing time was 0.6 seconds (94% faster), and for a 64×64 pixels image from 1640 measurements it was 3.5 seconds (approx. 99% faster). It is important to emphasize that the reconstruction time reduces with the increase of measurements used to perform the reconstruction.

The data management and all the measurement steps were now controlled through a LabVIEW™ software based application specifically developed for this purpose. This application software proved to be much faster than the MATLAB® one, in particular in the communication with the signal acquisition board and in the projection of the images containing the random binary measurement codes.

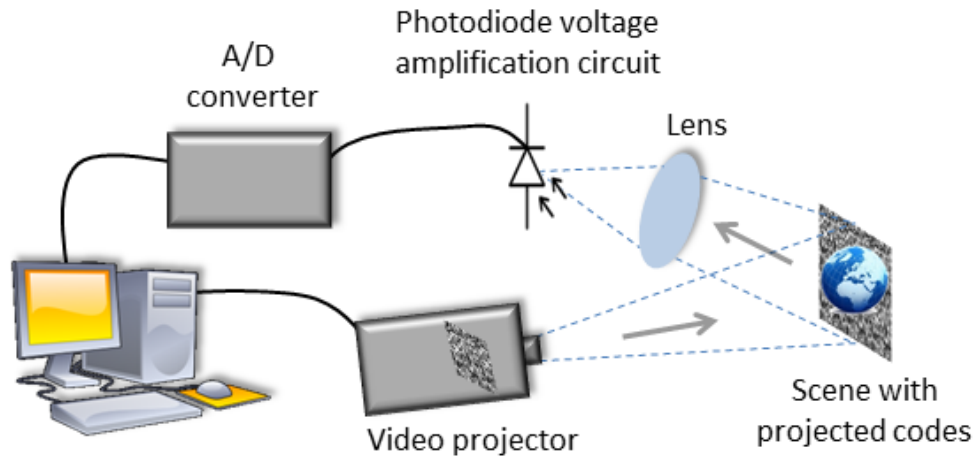


Figure 51 – Scheme of the compressive active illumination single-pixel imaging system.

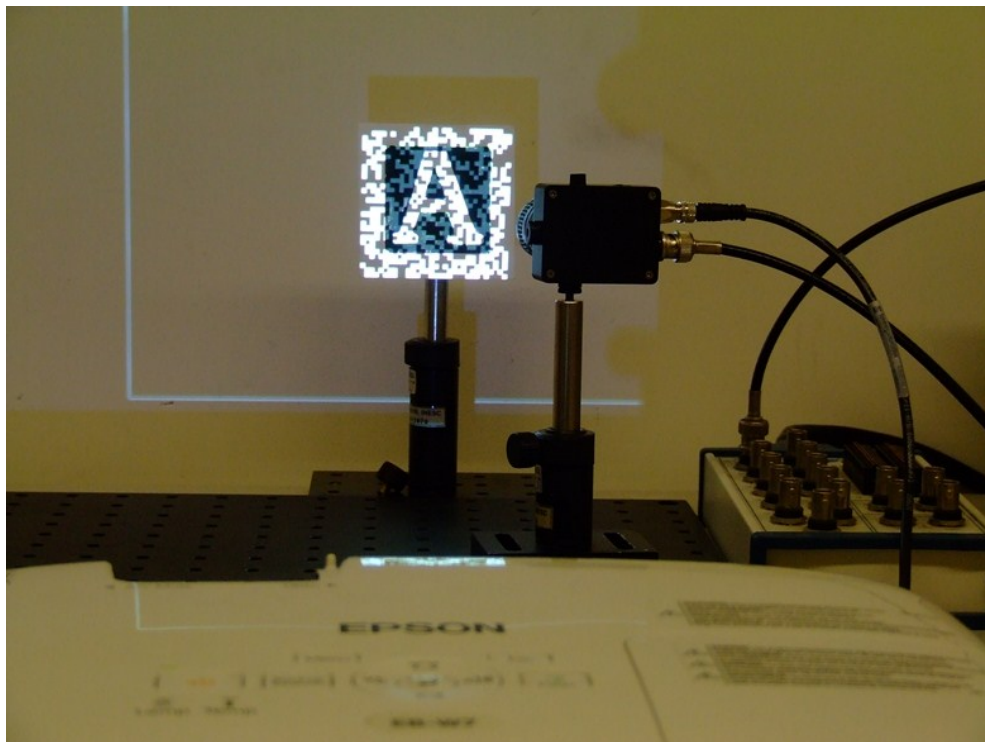


Figure 52 – Photo of the compressive active illumination single-pixel imaging system.

Results and discussion

In order to evaluate its performance, the setup was used for the acquisition of images of a wood object painted in black and white (see Figure 53). The object of Figure 53 is a square with 80 mm side. The dimensions of the “A” character are 50 mm × 45 mm and the thickness of the white border around is approximately 13 mm.



Figure 53 – Photo of the black and white wood object with character “A” taken with a conventional camera.

In Figure 54, images of the object depicted in Figure 53 reconstructed with different resolutions are shown on the left column. The central column contains the images represented on the left column after median filtering with a 3x3 kernel and contrast adjustment. On the right column, for comparison purposes, it can be seen the images acquired with a conventional camera (see Figure 53) downsized to the respective resolution. All the images presented in Figure 54 are displayed using an intensity map with 256 gray levels. It is important to refer that all the reconstructed images (left column) are displayed in raw.

For the acquisition of these images with the active illumination single-pixel camera, the sampling frequency was set to 250 kSamples/s and 10000 samples were acquired for each measurement. Then, the mean value for each set of 10000 samples was recorded as the voltage resulting from the respective projected compressive code. This averaging procedure was introduced because the liquid crystal displays (LCD) of the video projector are not static, even when a still image is being projected. Instead, they exhibit a variable modulation that results in fluctuations of the intensity of projected light. This modulation arises from the fact that if a liquid crystal cell is operated in DC it will be rapidly damaged due to the electrochemical reactions that will occur [70, 71]. In addition, one must also bring into account a ripple that is present in the emitted light. The frequency of this ripple has been analyzed and determined not to be constant. Regarding this issue, contacts have been established with the projector’s manufacturing company but it was not possible to obtain any clarification. To illustrate these aspects, Figure 55 shows the voltage signal output from the amplified photodiode circuit, when the video projector was being used for illumination. During these and all the subsequent experiments, the gain of the amplified photodiode circuit was set to a level that would ensure that when a white image was projected on the scene, the voltage output would be as close as possible to the maximum output voltage (10 V) without saturating. This ensured the measurements were performed making the best use of the maximum dynamic range and resolution of the data acquisition board (A/D converter), therefore increasing the SNR of the measurements.

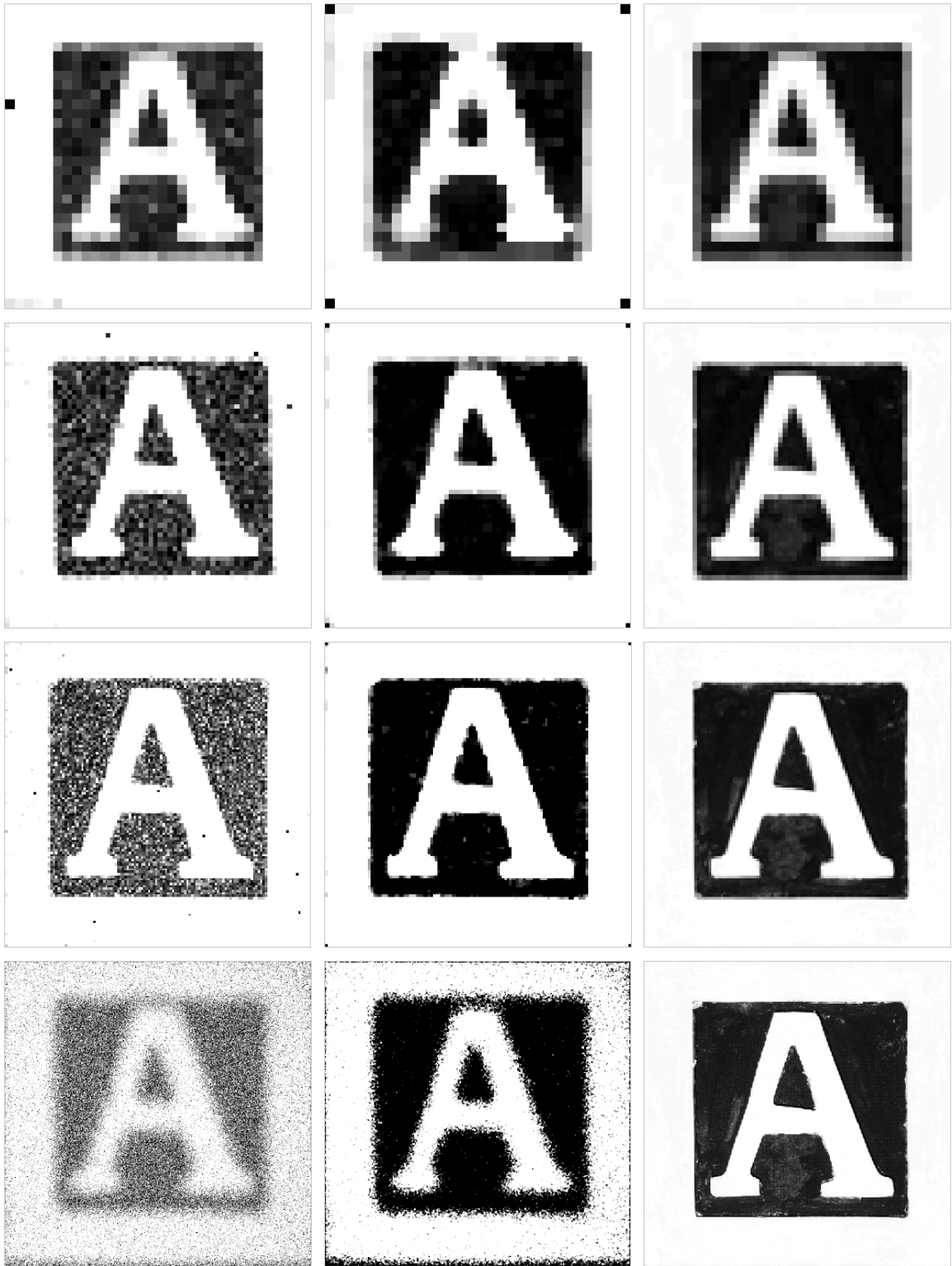


Figure 54 – Several images of the black and white wood object containing the character “A”. Image resolution (in pixels) from top to bottom: 32×32 ; 64×64 ; 128×128 ; 512×512 . Left column contains the images acquired with the active illumination single-pixel monochrome imaging system. Center column contains the images represented in left column after median filtering and contrast adjustment. Right column contains the images acquired with a conventional camera downsized for comparison purposes.

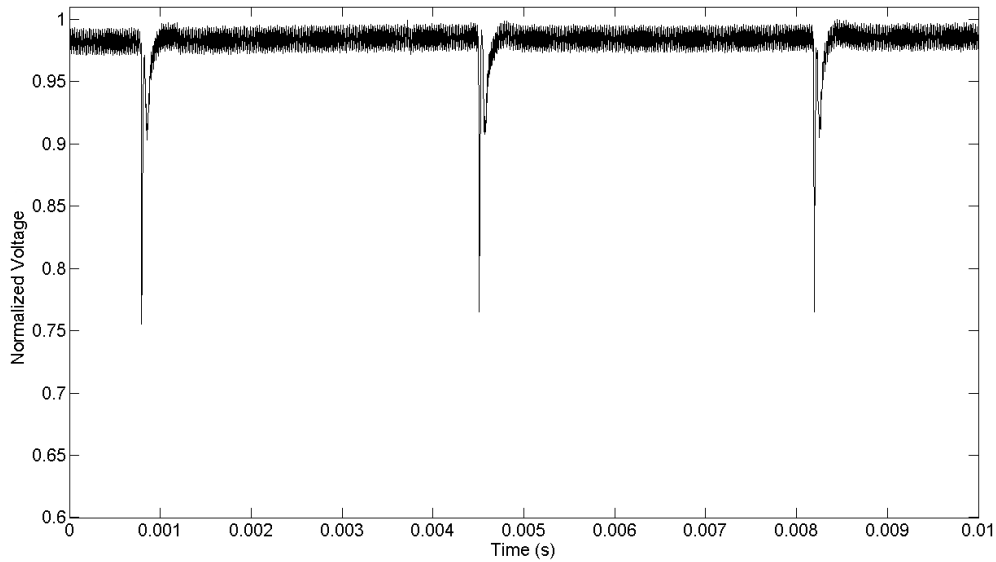


Figure 55 – Plot of the voltage signal on the output of the amplified photodiode circuit. The effect of the variable modulation and ripple of the light is clearly seen.

From the observation of the images presented in Figure 54, one can state that the quality of the images obtained with the single-pixel camera for lower resolutions, such as 32×32 pixels, is comparable to that of the images obtained with a conventional camera. However, for higher resolutions this fact does not hold true and the single-pixel camera images become noisier than the conventional camera counterparts. This arises from the fact that when the resolution is increased the pixels in the compressive codes are defined by a smaller number of pixels on the LCD, as suggested by the following explanation.

During these experiments the projector was positioned so that the projected codes matched the size of the object being imaged and that they were focused on the surface of the foresaid object. This was necessary because the projector was desired to be as close as possible to the object in order to maximize the density of light on its surface and because of the projector minimum working distance. So, as an example, when the system was projecting a 32×32 pixels compressive code, each pixel of the code was defined by 8×8 pixels on the LCD (256×256 pixels image), while in the case of a compressive code with 128×128 pixels each pixel of the code was defined by 2×2 pixels on the LCD (256×256 pixels image). As a result, the variation on the amount of projected light when one pixel of the 32×32 pixels compressive code was turned on and off was superior to that verified when one pixel of the 128×128 pixels compressive code was turned on and off. Thus, one can infer that the SNR of the measured signal drops with the increase of resolution of the projected compressive codes, if the real-world size of the projected image is kept constant. To overcome this drawback, one could use, for instance, a photomultiplier instead of a photodiode, or an analog-to-digital converter with even more resolution.

One particular note should be made to the case of the image reconstructed with 512×512 pixels (see Figure 54), where the projected compressive codes were not focused on the surface of

the object. This was due to the fact that for a 512×512 pixels compressive code, the smallest image one can define on the LCD is also defined by 512×512 pixels and the projector's working distance that would focus that image on the surface of the object would cause it to become much bigger than the object. Therefore, for that configuration, the projector was positioned close to the object so that the projected image only illuminated its surface, even causing the image to be completely out of focus. However, it is interesting to observe that it was still possible to reconstruct a perceptible image with 512×512 pixels. This can be justified by the fact that even not being focused on the object, the amount of projected light was still dependent on the codes applied to the LCD, therefore compressing the spatial information of the object under its illumination. This reinforces the fact that, if one scene is being randomly illuminated and one can find a model for that randomness, then it will be possible to reconstruct that scene with a single-pixel compressive imaging system.

Nonetheless, it is worth mentioning that by means of simple post-processing tasks, such as median filtering and contrast adjustment, it was possible to significantly improve the visual quality of the reconstructed images, closer to that obtained with a conventional camera (see Figure 54).

In order to quantify the similarity of the reconstructed images to the images acquired with the conventional camera, the PSNR values have been calculated for the images of Figure 54. These results are listed in Table 4. Except for the case of the image with 32×32 pixels, it is clear that, relatively to the raw images, there was an improvement of similarity between the post-processed images and those acquired with the conventional camera, translated by higher PSNR values. The different tendency exhibited by the image with 32×32 pixels can be justified by the smoothing verified in the top and bottom transitions between the black and white portions of the image caused by the post-processing operations. With the increase of the resolution, a decrease of similarity was verified. This can be justified by the fact that with lower resolutions, any eventual discrepancies between the images may not be resolved by the available number of pixels, while the same may not be verified with higher resolutions.

Table 4 – PSNR values obtained for the reconstructed images of Figure 54 relatively to the images acquired with the conventional camera.

Resolution (pixels)	PSNR (dB)	
	Raw image	Post-processed image
32×32	17.53	16.65
64×64	14.45	15.63
128×128	12.08	14.79
512×512	9.94	11.66

The normalized cross-correlation, $\gamma(u, v)$, has also been calculated for the images in Figure 54 according to the formulation provided by Lewis [72], which is presented below in equation 13. In equation 13, f , g , \bar{f} and \bar{g} are the images being analyzed and the respective means. $\bar{f}_{u,v}$ is the mean of f in the region under analysis.

$$\gamma(u, v) = \frac{\sum_{x,y} [f(x, y) - \bar{f}_{u,v}] [g(x - u, y - v) - \bar{g}]}{\sqrt{\sum_{x,y} [f(x, y) - \bar{f}_{u,v}]^2 \sum_{x,y} [g(x - u, y - v) - \bar{g}]^2}} \quad (13)$$

The normalized cross-correlation was used to ensure that the quality assessment conducted by the PSNR was not being biased by the intensities of the images. In Table 5, the maximum values of the normalized cross-correlation of the different images are presented.

Table 5 – Maximum values of the normalized cross-correlation obtained for the reconstructed images of Figure 54 relatively to the images acquired with the conventional camera.

Resolution (pixels)	Normalized cross-correlation [0, 1]	
	Raw image	Post-processed image
32 × 32	0.96	0.94
64 × 64	0.91	0.93
128 × 128	0.83	0.92
512 × 512	0.66	0.89

Analyzing the results presented in Table 5, one can verify that the tendency obtained with the PSNR was maintained, thus confirming its validity.

In the following tables, it can be seen, for different resolutions, the time taken to perform 100% of the measurements (see Table 6) and the time consumed to reconstruct the images for different levels of compression (see Table 7). For the results presented in Table 7, for instance, a compression of 30% means that 70% of the measurements were used for reconstruction.

The computational times presented in Table 7 were obtained with the NESTA software package executed with MATLAB® running on the same computer as indicated before.

Table 6 – Time taken to perform 100% of the measurements needed to reconstruct the images with different resolutions, using the Epson® video projector to project the compressive codes.

Resolution (pixels)	Time taken to acquire 100% of measurements (min)
32×32	3.7
64×64	14.7
128×128	60.6
512×512	1604

Table 7 – Time consumed during reconstruction for different compression levels and different resolutions.

Time consumed during reconstruction (s) vs. compression level (%)				
Resolution (pixels)	50%	30%	10%	0%
32×32	0.58	0.46	0.34	0.08
64×64	2.51	1.63	1.09	0.22
128×128	8.71	5.93	4.56	0.84
512×512	413.22	249.80	108.45	20.24

The active illumination single-pixel monochrome camera was also used for the acquisition of an image of a five-pointed black star filled with three different gray levels (see Figure 56). The five-pointed star of Figure 56 was printed in common paper with a width of 80 mm and a height of 73 mm.



Figure 56 – Five-pointed black star filled with three different gray levels.

The raw results for the reconstruction of the star represented in Figure 56 are presented on the left column of Figure 57. The center column contains the images of the left column after median filtering with a 3×3 kernel and contrast adjustment. For comparison purposes, it was acquired a photo of the five-pointed star with a conventional camera. This photo was subject to contrast adjustment and was then downsized to the different resolutions (see right column of Figure 57).

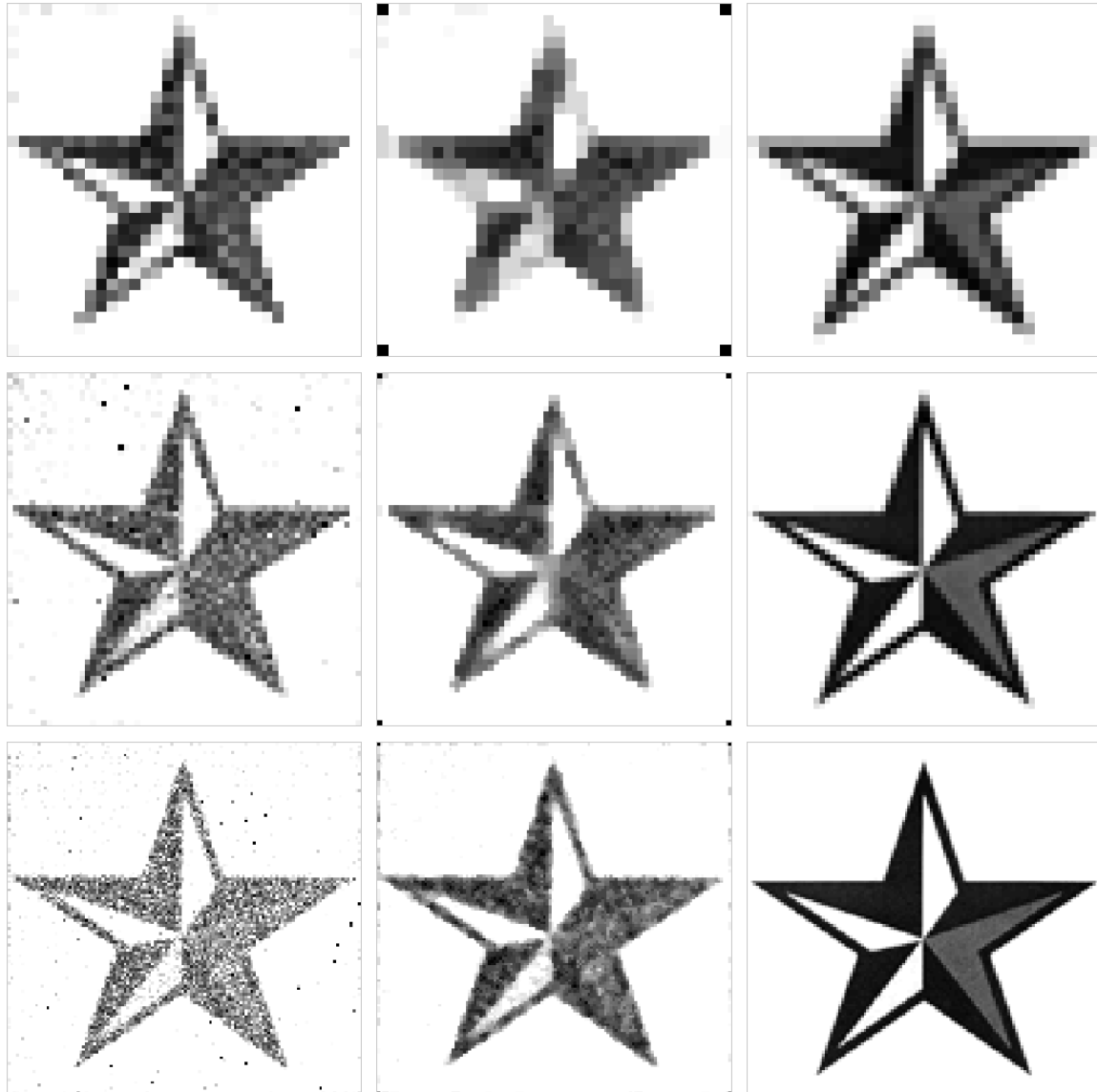


Figure 57 – Several images of the grayscale five-pointed star. Image resolution (in pixels) from top to bottom: 32×32 ; 64×64 ; 128×128 . Left column contains the images obtained with the active illumination single-pixel monochrome imaging system. Center column contains the images represented in left column after median filtering and contrast adjustment. Right column contains the images acquired with a conventional camera downsized for comparison purposes.

Similarly to the case of the images of Figure 54, the PSNR and the normalized cross-correlation were calculated for the reconstructed images of Figure 57 relatively to the images acquired with the conventional camera. The results obtained are presented in Table 8 and Table 9.

Table 8 – PSNR values obtained for the reconstructed images of Figure 57 relatively to the images acquired with the conventional camera.

Resolution (pixels)	PSNR (dB)	
	Raw image	Post-processed image
32×32	17.33	15.57
64×64	14.26	14.72
128×128	11.67	13.99

Table 9 – Maximum values of the normalized cross-correlation obtained for the reconstructed images of Figure 57 relatively to the images acquired with the conventional camera.

Resolution (pixels)	Normalized cross-correlation [0, 1]	
	Raw image	Post-processed image
32×32	0.92	0.87
64×64	0.88	0.89
128×128	0.8	0.89

Even though a human observer would consider the post-processed images of Figure 57 to present better visual quality and to be more similar to those acquired with a conventional camera, this was faintly confirmed by the used metrics as can be seen in the results presented in Table 8 and Table 9. Perhaps, the benefit of using post-processing was more evident with the images of Figure 54 because the scene they were describing can be considered to be less complex, due to its simpler spatial content and binary nature.

From the experiments it was also possible to conclude that it should exist a certain period of time between the moment the order for image display is issued and the moment the measurement is performed. For the Epson® video projector, this interval should be at least 130 ms.

4.1.2 Passive illumination single-pixel monochrome imaging systems

As it will be explained in this section, it is possible to implement single-pixel imaging systems that do not rely on the use of the illumination to compress the spatial information of the acquired scene, as it was demonstrated in the previous section. Hence designated passive illumination single-pixel imaging systems, such systems compress the spatial information combining the random binary codes with the incoming light field. The result of each combination is then integrated to produce the incoherent projection vectors.

In this context, passive illumination imaging systems may use ambient light but, during the experiments here presented, the room was completely dark and an auxiliary source of light was used in order to ensure the reproducibility of the illumination conditions. The use of an auxiliary source of light also provided some flexibility in the sense that it allowed to control aspects such as the area under illumination and the intensity of the illumination, which were important to provide good dynamic range for the measurements. In particular, the auxiliary source of light was the Epson® video projector.

Contrarily to the active illumination case which uses an LCD video projector for the definition of the compressive random codes, this system relied on a modular DMD development kit, instead. This DMD development kit is designated as “LightCommander™” and is designed and manufactured by Logic PD (*vide* <http://www.logicpd.com/>). The LightCommander can be used as a video projector in which the image to be projected is displayed on a DMD with a resolution of 1024×768 pixels (XGA resolution). Some photos of the LightCommander can be seen in Figure 58.



Figure 58 – Photos of the LightCommander™ development kit from Logic PD.

In Figure 58, the photo on the left shows a general view of the LightCommander™ and its casing, while the photo on the right shows a global view of the general assembly of the optical components, DMD controller board and illumination module with respective power unit. Since the optical assembly and DMD control were the main aspects of interest in the aim of the work here presented, the illumination module and its power unit were removed. As the LightCommander is a modular development kit, these removals did not compromise its operation neither they required any modification.

In Figure 59 it can be seen, with more detail, the schematics of the LightCommander's optical assembly, where M1, M2 and M3 are mirrors, and Tunnel is an internally mirrored light conduit. The main dimensions and distances of the various components are also presented. The principal specifications of the 50 mm f/1.8 Nikon lens (AF Nikkor 50mm f/1.8 D) that accompanies the LightCommander and that has been used throughout all this work are presented in Table 10.

Table 10 – Main specifications of the Nikon lens that accompanies the LightCommander.

Mount Type	Nikon F-Bayonet
Focal Length	50 mm
Maximum Aperture	f/1.8
Minimum Aperture	f/22
Minimum Focus Distance	0.45 m

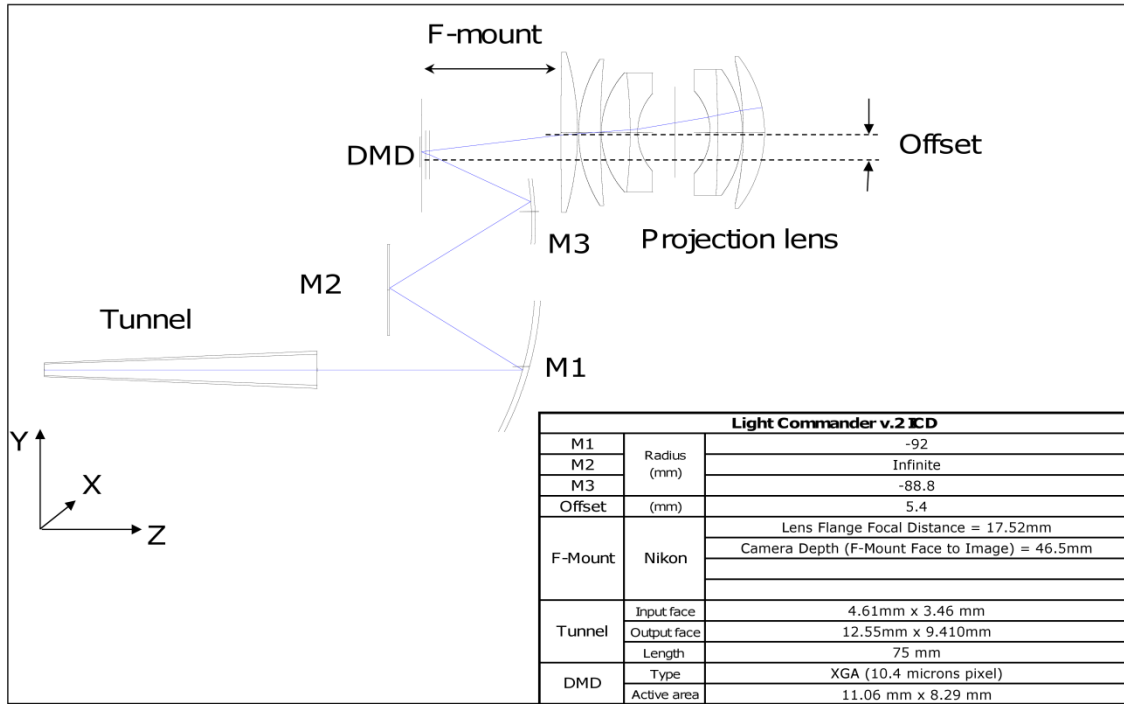


Figure 59 – LightCommander's optical schematics. (Kindly provided by LogicPD)

Figure 60 shows a photo of a DMD chip from Texas Instruments next to a 1 cent coin for size comparison.

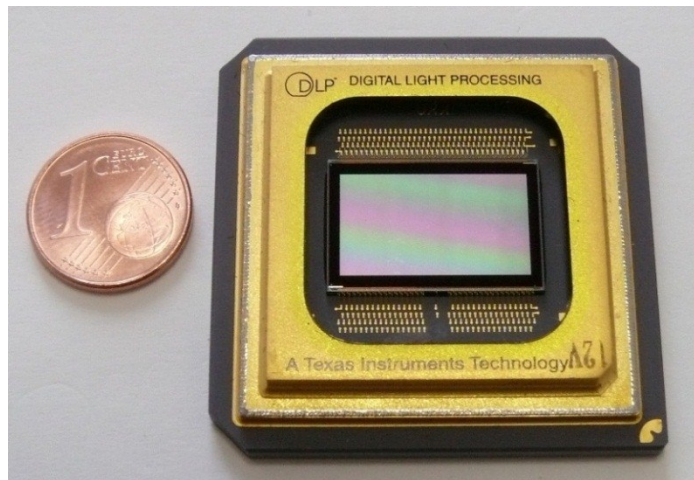


Figure 60 – Photo of a DMD chip from Texas Instruments next to a 1 cent coin for size comparison.

Picture reproduced from http://de.academic.ru/pictures/dewiki/68/DLP_Chip.jpg.

Figure 61 (a) illustrates two mirrors from a DMD and their principle of operation. There it can be seen the two positions ($\pm 10^\circ$) assumed to define either the “1” or the “0” logical state. In Figure 61 (b) it is shown a portion of an actual DMD array with an ant leg so that the observer can create an estimate of the scale.

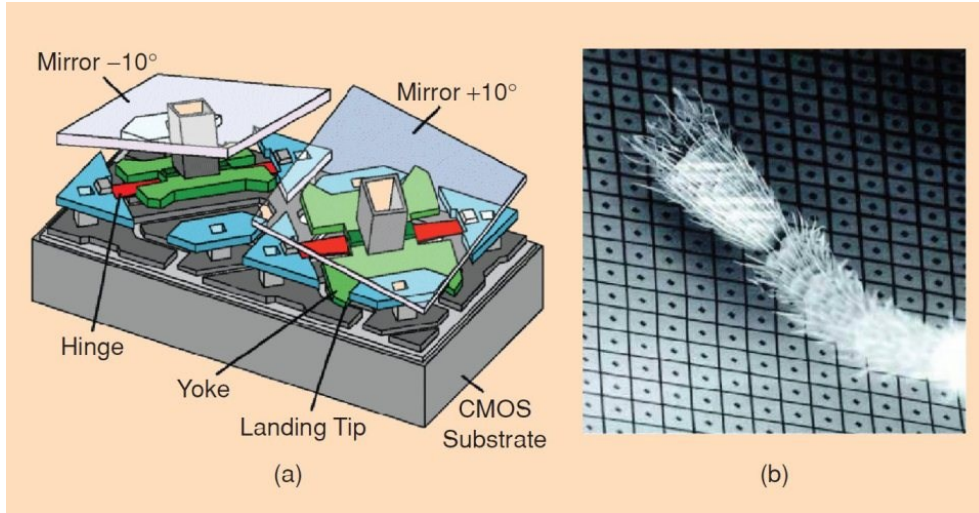


Figure 61 – (a) Schematic of two mirrors from a digital micromirror device (DMD), illustrating its principle of operation. (b) A portion of an actual DMD array with an ant leg for scale. Picture reproduced from [23].

In this work the LightCommander’s light path has been used in a reverse direction, turning it into a camera, instead of a light projector. By other words, the Nikon lens was used to collect the light from the scene and form an image of it on the DMD, where the compressive random codes were displayed. Depending on the codes, the amount of light directed towards the M1, M2 and M3 mirrors would vary and would be, finally, measured by the amplified photodiode circuit placed at the exit of the light tunnel. The output voltage was then converted to the digital domain by means of the National InstrumentsTM PCI-6221 DAQ board that was connected to the computer in control. This configuration has been used to acquire images of the same objects (see Figure 53 and Figure 56) acquired with the active illumination system. Figure 62 shows the scheme of the passive illumination single-pixel monochrome imaging system, while Figure 63 shows a photo of the implemented experimental setup.

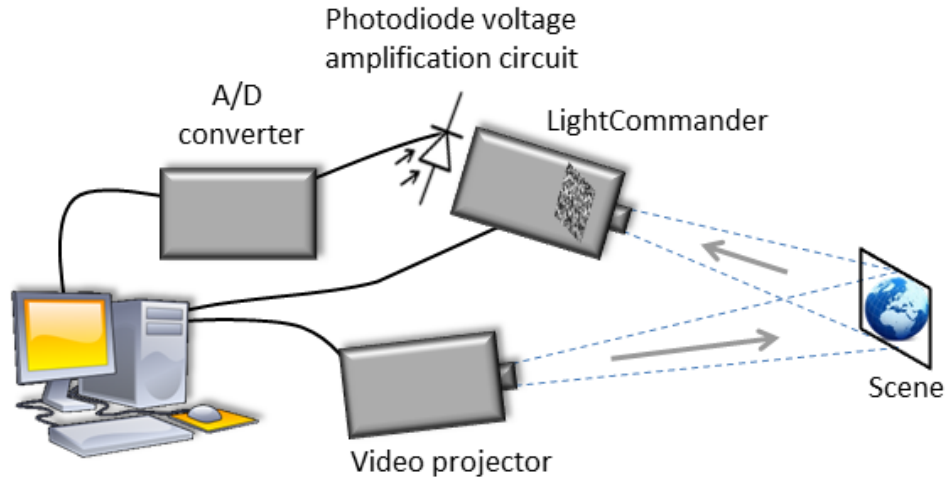


Figure 62 – Scheme of the passive illumination single-pixel monochrome imaging system.

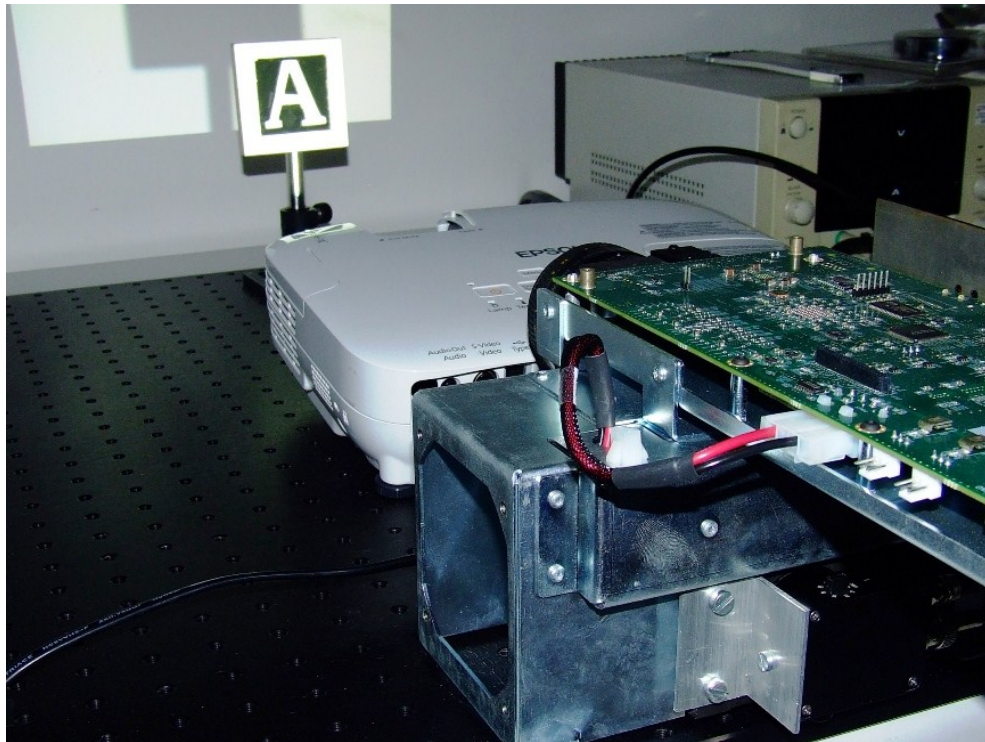


Figure 63 – Photo of the passive illumination single-pixel monochrome imaging system illuminating the black and white wood object of Figure 53.

In these images it is possible to see that the Epson® video projector has been used to provide a uniform illumination of the scene, while the LightCommander was collecting the light to form an image of the scene on its DMD.

Results and discussion

Figure 64 presents the raw images obtained with different resolutions using this setup for the black and white wood object containing the character “A” (see Figure 53). Next to each of the images

obtained, an image acquired with a conventional camera and downsized to the same resolution for comparison is also presented.

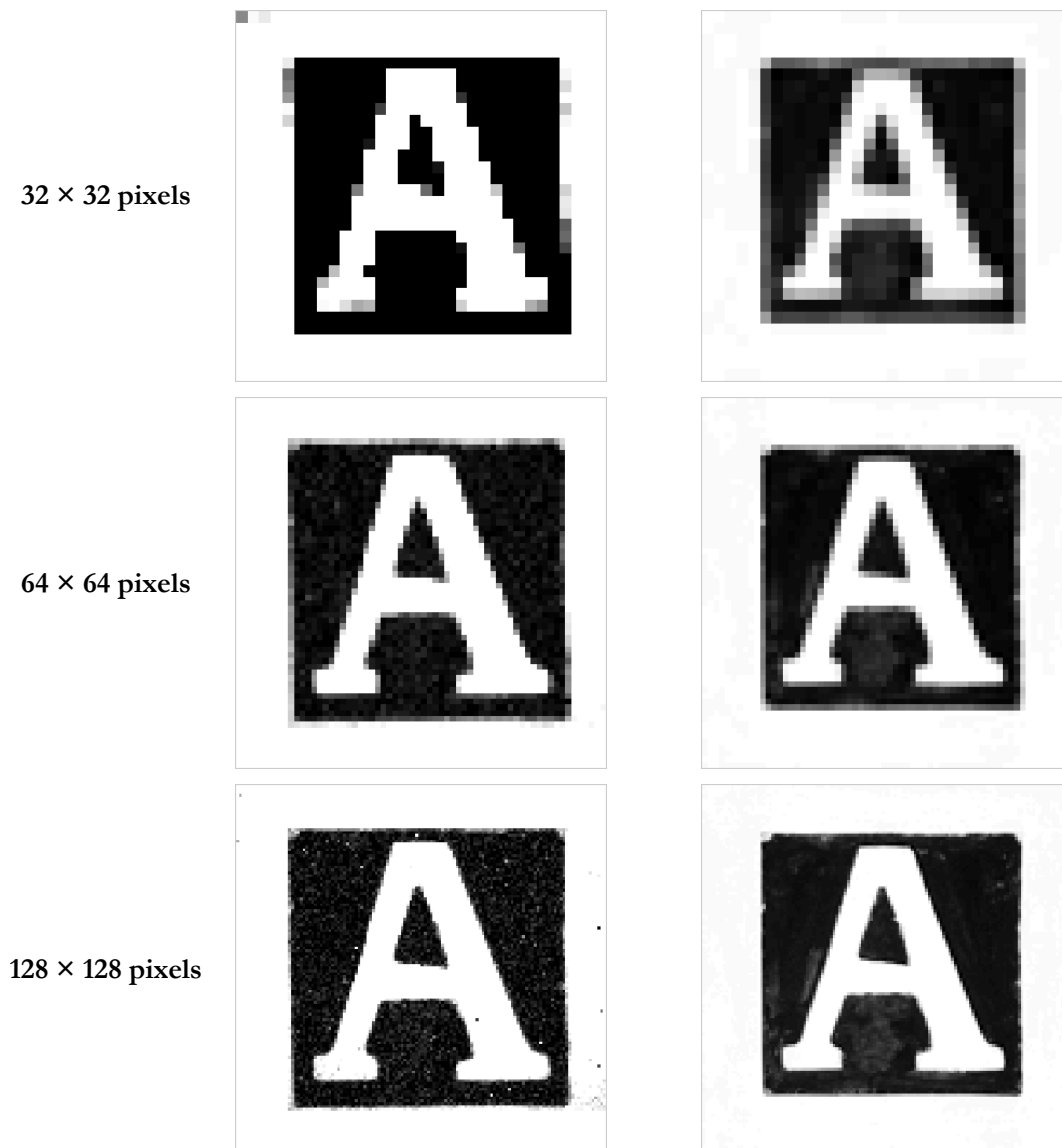


Figure 64 – (left) Several images of the black and white wood object containing the character “A” acquired with the passive illumination single-pixel monochrome imaging system. (right) Images acquired with a conventional camera downsized for comparison purposes.

Next, one can find the results obtained with the PSNR and with the normalized cross-correlation for the reconstructed images of Figure 64 relatively to the images acquired with the conventional camera.

Table 11 – PSNR values obtained for the reconstructed images of Figure 64 relatively to the images acquired with the conventional camera.

Resolution (pixels)	PSNR (dB)
32×32	11.35
64×64	11.62
128×128	11.15

Table 12 – Maximum values of the normalized cross-correlation obtained for the reconstructed images of Figure 64 relatively to the images acquired with the conventional camera.

Resolution (pixels)	Normalized cross-correlation [0, 1]
32×32	0.83
64×64	0.82
128×128	0.8

Unless stated otherwise, for these and all the subsequent experiments with the LightCommander, an active area comprising 768×768 mirrors on the DMD has been used to apply the compressive codes. Therefore, as the working distance was kept constant, in order to maintain the FOV for the different resolutions, a relation for the number of mirrors used to define a pixel of the compressive codes was established. For instance, blocks of 24×24 mirrors were used to define a pixel of the 32×32 compressive codes and blocks of 6×6 mirrors were used to define a pixel of the 128×128 compressive codes. This guaranteed that the FOV was always defined by the 768×768 mirrors area on the DMD.

This setup has also been used to acquire images of the grayscale five-pointed star (see Figure 56) and the results are presented in Figure 65.

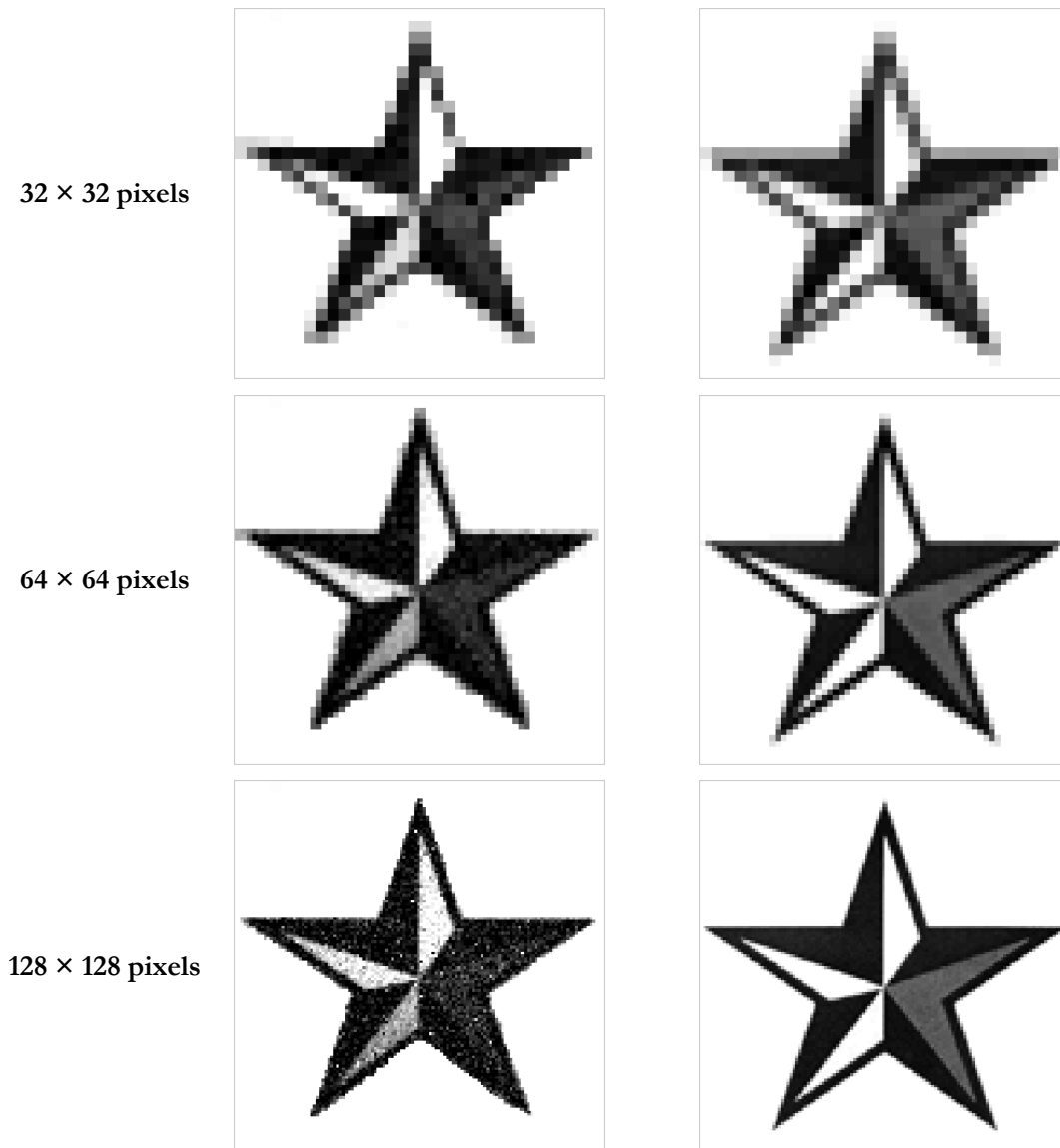


Figure 65 – (left) Several images of the grayscale five-pointed star acquired with the passive illumination single-pixel monochrome imaging system. (right) Images acquired with a conventional camera downsized for comparison purposes.

In order to quantify the quality and similarity of the images of Figure 65 relatively to the images acquired with a conventional camera, the PSNR values and the maximum values of the normalized cross-correlation were obtained for those images. Table 13 and Table 14 contain the results of that assessment.

Table 13 – PSNR values obtained for the reconstructed images of Figure 65 relatively to the images acquired with the conventional camera.

Resolution (pixels)	PSNR (dB)
32×32	14.43
64×64	12.54
128×128	11.75

Table 14 – Maximum values of the normalized cross-correlation obtained for the reconstructed images of Figure 65 relatively to the images acquired with the conventional camera.

Resolution (pixels)	Normalized cross-correlation [0, 1]
32×32	0.85
64×64	0.88
128×128	0.86

The images in Figure 64 and Figure 65 acquired with the passive illumination single-pixel monochrome imaging system are presented without any noise filtering or contrast adjustment. Based on the opinions of human observers, one can state that the similarity of these images to those acquired with a conventional camera is notorious. The biggest difference is the noise presented by the images acquired with the single-pixel imaging system, which could arise from the measurements and from the reconstruction process. Furthermore, visually comparing these results with those obtained with the active illumination homologous system, it can be affirmed that the results obtained with the passive illumination imaging system are better in the sense that they exhibit less noise and are more similar to the images obtained with a conventional camera, even without the use of any filter or post-processing. Perhaps surprisingly, if we rely on the results obtained with the PSNR and with the normalized cross-correlation to compare the two systems, the same cannot be said. In other words, the two metrics indicate that the images obtained with the active illumination single-pixel monochrome imaging system are more similar to the images acquired with the conventional camera. Different alignments, different lighting conditions and even small variations in the field of view could be in the origin of discrepancies in the images that precluded the adequate judgment with the metrics and caused the results to be contradictory to the human opinion, which is here considered to be more correct.

As in the case where the LCD video projector was used to spatially modulate the light, with the LightCommander there is also the need to wait a certain amount of time to ensure that the image transmitted by the video signal was already being displayed in the DMD by the time the measurement order has been issued. For the LightCommander it has been determined that one should wait at least 95 ms.

Table 15 displays the time taken to perform 100% of the measurements needed to reconstruct the images with different resolutions. As expected, the system with the LightCommander performs faster than the system with the video projector (see Table 6).

Table 15 – Time taken to perform 100% of the measurements needed to reconstruct the images with different resolutions, using the Lightcommander's to project the compressive codes.

Resolution (pixels)	Time taken to perform 100% of measurements (min)
32 × 32	3.1
64 × 64	12.6
128 × 128	51.9

It is important to emphasize that when the DMD is used to display the random binary compressive codes the light output does not exhibit any ripple, in opposition to what was observed with the LCD video projector (see Figure 55). For this reason, one could acquire a smaller amount of samples without compromising the quality of the results, thus reducing the time required to perform all the required measurements. However, during these experiments the same amount of samples (10000) was acquired because the Epson® video projector was being used for illumination and the same ripple of Figure 55 was verified in the acquired signals. This also allowed to independently evaluate the benefit of reducing the delay time to 95 ms.

For comparison, it was used a LED source of light without any ripple and it was acquired a 128×128 pixels image considering the same sampling frequency and 10 samples sets for the measurements associated with the different projected codes. The time taken to perform 100% of the measurements for that image was 41.1 minutes (~ 20.8 % faster) and the result was identical to that acquired before with the Epson® video projector as the light source.

If one is interested in the spatial resolution of the imaging system, one might establish a relation between the number of pixels of the acquired image and the real-world dimensions of the corresponding scene. In our system, as the number of mirrors used on the DMD to apply the codes was kept unaltered, the FOV had to be adapted to the dimensions of the scene by changing the distance of the imaging lens to the scene (working distance). Therefore, the imaging system exhibits different spatial resolutions at different working distances. The throw ratio (TR) of a projector results from the division of the distance between the projector lens and the projection screen (D) by the width of the image being projected (W), or more simply $TR = D/W$ (see Figure 66). For the case of an imaging system such as the one presented in this section this explanation shall be adapted accordingly. Hence, W is related to the width of the scene being acquired and D is referring to the working distance of the imaging lens.

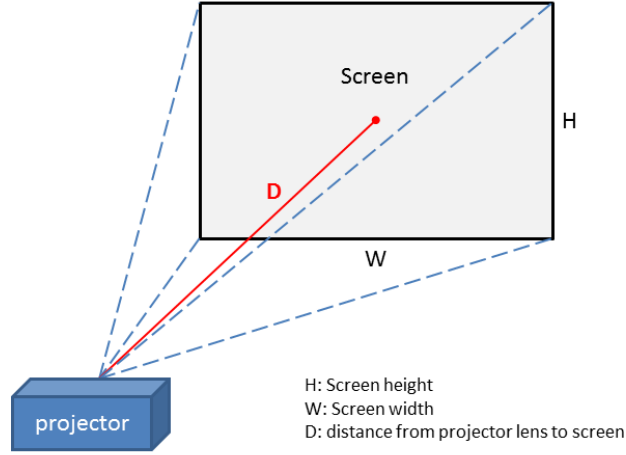


Figure 66 – Illustration for the definition of a projector's throw ratio.

So, in our case, knowing the throw ratio of the LightCommander (3.6) it was possible to establish a relation between the working distance (D) and the spatial resolution. For that, all one had to do was to calculate the horizontal dimension (W) in real-world units and divide it by the corresponding number of pixels (1024). Picking an example of a working distance of 1000 mm, it comes:

$W = 1000 \text{ mm} / 3.6 \approx 277.78 \text{ mm}$, which corresponds to a spatial resolution of $\approx 0.27 \text{ mm/pixel}$. This value holds true for a fixed working distance and as long as the number of pixels of the acquired image remains the same as the number of mirrors used on the DMD to apply the compressive codes (768×768). As the later aspect was not verified for other image resolutions, it shall be multiplied by the specific proportion. For example, the spatial resolution for a 32×32 pixels image is given by $24 \times 0.27 \text{ mm/pixel}$, which is equal to 6.48 mm/pixel . As it has been previously referred, 24 signifies that each pixel of the acquired image with 32×32 pixels is defined by blocks of 24×24 mirrors on the DMD. For a 128×128 pixels image the spatial resolution comes 1.62 mm/pixel .

In order to adjust the working distance of the imaging lens, before the images were acquired, an all-white 768×768 pixels image was displayed on the DMD and the LightCommander's tunnel was flooded with light. Doing so, the illuminated region was indicative of the FOV and the necessary adjustments could be made.

4.1.3 Transmissive single-pixel imaging system

Within the work here presented, it was also our intent to extend its scope to the development of alternative configurations that would disregard the need for an active illumination source and operate in a transmissive mode rather than reflective. For that purpose, the use of a liquid crystal display (LCD) as the spatial modulation device for the light coming from the scene being imaged was envisaged.

The scheme for this approach is depicted in Figure 67.

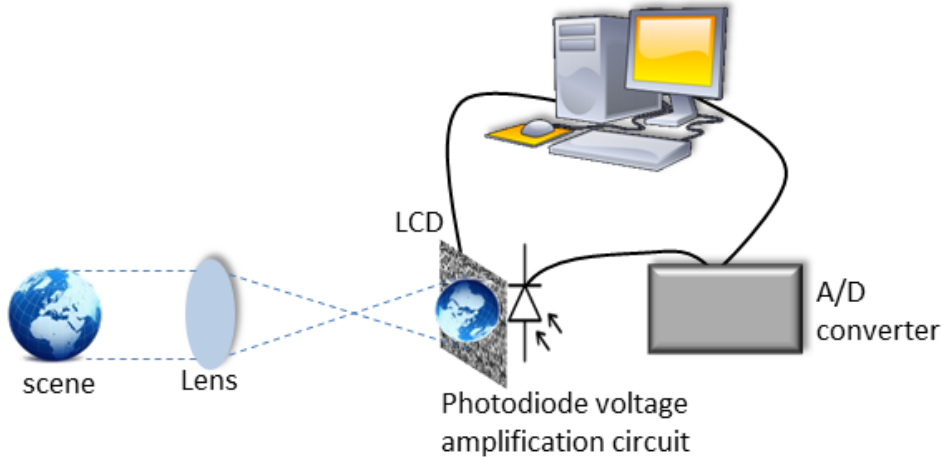


Figure 67 – Scheme of the transmissive single-pixel imaging system.

As it can be seen, by means of a lens system the image of the scene being acquired is formed on the surface of the LCD, behind which lies the photodiode (single-pixel) active region. The LCD was placed between two properly oriented linear polarizers. The photodiode (Thorlabs FDS1010) was part of a voltage amplification circuit (Thorlabs PDA200C) whose output was connected to an analog-to-digital (A/D) converter (National Instruments™ USB-6210) that enabled data acquisition by a computer for subsequent processing. The LCD was controlled via the projector that was receiving the video signal containing the coding patterns from the computer.

Basically, the system applied random binary codes to the LCD and measured the corresponding output voltage from the amplification circuit. As previously stated, based on CS theory, this process can be repeated K times, with K much smaller than the image full dimensionality (N). Afterwards, using combinatorial optimization algorithms (NESTA software package, more in particular), the image that in conjunction with the used codes gave rise to the corresponding voltage measurements is reconstructed.

This transmissive single-pixel camera was then exploited on an optical microscope (see Figure 68), since its optical system is well known and allows an easy configuration of both the optical magnification and working distance. At the same time, with this microscope we could mount a conventional camera on the other optical path and acquire conventional images of the scenes being imaged. This was of great help while focusing and aligning the system, and also because it was possible to acquire images for comparison with the results of the single-pixel camera.

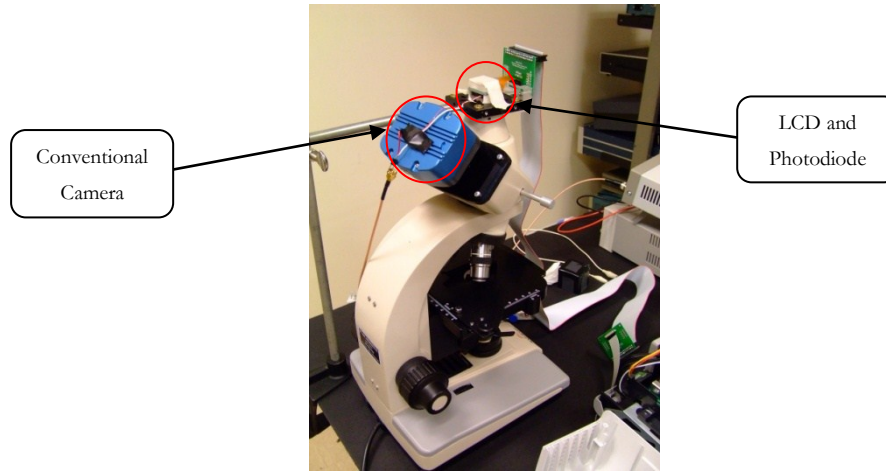


Figure 68 – Transmissive single-pixel camera mounted on a microscope, placed on the vertical optical path. Note the conventional camera (in blue) mounted on the other optical path.

The LCD, having a maximum resolution of 800×600 pixels (active area: $11.2 \text{ mm} \times 8.4 \text{ mm} = 94.08 \text{ mm}^2$), was taken from an Epson® PowerLite S5 projector (see Figure 69). The central part of the LCD (512×512 pixels) was used to apply the random binary codes. The Thorlabs FDS1010 is a silicon photodiode with an active area of 94.09 mm^2 ($9.7 \text{ mm} \times 9.7 \text{ mm}$), whose responsivity is depicted in Figure 70. The photodiode amplifier (Thorlabs PDA200C) that has been used during these experiments, exhibits an analog voltage output ranging from 0 to 10 V, and full scale current measurement ranging from 100 nA to 10 mA (in decade steps), with an amplification varying from $1 \times 10^8 \text{ V/A}$ to $1 \times 10^5 \text{ V/A}$, respectively.

The active areas values confirm the suitability of the LCD and the chosen photodiode to be used together to spatially encode and measure the light, respectively.



Figure 69 – Photo of the LCD module taken from the Epson® PowerLite S5 projector that has been used in the transmissive single-pixel camera (active area: $11.2 \text{ mm} \times 8.4 \text{ mm}$).

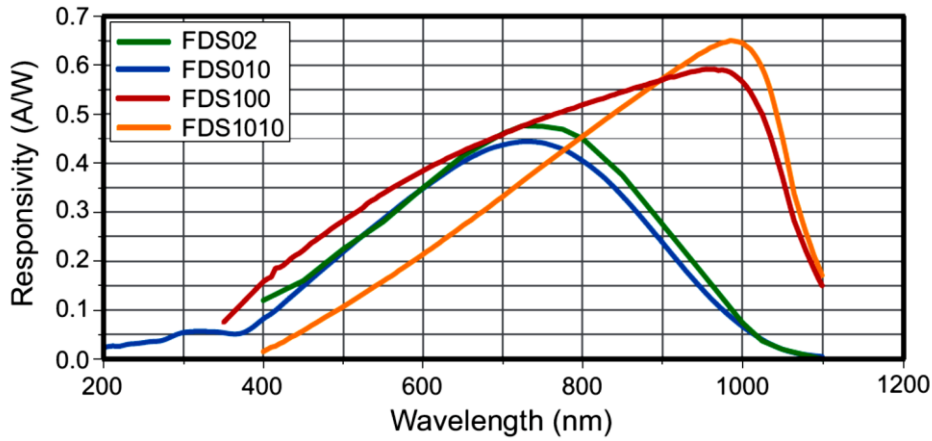


Figure 70 – Thorlabs FDS series photodiode responsivity curves. The yellow curve relates to the photodiode (FDS1010) used on the transmissive single-pixel camera setup. Picture reproduced from <http://www.thorlabs.de/Thorcat/2700/2739-s01.pdf>.

As seen before in section 2.3, random matrices are largely incoherent with any fixed basis Ψ and, therefore, for the measurement or sensing matrices, again, we used Hadamard-based random binary codes. This choice revealed to be of great importance because the Hadamard-based random binary codes could be built on real time, during the measurement and reconstruction phases, avoiding the memory consumption that otherwise would be required to save all the codes.

Results and discussion

One of the scenes acquired with the proposed imaging system is represented in Figure 71. Since the conventional camera sensor size ($\frac{1}{2}$ -inch CCD) was smaller than the LCD size, we had to stitch 4 separate pictures taken with the conventional camera in order to get an image containing the single-pixel imaging system field of view. For the case of the single-pixel imaging system, ideally, its field of view would correspond to the size of the LCD. In particular, the actual field of view was defined by a 512×512 pixels region centered on the LCD active region.



Figure 71 – Image of one of the acquired scenes. This image was obtained from the stitching of 4 separate pictures taken with the conventional camera due to its sensor size ($\frac{1}{2}$ -inch CCD) when compared to the size of the LCD active region. The red inset indicates the region acquired with our single-pixel camera.

Next, some results obtained with the setup of Figure 68 are presented.

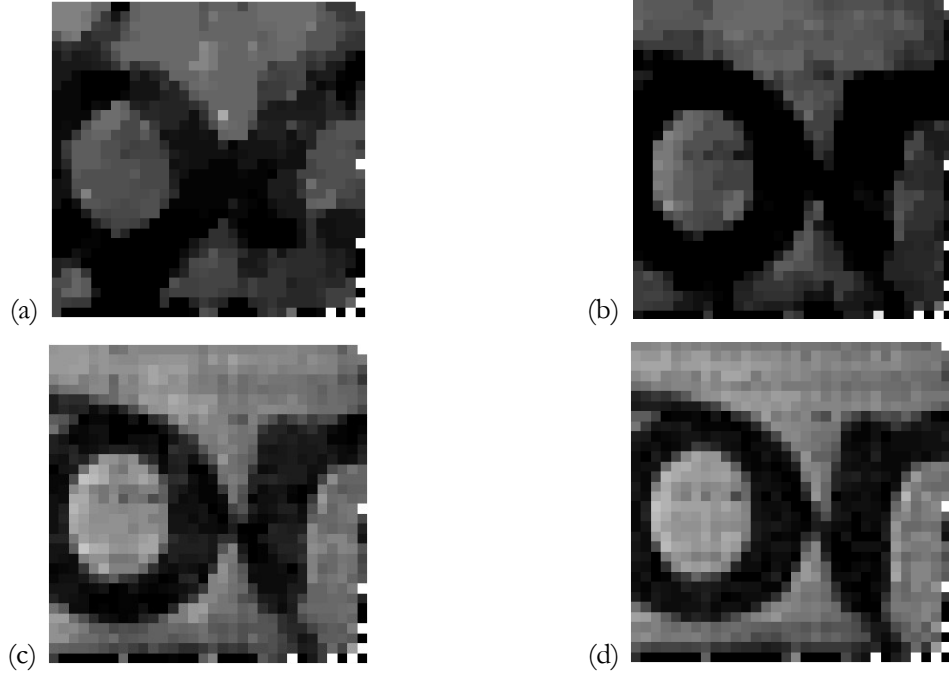


Figure 72 – Reconstruction of an image with 32×32 pixels ($N = 1024$) from: (a) 25% ($K = 256$); (b) 50% ($K = 512$); (c) 75% ($K = 768$); (d) 100% ($K = 1024$) measurements. For each reconstructed image, the PSNR has been calculated relatively to the image reconstructed using 100% ($K = 1024$) of the measurements: (a) PSNR = 12.85 dB; (b) PSNR = 14.34 dB; (c) PSNR = 25.89 dB.

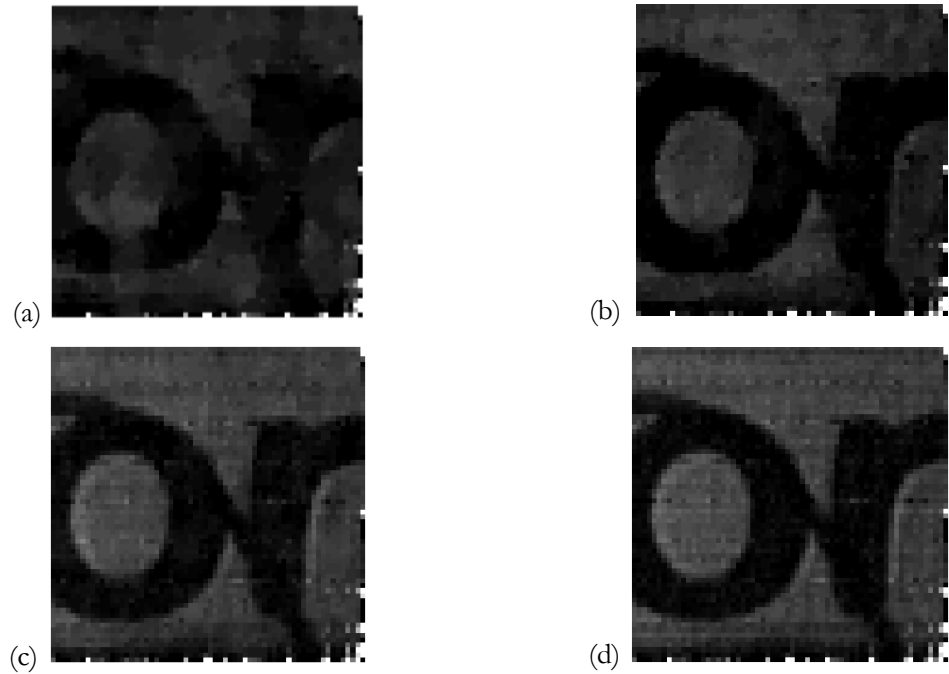


Figure 73 – Reconstruction of an image with 64×64 pixels ($N = 4096$) from: (a) 25% ($K = 1024$); (b) 50% ($K = 2048$); (c) 75% ($K = 3072$); (d) 100% ($K = 4096$) measurements. For each reconstructed image, the PSNR has been calculated relatively to the image reconstructed using 100% ($K = 4096$) of the measurements: (a) PSNR = 20.27 dB; (b) PSNR = 22.63 dB; (c) PSNR = 32.44 dB.

The results presented in Figure 72 and Figure 73, correspond to reconstructions of the scene contained within the red inset of Figure 71. From the analysis of these results, it is clear that the quality of the reconstructed images increased with the growth of the number of measurements used for reconstruction, as well as with the growth of the reconstructed image dimensionality. These facts are supported by the PSNR values presented for each of the reconstructed images relatively to the image of the same size reconstructed using a number of measurements equal to its full dimensionality, i.e., $K = N$. Also, as expected, the images with higher resolution exhibit smoother contours and are more perceptible.

Even though the results shown are satisfactory, they suffer from lack of contrast. This can be justified by two aspects, one being the presence of a variable modulation and ripple on the voltage output and another being the incapacity of the LCD to efficiently filter the near-infrared radiation coming from the microscope halogen lamp which was detected by the photodiode.

Concentrating on the first aspect, as the light coming from the scene was captured by a microscope objective its intensity was significantly reduced, thus shortening the full range of measurement, defined when the LCD was completely blocking or allowing the light to pass, and affecting the SNR of the measurements. Therefore, as the relative variations of the output voltage imposed by the random binary patterns were so small, any significant noise would compromise the quality of the results. The averaging applied to the 10000 samples acquired for each measurement was useful to attenuate the effect of this interference. Furthermore, after some experiments we came to the conclusion that the source of the variable modulation and ripple was mainly the LCD because it always appeared when the LCD was turned on and disappeared when it was turned off. This effect was again attributed to the polarization of the liquid crystals as it has been evidenced before when a video projector was used for illumination purposes (see Figure 55).

Relatively to the second aspect, as it can be seen in the photodiode responsivity curve from Figure 70, its maximum occurs at 1000 nm, which is already in the near-infrared region of the spectrum. The emission spectrum of the microscope halogen lamp, as shown on Figure 74, ranges from ~ 400 nm (visible region of spectrum) up to 1000 nm (near-infrared region of the spectrum). Therefore, the LCD, which was made to filter light in the visible region of the spectrum, did not have the capability to block the near-infrared light that, subsequently, was detected by the photodiode, masking the variations imposed by the patterns applied to the LCD.

Even with the use of a near-infrared filter, the overall quality of the results did not improve significantly, due to the relatively low responsivity of the photodetector in the visible region of the spectrum and relatively low intensity of light collected from the scene through the objective lens.

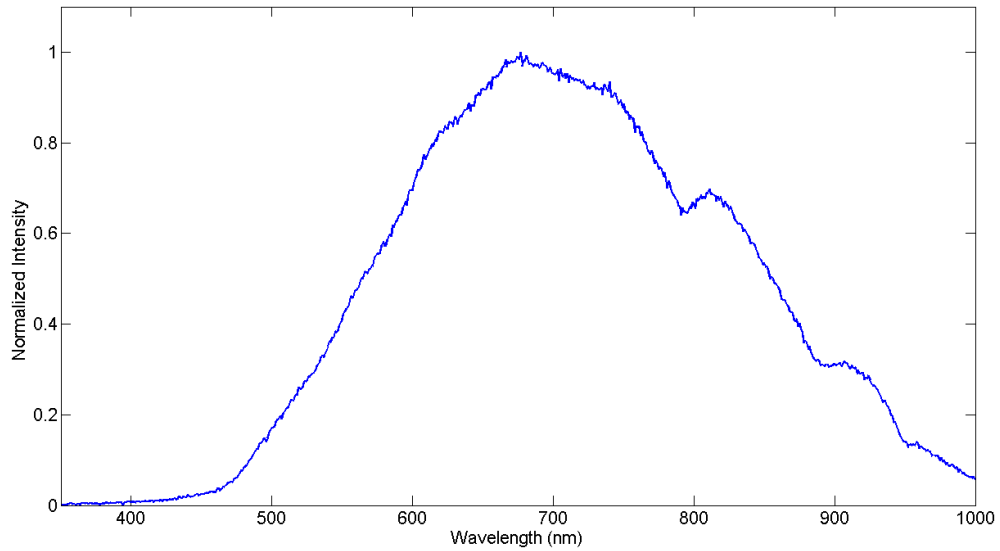


Figure 74 – Halogen lamp emission spectrum, obtained with a commercial spectrometer.

4.1.4 Concluding remarks

For certain applications, a single-pixel camera, both based on active and passive illumination, can represent a good way for reducing deployment complexity and costs, while expanding the performance and capabilities of data acquisition and processing systems.

In the previous sections, several compressive imaging systems were presented and their operation was successfully demonstrated. It was proved that it is possible to reconstruct images based on the spatial modulation of the light used for illumination of the scene. Such systems may be particularly useful in scenarios with low level or null ambient lighting.

It was also attested that the same spatial compression can be applied to the light field coming from the scene to be acquired, and capture an image in a similar way to that of a conventional camera.

The assumptions made from the results obtained with the preliminary system proved to be correct and largely contributed to the development and implementation of single-pixel imaging systems based on active or passive illumination with improved performance. All this was achieved using very similar setups and making use of standard devices that have not been subjected to any change.

It should be stated that the bottleneck of these imaging systems was the time consumed to perform all the measurements. This fact was strongly related with the time required to ensure that the images transmitted by the video signal were indeed being displayed, either on the LCD, or on the DMD, when the measurement orders have been issued. From the experiments, it was possible to conclude that this delay corresponds to 130 ms for the case of the LCD video projector and 95 ms for the case of the LightCommander.

The transmissive single-pixel imaging system can be seen as a compact implementation of a passive illumination compressive imaging system. It does not require precise alignment or any geometric calibration since the detector has only one pixel and due to the larger dimensions of the spatial light modulator and photodiode, when compared with the dimensions of a $\frac{1}{2}$ inch conventional image sensor, it also exhibited a larger field of view. Being easily assembled on a microscope and taking advantage of the already existing optical system, the transmissive single-pixel imaging system demonstrated the flexibility of this type of systems.

Finally, the work presented in the previous sections inevitably leads us to the comparison between LCD and DMD as spatial light modulators. Although some of the features here presented are not directly related with the work at hands, it was considered worthy to mention them.

Deriving from their different nature and manufacturing processes, the gap between the mirrors in a DMD array is smaller than the gap between the pixels in an LCD display, resulting in a sharper display for the DMD. LCD are typically slower than DMD, although faster LCD exist at a higher cost. By the contrary, faster DMD are relatively cheaper and widely available. It is common nowadays to find commercial video projectors that use DMD as spatial light modulators. The commonly found LCD usually operate in the visible region of the spectrum, while DMD easily operate in the visible and near-infrared regions of the spectrum. DMD with coatings suitable for operation in other ranges of the spectrum, such as ultraviolet, for instance, can also be easily accessed. While DMD can maintain the state of its mirrors, LCD pixels have to be modulated. Within the context of this thesis, this is reflected in the ripple verified in the measured signals when LCD are used (see Figure 55), which affects the dynamic range of the measurements thus compromising the quality of the results (compare the results of Figure 57 and Figure 65, for instance). LCD operate in transmission, which can facilitate the construction of more compact optical systems. However, there are also DMD projection systems commercially available that are already very compact (these systems are also known as “picoprojectors”). Comparatively to LCD, the main difficulty in using DMD for the development of optical systems arises from the “off-axis” characteristic they impose due to their angular principle of operation. The inherent polarization associated with the LCD principle of operation may eventually be explored in the development of compressive imaging based systems in which polarization would be the variable to be quantified. However, depolarization has been identified as one of the effects that compromises the contrast obtained with LCD.

For the reasons aforementioned it appears that DMD are a better option to adopt when one is interested in the development of single-pixel imaging systems.

4.2 Color Imaging Systems

Instead of representing only the spatial content of a scene by means of intensity mapping, as in the case of monochrome imaging systems, color imaging systems expand their functionality producing images that associate spectral information (characteristically broad and in the visible region of the spectrum) to the spatial content of the scene. Color images are typically defined in color spaces, being one of the most used the RGB color space given its similarity with the way the human eye senses colors. The images acquired with the systems presented in the following sub-sections will then be represented in the RGB color space.

Operating either on active illumination mode or on passive illumination mode, the systems introduced in this section acquire images relative to different spectral regions and combine them afterwards into a single color image. As will be seen, the spectral filtering that dictates the color content of the images may be verified either on the illumination end, or on the detection end.

4.2.1 Active illumination single-pixel color imaging systems

This section focuses on two configurations that were implemented for the development of color imaging systems and that relied on the use of the illumination to compress the spatial content of the scene being acquired.

During operation, both configurations acquired an image for each of the RGB channels, combining them afterwards to obtain the final RGB color image. The difference relied on the process used to separate each of the color components. One system took advantage of the color filters existent inside the projector, while the other used RGB color filters in front of the light detection device.

4.2.1.1 Spectral filtering on the illumination end

As in the case of the active illumination single-pixel monochrome imaging system, some preliminary experiments regarding the reconstruction of colored images were also conducted with the setup of Figure 44. In this case, the object to be imaged was a red squared contour on a green background painted with marker pens on normal paper (see Figure 75 (a)). For this experiment, the object was fixed and only the random patterns were projected. For each color channel of the RGB color space, 410 values were measured and a single image was reconstructed. In this experiment, the random patterns projected to obtain the measurements to reconstruct each of the RGB images were not black and white but red and black, for the case of the red channel, green and black for the green case and blue and black for the remaining case. This procedure was adopted to boost the independent influence of the RGB colors in the scene on their respective measurements.

The final image corresponds to the combination of the three RGB images in order to create the colored image (see Figure 75 (b)).

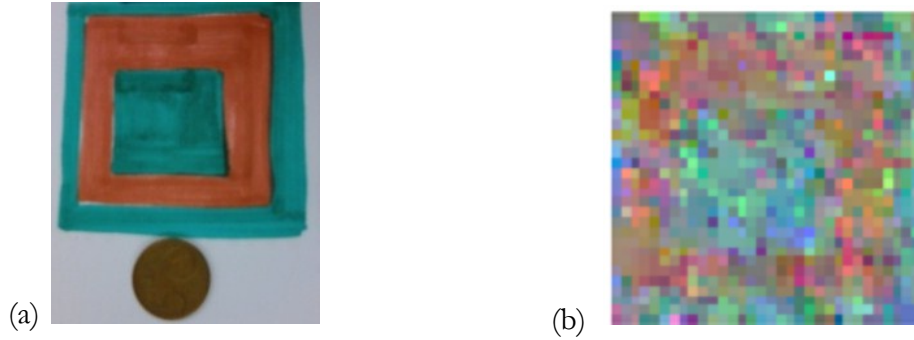


Figure 75 – (a) Piece of paper with the painted red contour and green background (the coin is present only for size comparison). (b) Color image of the painted area in (a), reconstructed with 32×32 pixels (410 measurements were acquired for each of the RGB channels).

Even though it is possible to recognize the red squared contour and the green background, the result is not very well defined. Besides the compression level and the reduced size of the painted area, we believe that the low reflectivity of the paper surface and the spectral signature of the projected color components strongly conditioned the results. It must also be emphasized that the contours were not sharp, therefore, their lack of detail in face of the low spatial resolution with which the images were reconstructed.

In the same manner, we tried to reconstruct a color image of the real scene depicted in Figure 48 (a). The results obtained are presented in Figure 76. In this case the quality of the reconstruction is significantly better and this is mainly due to the objects' materials, which are more reflective than paper.

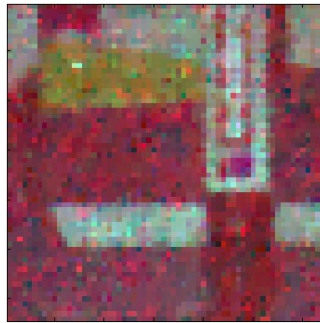


Figure 76 – Color reconstruction of a 64×64 pixels image of the real scene depicted in Figure 48 (a). 40% of the measurements were used to reconstruct each image associated with the RGB channels.

With these initial results it was possible to demonstrate that the same setup that has been used for the case of the active illumination single-pixel monochrome imaging system can also be used for the acquisition of color images. However, its performance suffered from the same limitations and, therefore, new results were acquired with the improved system of Figure 52.

For the experiments related with the acquisition of color images, a wood object with a character “B” painted in blue inside a green background with a dark orange border around (see Figure 77) has been used. The object's outer squared contour measured $65 \text{ mm} \times 65 \text{ mm}$. The green rectangle measured $53 \text{ mm} \times 47 \text{ mm}$ and the blue “B” character measured $40 \text{ mm} \times 35 \text{ mm}$.

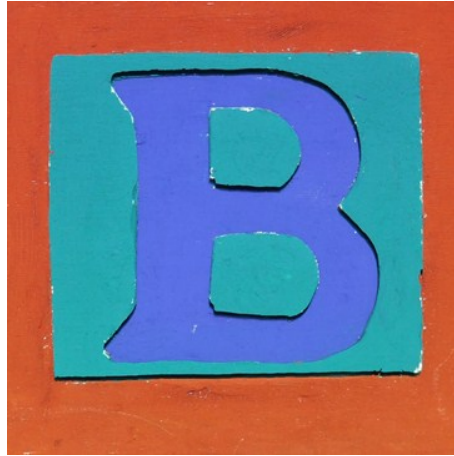


Figure 77 – Photo of the colored wood object with character “B”.

The delineation of the spectral bands used for illumination was then defined by the color filters existing on the projector’s optical path and, again, instead of the binary black and white compressive codes, the projected codes were red and black, green and black and blue and black. To clarify, the image corresponding to the red channel of an RGB image was obtained from the measurements resulting from the projection of the red and black binary codes. The same was respectively verified for the green and blue channels (see Figure 78). Therefore, the time consumed to obtain a color image was threefold the time taken to obtain a monochrome image. It should also be said that the room where the experiments took place was completely dark and no other source of light was being used.

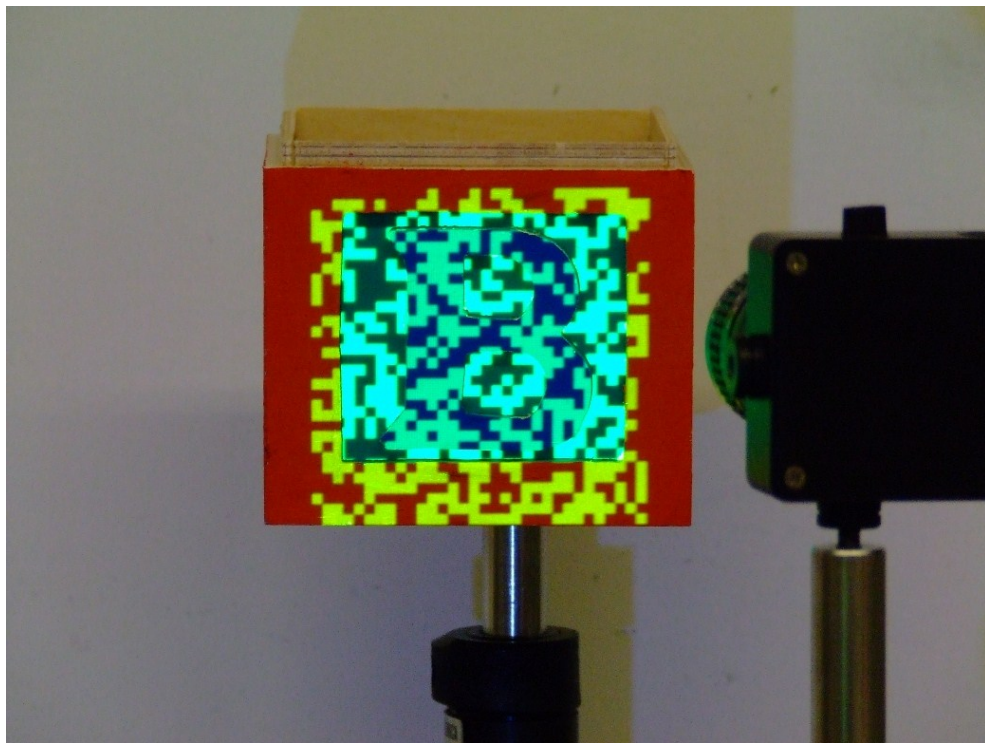


Figure 78 – Photo with detail of the colored wood object being illuminated with a green and black random binary compressive measurement code with 32×32 pixels.

The spectra of the broad individual color components (RGB) used to illuminate the scene, as well as, the spectrum emitted when the three color components are combined (“white” light), are depicted in Figure 79.

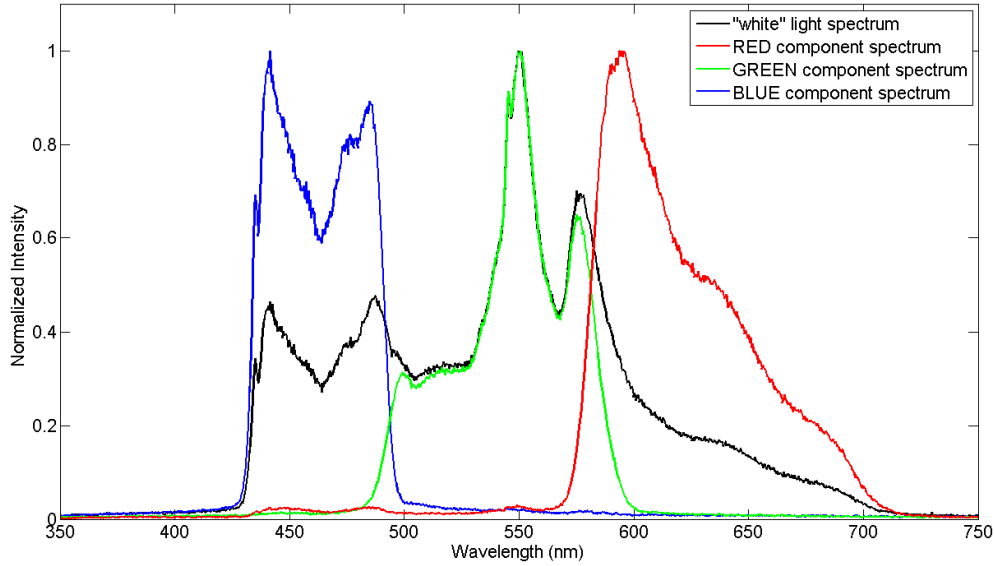


Figure 79 – Spectra of the RGB components used for illumination along with the spectrum of the “white” light resulting from their combinations.

Comparing the spectra displayed in Figure 79 it is possible to infer the relative intensities of the different color components.

Results and discussion

Next, in Figure 81, results for the reconstruction of the object presented in Figure 77 with this active illumination single-pixel color imaging system are shown. Again, on the left column one can find the images acquired with the single-pixel camera, on the center column one can find the images acquired with the single-pixel imaging system after median filtering with a 3×3 kernel and on the right column one can find images acquired with a conventional camera and that were downsized afterwards for comparison purposes. It is important to indicate that the images present on the left column of Figure 81 were filtered for noisy points which were subsequently affecting the normalization of the values from each color channel of the reconstructed images to the desired range $[0, 255]$. For this, inside a 3×3 neighborhood, if the central point represented either the maximum or minimum value, and its absolute difference to any of the other values was bigger than a predefined threshold (50 in this case), then the median value of that neighborhood was assigned to it (see Figure 80). This algorithm will be designated, from now on, as selective local median filter.

Initial stage					Final stage after application of median filtering					Final stage after application of the post-processing algorithm				
22	27	40	11	9	22	27	40	11	9	22	27	40	11	9
13	30	11	18	11	13	30	11	18	11	13	30	11	18	11
9	20	300	25	17	9	20	20	25	17	9	20	20	25	17
15	18	14	30	20	15	18	14	30	20	15	18	14	30	20
22	42	37	25	22	22	42	37	25	22	22	42	37	25	22

22	27	40	11	9	22	27	40	11	9	22	27	40	11	9
13	30	300	18	11	13	30	300	18	11	13	30	300	18	11
9	20	11	25	17	9	20	20	25	17	9	20	11	25	17
15	18	14	30	20	15	18	14	30	20	15	18	14	30	20
22	42	37	25	22	22	42	37	25	22	22	42	37	25	22

22	27	40	11	9	22	27	40	11	9	22	27	40	11	9
13	30	15	18	11	13	30	15	18	11	13	30	15	18	11
9	20	11	25	17	9	20	18	25	17	9	20	11	25	17
15	18	14	30	20	15	18	14	30	20	15	18	14	30	20
22	42	37	25	22	22	42	37	25	22	22	42	37	25	22

Figure 80 – Illustrative examples of the application of the post-processing algorithm (selective local median filter) and median filtering to filter noisy points. The white portion of the matrix with a thicker black border represents the 3×3 neighborhood under analysis.

Several examples for the application of the selective local median filter algorithm in comparison with median filtering can be found in Figure 80. On the left column of Figure 80 one can find matrices representing a 5×5 pixels portion of a raw image obtained from the reconstruction process. On the center column that same portion is presented after median filtering the central point of a 3×3 central neighborhood. Finally, on the right column it can be seen the output of the selective local median filter algorithm applied to the same 3×3 neighborhood.

From the analysis of the content of Figure 80 one can infer that the effect of the selective local median filter is only seen in the cases where spurious noisy points eventually arise, preserving the remaining information intact. By the contrary, in the case of median filtering, the filter is applied to the entire image, independently of the pixels' values, outputting a smoother result. These spurious noisy points could be arising from noise introduced during the measurements and from the reconstruction process itself.

It can then be concluded that the selective local median filter is very useful in the cases that one wants to keep the raw information and just filter noisy points that may compromise the normalization process and consequently affect the visual quality of the final color image. The median filter not only filters the noisy points but also smooths the spatial content of the image. The inconvenient of the selective local median filter algorithm relies on the definition of the associated threshold, which in some cases may differ for all the three images associated with each of the color components.

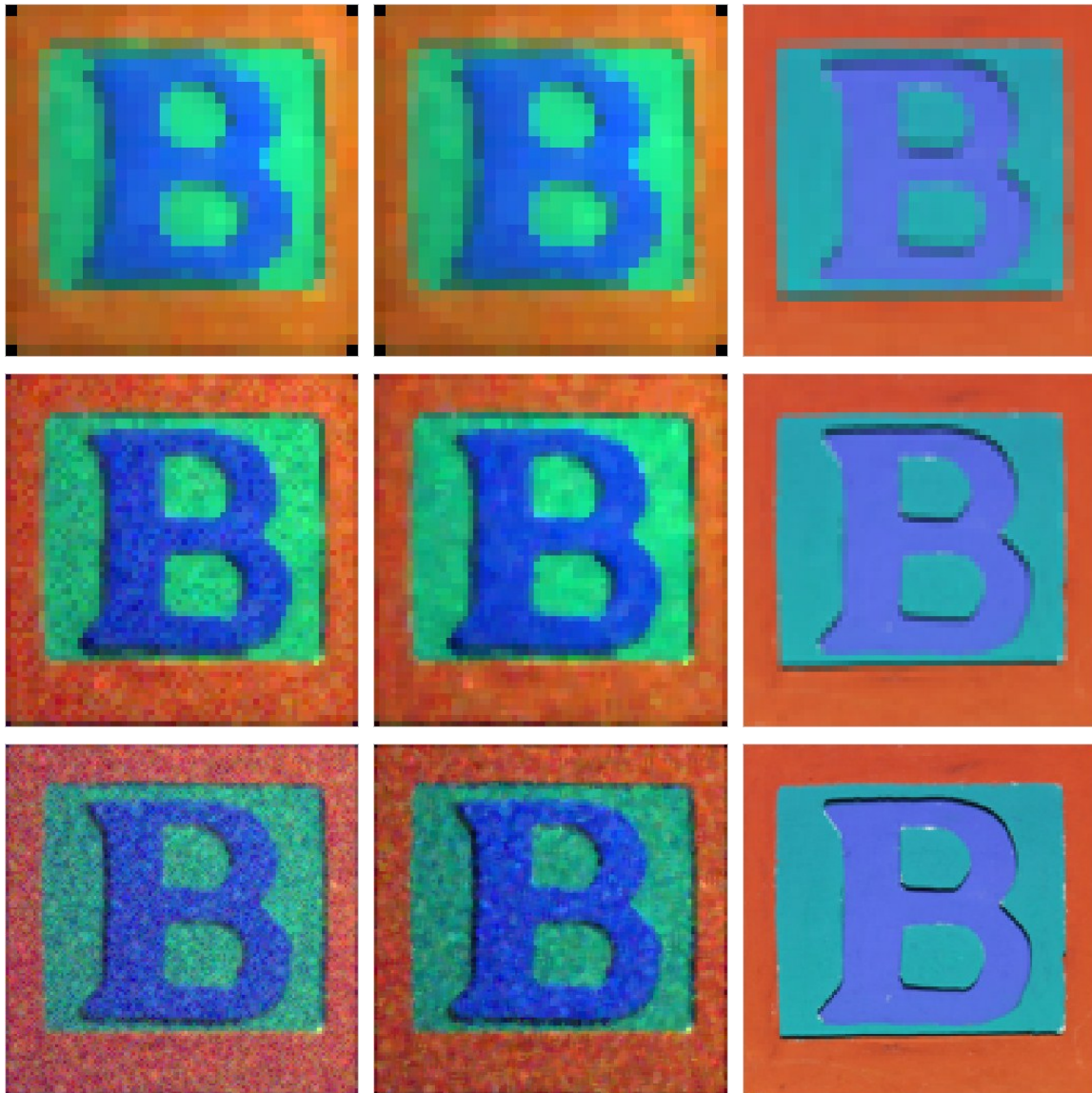


Figure 81 – Images of the colored wood object containing the character “B” acquired with the active illumination color imaging system with spectral filtering on the illumination end. Image resolution (in pixels) from top to bottom: 32×32 ; 64×64 ; 128×128 . (left) Color images filtered with the selective local median filter. (center) Color images after median filtering. (right) Images acquired with a conventional camera downsized for comparison purposes.

The PSNR values and the maximum values of the normalized cross-correlation have been obtained for the images in Figure 81 and are presented in Table 16 and Table 17, respectively. For both metrics, the RGB color images have been converted to grayscale intensity images using MATLAB® function *rgb2gray*. This function makes the conversion by eliminating the hue and saturation information while retaining the luminance.

Table 16 – PSNR values obtained for the reconstructed images of Figure 81 relatively to the images acquired with the conventional camera.

Resolution (pixels)	PSNR (dB)	
	Selective local median filter	Median filter
32×32	20.89	21.00
64×64	17.32	17.91
128×128	17.71	15.69

Table 17 – Maximum values of the normalized cross-correlation obtained for the reconstructed images of Figure 81 relatively to the images acquired with the conventional camera.

Resolution (pixels)	Normalized cross-correlation [0, 1]	
	Selective local median filter	Median filter
32×32	0.57	0.57
64×64	0.60	0.61
128×128	0.48	0.52

Based on the results obtained with the two metrics, it can be said that the quality of the images processed with the selective local median filter and with the median filter is almost identical. The slightly better results obtained with the images that have been median filtered may be justified by the remaining noise in the images processed with the selective local median filter. These statements are in agreement with the visual evaluation conducted by human observers.

4.2.1.2 Spectral filtering on the detection end

When the separation of the color components was done on the detection end, three independent color filters were used (one for each of the RGB components). These filters were placed in front of the photodiode active region, so that its response would only be stimulated by the part of the spectrum that was not filtered. In this configuration the projected compressive codes were again black and white and three images were also acquired (one for each of the RGB color channels). As

expected, it took three times longer to acquire a color image than it took to acquire a monochrome image.

The spectra of the different color components resulting from the filtering of the “white” light emitted by the projector can be seen in Figure 82.

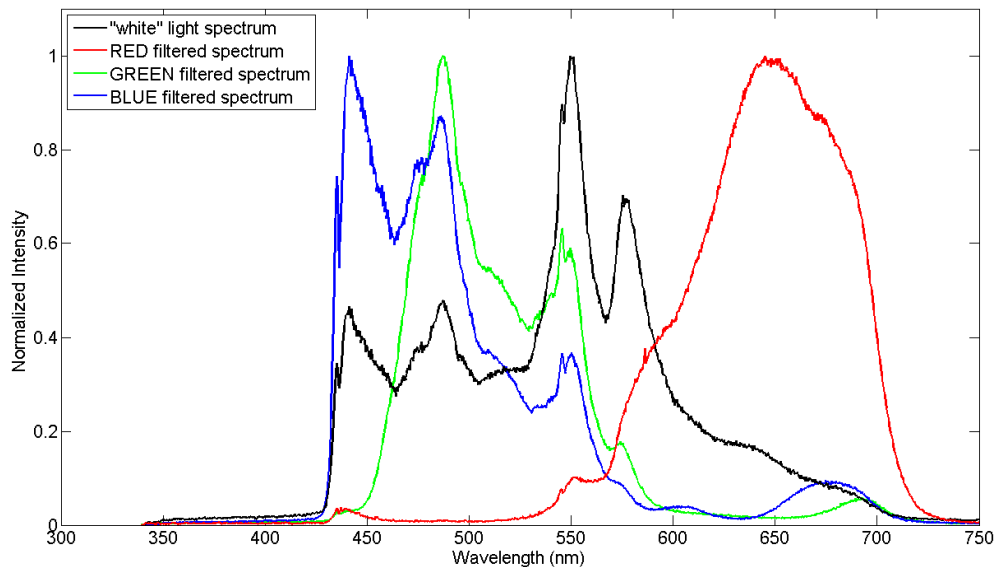


Figure 82 – Spectra of the RGB components resulting from filtering the “white” light emitted by the projector.

From the analysis of the spectra contained in the plot of Figure 82, one can infer the relative intensities of each of the color components. Also noticeable is the superposition of the blue and green spectra.

Results and discussion

Images of the wood colored object with character “B” (see Figure 77) were also acquired with this setup and the results are presented in Figure 83. On the left column one can find the raw images, while on the center column one can find the result of filtering the noisy points present in the images of each color channel, with the algorithm previously presented and described (see section 4.2.1.1 and Figure 80). For this filtering, the threshold value has been experimentally determined for each color channel in order to provide the best results. Median filtering the raw images did not result satisfactorily, as can be seen in Figure 84, mainly because of the reduced contrast of the images representative of the green and blue channels (see Figure 85). This was mainly due to the fact that the green and blue spectral components obtained after filtering were highly superposed (see Figure 82). On the rightmost column one can see images acquired with a conventional camera and that were afterwards downsized for comparison purposes.



Figure 83 – Images of the colored wood object containing the character “B” acquired with the active illumination color imaging system with spectral filtering on the detection end. Image resolution (in pixels) from top to bottom: 32×32 ; 64×64 ; 128×128 . (left) Color images resulting from the combination of the raw images representative of the RGB channels. (center) Color images filtered with the selective local median filter. (right) Images acquired with a conventional camera downsized for comparison purposes.

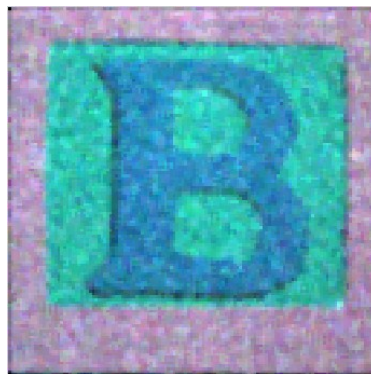


Figure 84 – 128×128 pixels image obtained after median filtering the raw images representative of the RGB channels.

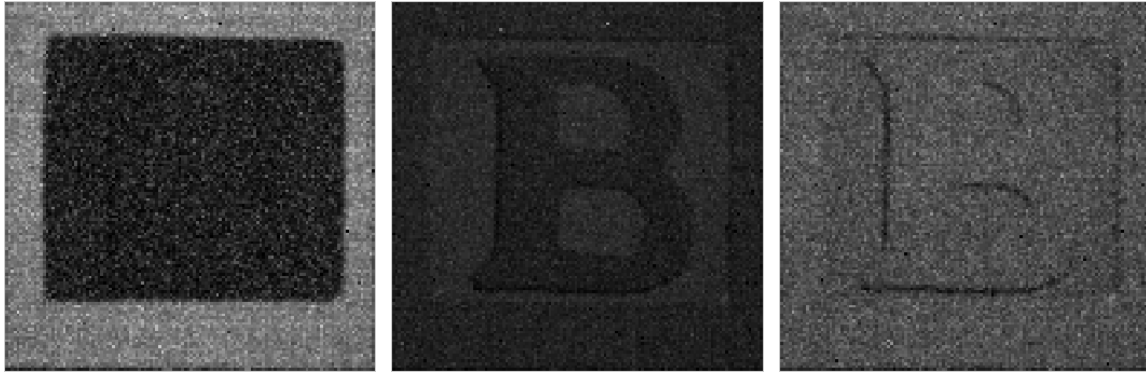


Figure 85 – From left to right, images representative of the Red, Green and Blue components with 128×128 pixels.

Following, Table 18 and Table 19 present the results obtained with the PSNR and with the normalized cross-correlation for the images of Figure 83.

Table 18 – PSNR values obtained for the reconstructed images of Figure 83 relatively to the images acquired with the conventional camera.

Resolution (pixels)	PSNR (dB)	
	Raw	Selective local median filter
32×32	16.53	16.71
64×64	19.62	18.90
128×128	19.23	19.65

Table 19 – Maximum values of the normalized cross-correlation obtained for the reconstructed images of Figure 83 relatively to the images acquired with the conventional camera.

Resolution (pixels)	Normalized cross-correlation [0, 1]	
	Raw	Selective local median filter
32×32	0.38	0.40
64×64	0.35	0.37
128×128	0.32	0.34

Based on the results presented in Table 18 and in Table 19 one can state that the quality of the reconstructed images of Figure 83 is similar, either filtering has been applied or not. Comparing these results with those presented in Table 16 and Table 17, one can say that the overall tendency, mainly defined by the results of the normalized cross-correlation, leads to the conclusion that the images acquired with the active illumination color imaging system with spectral filtering on the illumination end have better quality and are more similar to those acquired with a conventional camera. This conclusion falls within the human opinion based on the visual evaluation of the images.

4.2.2 Passive illumination single-pixel color imaging systems

Similarly to the case of the active illumination single-pixel color imaging systems, the two configurations here presented are also capable of acquiring color images, through the combination of images representative of the RGB channels. The difference to the active illumination system relies on the fact that here the compression of the spatial content is applied to the light field coming from the scene. This is possible thanks to the use of the LightCommander as a camera, in the same manner as it was used in the setup of the passive illumination single-pixel monochrome imaging system (see section 4.1.2). The definition of the spectral content used for the acquisition of the images representing each of the RGB channels was either dictated by the filters inside the video projector used to illuminate the scene or by the use of RGB color filters placed in front of the light detection device.

4.2.2.1 Spectral filtering on the illumination end

The principle of operation of the system here presented is very similar to that of the passive illumination single-pixel monochrome imaging system with the exception that in the color imaging system the illumination of the scene enclosed the spectral content of the image to be acquired. This later aspect was defined by the filters existent inside the video projector, as it was in the case of the active illumination color imaging system with spectral filtering on the illumination end. Therefore, the setup implemented for this system was the same as the one previously depicted in Figure 62 and Figure 63. The main difference was that in this case the projected illumination was not white, but red, green and blue, instead, as defined by the spectra represented in Figure 79.

This system has then been used for the acquisition of images of the colored wood object with character “B” represented in Figure 77. The results are presented in Figure 86. The column on the left contains the color images resulting from the combination of the raw images, associated with each color channel, filtered with the selective local median filter. The results for the combination of the raw images after median filtering are shown in the central column. Finally, the column on the right contains images acquired with a conventional camera that were downsized for comparison purposes.

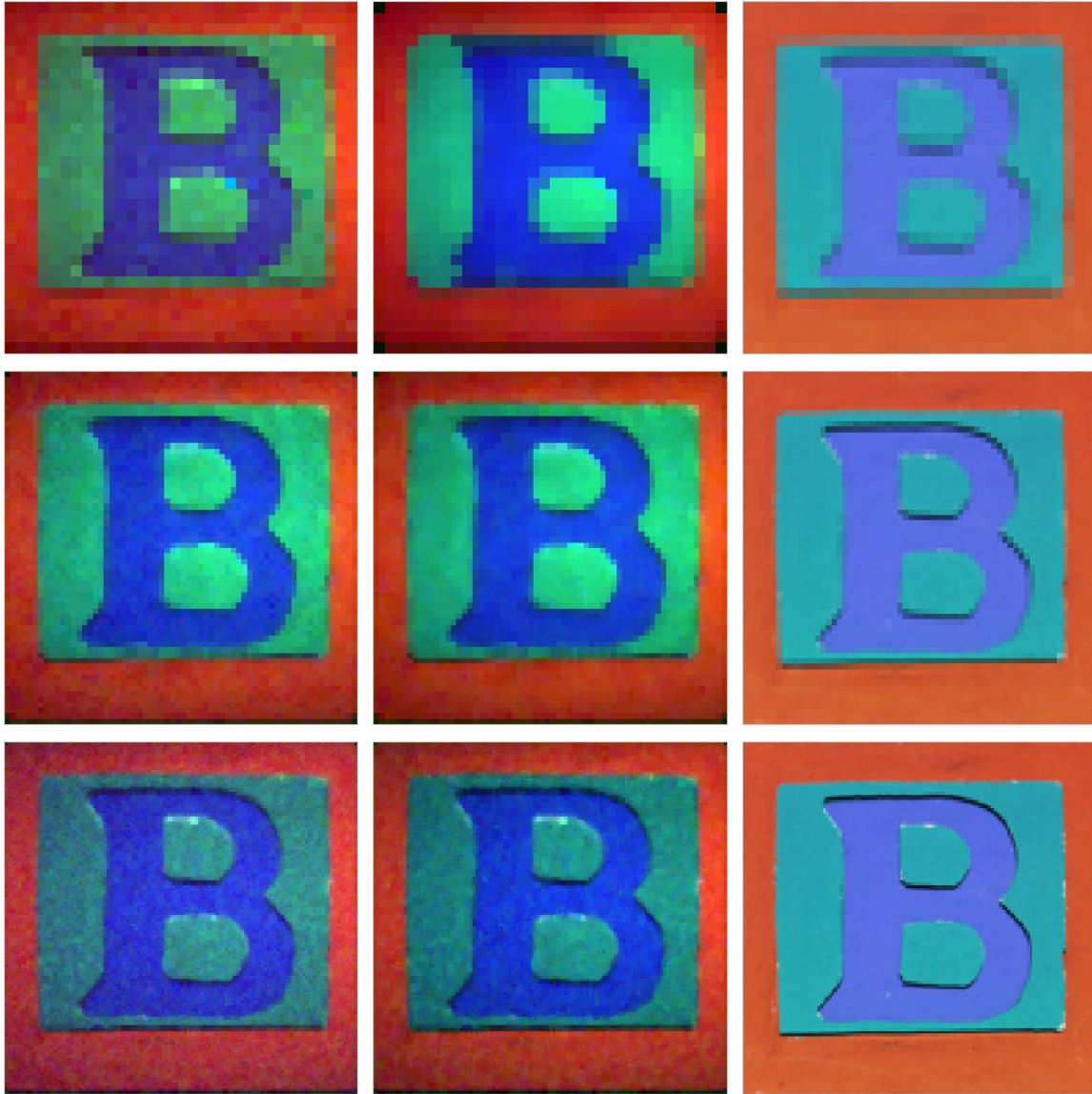


Figure 86 – Images of the colored wood object containing the character “B” acquired with the passive illumination color imaging system with spectral filtering on the illumination end. Image resolution (in pixels) from top to bottom: 32×32 ; 64×64 ; 128×128 . (left) Color images filtered with the selective local median filter. (center) Color images after median filtering. (right) Images acquired with a conventional camera downsized for comparison purposes.

Once more, the PSNR and the normalized cross-correlation were used to evaluate the quality of the reconstructed images relatively to the images that were captured with a conventional camera. The results obtained with the two metrics for the images in Figure 86 are presented in Table 20 and Table 21. Based on this evaluation, it is not evident which of the filtering methods yielded better results. Despite the small differences indicated by the two metrics for the two filtering methods, the PSNR shows better results for the images to which the selective local median filter has been applied, while the normalized cross-correlation obtained better results for the images smoothed with the median filter. Based on human opinion, it can be said that it is evident the similarity of the reconstructed images after being processed with each of the filters, although the images to which

the median filter has been applied seem slightly better, mainly because they are smoother, i.e., they have less noise.

Table 20 – PSNR values obtained for the reconstructed images of Figure 86 relatively to the images acquired with the conventional camera.

Resolution (pixels)	PSNR (dB)	
	Selective local median filter	Median filter
32×32	14.61	13.42
64×64	14.58	14.51
128×128	14.20	13.52

Table 21 – Maximum values of the normalized cross-correlation obtained for the reconstructed images of Figure 86 relatively to the images acquired with the conventional camera.

Resolution (pixels)	Normalized cross-correlation [0, 1]	
	Selective local median filter	Median filter
32×32	0.47	0.53
64×64	0.43	0.44
128×128	0.38	0.40

4.2.2.2 Spectral filtering on the detection end

Regarding the other configuration which has been assumed for the acquisition of color images by means of passive illumination, it can be stated that it used the same setup of the previous section. The only difference was that the light used to illuminate the scene was white and the spectral content of the images to be acquired was defined by RGB filters placed in front of the photodiode. It has also been used to acquire images of the colored wood object with character “B” and the results are presented in Figure 87. The color images obtained after combining the raw images, associated with each color channel, filtered with the selective local median filter can be found in the left column. The center column contains the color images resulting from the combination of the reconstructed raw images representative of each color channel after median filtering. Right column contains the images acquired with a conventional camera downsized for comparison purposes.

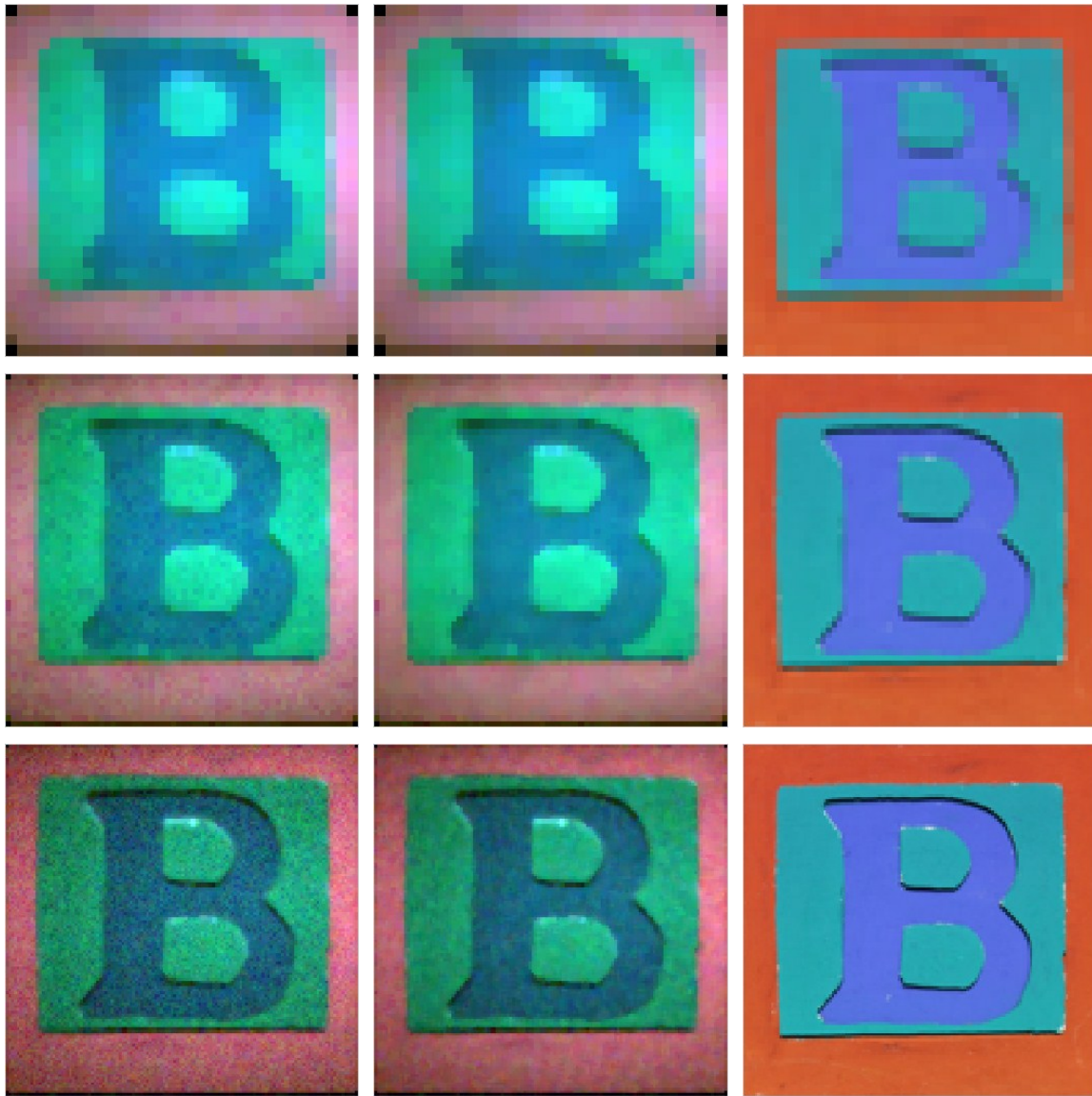


Figure 87 – Images of the colored wood object containing the character “B” acquired with the passive illumination color imaging system with spectral filtering on the detection end. Image resolution (in pixels) from top to bottom: 32×32 ; 64×64 ; 128×128 . (left) Color images filtered with the selective local median filter. (center) Color images after median filtering. (right) Images acquired with a conventional camera downsized for comparison purposes.

The quality of the reconstructed images of Figure 87 has been evaluated with the PSNR and with the normalized cross-correlation metrics, comparatively to the images captured with a conventional camera, and the results obtained are enumerated in Table 22 and Table 23. Based on the evaluation provided by both metrics it can be said that there are no significant differences between the images smoothed with each of the filters. As expected, the only visual difference marked by human visual assessment was the noisier content of the images smoothed with the selective local median filter.

Table 22 – PSNR values obtained for the reconstructed images of Figure 87 relatively to the images acquired with the conventional camera.

Resolution (pixels)	PSNR (dB)	
	Selective local median filter	Median filter
32×32	19.23	19.23
64×64	18.63	18.74
128×128	15.57	15.8

Table 23 – Maximum values of the normalized cross-correlation obtained for the reconstructed images of Figure 87 relatively to the images acquired with the conventional camera.

Resolution (pixels)	Normalized cross-correlation [0, 1]	
	Selective local median filter	Median filter
32×32	0.50	0.49
64×64	0.47	0.48
128×128	0.42	0.43

4.2.3 Concluding remarks

Comparing the active and the passive illumination color imaging systems based on human visual judgment, it can be concluded that the passive illumination system was the one that presented the best results. In other words, the results obtained with the passive illumination system have less noise and are more similar to those acquired with the conventional camera. This corroborates the same conclusion drawn for the case of the monochrome imaging systems, and can again be supported by the benefit of using the DMD as the spatial light modulator.

However, based on the results obtained with the applied metrics, one would say that the active illumination system achieved better performance, both in the case that the spectral filtering happened on the illumination end or on the detection end, which would conflict with the human opinion. Because of this, one could be lead to question if the conversion of the RGB images to grayscale intensity images might have caused this difference. The fact that the same difference was verified in the case of the monochrome imaging systems dissipates any eventual doubt relatively to effect that the conversion of the RGB images to grayscale intensity images might have had. Therefore, once again, this difference can be supported by changes in the images deriving from different optical alignments, different lighting conditions and even small changes in the field of view, verified for the different imaging setups. These differences may have caused the images to

appear translated, rotated, scaled, distorted and with different brightness and/or contrast distributions, even though care was exerted to minimize these effects.

From a general perspective, regarding the single-pixel color imaging systems presented in the previous sections, it is important to point out that the systems in which the spectral separation was encoded in the light source provided results with more vivid and more realistic colors. This can be supported by the fact that the RGB color components emitted by the projector (see Figure 79) were much more defined than in the case in which the color separation happened by means of filters placed in front of the photodiode. In the latter case, a large superposition of the blue and green spectra was verified (see Figure 82), thus leading to the reduced color contrast verified in the images obtained when those components were being used (see Figure 85). Furthermore, the spectral windows of the RGB filters used on the detection end were broader and exhibited lower transmittance than those of the filters existent inside the projector. These facts largely contributed to the relatively worse results obtained with the systems whose spectral filtering was performed on the detection end.

Another aspect of interest is that despite the intensity of the spectra in the “red” region was relatively low, the images obtained for the red component exhibited good contrast. Besides the good spectral separation verified for that region of the spectrum, this can also be supported by the photodiode’s spectral responsivity which is always increasing with wavelength until approximately 1000 nm (see Figure 50), therefore causing the signal-to-noise ratio of those measurements to become improved.

Nonetheless, the results obtained proved the potential of such systems and it is believed that if both the emitted spectra and the filtered spectra were optimized the different systems would perform similarly well.

It should also be said that even though a conventional camera (FujiFilm™ S5600) has been used for comparison purposes, it was not possible to obtain the spectral response of its CCD sensor (5th Generation Super CCD HR), but it is very likely for it to be different from that of the used photodiode. It is also very probable that the Bayer color filter present in front of the CCD exhibits a spectral signature different from that of the single-pixel color imaging systems. Certainly, these facts also contributed to the difference of colors verified in the images acquired with the single-pixel imaging systems when compared to those acquired with the conventional camera.

4.3 Multispectral Imaging Systems

A multispectral imaging system is one that is capable of capturing images at specific spectral bands. These bands do not need to be contiguous and may be, for instance, separated by filters or by the use of instruments that are sensitive to particular wavelength ranges. The acquired images can be combined to create composite images. Spectral imaging with more bands, higher spectral resolution or broader spectral coverage is called hyperspectral, as can be seen later in this document. In the following sections an active and a passive illumination single-pixel imaging system for the acquisition of multispectral images will be demonstrated and compared.

4.3.1 Active illumination single-pixel multispectral imaging system

In the system presented in this section, the spectral bands chosen to represent the scene were defined in the light used to illuminate the scene. As in the previously presented active illumination systems, this system also incorporates the compressive measurement codes into the illumination to encrypt the spatial information of the scene.

The setup of the implemented active illumination single-pixel multispectral imaging system is displayed in Figure 88.

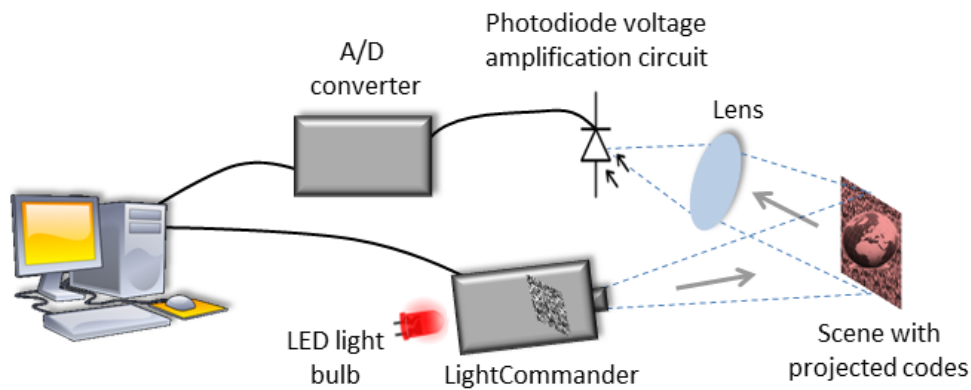


Figure 88 – Scheme of the setup for the active illumination single-pixel multispectral imaging system.

In this setup the light sources consisted of three LED light bulbs with 15 LED each that have been used at a time. These light bulbs were independently emitting in the red, green and blue regions of the visible spectrum. The luminous intensity of the red, green and blue LED bulbs was 4 candela, 12 candela and 6 candela, respectively.

The normalized emission spectra of the three light bulbs are shown in Figure 89.

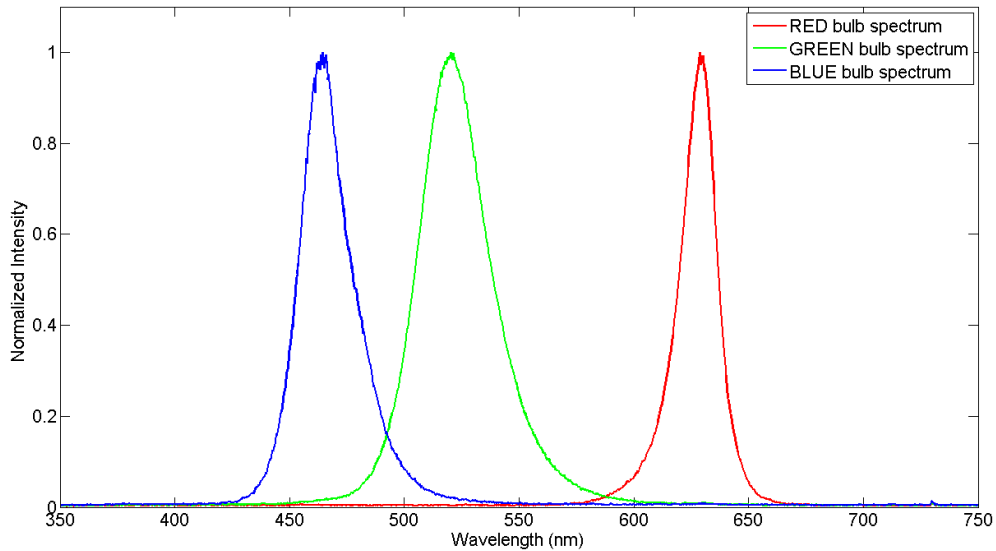


Figure 89 – Normalized emission spectra of the red, green and blue LED light bulbs used for illumination in the active illumination single-pixel multispectral imaging system.

The measured FWHM of the LED light bulbs was 17.2 nm for the red bulb, 34.2 nm for the green bulb and 24.5 nm for the blue bulb.

The LED light bulbs were placed in front of the LightCommander's tunnel in order to flood it with light. As the angular emission of the LED was very wide, the light reaching the DMD was homogeneously distributed. The amplified photodiode and DAQ board were the same as in the other active illumination setups.

In Figure 90 two photos of the experimental setup of the active illumination single-pixel multispectral imaging system are presented. The photo on the left exhibits the LightCommander without its native illumination module and respective power unit. There it can be seen the blue LED light bulb launching light into the LightCommander's tunnel. The photo on the right shows a detailed view of the amplified photodetector and lens capturing the light coming from the scene illuminated with a random binary code.

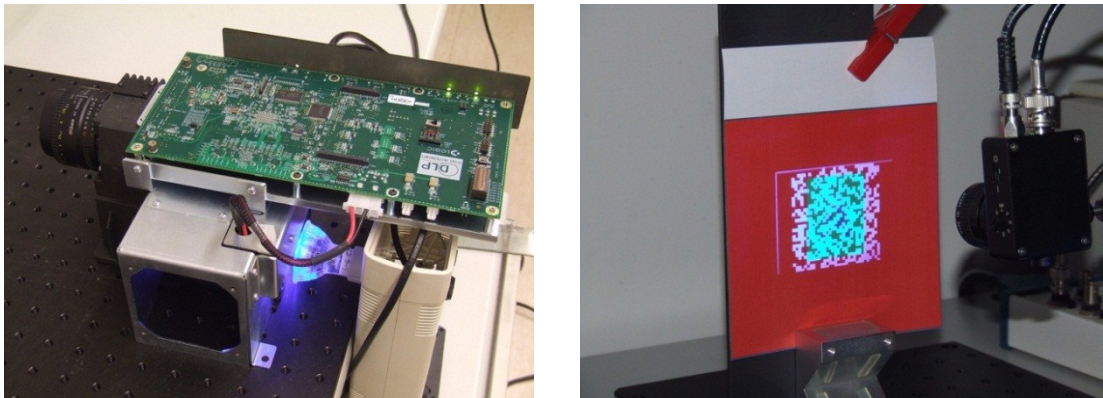


Figure 90 – Photos of the active illumination single-pixel multispectral imaging system. Left: Light from the blue LED light bulb is being launched into the Lightcommander's tunnel. The LightCommander's illumination module and respective power unit have been removed. Right: Detailed photo of the amplified photodiode and of the scene being illuminated with a binary random code.

Results and discussion

The object that was used to evaluate the performance of this system is depicted in Figure 91.

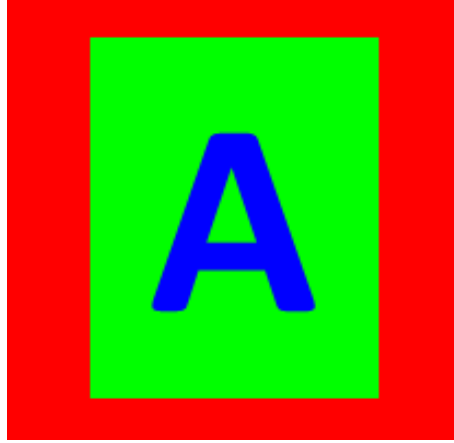


Figure 91 – RGB scene composed to be used on the performance evaluation of the active illumination single-pixel multispectral imaging system.

The object of Figure 91 was printed in standard paper and the green rectangle measured $35\text{ mm} \times 44\text{ mm}$, while the blue character “A” measured 20 mm in the wider end and 5 mm in the thinner end. The red border was 10 mm and 5mm thick. The RGB colors were coded with 8 bits as pure red [R:255; G:0; B:0], pure green [R:0; G:255; B:0] and pure blue [R:0; G:0; B:255], for the border, rectangle and character “A”, respectively.

Figure 92 displays the images captured with the active illumination single-pixel multispectral imaging system, with different resolutions. On the left column, one can find the result of combining the raw images obtained for each color channel after selective local median filtering. On the center column, one can find the same raw images used to obtain the results of the left column after median filtering with a 3×3 kernel. The column on the right contains images acquired with a conventional camera downsized for the different resolutions for comparison purposes.

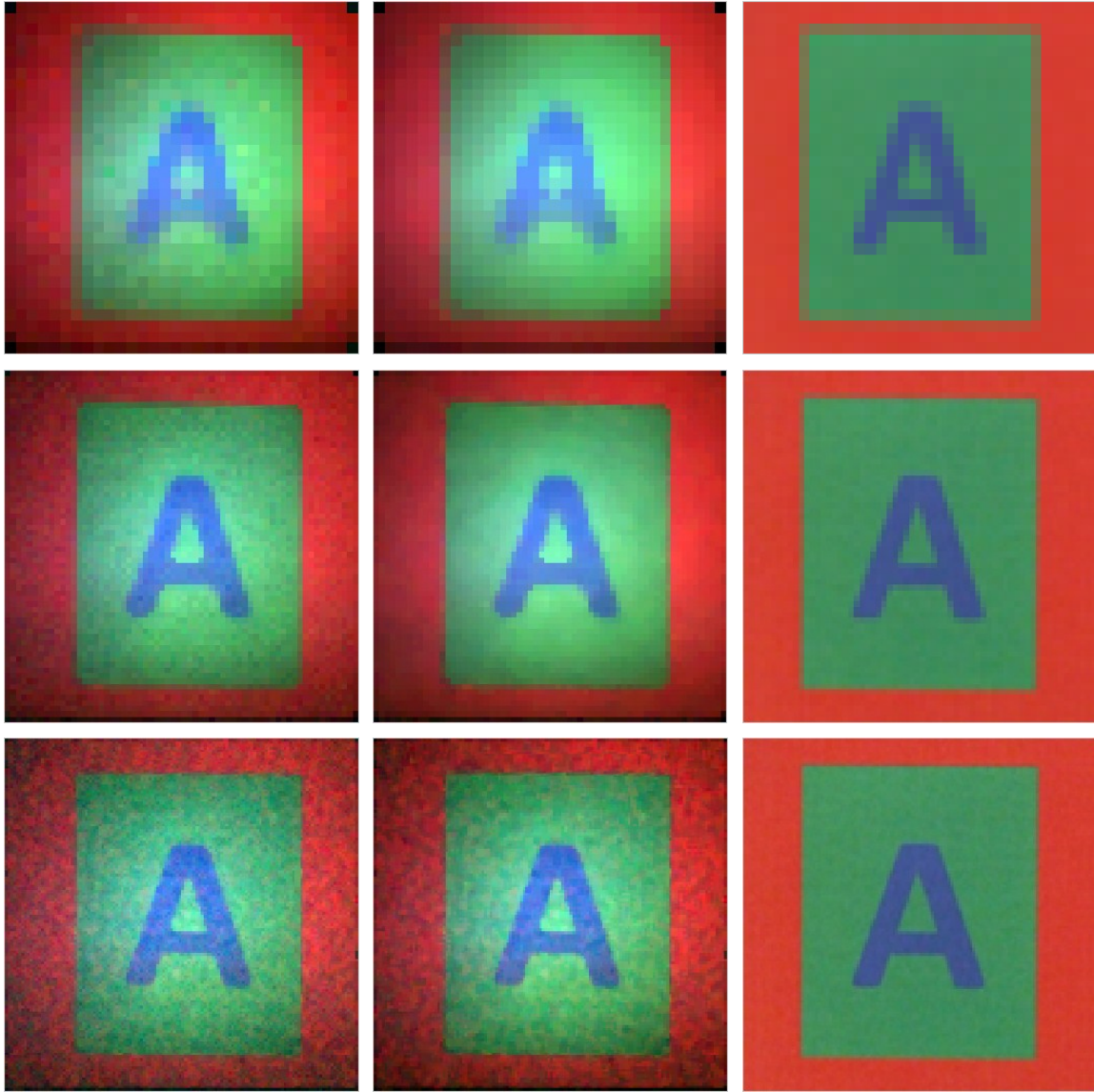


Figure 92 – From top to bottom: 32×32 ; 64×64 ; 128×128 ; pixels images captured with the active illumination single-pixel multispectral imaging system. The RGB images resulting from the combination of the raw images after selective local median filtering can be seen on the left column, while the center column contains the RGB images resulting from the combination of the raw images after median filtering. On the right column, it can be seen the images acquired with a conventional camera downsized for comparison purposes.

The contents of Table 24 and Table 25 summarize the results of the evaluation performed with the PSNR and normalized cross-correlation metrics for the images of Figure 92, relatively to the images acquired with the conventional camera. These results quantify those images to be of similar quality, independently of the filtering method. Despite the residual noise of the images processed with the selective local median filter, this is consistent with the opinion based on the visual assessment held by human observers.

Table 24 – PSNR values obtained for the reconstructed images of Figure 92 relatively to the images acquired with the conventional camera.

Resolution (pixels)	PSNR (dB)	
	Selective local median filter	Median filter
32×32	15.81	15.62
64×64	16.59	16.58
128×128	17.51	16.74

Table 25 – Maximum values of the normalized cross-correlation obtained for the reconstructed images of Figure 92 relatively to the images acquired with the conventional camera.

Resolution (pixels)	Normalized cross-correlation [0, 1]	
	Selective local median filter	Median filter
32×32	0.63	0.64
64×64	0.61	0.61
128×128	0.58	0.58

In order to perceive the reflective properties of the content in the scene, we acquired three images with our system and with a conventional camera when it was being independently illuminated with each of the three LED bulbs. Those images can be seen in Figure 93. It should be noted that the images referring to the conventional camera are displayed with the real colors with which they have been acquired, while the images acquired with our system were mapped into the respective color channel with 256 levels, being the images corresponding to the other channels set to black. From their analysis one can state that the images exhibiting best contrast are those relative to the green illumination. These can be supported by two facts: the higher luminous intensity of the green LED bulb and the higher sensitivity the human eye possesses in that range of the visible spectrum [73].

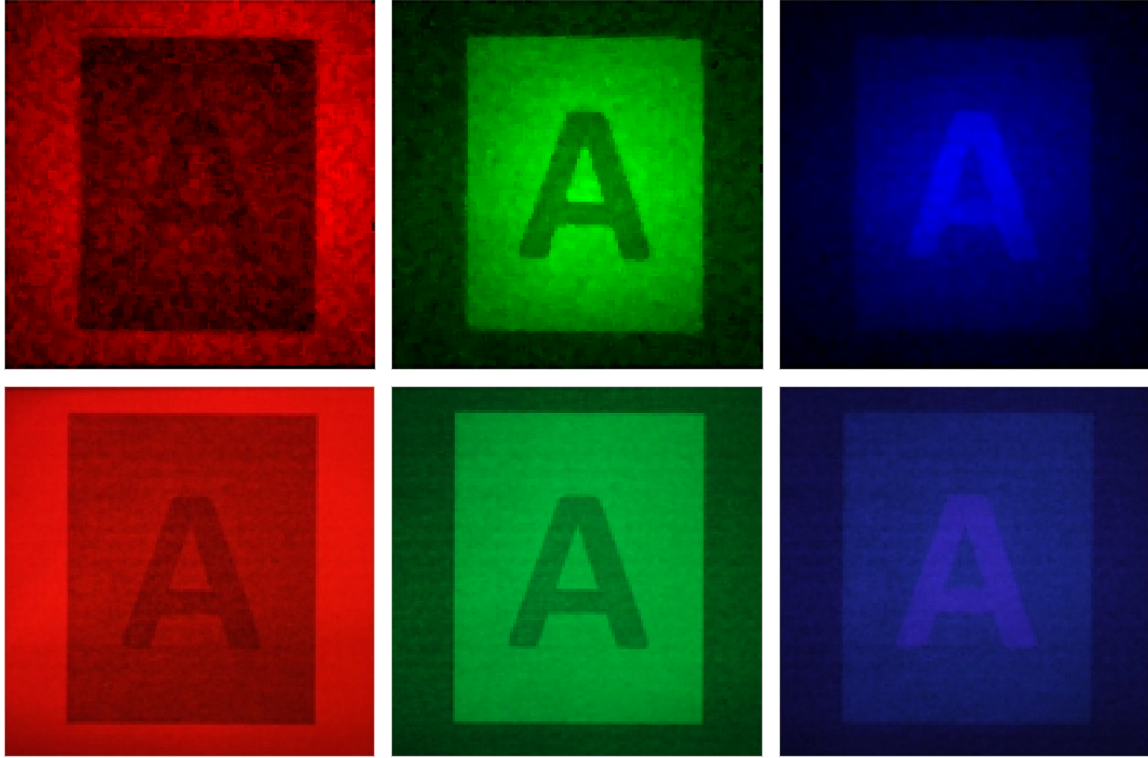


Figure 93 – 128×128 pixels images acquired to evaluate the reflective properties of the content of the printed scene of Figure 91. On the top row it can be seen the images acquired with the active illumination single-pixel multispectral imaging system after median filtering. The photos acquired with a conventional camera are displayed on the bottom row. The images represented from left to right, illustrate the acquisitions made when the scene was being independently illuminated with the red, green, and blue LED bulb, respectively.

As previously stated, each 10000 samples set was averaged afterwards in order to obtain the measurement produced with the respective code. This averaging process proved to be particularly useful, due to the AC modulation of the light emitted by the LED bulbs. With it, ideally, one obtains the change on the DC value of the output voltage, caused by the projected code, and eliminates the influence of the AC modulation. This modulation can be substantiated in the plot of Figure 94.

From the images present in Figure 92 and Figure 93, it is evident that there was an intensity profile on the used illumination. It becomes more obvious near the corners of the red border, where the images appear darker, and near the center of the image, where the images look brighter. As the density of projected light reduces in a square fashion with the increase of distance, and we wanted the maximum amount of light to be reflected from the scene towards the photodiode, the scene was placed in the shortest distance possible dictated by the field of view and the working distance of the projection lens. At such distance, the light distribution over the scene was not perfectly homogeneous, which was also conditioned by the LED bulbs emission diagram that is not homogeneous either.

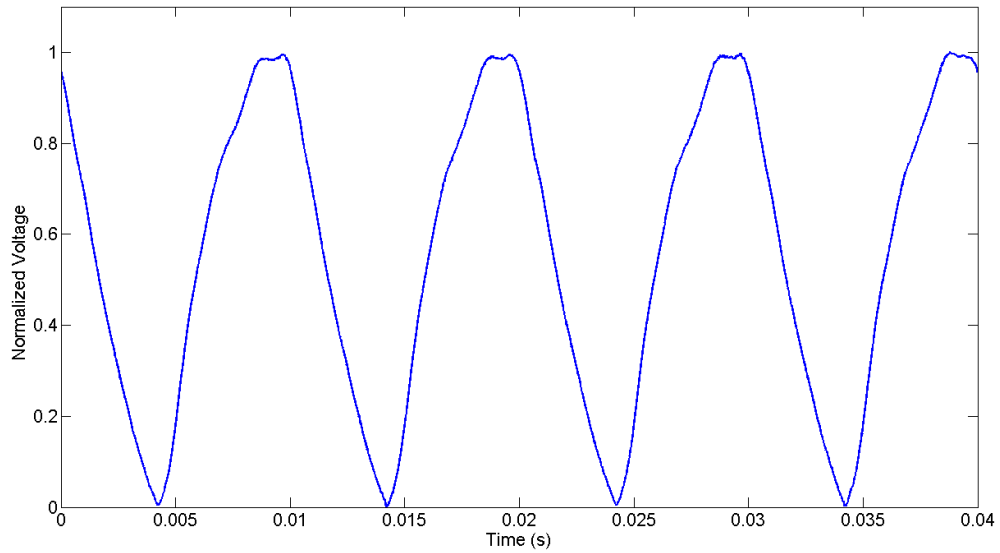


Figure 94 – Plot of the normalized voltage on the output of the amplified photodiode circuit when one LED light bulb was being used for illumination of the scene being acquired.

This latter fact, to a certain extent, also caused the light reaching the peripheral region of the DMD not to be projected, due to the angular operation of its mirrors. The major difference relies on the content associated with the red color, which appears to have lower intensity, which can significantly be justified by the relatively smaller area it occupies in the scene and by the relatively smaller luminous intensity of the red LED bulb. These facts cause a comparatively smaller reflection of the light emitted when the red LED bulb was being used, thus yielding lower SNR to the associated measurements. Despite these minor aspects, the obtained images look particularly faithful to those obtained with the conventional camera.

4.3.2 Passive illumination multispectral single-pixel imaging system

In this section it is presented the passive illumination counterpart of the multispectral system presented in the previous section. In this system, the positions of the illumination source and of the light detector were interchanged, thus causing the optical path to be used in a reverse direction, in a manner similar to that of a conventional camera. The spectral content was again defined by the illumination sources but the compressive codes for spatial compression were applied to the light field captured by the imaging system. A scheme describing the setup of the implemented system is depicted in Figure 95. In Figure 96 a photo of the experimental setup can be observed.

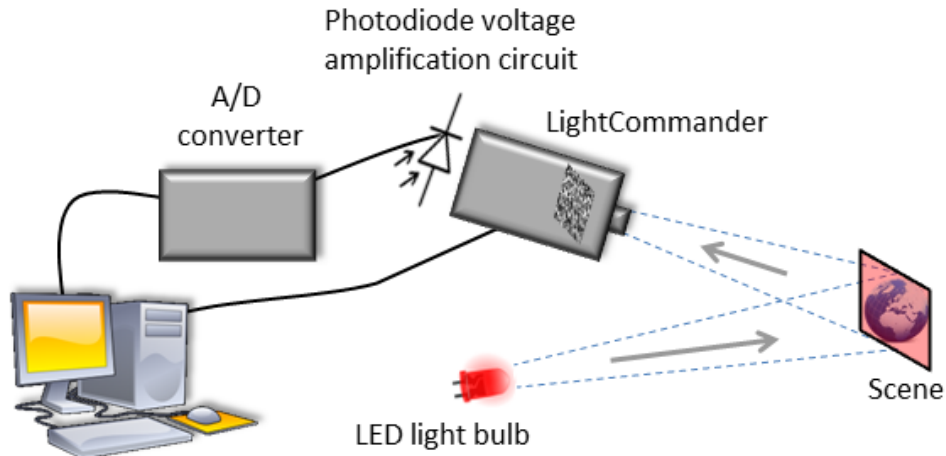


Figure 95 – Scheme of the setup for the passive illumination single-pixel multispectral imaging system.

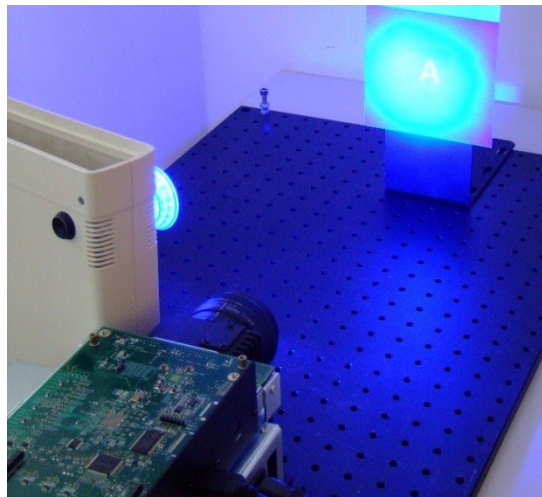


Figure 96 – Photo of the passive illumination single-pixel multispectral imaging system during operation.

This system has been used to acquire RGB images of the composed RGB scene displayed in Figure 91 and the results are depicted in Figure 97. In order to acquire the different images corresponding to each of the colors channels, the agreeing LED light bulb had to be used. The images on the left column result from the combination of the raw images obtained for each of the color channel after applying the selective local median filter, while the center columns contains the images resulting from the combination of the raw images of each color channel after median filtering with a 3×3 kernel. On the right column are displayed images acquired with a conventional camera that were downsized for comparison purposes.

In order to maximize the amount of light collected by the imaging system, the distance between the imaging lens and the scene was the shortest possible. That distance resulted from the lens' working distance which ensured that the FOV was adequately covering the scene. Observing the results of Figure 97 it can be concluded that the intensity of the red portion in the images

acquired with the single-pixel system is partially reduced near the outer edges. This result comes from the emission diagram of the LED light bulbs, which is not homogeneous and is more intense in the central region, and from its reduced luminous intensity, when compared to the other LED bulbs. These facts combined with the angular operation of the DMD mirrors reduce the efficiency of light acquisition for those regions of the image. Despite these aspects, based on human opinion, it can be said that the acquired images closely represent those acquired with a conventional camera.

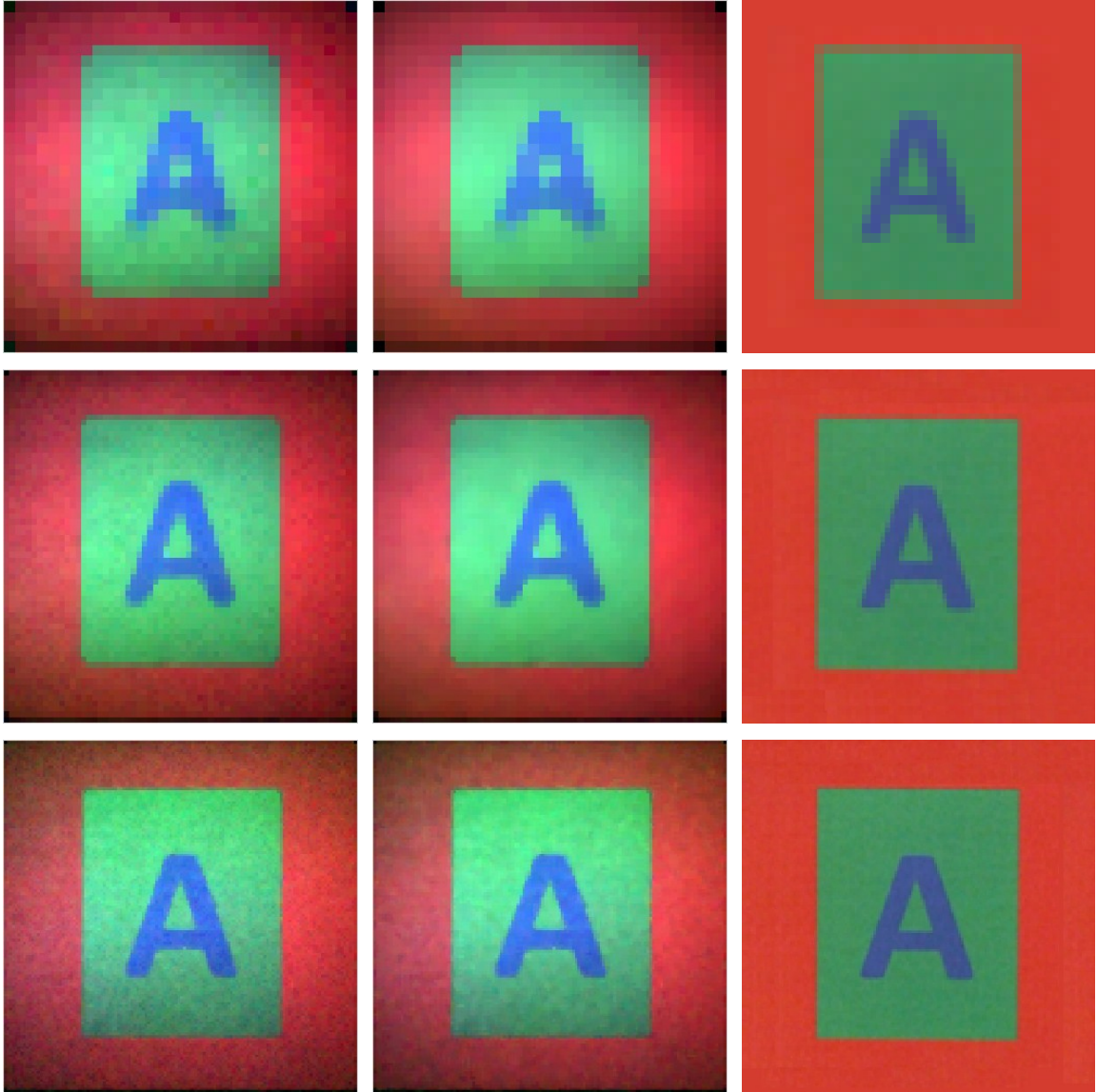


Figure 97 – From top to bottom: 32×32 , 64×64 and 128×128 pixels images captured with the passive illumination single-pixel multispectral imaging system. On the left column are the RGB images obtained after filtering each color channel raw image with the selective local median filter. The center column contains the RGB images obtained after median filtering each color channel raw image. On the right column, it can be seen images acquired with a conventional camera downsized for comparison purposes.

As it was the case for the previously presented imaging systems, the quality assessment based on the PSNR and normalized cross-correlation metrics is presented now for the images of Figure 97 relatively to the images acquired with a conventional camera. The results obtained are shown in Table 26 and Table 27. Based on the results of the metrics, it can be stated that both filtering methods yielded images with similar quality, which is corroborated by human visual assessment.

Table 26 – PSNR values obtained for the reconstructed images of Figure 97 relatively to the images acquired with the conventional camera.

Resolution (pixels)	PSNR (dB)	
	Selective local median filter	Median filter
32×32	16.25	16.28
64×64	16.50	16.35
128×128	16.96	16.73

Table 27 – Maximum values of the normalized cross-correlation obtained for the reconstructed images of Figure 97 relatively to the images acquired with the conventional camera.

Resolution (pixels)	Normalized cross-correlation [0, 1]	
	Selective local median filter	Median filter
32×32	0.55	0.55
64×64	0.54	0.55
128×128	0.54	0.54

4.3.3 Concluding remarks

This section demonstrated the capability of single-pixel imaging systems to acquire multispectral images. In particular, the active illumination, which has already been used for the compression of a scene's spatial content, was also used to integrate spectral information into the system's operation. In the passive illumination case, the illumination was only used to define the spectral content and the spatial compression was applied, on the acquisition side, to the incoming light field.

Comparatively to the images acquired with the various color imaging systems already presented, based on the opinion of human observers, it can be said that the colors of the images reconstructed with these systems were significantly closer to those of the images acquired with a conventional camera. To a great extent, this is due to the much narrower spectra of the LED illumination sources (see Figure 89). It should be pointed-out that it was possible to add

multispectral functionality to the active and passive illumination single-pixel imaging systems already presented only with the change of the light source, therefore confirming the flexibility of these systems.

If these multispectral imaging systems are compared to each other based on the used metrics, the system that performed better was the one using active illumination, mainly due to the results obtained with the normalized cross-correlation. However, a confident conclusion cannot be easily drawn because of the small differences existent between the results obtained with both metrics.

On the other hand, based on human judgment, which is considered to be correct, it can be concluded that the results obtained with the passive illumination system are better because they exhibit less noise and more intense colors, even though both systems have used the same illumination sources and a DMD as a spatial light modulator. The difference resides in the fact that the intensity of light projected by the active illumination system was smaller than that acquired by the passive illumination system. This is verified because it was not possible to launch all of the light emitted by the LED bulbs into the LightCommander's tunnel and the incorporation of the compressive codes into the launched light reduced even more its intensity (statistically, by approximately 50%). This was reflected in a smaller dynamic range in the measurements and/or smaller SNR. In the case of the passive illumination system, the LED bulbs were directly illuminating the FOV with their maximum intensity, therefore resulting in a higher amount of light collected by the imaging lens of the LightCommander, and, finally, in a more intense signal at the photodiode placed in the exit of the light tunnel.

Another important aspect is that exactly the same equipment has been used in both systems, thus demonstrating their versatility, which can prove useful in certain scenarios.

As a final point, the multispectral systems here presented acquired results in the visible range of the spectrum but their operation could similarly be verified in other regions of the spectrum, as long as the radiation sources and/or detection devices were adequately changed.

4.4 Hyperspectral Imaging Systems

Hyperspectral imaging (HSI), also designated imaging spectroscopy or imaging spectrometry, is defined as “the acquisition of images in hundreds of contiguous, registered, spectral bands such that for each pixel a radiance spectrum can be derived”, as originally coined by Goetz *et al.* in 1985 [74].

Hyperspectral imaging is an emerging technique that was initially developed for remote sensing [75] but has since found applications in different fields such as security and defense [76], food inspection [77], biology [78], pharmaceuticals [79] and astronomy [76].

Conventional imaging systems produce 2D – (x,y) – spatial matrices of scalar values representing the intensity of a scene. A hyperspectral imaging system, in contrast, generates a vector for each pixel of the 2D spatial matrix, which contains spectral information for that particular

spatial location. Therefore, we have a 3D – (x, y, λ) – spectral data representation that is usually known as *datacube*.

Typically, hyperspectral systems suffer from tradeoffs between spatial resolution, spectral resolution, light collection and acquisition rate. Even though there are some designs that enable the simultaneous control of several parameters [80-82], some limitations still remain. For that reason, as previously seen in section 3.7, two compressive completely static, single-shot spectral designs with the main goal of controlling all the four operational quantities have been presented [40, 41]. Although these approaches were quite successful, their main constraints are related with the compromise between spectral and spatial resolution, the difficulty or impossibility to resolve point sources and the amount of compressibility that can be achieved. In 2009, Sun and Kelly [42] presented a compressive sensing (CS) based hyperspectral imager capable of reconstructing images with nanometer (0.8nm) spectral resolution. Their system simultaneously acquires and compresses the datacube which greatly decreases the acquisition time and data volume, while increasing the overall image quality when compared to its raster scan counterpart.

Here, the focus will reside on the study of two compressive sensing based single-pixel hyperspectral imaging systems. These systems can also operate either on an active illumination or on a passive illumination mode. The main difference between the two modes of operation relies on the illumination and on the light detection device. On the active illumination case, the spectral information is included in the projected codes used for compression of the spatial content and the single-pixel light detection device can have a broad spectral response, as long as it is sensitive to the spectral content. Additionally, the spectral information is included by the use of light sources with very sharp spectral signatures, such as lasers. By the contrary, on the passive illumination case, the light used to illuminate the scene is broad over all the spectral region of interest and does not incorporate any coding process. The hyperspectral capability of the system comes from the use of a light detection device with very high spectral resolution. The compression of the spatial content is applied to the light field coming from the scene.

4.4.1 Active illumination single-pixel hyperspectral imaging system

In this section an active illumination single-pixel hyperspectral imaging system is presented. As in the previously presented active illumination systems, this system incorporates the compressive measurement codes into the illumination. Its hyperspectral capability comes from the use of light sources with very narrow spectral signatures.

The setup of the implemented active illumination single-pixel hyperspectral imaging system can be seen in Figure 98.

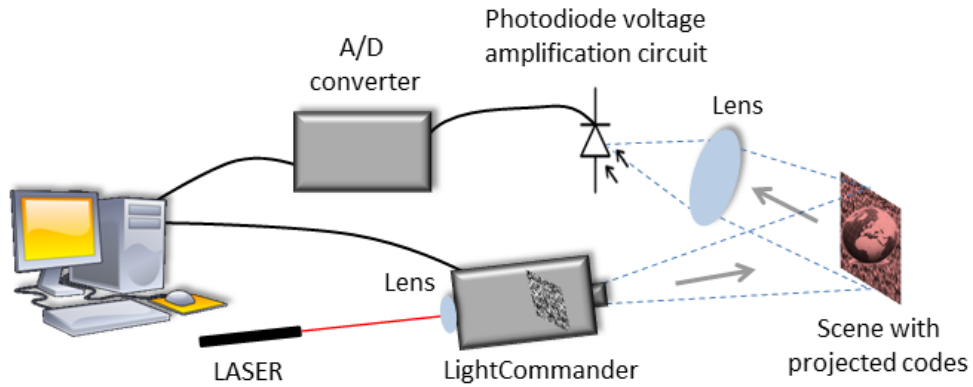


Figure 98 – Setup of the active illumination single-pixel hyperspectral imaging system.

In this setup the illumination was originated in two laser sources: a He-Ne laser emitting at 632.8 nm (red) with 8 mW and a Nd:YAG laser emitting at 532 nm (green) with 50 mW power.

The laser radiation was launched into the LightCommander's tunnel by means of a microscope objective. This lens also served to broaden the laser beam causing the DMD to be entirely illuminated. The amplified photodiode and DAQ board were the same as in the other active illumination setups.

In Figure 99 a photo of the experimental setup of the active illumination single-pixel hyperspectral imaging system can be seen. In the closest plane to the observer, part of the He-Ne laser tube can be seen. It can also be seen the LightCommander without the illumination module and power unit, having a mechanical part to hold the microscope objective in front of the light tunnel, instead. On a farther plane, one can see the amplified photodiode with the objective lens and the scene being illuminated with the laser light modulated by the DMD with a binary random code.

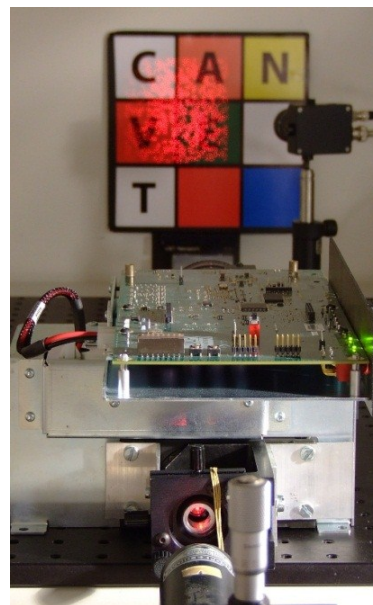


Figure 99 – Photo of the active illumination single-pixel hyperspectral imaging system.

Results and discussion

In order to evaluate the performance of the active illumination single-pixel hyperspectral imaging system, the object of Figure 100 was chosen to be imaged. This object consisted of a paper with the characters “V” and “E” printed in black in a red and green background, respectively. Between the two colored backgrounds there was a black line separating them. The height of both characters was 31 mm. The “V” character measured 28 mm in the wider end and 8 mm in the thinner end, while the “E” character measured 19 mm across. The size of the entire scene was 10 cm × 6 cm.



Figure 100 – Paper with “V” and “E” characters printed in black in a red and green background, respectively.

During operation each laser source was turned on at a time and an image was acquired for each case. Some of the images acquired with this system are presented in Figure 101. These images were acquired with 32×32 pixels, 64×64 pixels and 128×128 pixels and were cropped afterwards to avoid saturated regions originated by the very intense reflections there verified. These intense reflections were justified by the glossy finish and texture of the paper.

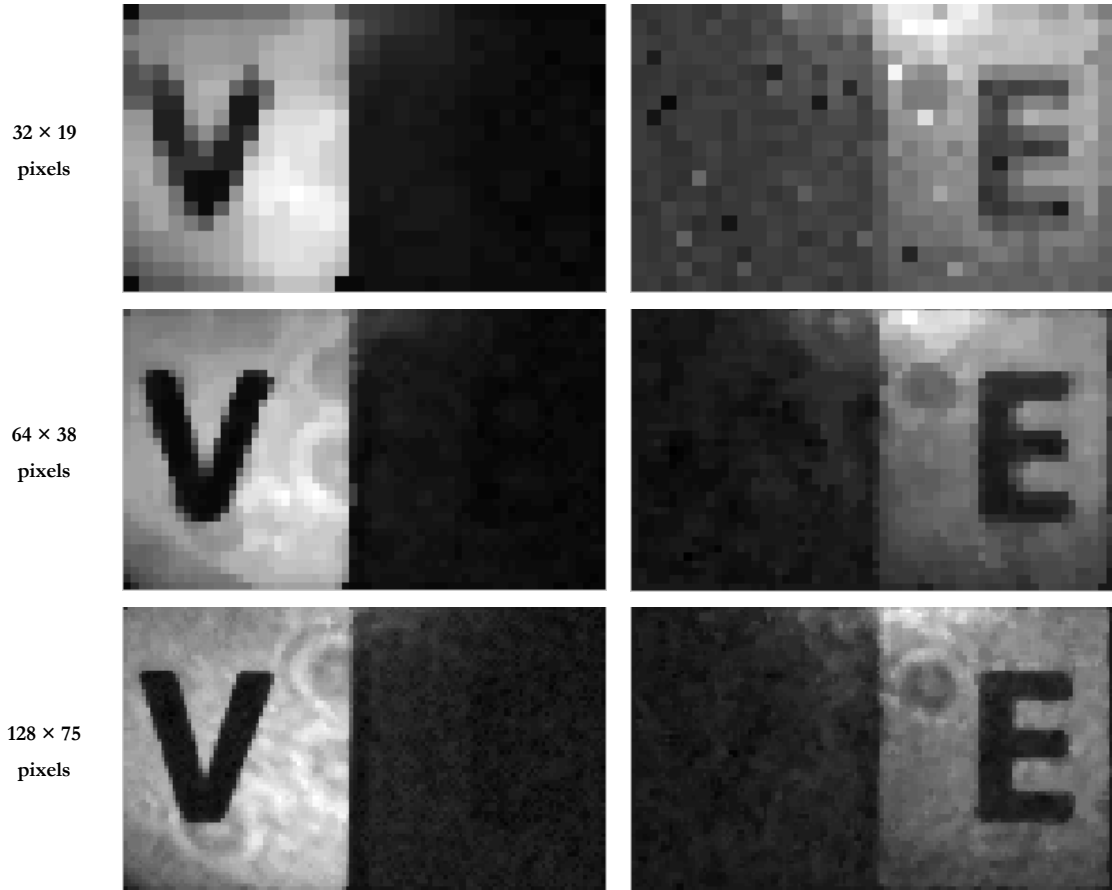


Figure 101 – Images with different resolutions obtained with the active illumination single-pixel hyperspectral imaging system for the paper object with the characters “V” and “E” printed in black in a red and green background, respectively (see Figure 100). The images on the left column were obtained when the He-Ne laser (red) was on and the images on the right column were obtained when the Nd:YAG laser (green) was on.

Both 128×75 pixels images from Figure 101, were converted to RGB images, according to the CIE 1931 2-degree standard, using MATLAB® functions provided in the MathWorks community website (*vide* <http://www.mathworks.com/>). These functions convert the CIE chromatic coordinates associated with the spectral color, specified by a wavelength in the visible region of the spectrum, to its RGB values in the sRGB color space [83, 84]. sRGB is a standard RGB color space that is widely accepted and used in monitors, printers and in the internet [85].

The result of that transformation is presented in Figure 102. Afterwards, those images were added into a single RGB image and the result can be seen in Figure 104. In Figure 103, it can be seen the Red and Green channels of the RGB photos taken with a conventional camera when the scene was being independently illuminated with each of the laser sources.

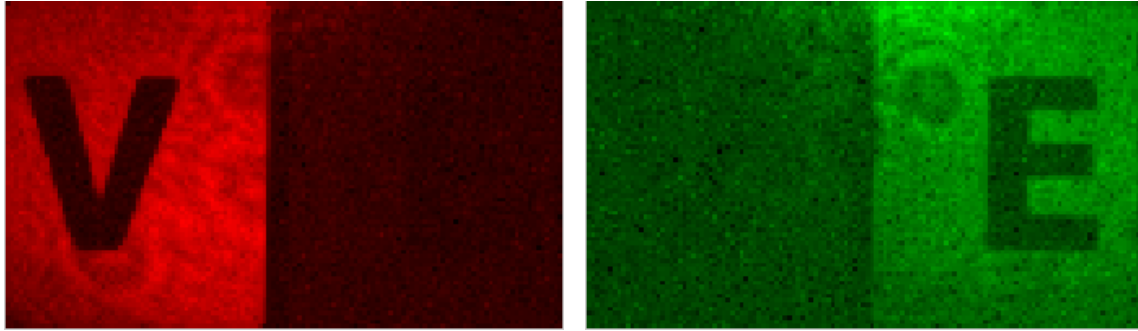


Figure 102 – 128×75 pixels images, from Figure 101, converted to RGB images.

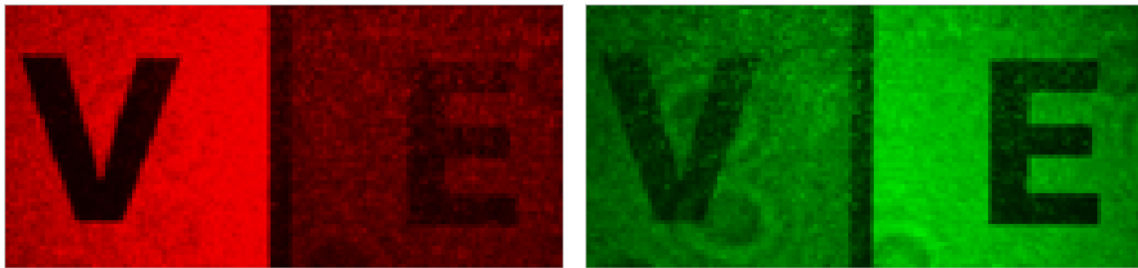


Figure 103 – Red (left) and Green (right) channels of the RGB photos taken with a conventional camera when the scene was being illuminated with the He-Ne laser (on the left) or with the Nd:YAG laser (on the right). These photos have been resized to 128×60 pixels for comparison with the images displayed in Figure 102.



Figure 104 – RGB image resulting from the addition of the images of Figure 102.

Even though care was exerted in order to ensure the entire scene was evenly illuminated, the Gaussian nature of the laser beam is noticeable on the brighter portion observable on the top-left corner of the green region in Figure 104.

Although one can acquire hyperspectral images with a conventional camera, as it was the case for the photos shown in Figure 103, if we compare them to those in Figure 102 it is evident that the results are not equal. This difference is most noticeable in the regions of the scene whose background color differed from the color of the laser light that was being used for illumination. In

those regions, the images acquired with the active illumination single-pixel hyperspectral imaging system exhibit much lower intensities than the images acquired with the conventional camera.

In order to find a justification for the differences verified in the images acquired with the two imaging systems, the reflectance spectra of the red and green regions of the scene were measured at normal incidence when a halogen bulb was being used for illumination (see Figure 105).

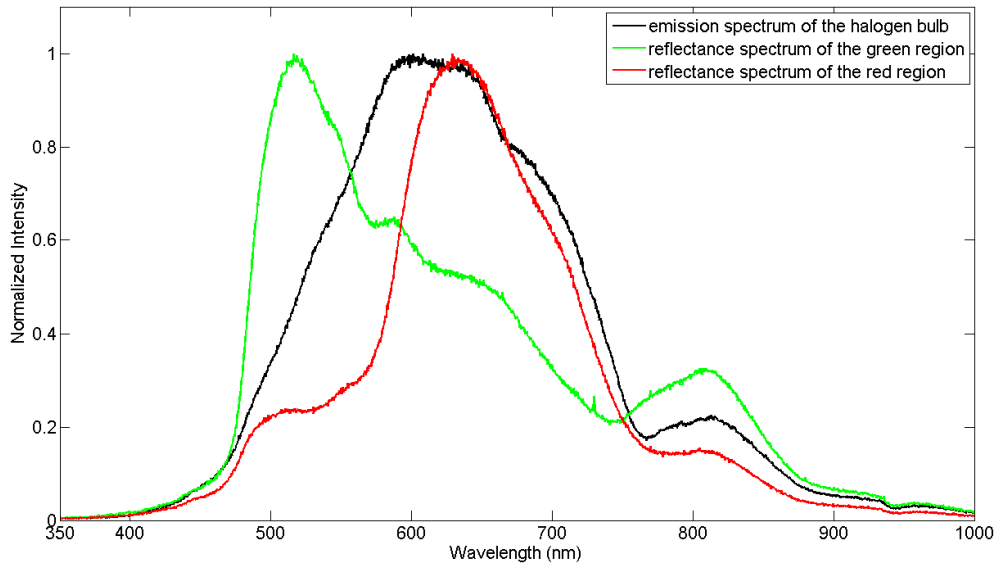


Figure 105 – Reflectance spectra of the red and green regions of the scene presented in Figure 100. In black it is also presented the emission spectrum of the halogen bulb that was used for illumination.

From the observation of Figure 105 it is possible to conclude that despite the maximum reflectance of the red (~ 635 nm) and green (~ 516 nm) regions occur within the correct spectral regions, both regions strongly reflect other wavelengths.

The optics used for collection of the light reflected from the scene also differed among the two imaging systems, being the aperture of the lens used in the single-pixel camera much narrower which caused it to collect less light.

Because of the facts mentioned above, the conventional camera was able to capture the content of the green region when the red laser was being used for illumination and vice-versa. The same was not verified with the active illumination single-pixel hyperspectral imaging system.

It should, however, be said that if the spectral content within the field of view was controlled, the results obtained with both imaging systems should have been the same.

4.4.2 Passive illumination single-pixel hyperspectral imaging system

Here, we describe a hyperspectral compressive sensing based single-pixel camera with high spectral resolution built using a Digital Micro-mirror Device (DMD), to optically compress the image to be acquired by applying binary random codes, and an optical spectrum analyzer (OSA), to enable high spectral resolution acquisition. The optical-domain compression causes each spectral line to be

measured by the OSA as the inner product between the incoherent random measurement vectors and the image of interest. We demonstrate the successful reconstruction of images of a scene illuminated by a He-Ne laser which has a very sharp and distinct spectral signature. Due to its excellent spectral resolution the reconstructed images show the ability of our system to extract the information existent in the scene corresponding to that specific spectral region. We also present the reconstruction of high spatial resolution images of an elaborated scene.

The implementation of our system was based on the use of a DLP™ (Digital Light Processing) projector (Infocus LP120 – 1024 x 768 square pixels – 0.7 inches diagonal) in a reverse way – i.e., rather than using it for projection, it was used as part of an image acquisition system –. In this configuration, it was possible to take advantage of the integrated and optimized optical assembly of the projector, as well as of all the existing video signal conditioning and control. The Infocus LP120 projector (see Figure 106) incorporates a zoom lens with manual focus and manual zoom adjust and exhibits a throw ratio of 1.8 – 2.1:1 (typical) and a minimum projection distance of 1.5 m (maximum distance 5 m).



Figure 106 – Photo of the Infocus LP120 video projector.

Similarly to the work of Takhar *et al.* [15], the application of the random binary measurement patterns is made through a DMD. In our setup, this device is part of the projector's optical engine and by means of the projector's lensing system the image of the scene being acquired is formed on the DMD surface. The dimensions of the mirrors of the DMD being used were approximately 12.7×12.7 microns² and, in our case, an active area of 512×512 elements of the DMD was used. When electrically actuated, the mirrors of the DMD exhibit a tilt angle of $\pm 12^\circ$, which is used to either direct the light along the projection path ("ON" state), or to deviate the light towards a light absorber (OFF state). Therefore, depending on the applied code, the light hitting the DMD pixels at "ON" state is reflected towards the place where the projector lamp was originally located. There, after the light tunnel, instead of the lamp, a 10x microscope objective with 0.25 numerical aperture (NA) was inserted to launch light into a 50/125 μm multi-mode fiber with 0.2 NA that was

connected to a single-mode optical fiber at 633 nm with 0.14 NA, which, in turn, was connected to the OSA input.

The OSA (ANDO AQ6317B) is implemented on a Zollner-Thurnar's type monochromator. The principle of operation can be described as follows (see Figure 107): the single-mode fiber acts as the input slit of the monochromator, being the divergent input beam collimated by a concave mirror to illuminate a grating that acts as a diffractive element. An output slit is arranged at a position where the reflected light from a focusing mirror is focused, enabling that only a specific spectral component exits at the slit towards the photodetection block. The detected spectral window can be tuned by rotating the grating, while the spectral resolution can be changed by changing the width of the output slit.

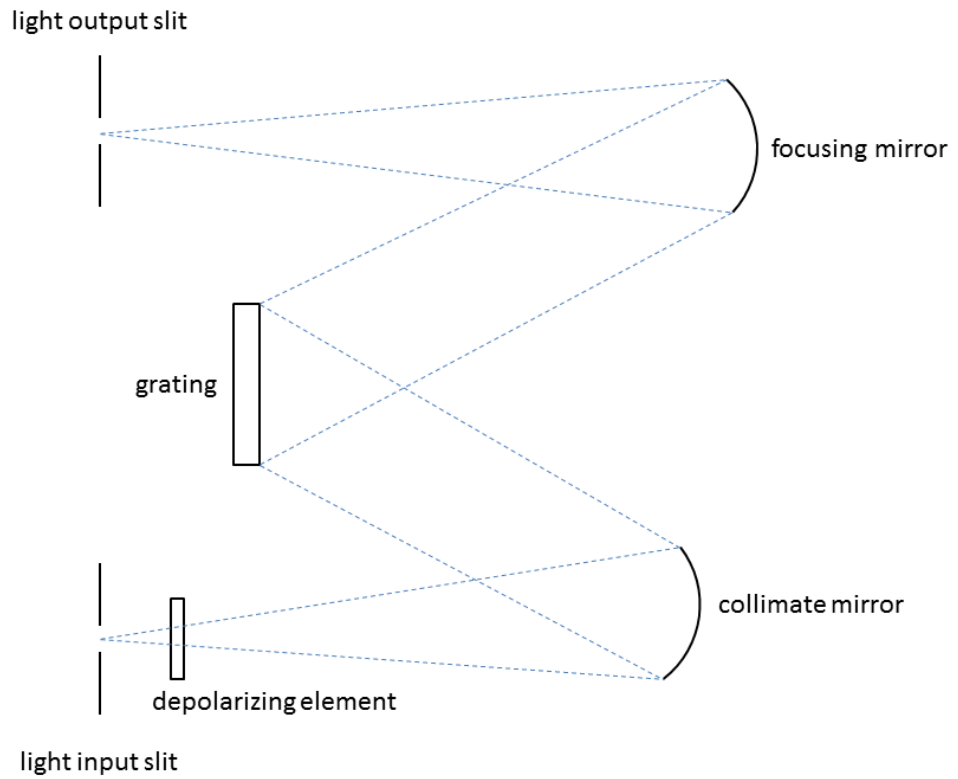


Figure 107 – Scheme depicting the principle of operation of the Zollner-Thurnar's type monochromator of the ANDO AQ6317B optical spectrum analyser (OSA).

Finally, the light intensity at each spectral line was measured by the single photodetector of the OSA and the resulting linear vector was stored for each binary random code. Depending on the dimensionality of the used random codes, the number of DMD pixels (mirrors) that were used to encrypt a pixel of the reconstructed image would vary. For instance, for a reconstructed image with 64×64 pixels, each pixel would correspond to a set of 8×8 DMD elements, since an active area of 512×512 elements was being used on the DMD. The spatial resolution of the reconstructed images is, then, defined by the dimensionality of the random codes used for measurement.

One image can be reconstructed for each of the measured wavelengths and, in that manner, a datacube - (x, y, λ) - can be built. In order to access the spectrum of a particular part of an image, the values along the datacube (i.e., along the λ dimension), for that (x, y) region of interest can be selected. The spectral resolution of the resulting spectrum is directly related with the resolution with which the measurements were performed by the OSA.

A scheme depicting our hyperspectral camera principle of operation can be found in Figure 108. In Figure 109 a detailed photo of the optical engine of the Infocus LP120 projector can be seen and in Figure 110 a detailed photo of the Infocus LP120 with the 10x microscope objective launching light into the optical fiber is presented. The M1-DA video input port of the projector was connected to the computer's VGA D-sub 15 pin interface. The synchronization of the measurements and the communication between the OSA and the computer was established via General Purpose Interface Bus (GPIB) protocol according to the ANSI/IEEE Standard 488.1.

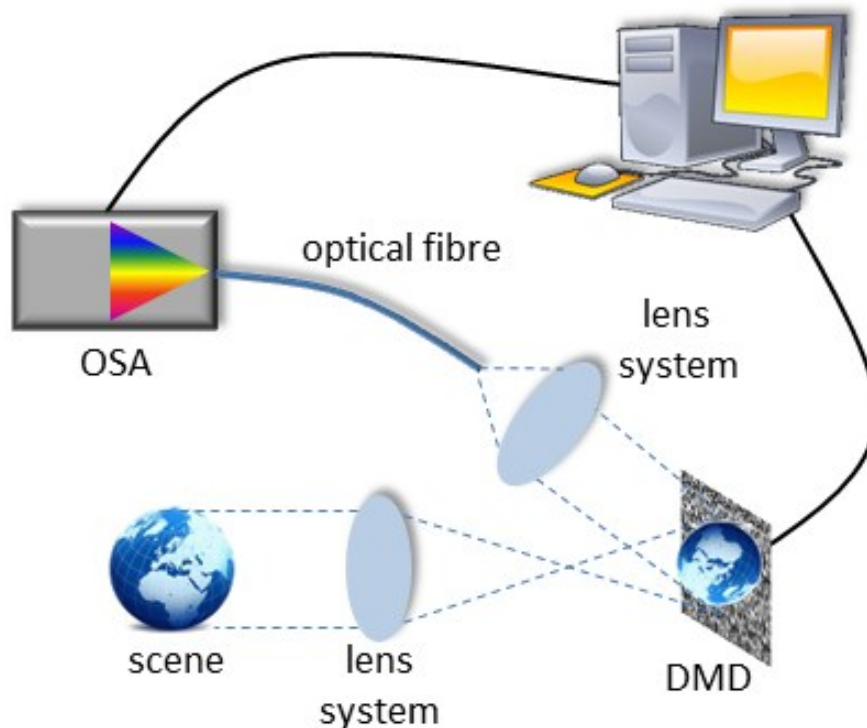


Figure 108 – Scheme depicting the principle of operation of the passive illumination single-pixel hyperspectral imaging system.

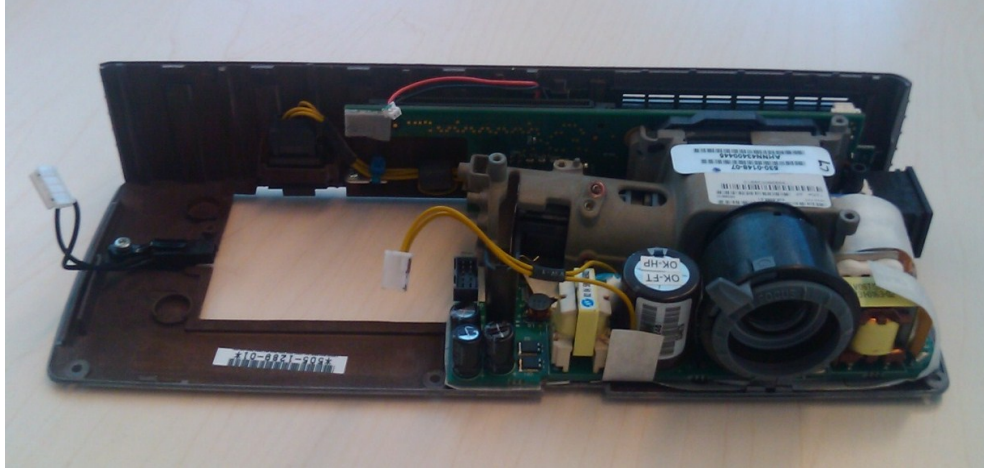


Figure 109 – Optical engine of the Infocus LP120 projector.



Figure 110 – Detailed photo of the Infocus LP120 with the 10x microscope objective launching the light into the 50/125 μm multi-mode optical fiber.

Results and discussion

The implemented system was used to acquire specific images to assess its performance. One initial scene consists of a vertical line projected by a He-Ne laser at 632.8 nm into a mirror.

The normalized emission spectrum of the He-Ne laser is shown in Figure 111 (red trace). This spectrum has been directly measured on the OSA with a resolution of 10 pm and span of 500 pm, corresponding to a wavelength range from 632.61 nm to 633.11 nm. Also in Figure 111, the normalized reconstructed spectrum (black trace), which was obtained along the reconstructed datacube in a spatial position where the laser line was imaged, is represented. As can be seen, the spectrum along the datacube closely matches the measured spectrum.

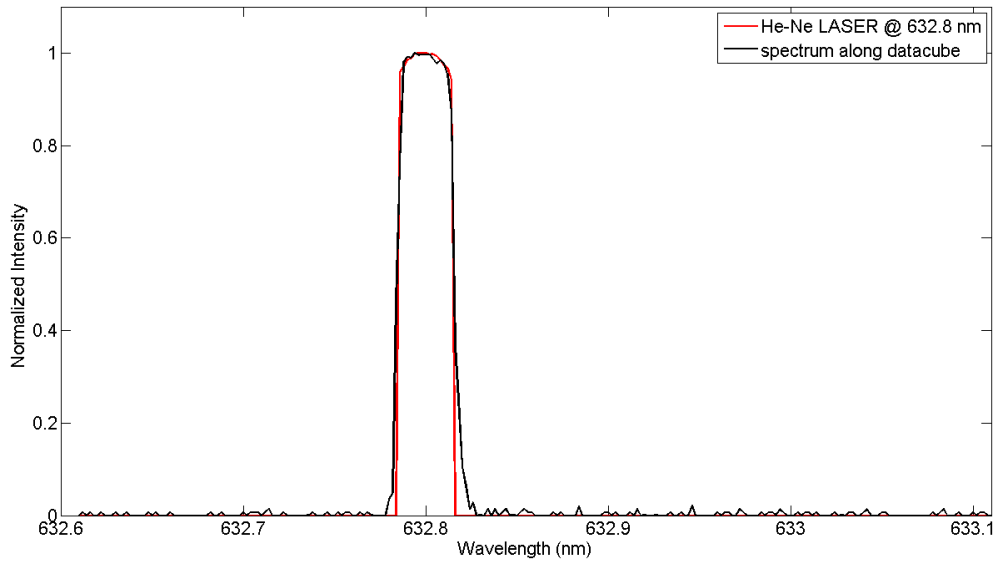


Figure 111 – Normalized reconstructed spectrum obtained along the reconstructed datacube in a fixed spatial position where the laser line was imaged (black trace). The red trace represents the normalized spectrum of the He-Ne source measured with the OSA.

Figure 112 shows the images reconstructed at 632.800 nm, representing the laser line, and the images reconstructed at 632.790 nm, representing the absence of any relevant feature at that particular wavelength. Along with these images the normalized intensity of corresponding pixels is shown in a 3D mapping, which stresses the fact that when one observes the image representing the laser line, at its particular location, those pixel values are much greater than all the remaining pixel values in the image. The same is not verified for wavelengths in which the laser line cannot find representation.

Since the results presented in Figure 112 show the minimum spectral separation required to have an image where the laser line is present and another image where it is not, one can state that the demonstrated spectral resolution of the proposed system is 10 pm.

During the acquisition of the images shown in Figure 112 the field of view corresponded to a square area with 40 mm side. Therefore, one can state that the spatial resolution for the 32×32 pixels images was 1.25 mm/pixel, while for the case of the images with 64×64 pixels the spatial resolution was approximately 0.63 mm/pixel.

In the meantime, an improved passive illumination single-pixel hyperspectral imaging setup has been implemented. For that, the disassembled Infocus LP120 video projector has been substituted by the LightCommander. A Newport fiber optic positioner with 5 degrees of positioning has been adapted in order to hold and position the SMA connectorized optical fiber, in front of the microscope objective, which was used to collect the light coming from the LightCommander's light tunnel and launch it into the fiber. In Figure 113 it can be seen a photo of this assembly.

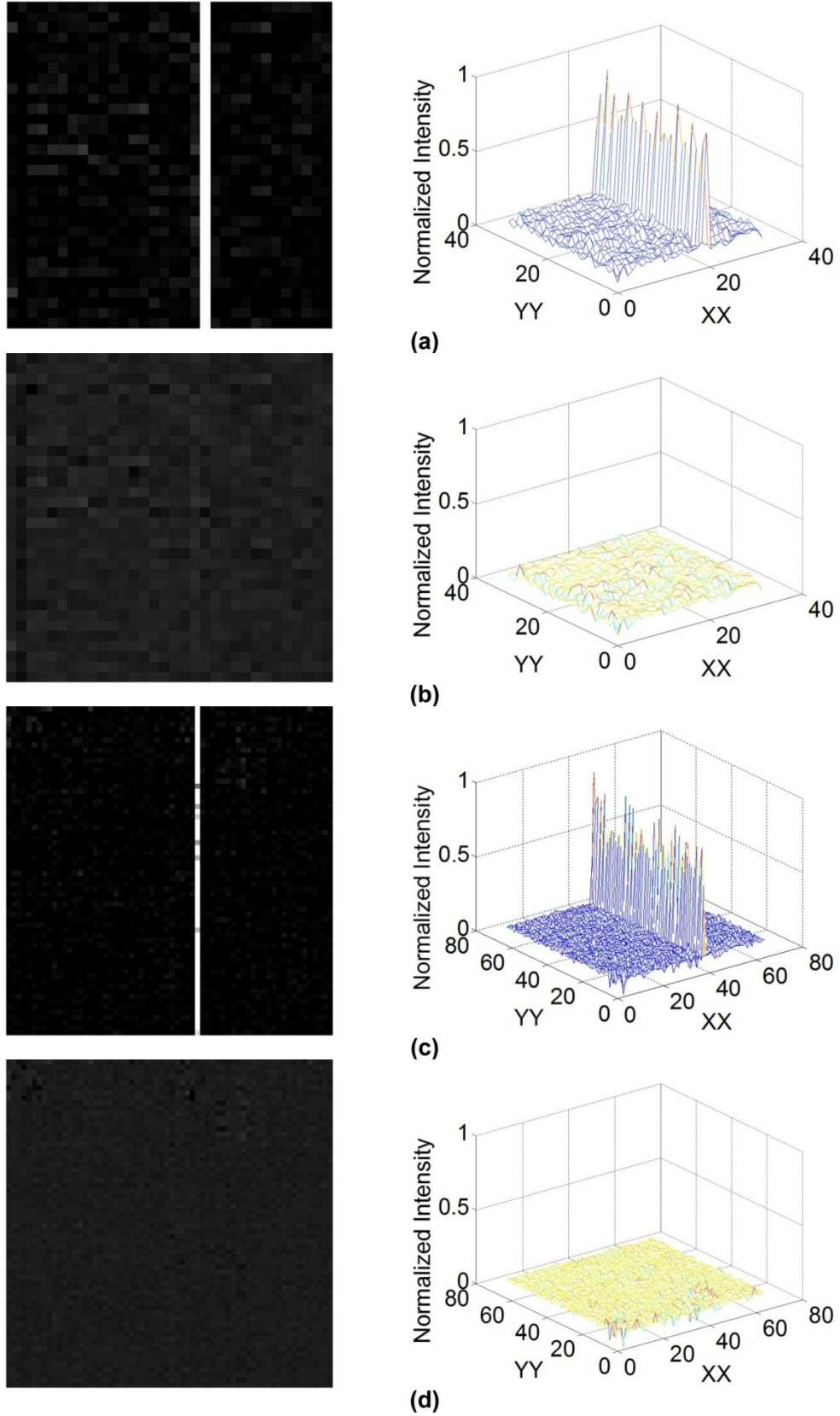


Figure 112 – Rows (a) and (c) represent the images reconstructed at 632.800 nm with 32×32 and 64×64 pixels, respectively, along with a 3-D representation of their normalized intensities. Rows (b) and (d) represent the images reconstructed at 632.790 nm with 32×32 and 64×64 pixels, respectively, along with a 3-D representation of their normalized intensities.

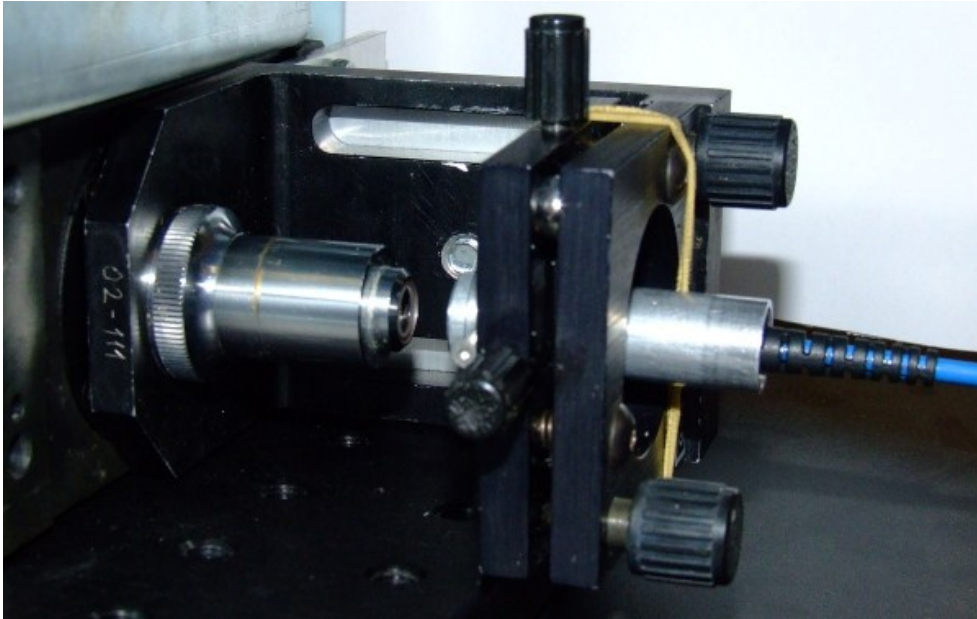


Figure 113 – Detailed photo of the assembly used for launching light coming from LightCommander's light tunnel into the optical fiber.

As the image of a line is already sparse in the spatial domain, we chose another scene, more elaborated this time, to demonstrate the usefulness of this hyperspectral system in such situation and to prove the ability of the system to reconstruct larger and more complex images. For this, we reconstructed an image of a lit light bulb with 15 red LED, at 630.900 nm, which was the central wavelength of the emission peak ($\text{FWHM} = 17.2 \text{ nm}$), with 512×512 pixels (see Figure 114). As it can be seen in Figure 114, the image reconstructed with our camera closely represents the image taken with a conventional camera, thus confirming its feasibility. For this acquisition, the field of view corresponded to a square area with 60 mm side, thus resulting in a spatial resolution of approximately 0.12 mm/pixel.

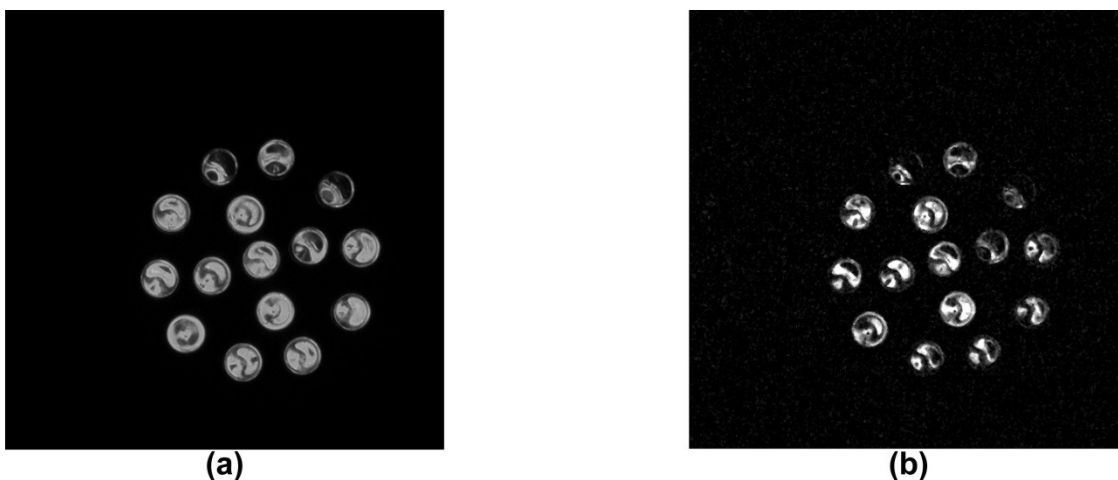
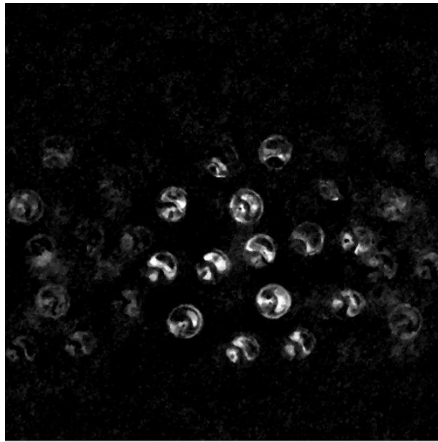


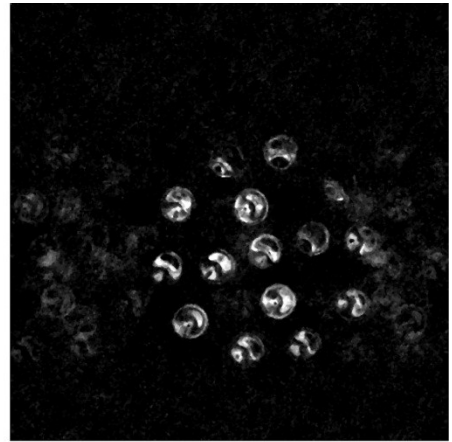
Figure 114 – 512×512 pixels photo of the lit LED lamp acquired with: (a) conventional camera; (b) with passive illumination single-pixel hyperspectral camera, at 630.900 nm.

Since the measurement rate was limited both by the rate at which the codes were displayed on the DMD and by the OSA scanning speed, the measurement process for this image took approximately 28 hours. Notwithstanding, as can be seen, this fact does not impair the potential of this camera to reconstruct more complex and larger images.

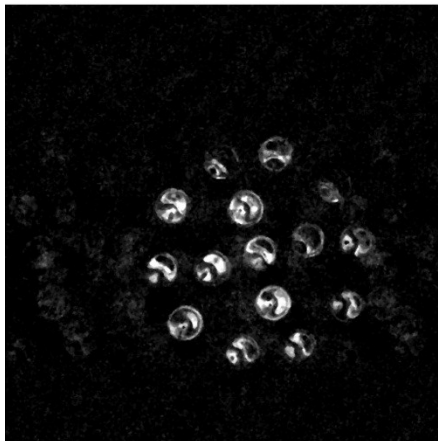
Next, in Figure 115, one can observe different reconstructions of the image of the lit LED bulb acquired with our camera. The associated Peak Signal-to-Noise Ratio (PSNR) values were calculated relatively to the image reconstructed using 100% of the measurements (see Figure 114 (b)), and reflect the quality improvement obtained with the increase of measurements used to reconstruct the image.



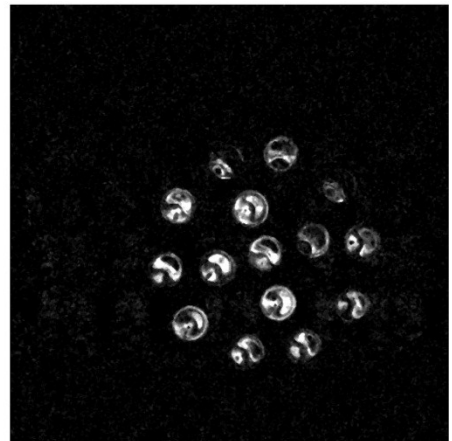
60% of the measurements
PSNR = 28.51 dB



70% of the measurements
PSNR = 29.64 dB



80% of the measurements
PSNR = 32.02 dB



90% of the measurements
PSNR = 35.52 dB

Figure 115 – PSNR versus the percentage of measurements used to reconstruct the 512×512 pixels images of the lit LED bulb with respect to their full dimensionality. All the PSNR values were calculated relatively to the 512×512 pixels image reconstructed using 100% of the measurements [see Figure 114 (b)].

Comparing our work to the CASSI systems developed at Duke University [40, 41] some advantages and disadvantages can be identified. The main difference is that while these systems measure two-dimensional coded spectral or spatio-spectral projections of the three-dimensional datacube that represents the scene, our system simultaneously acquires and compresses the datacube into one-dimensional arrays. Despite both systems involve a software-based reconstruction final step, the CASSI systems operate with a single-shot, while our system requires several measurements to be performed in order to gather the required information. As our system only requires a single element detector, it can incorporate, for instance, large area photodiodes, causing its sensitivity to be much higher than that of the pixels of the detector array used in the CASSI systems; therefore our system exhibits higher potential of working in lower lighting conditions. Furthermore, as our compressive measurements always capture approximately 50 percent of the total light from the scene, the signal to noise ratio is much higher than that of the CASSI systems.

In the CASSI systems, prisms were used as dispersive elements and since the dispersion of a prism is nonlinear, the spectral resolution of this instrument varies with wavelength. By the contrary, the spectral resolution of our system is linear and much higher than those obtained by the CASSI systems, being 3.6 nm the lowest of the two CASSI systems.

The CASSI authors also state that in their systems there is a compromise between spatial and spectral resolution and that it can be difficult to spectrally or spatially resolve point sources. These facts do not constitute a limitation for our system.

Regarding the previously referred work of Sun and Kelly [42], one can state that the main difference relies on the instrumentation level, in particular, in the light detection equipment. Their system made use of a spectrometer with 1044 spectral bands responsive from 200-1100 nm, therefore their statement of 0.8 nm of maximum spectral resolution.

In our work we have used an OSA responsive from 600-1700 nm that is capable of providing excellent resolution over the full spectral range, as previously explained. Furthermore, in our case, optical fibers were used to guide the light till the OSA, which increases the flexibility of the system.

Following these experiments, we implemented a smaller version of the passive illumination single-pixel hyperspectral imaging system. To accomplish this we replaced the OSA by a miniature fiber optic spectrometer from Ocean Optics (model USB 2000) as the one depicted in Figure 116. The dimensions of the spectrometer are 89 mm (length) \times 64 mm (width) \times 34 mm (height) and weights 270 grams with the USB cable.



Figure 116 – Photo of an Ocean Optics USB 2000 miniature fiber optic spectrometer. Image reproduced from <http://www.oceanoptics.com/Products/usb2000.asp>.

In Figure 117, on the left, it is shown a USB 2000 spectrometer without cover, unveiling its internal optical arrangement, and, on the right, one can see a scheme illustrating the path that light assumes inside the spectrometer. In the image on the right, number 1 represents the input optical fiber that is secured with an SMA connector (number 2), behind which it is mounted a slit. This slit consists of a dark piece of material containing a rectangular aperture, which measured $25\ \mu\text{m}$ in our case. This aperture regulates the amount of light that enters the spectrometer. Number 3 represents the collimating mirror that focuses light entering the optical path towards the grating (number 4). The grating, in turn, diffracts light from the collimating mirror and directs it onto the focusing mirror (number 5). The focusing mirror receives light reflected from the grating and focuses the light onto the CCD detector (number 6). The CCD detector collects the light received from the focusing mirror and converts the optical signal to a digital signal (12 bits analog-to-digital converter). Each pixel on the CCD detector responds to the wavelength of light that strikes it, creating a digital response. The detector is a Sony ILX511 linear silicon CCD array, responsive from 200 nm up to 1100 nm with 2048 pixels ($14\ \mu\text{m} \times 200\ \mu\text{m}$ each). The spectrometer then transmits the digital signal to the computer application via USB.

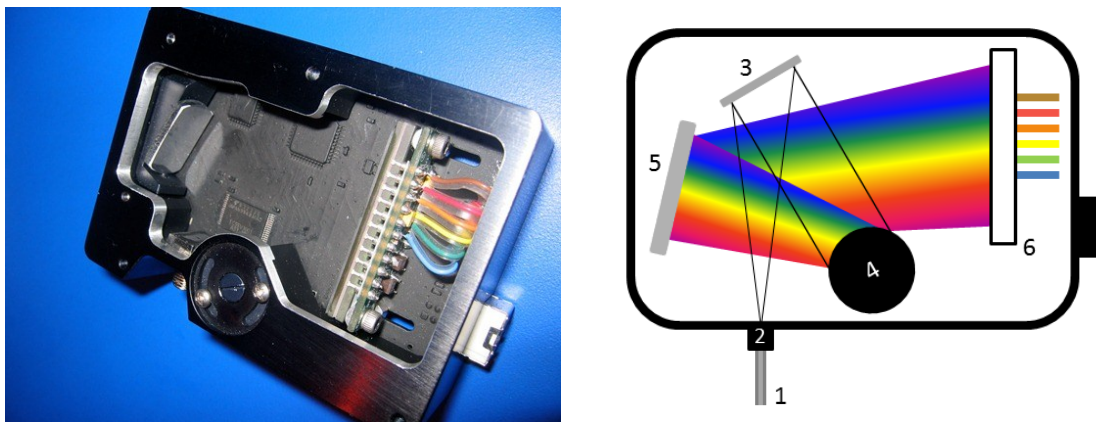


Figure 117 – (left) Ocean Optics USB 2000 miniature fiber optic spectrometer without the cover. (right) Scheme of the light path through the optical arrangement of the USB2000. The photo on left was reproduced from http://www.biophotonicsworld.org/system/uploads/0000/0037/IMG_9538.JPG.

According to the information provided by the manufacturer in its website (*vide* <http://www.oceanoptics.com>), the spectral resolution of the spectrometer can be obtained from the product between dispersion and pixel resolution. The dispersion can be expressed in nm/pixel and results from the division of the spectral range of the grating by the number of pixels of the detector. For our spectrometer, the spectral range of the grating (#3) was 650 nm, and the detector had 2048 pixels. Therefore, the dispersion equals approximately 0.32 nm/pixel. The pixel resolution varies with the width of the entrance aperture and can be defined either by the slit size or by the diameter of the optical fiber. As we used a 600 μm diameter fiber and the slit size was 25 μm , the pixel resolution has been determined by the slit size as ~ 4.2 pixels. As a result, the spectral resolution of this system was $0.32 \text{ nm/pixel} \times 4.2 \text{ pixels} \approx 1.34 \text{ nm}$. This fiber with larger diameter has been used instead of the previously used ones, because the sensitivity of the spectrometer is smaller compared to that of the OSA and we wanted to place as much light as possible at the entrance slit of the spectrometer.

This setup has then been used to acquire hyperspectral images at specific wavelengths of a scene composed by the previously imaged red LED bulb (see Figure 114) when it was being hit in a spot by a red laser emitting at 654 nm. All the synchronization for the projection of the compressive codes and the acquisition of the spectra measured by the spectrometer was executed by a LabVIEW™ application specifically designed for that purpose. The communication between the control computer and the spectrometer has been established via USB and the communication with the LightCommander has been established via HDMI, as before. As the spectral contents of the LED bulb and of the laser line were very close, it was not possible to discern the laser spot in a photo acquired with a conventional camera (see Figure 118). The spectrum of both light sources can be seen in the plot of Figure 119. There, in black it is represented the normalized spectrum measured by the USB 2000 spectrometer when the LightCommander was collecting all the light from the scene, i. e., its DMD was displaying an all-white image. In red, one can find the normalized spectrum obtained along the reconstructed datacube in a spatial position where both the LED bulb and the laser spot were represented. The spectrometer integration time was set to 150 ms. From the results of Figure 119, it can be stated that the reconstructed spectrum closely follows the original one. The discrepancies verified may be due to measurement noise and to artifacts introduced by the reconstruction process.



Figure 118 – Conventional camera photo of the composed scene of a red LED bulb being hit by a spot of a laser emitting at 654 nm.

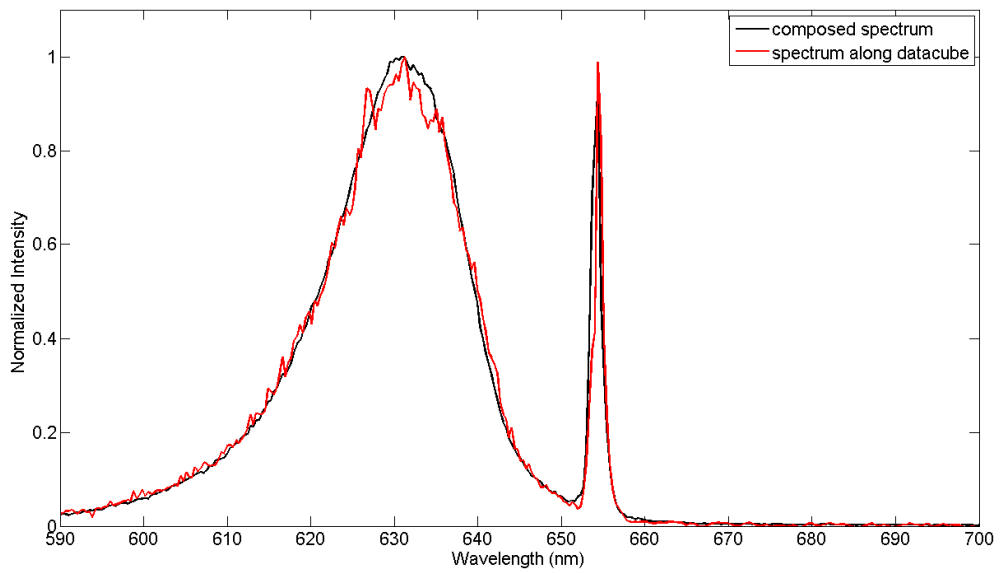


Figure 119 – Spectrum of the scene composed by a red LED bulb and by a laser spot at 654 nm. The spectrum directly measured with the USB 2000 spectrometer is represented in black while the spectrum obtained along the reconstructed datacube is represented in red.

Figure 120 illustrates the images reconstructed with 128×128 pixels at 630.88 nm and 654.03 nm, representing the red LED bulb and the laser spot, respectively. These images have been median filtered with a 3×3 kernel.

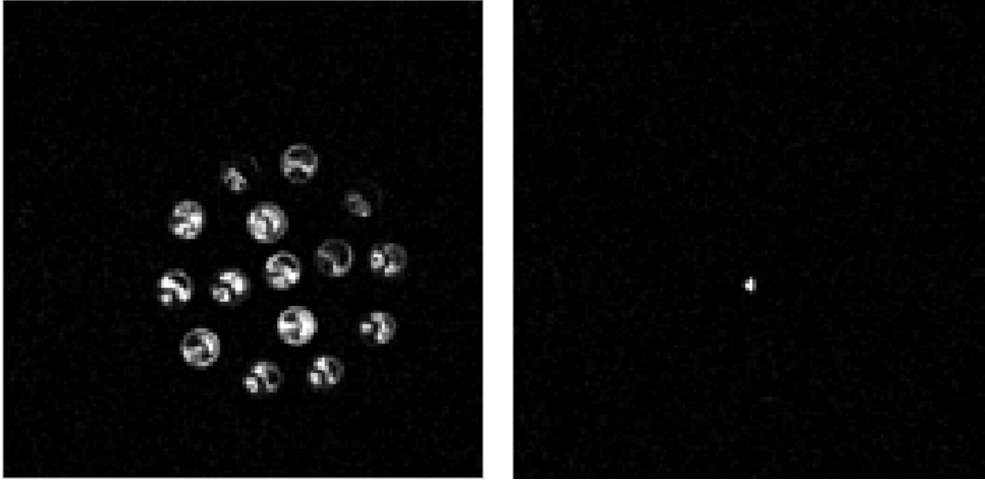


Figure 120 – 128×128 pixels images reconstructed at 630.88 nm and 654.03 nm, representing the red LED bulb and the laser spot, respectively.

The system took approximately 80 minutes to acquire 100% of the measurements for the reconstruction of the datacube.

4.4.3 Concluding remarks

In the case of the active illumination single-pixel hyperspectral imaging system, though only two laser wavelengths were used, one can assume that such system would perform equally well if a tunable laser would have been used, instead. If that was the case, the spectral resolution of the system would have been dictated by the spectral resolution of the tunable laser.

Regarding the passive illumination implementation, it was demonstrated, for the first time, a hyperspectral CS-based imaging system using optical-domain compression with a spectral resolution of 10 picometers. This system is also capable of providing access to the spectrum along the reconstructed datacube for a specific spatial region in the image. Another relevant aspect of the passive illumination system is the fact that it measures all wavelengths at once; therefore, it offers the ability to simultaneously acquire images with high spectral resolution from a large spectral range. The performance of the compact passive illumination hyperspectral single-pixel imaging system was comparable to that of the system incorporating an OSA at the expense of worse spectral resolution (1.34 nm). Due to its compactness and versatility, it is believed that this system may be an excellent option for the development of a carry-on hyperspectral imaging system that can find applications in agro-food industry or oil industry, for instance.

In addition, if a DMD is used with dedicated controller boards, its display rate can go up to 30k patterns/second. At such rate, the only requirement would be the OSA, the spectrometer or the light detection device to have an adequate sampling rate and sensitivity.

In the scope of CS theory, since fewer measurements are required, a design incorporating CS into HSI can significantly reduce the image acquisition time and provide images with high spatial and spectral resolutions, even under reduced illumination conditions.

Moreover, the presented implementations can also be extended to work in spectral regions currently inaccessible to conventional imaging arrays, with applications in biology, sensing and spectroscopy. Generally speaking, changing the lasing and photodetection range would be the major differences one would have to make, since the LightCommander's optical path can operate up to 1500 nm with minor decrease in the transmittance (this information has been provided by Texas Instruments, which is the DMD manufacturing company). If operation in other ranges of the spectrum is desired, then, it is possible to find DMD with adequate optical coatings.

4.5 High Dynamic Range Compressive Imaging Systems

High dynamic range imaging (HDRI or HDR) is related with the acquisition of images that contain a broad range of brightness levels which conventional imaging systems are not able to fully apprehend. This can be due to the range of colors, the reflective or transmissive properties, the illumination pattern, etc. In a typical digital camera, the value for each color (red, green, and blue) is stored using 8 bits. Assuming that minimum intensity is equal to 1 and maximum intensity is equal to 256, the dynamic range of such camera is about $20 \times \log_{10}(256) = 48dB$ for each color. To capture a scene that requires a dynamic range of more than 48 dB for each color, a new imaging technique is necessary. For that, one of the most popular methods is to capture images of the same scene with different exposure times and gains, and then combine the resulting images to construct an image with high dynamic range [86, 87].

Early work in this area was done by Mann [88, 89], who proposed an algorithm to combine different images of the same scene captured with different exposure times. The proposed combination algorithm made use of a certainty function that was the derivative of the camera's response function. Another work in this field was reported by Madden [90] where, once again, multiple images of a scene were captured with a CCD using different exposure times. The exposure time was changed such that at minimum exposure time there was no saturated pixel, and at maximum exposure time some pixels became saturated. By examining each pixel at different exposure times, it could be stated that pixels might:

- be saturated at long exposure time and their values become the maximum allowable;
- remain dark from either short exposure time or simply lack of light;
- take values below saturation and above noise level.

To construct the final HDR image, each pixel of the HDR image was chosen from the images to have a value below saturation and to be the most precise relatively to the minimum quantization error.

There are also some works on extending the dynamic range of color images. Moriwaki [91] used the same principle of combining images with different exposure times and constructing an adaptive exposure color image. It was shown that the constructed image had better accuracy in applications like color discrimination. A work reported by Debevec and Malik [86] used images with different exposure times to find the response function of the imaging process up to a scale factor and then used this response function to construct HDR images. Mitsunaga and Nayar [92] used images obtained with different exposure times to calculate the response time of the imaging system and using only the ratio of different exposure times it was possible to accurately recover the response function.

Another technique for improving the dynamic range of an image is to change the exposure or intensity of each pixel individually. Nayar and Mitsunaga [93] proposed an imaging system where neighboring pixels had different exposures. Their system used a mask with different transparencies in front of the detector. Mannami *et al.* [94] proposed HDR imaging by means of reflective liquid crystal. They used LCoS (liquid crystal on silicon) as a spatial light modulator in front of a camera to spatially modulate the intensity of each pixel. One of the issues here was the geometric alignment between the pixels of the camera and the LCoS and homography was used for geometric calibration. Also, an off-line calibration was conducted to infer the radiometric properties of the system. At each step they changed the values of the LCoS pixels so that the values of the corresponding camera pixels became equal to an optimal value. This optimal value corresponded to optimal radiance. Adeyemi *et al.* [95] used a digital micromirror device (DMD) to acquire an HDR image in a microscopy system. They also used the geometrical calibration for corresponding pixels of the camera and the DMD. Also, the DMD was characterized for its reflected power in terms of the digital values of DMD pixels. They reported that with their system, in principle, they could improve dynamic range of an image by a factor of 573, although their experimental results showed improvement by only a factor of 5.

Commercially, there are some HDR imaging systems, such as Viper FilmStream, SMal, Pixim, and SpheronVR [87], that can capture and record HDR images in one shot. Fujifilm has introduced point-and-shoot cameras that capture HDR from two images with different exposure times [96].

Having pointed out this, in a preliminary approach, some experiments regarding the subject of high dynamic range imaging, in particular the control of image intensity during acquisition, have been conducted and will be explained hereafter. For that, consider a situation in which it is required to obtain information about the tridimensional profile of an object's surface, as the one shown on Figure 121, by means of image analysis techniques and optical interferometry.



Figure 121 – Picture of a hemispherical surface.

In these cases, usually, a fringe pattern, as shown in Figure 122, is projected into the object. Afterwards, the distortion caused by the object surface on the projected pattern is analyzed and that allows the determination of the tridimensional profile of the object's surface.

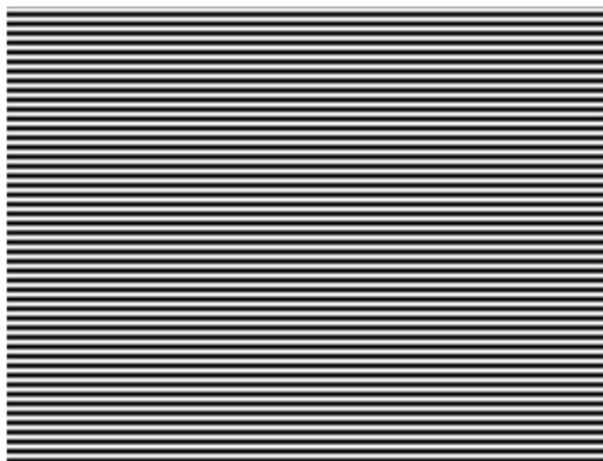


Figure 122 – Example of a sinusoidal fringe pattern used for the extraction of 3D information about the object into which it is projected.

However, due to the object's shape and material it may be impossible to acquire a single image that enables the analysis of the complete scene at once. This limitation is perfectly visible in Figure 123, where it was necessary to adjust the camera's gain and exposure time to acquire these particular situations.

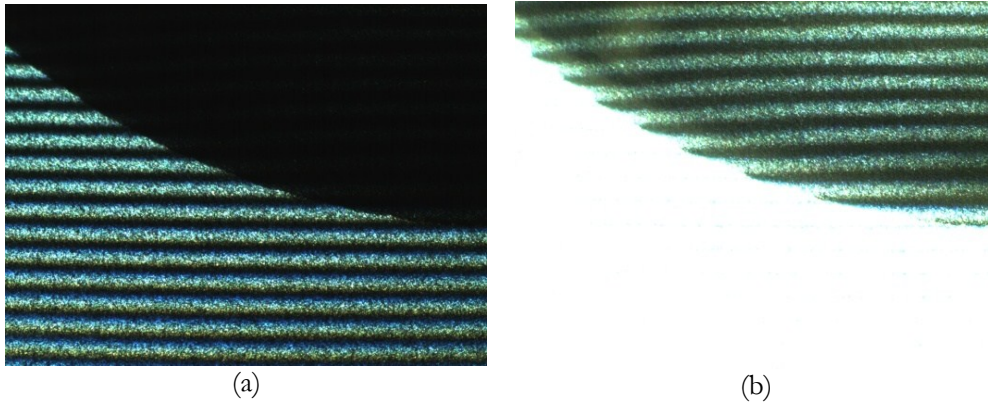


Figure 123 – Photos of the hemispherical object from Figure 121 with a sinusoidal pattern projected on its surface, acquired with a conventional camera using different exposure times and gains: (a) exposure time: 31 ms, gain: 14; (b) exposure time: 230 ms, gain: 81.

In our case, the sinusoidal pattern seen in Figure 123 did not result from an interference process but rather it was projected by a video projector that was connected to the computer, therefore, avoiding the need for vibration and temperature compensation systems well-known in interference based methodologies. For the application in hands, a video projector was also more flexible and easy to configure. As it is clear from the photo in Figure 123 (a), the use of low exposure times and gain values did not enable the imaging of the fringes projected on the hemispherical surface. By contrast, when higher exposure times and gain values were used (Figure 123 (b)) it was possible to see the fringes projected on the hemispherical surface but the remaining of the image appeared saturated.

In order to overcome this problem, a setup for high dynamic range imaging with adaptive intensity control has been devised. Then, for the control of each pixel's luminous intensity, we used an LCD as the one we used in our transmissive single-pixel camera (see section 4.1.3), which was connected to the projector that in turn was controlled by the computer. This LCD exhibited a dynamic range of 256 levels, ranging from totally clear to totally blocked. The camera we have used (Guppy F-046C) had a 780×582 pixels resolution and 8 bit color depth. The used lenses had manual zoom and a working distance of 90 mm. As the resolution of the LCD and camera were not the same, neither the size of their pixels was, the system had to be initially calibrated. For this, reference points were displayed on the LCD and an image of them was acquired with the camera. Then, a scale factor was determined for both the vertical and horizontal axes of the image in order to establish a correspondence between the pixels on the LCD and those on the camera's sensor. Given the good optical alignment achieved with the implemented setup, no other aspect had to be compensated during the calibration phase.

A scheme and a photo of the experimental setup that has been implemented can be found in Figure 124 and Figure 125, respectively.

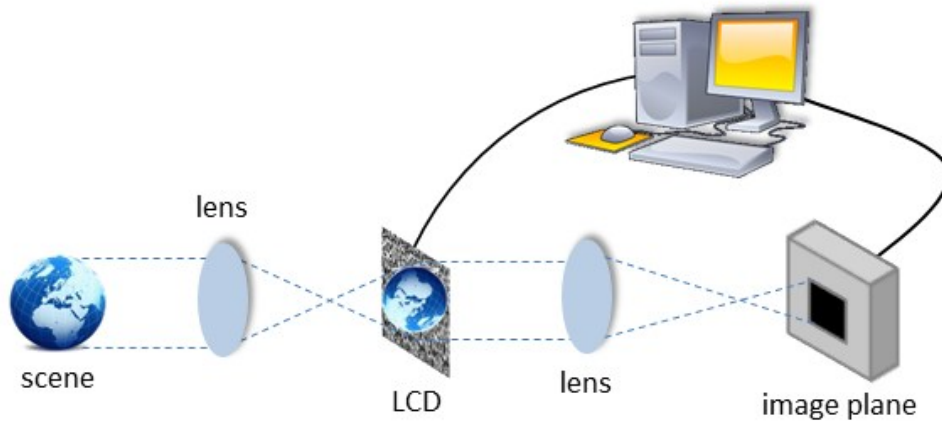


Figure 124 – Scheme of the experimental setup used for high dynamic range imaging with adaptive intensity control.

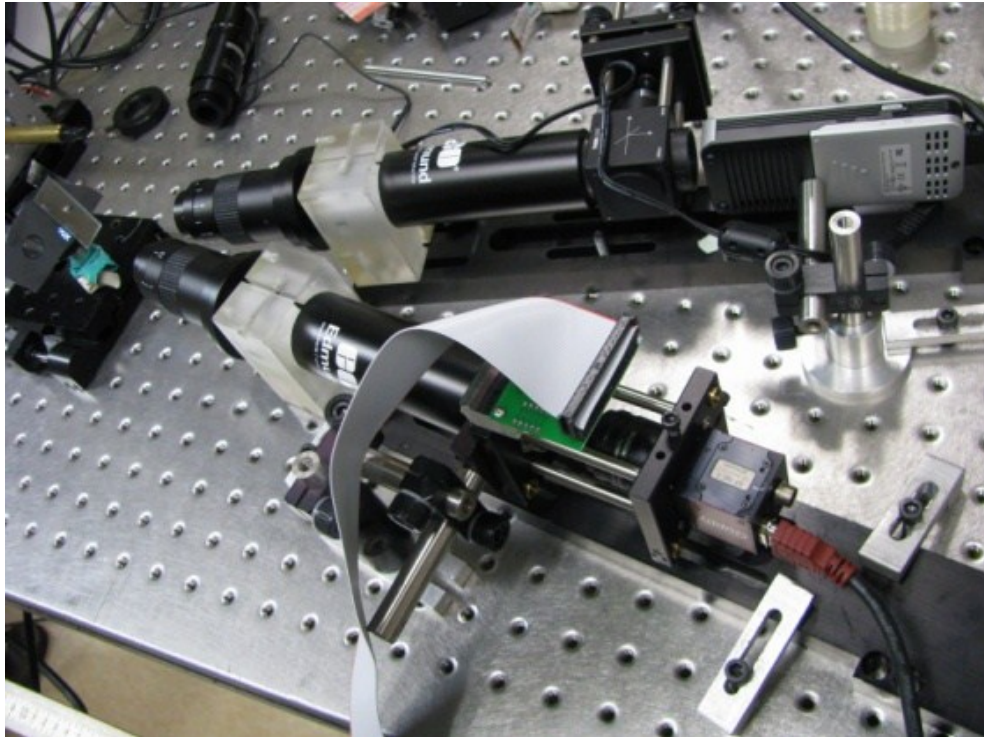


Figure 125 – Photo of the experimental setup used for high dynamic range imaging with adaptive intensity control.

A LabVIEW™ application was developed to control all the acquisition parameters from the camera and perform all the image processing and analysis tasks. Finally, the information obtained was used to create a mask that would be applied to the LCD and that would allow to control the intensity of the different regions in the image.

A flowchart for the developed application can be found in Figure 126.

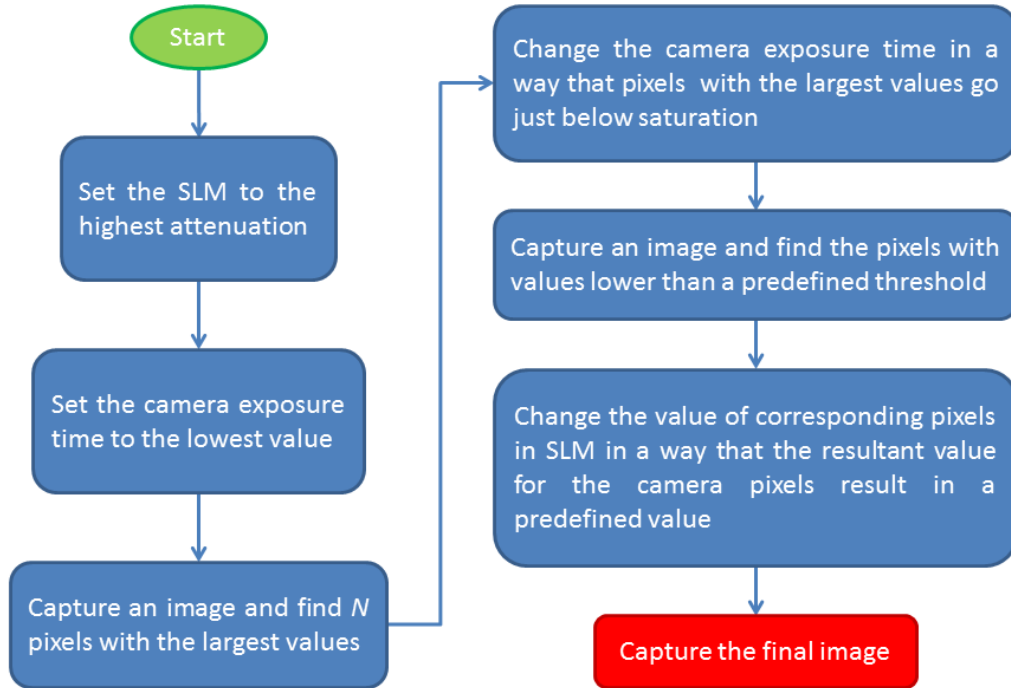


Figure 126 – Flowchart of the application developed for adaptive intensity control.

In the beginning of the application, the mask applied to the LCD induced the maximum possible attenuation to all the pixels and the camera's exposure time was configured to the minimum possible. After, an image was acquired and the N pixels with highest intensity were analyzed. Based on that, the camera's exposure time was adjusted so that the intensity of those N pixels would become close to the saturation level (maximum end of the dynamic range). Next, a new image was acquired and the pixels whose intensity was below a predefined threshold were located. In the end, the corresponding LCD pixels were changed so that the resulting intensity of the respective pixels would become close to a predefined level (minimum end of the dynamic range).

Figure 127 shows some of the results obtained with the previously described system.

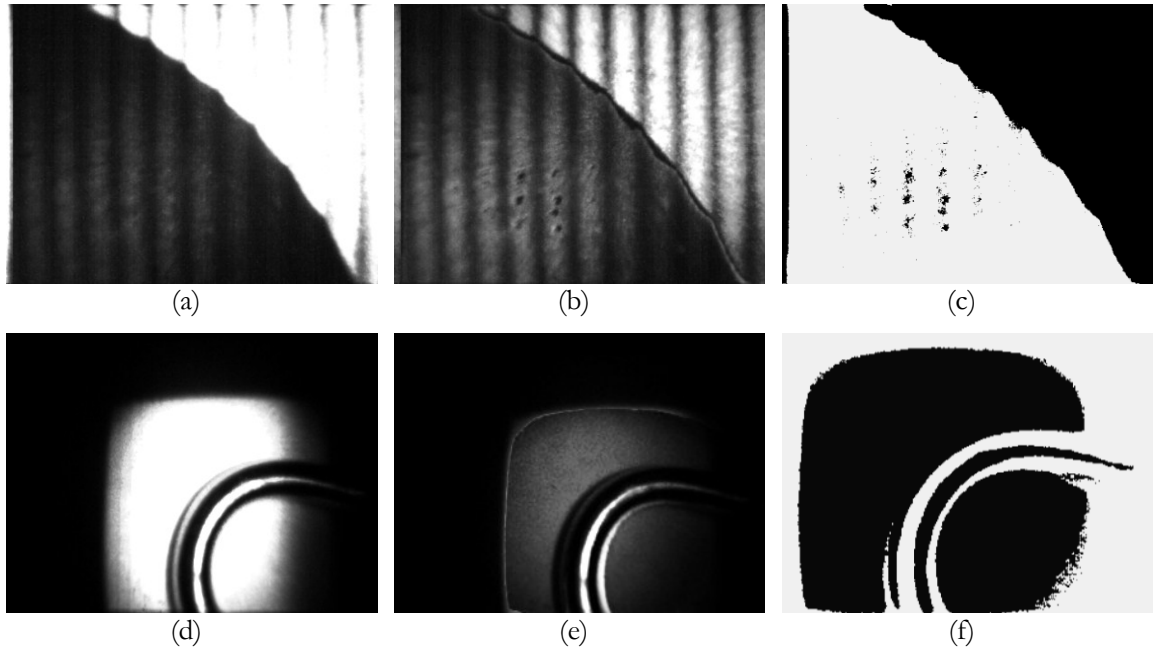


Figure 127 – Results obtained with the adaptive intensity control imaging system for the acquisition of high dynamic range images of a hemispherical surface (top row) and of a metallic and highly reflective object (bottom row): (a) and (d) initial image; (b) and (e) final image; (c) and (f) mask applied to the LCD that provided the acquisition of the final image.

From the analysis of the images in the top row of Figure 127, it can be stated that the final result served its purpose as we can clearly distinguish the fringe pattern where previously was an almost totally saturated region. The same holds true for the results shown in the bottom row of Figure 127, but in this case, due to the limited dynamic range of the LCD, the applied mask was not able to attenuate the intensity of the saturated pixels as much as it would be desirable.

From a general standpoint, it can be concluded that the goal to which we had proposed ourselves has been attained, using an LCD as a spatial light modulator. However, as we can see from the images of Figure 127, an LCD with a higher dynamic range could reveal itself advantageous in situations where the objects present evident reflective properties. It can also be stated that the results obtained strongly depend on the lighting conditions and on the object's shape and material, therefore, reinforcing that there will always be a strong compromise between the values used for the camera's parameters, such as exposure time and gain, for instance, and the final results. Above all, this preliminary approach showed to be effective regarding the control of local intensity during acquisition of images with very contrasting reflectivity profiles.

Following these experiments, the combination of high dynamic range imaging and compressive imaging has been envisioned as it could benefit from the advantages of both imaging modalities, such as increasing the dynamic range of an image and create the image faster and/or in wavelengths where conventional cameras do not work. For example, in fluorescence imaging there

is a demand for HDR cameras suitable for the infrared region of the spectrum [97]. Such cameras are expensive, so high dynamic range compressive imaging (HDRCI) may be a solution for this type of imaging.

Therefore, HDRCI constitutes a computational imaging system capable of controlling its radiometric properties and construct an image with extended dynamic range based on the data obtained with a single detector. As with the other imaging systems previously described in this thesis, the HDRCI system can also operate in active illumination mode or in passive illumination mode, as will be presented after. In order to demonstrate the potential and benefit of using the HDRCI system, a synthetic scene consisting of some black characters on a white and gray background (see Figure 128) was created. On the left half of the scene, the background was represented in a dark gray tone to mimic a shadow or a region with reduced illumination, thus causing that portion of the image to have low contrast. The full scene measured $11 \times 11 \text{ cm}^2$ and the characters exhibited a height of 45 mm with widths ranging from 9 mm (character “I”) to 40 mm (character “C”).



Figure 128 – Synthetic scene created to evaluate the performance of the HDRCI system.

This scene was printed on a standard white paper and a conventional camera has been used to capture images of it (see Figure 129).

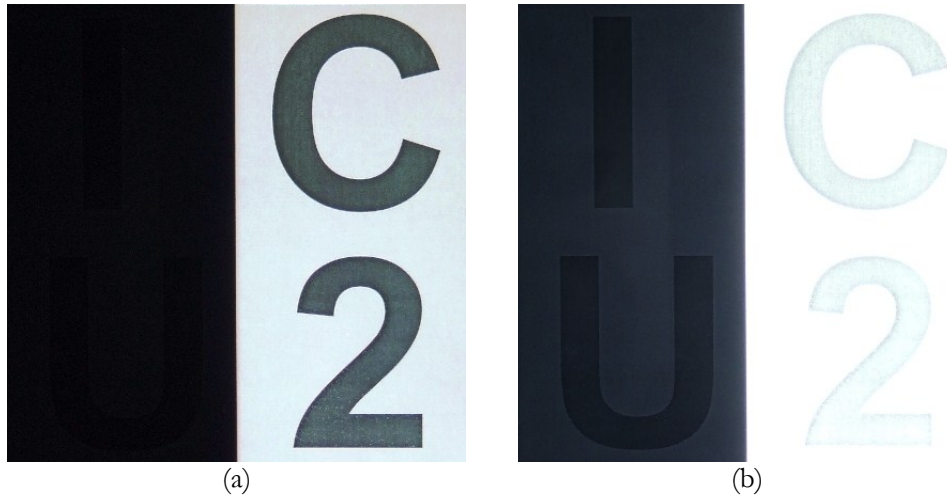


Figure 129 – Photos of the scene depicted in Figure 128, acquired with a conventional camera, using different exposure times: (a) 1/320 s; (b) 1/25 s.

As one can easily conclude from the photos of Figure 129, it is difficult to simultaneously acquire with good contrast both halves of the scene. Therefore, in order to cope with this difficulty, these photos were combined into a high dynamic range image with MATLAB®. The resulting image can be seen in Figure 130. Tone mapping has been used in order to display the high dynamic range image on an 8-bit display (a low dynamic range display).



Figure 130 – 128×128 pixels high dynamic range image resulting from the combination of the photos from Figure 129 captured with different exposure times.

It is clear from Figure 130 that the content in the left half of the image is now clearly perceptible and the right half of the image is not saturated. The following sub-sections will explain how compressive imaging systems can be used to obtain similar results, either with active illumination, or with passive illumination.

4.5.1 Active illumination high dynamic range compressive imaging system

As it has been described and analyzed before in this thesis, the light used to illuminate a scene may contain random codes used to compress the spatial information and enable the reconstruction of images based on the data acquired with a single light detector. Here, the potential of that active illumination will be extended to enable the reconstruction of high dynamic range images.

It has also been previously reported [86-92] that a common technique for HDR imaging is to combine a series of images acquired with different exposure times. In the context here presented, changing exposure time in compressive imaging has different meaning from what it does in conventional imaging. Therefore, in compressive imaging, exposure time cannot be changed as in conventional imaging and a parameter equivalent to exposure time has to be defined. Equivalent exposure time can be defined as a combination of masking some regions/pixels and changing the radiance, the integration time of the single detector (e.g. photodiode) or the gain of the amplification circuit. In other words, for changing the equivalent exposure time, some pixels are blocked/unblocked and the second parameter, which is radiance from object, integration time of detector, and/or gain of amplification circuit, is increased/decreased.

The basic concept of this high dynamic range compressive imaging technique is depicted in the flowchart of Figure 131. First, an image is acquired using standard compressive imaging, then regions/pixels with relatively high intensity are identified and a corresponding mask is created. Those regions/pixels are the ones that most likely will be saturated when the equivalent exposure time is increased and as a result no relevant information can be extracted from them. The threshold used to select which regions/pixels are blocked can be defined from the histogram or some other statistics of the reconstructed image. All the codes for acquiring the next image, via compressive imaging technique, are multiplied by the mask in order to block regions/pixels with high intensity. Since the mask used in this technique is binary and the compressive codes are binary too, the result of their combination will also be binary. This procedure is finished when the maximum number of iterations is reached. This means, for instance, that the equivalent exposure time cannot be further adjusted, that a sufficient number of images has been acquired or that another criterion has been met. In this description, the terms regions and pixels have been distinguished because one might want to operate either at the pixel level or at the region level (group of pixels), depending on the problem at hands.

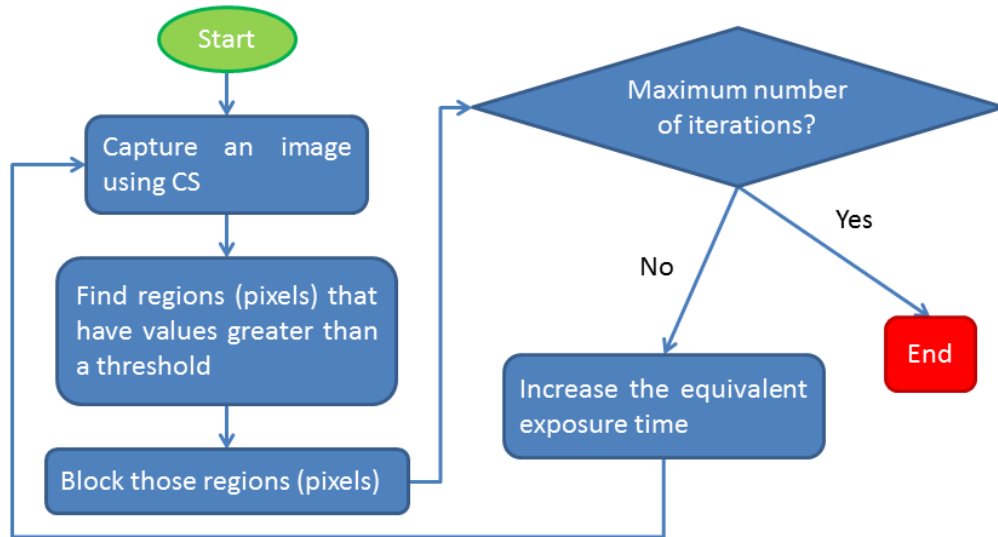


Figure 131 – Flowchart describing the procedure for HDRCI by means of acquiring images with different equivalent exposure times.

The setup that has been used for these experiments is the same that has been used for the definition and characterization of the active illumination single-pixel monochrome imaging system (see Figure 51 and Figure 52). The software has only been changed in order to incorporate the mask into the projected codes. In Figure 132 a photo of the active illumination HDRCI system under operation can be seen.

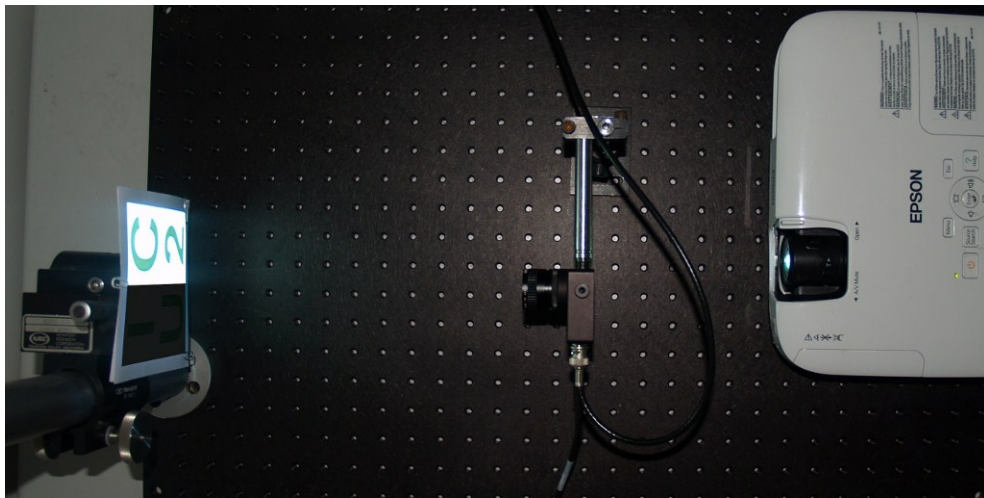


Figure 132 – Photo of the active illumination HDRCI system under operation.

For the acquisition of the first image, the gain of the amplified photodiode circuit was set to 50 dB so that when a white image was projected on the scene, the voltage output would become as close as possible to the maximum output voltage (10 V) without saturating. This was important to attain the largest possible dynamic range for the measurements and consequently be able to distinguish from noise the small variations of the voltage output caused by the compressive codes.

Then, all the binary compressive codes were projected and the respective measurements were performed. The image resulting from this process is presented in Figure 133 and can be understood as the equivalent of acquiring an image with a conventional camera using a low exposure time.

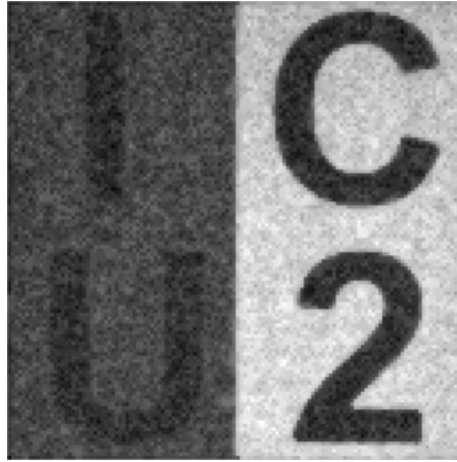


Figure 133 – 128×128 pixels image initially obtained with low equivalent exposure time and without mask, using the active illumination HDRCI system.

Next, the right half of the image has been identified as the region that most likely would become saturated when the equivalent exposure time would be increased and, therefore, it was defined a black mask for that region. After, a half-white half-black image has been projected on the scene, with the black half corresponding to the right half of the scene, and the gain of the amplified photodiode circuit has been adjusted in order to place again the output voltage as close as possible to the maximum value without saturating. The gain value that has been found to accomplish this was 70 dB. Finally, all the measurements relative to the compressive codes including the mask were conducted and the image of Figure 134 was reconstructed. This image can be seen as the equivalent of acquiring an image with a conventional camera using a longer exposure time, disregarding the information contained in the overexposed region (right half).

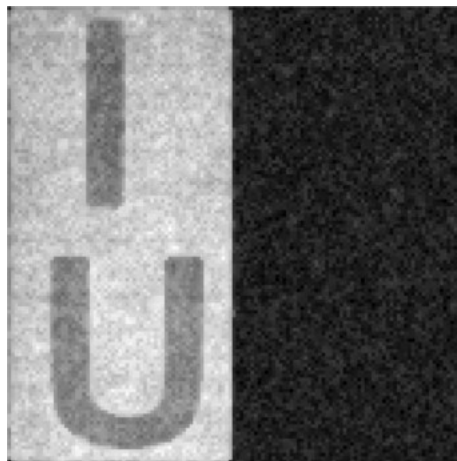


Figure 134 – 128×128 pixels image obtained with equivalent long exposure time and with a mask totally blocking the right half part, using the active illumination HDRCI system.

The results presented in Figure 133 and Figure 134 have been filtered with the selective local median filter (see Figure 80) in order to remove spurious noisy points that could arise from the reconstruction process and from noise in the measurements.

In the end, the two images obtained with different equivalent exposure times were combined into a high dynamic range image with MATLAB® and were tone-mapped into 8 bits for display. The resulting high dynamic range image is presented in Figure 135. The PSNR and normalized cross-correlation metrics were used to quantify the similarity of this image with that resulting from the combination of the two images acquired with a conventional camera using different exposure times (see Figure 130) and the obtained values were 10.73 dB and 0.46, respectively.

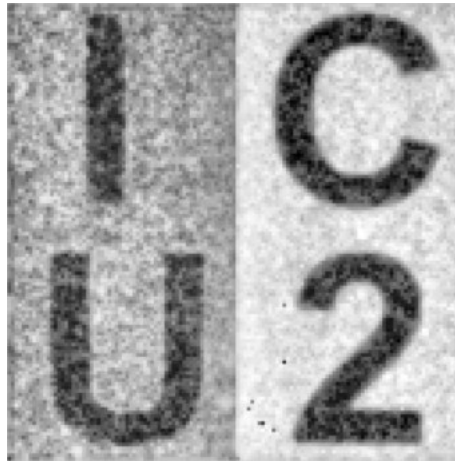


Figure 135 – 128×128 pixels high dynamic range image resulting from the combination of the images acquired with different equivalent exposure times of Figure 133 and Figure 134. Tone mapping has been used to display the image with 8 bits.

From the result of Figure 135, it can be said that it was possible to increase the pixel values of the regions with very low reflectance without compromising the quality of the image corresponding to bright regions, hence increasing the dynamic range of the imaging system.

As stated before [93-95], another technique that is commonly used in HDRI adaptively controls the scene radiance for each region/pixel. Then, the information relative to the radiance of each pixel is combined with the acquired images in order to produce HDR images. Here, we have again used the projected light to compress the spatial information but it has also been used to control the radiance or intensity of the scene.

The flowchart describing the algorithm implemented for this HDRCI technique is depicted in Figure 136.

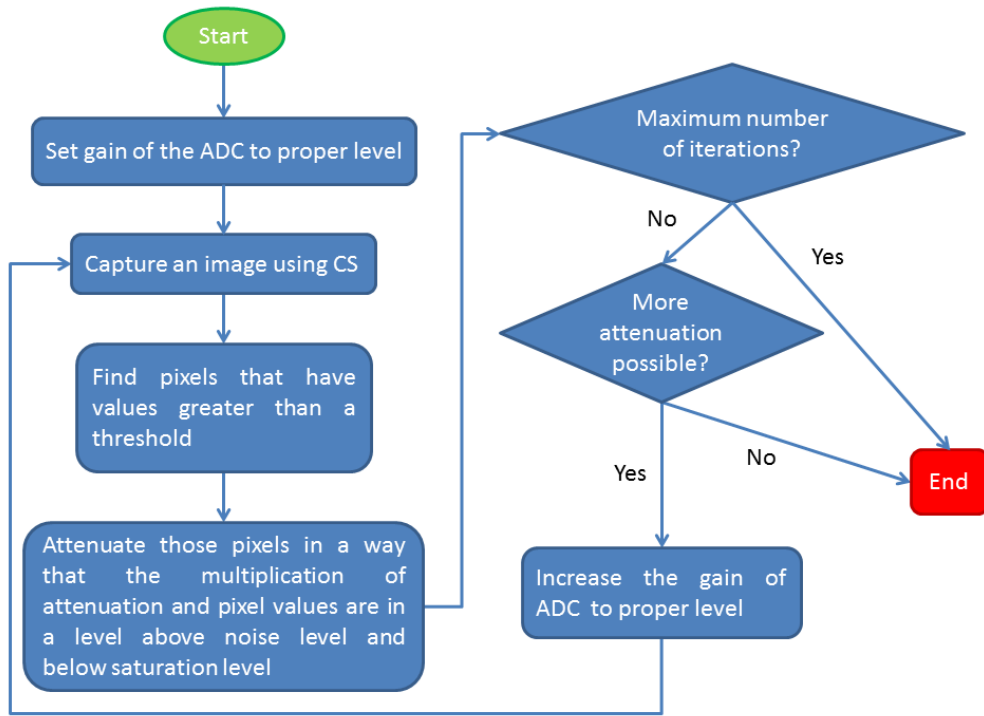


Figure 136 – Flowchart of the algorithm implemented for HDRCI by means of intensity control.

First, we select a proper level for the ADC gain. The proper level at this step can, again, be defined as the level at which the output voltage becomes as close as possible to the maximum of the voltage range, without saturating, when a white image is being projected on the scene. Second, an image is constructed by the use of the compressive imaging technique. Pixels that have values greater than a threshold are identified and, again, this threshold value can be defined on the basis of the histogram of the reconstructed image or some other statistics of the reconstructed image. Next, the identified pixels with values greater than the threshold are attenuated in such a way that their values reach above the noise level and far below saturation. This level depends on the number of steps the algorithm will iterate and the amount of increase in the ADC gain. For example, suppose that the number of iterations for the algorithm is two and that each pixel of the attenuator has 8 bits. Therefore, on average, for each iteration 4 bits can be used, giving an attenuation factor of 16 (2^4). Hence, a pixel with maximum intensity (or a saturated pixel) can be reduced by a factor of 16 relative to the highest possible level (saturation level). The level of ADC gain shall be determined accordingly, based on the percentage of attenuation for the whole image. For instance, if the average attenuation of image intensity is 80% (for an attenuation factor of $1/\left(1 - \frac{80}{100}\right) = 5$), then the gain of ADC will be increased by a factor of 5. As the ADC gain changes, the noise level will also change, thereby affecting the noise level of quantized samples, unless the dominant noise of quantized samples is the noise of the ADC for all gain levels; therefore, increasing the ADC gain would not change the noise level significantly. This is an acceptable assumption for the

implemented system. The average responsivity of the photodiode is approximately 0.5 A/W, and the bandwidth of the system varies with the selected gain. The following table presents the noise equivalent power of the photodiode and the maximum noise current for 50 dB and 60 dB gains, which were the minimum and maximum gain values used during these experiments.

Table 28 – Noise equivalent power and maximum noise current for the PDA100A amplified photodiode when the gain of 50 dB or 60 dB was chosen.

Gain	Bandwidth	Noise equivalent power	Maximum noise current
50 dB	20 kHz	$3.0 \times 10^{-12} \text{ W}/\sqrt{\text{Hz}}$	$3.0 \times 10^{-12} \times \sqrt{20 \times 10^3} \times 0.5 = 21.21 \times 10^{-11} \text{ A}$
60 dB	6 kHz	$2.2 \times 10^{-12} \text{ W}/\sqrt{\text{Hz}}$	$2.2 \times 10^{-12} \times \sqrt{6 \times 10^3} \times 0.5 = 8.52 \times 10^{-11} \text{ A}$

The corresponding gain factors are $2.38 \times 10^5 \text{ V/A}$ and $0.75 \times 10^6 \text{ V/A}$, which result in noise voltages of 50.48 μV and 63.90 μV , for a gain of 50 dB and 60 dB, respectively. Since the sensitivity of the ADC (National Instruments™ PCI-6221 DAQ board) is 97.6 μV at maximum voltage range, it can be said that the dominant noise is ADC noise at all gain levels.

Next, the results obtained with this HDRCI technique are presented. As expected, the image acquired initially using standard compressive imaging was equal to that of Figure 133 and the image reconstructed after applying an attenuation mask to the projected compressive codes is shown in Figure 137 (a) along with the used mask (see Figure 137 (b)).

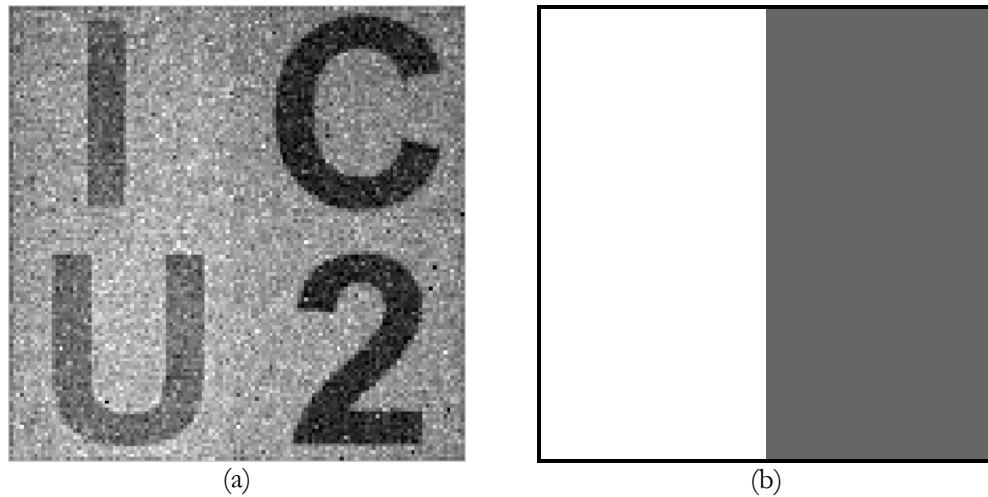


Figure 137 – (a) 128×128 pixels image reconstructed with the active illumination HDRCI system when the mask displayed in (b) was used. The mask reduced 60% the radiance of the right half of scene.

In order to obtain the HDR image, the image in Figure 137 (a) has been divided, pixel by pixel, by the mask displayed in Figure 137 (b). Tone mapping has been used to display the HDR image with 8 bits (see Figure 138).

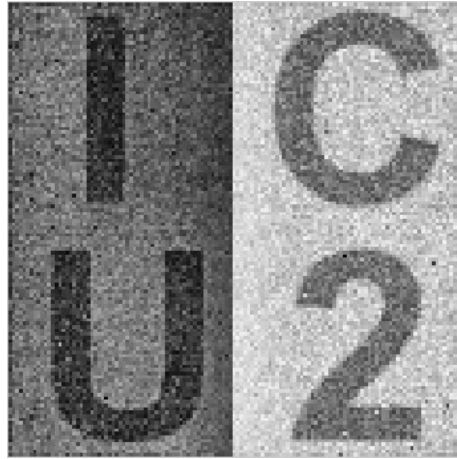


Figure 138 – 128×128 pixels high dynamic range image resulting from the division of the image in Figure 137 (a) by the mask displayed in Figure 137 (b). Tone mapping has been used to display the image with 8 bits.

Once again the metrics were used to quantify the quality of the reconstructed images and the PSNR and the maximum of the normalized cross-correlation obtained for the image of Figure 138 relatively to the image of Figure 130 were, respectively, 13.63 dB and 0.81. These values support the opinion derived from human visual assessment that the image of Figure 138 has better quality than the image of Figure 135.

In this active illumination setup, the increase in dynamic range of the image is limited by the dynamic range of the projector. Figure 139 shows the intensity range of the projector as it projects a series of grayscale images ranging from darkest (an image with pixel values of 0) to brightest (image with pixel values of 255). For each gray level, 10000 samples were acquired and averaged to define the corresponding intensity. The dynamic range of the projector is ~ 134.32 , which is ~ 21.28 dB. So theoretically, using this setup, the dynamic range of an image can be enhanced by as much as 21.28 dB.

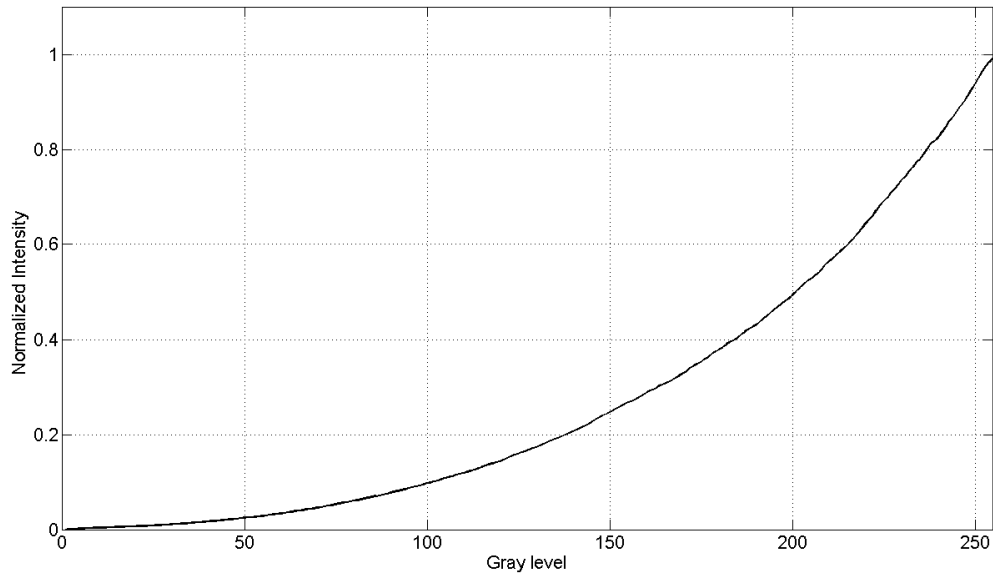


Figure 139 – Normalized intensity measured by the photodiode as a function of the gray level $[0, 255]$ of the image projected with the Epson® video projector.

4.5.2 Passive illumination high dynamic range compressive imaging system

Here, the HDRCI techniques that were applied in the previous section will be exploited in a passive illumination configuration. For these experiments, the scene was being illuminated by the projector with a white image and the LightCommander was collecting the light from the scene and forming an image of it on the DMD. There, the compressive codes for spatial compression and the attenuation masks were applied to the incoming light field resulting in incoherent projections that were captured by the photodiode. The corresponding output voltages were then acquired by the computer by means of the ADC and gathered to enable the subsequent reconstruction of the respective image. In Figure 140 it can be seen a scheme of the implemented setup.

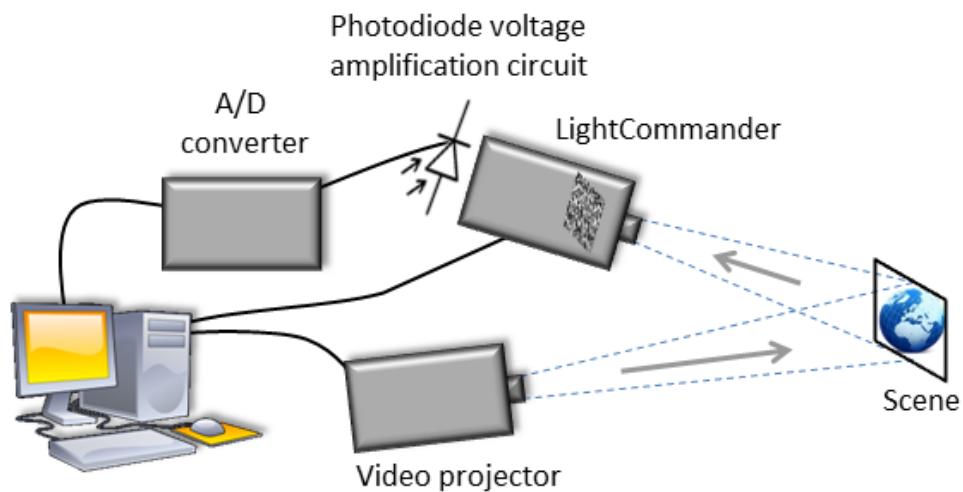


Figure 140 – Scheme of the passive illumination HDRCI system.

In Figure 141 a photo with a top view of the setup used for passive illumination HDRCI can be seen. It is possible to observe the scene being illuminated with a white image projected by the Epson® video projector and the LightCommander. In Figure 142, it is presented another photo of this setup from another angle, from which it is visible the amplified photodiode mounted in front of the LightCommander light tunnel.

This setup has also been used to acquire high dynamic range images of the synthetic scene depicted in Figure 128. Similarly to what has been previously reported for other compressive imaging systems, during these experiments the sampling frequency was 250 kSamples/s and 10000 samples were averaged for each measurement.

Initially, the technique of combining images acquired with different exposure times into a single HDR image has been used. For that, the scene was illuminated by the video projector with a white image and the gain of the amplified photodiode circuit was set to 50 dB because that was the gain that would cause the output voltage to become as close as possible to maximum value (10 V), without saturating. Then, an image has been acquired and the result is shown in Figure 143.



Figure 141 – Top view photo of the passive illumination HDRCI system.

The image in Figure 143 can be seen as the equivalent of acquiring an image with a conventional camera using a low exposure time. Consequently, the right half of the scene has been identified as the one that would likely become saturated when the equivalent exposure time would be increased and it was decided that a black mask should be applied to that region. Then, a half-white half-black image was projected on the scene and the gain of the amplified photodiode circuit was adequately adjusted in order to increase the equivalent exposure time. The new gain value has then been set to 60 dB. Finally, the black mask was included in the codes and all the measurements were performed. The resulting image is displayed in Figure 144 and can be interpreted as the equivalent of acquiring an image with a conventional camera using a longer exposure time, disregarding the information contained in the overexposed region (right half).

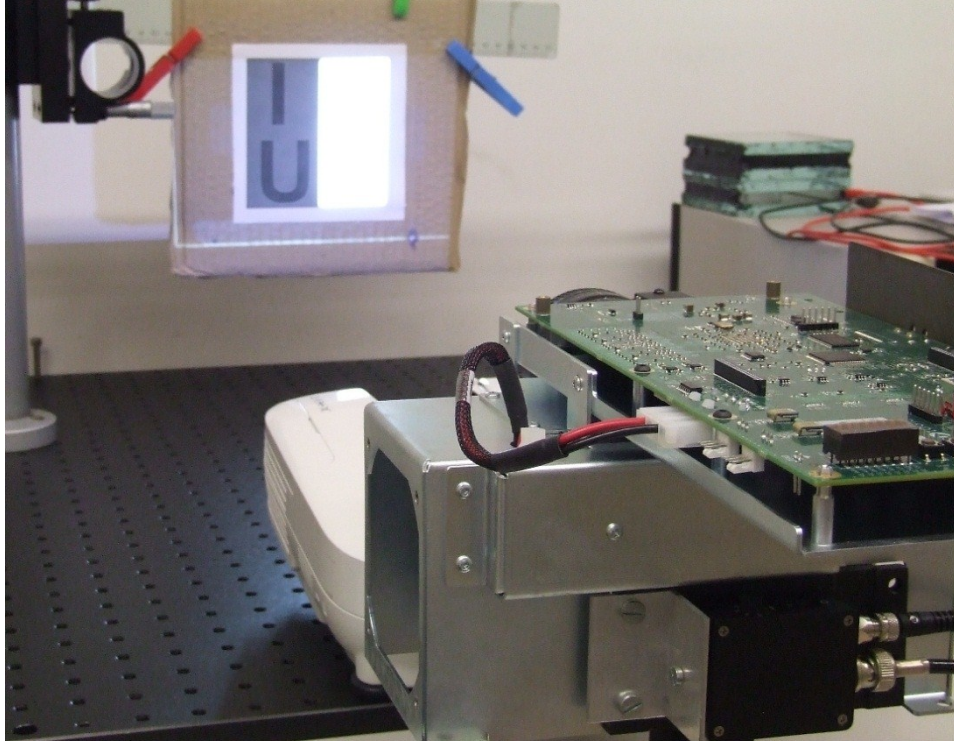


Figure 142 – General view of the passive illumination HDRCI system during operation. Next to the lower right corner of the photo, it is possible to see the amplified photodiode mounted in front of the LightCommander light tunnel.



Figure 143 – 128×128 pixels image initially obtained with low equivalent exposure time and without mask, using the passive illumination HDRCI system.

The images in Figure 143 and Figure 144 were filtered with the selective local median filter to remove spurious noisy points. These two images were combined into a HDR image and the result of that combination is presented in Figure 145. Tone mapping has been used to display this image with 8 bits. From the analysis of that image one can state that it yields good contrast all over its representation, therefore leading to the conclusion that the system was able to effectively extend the dynamic range of the acquired image. The results of the quality assessment obtained with the PSNR and normalized cross-correlation for the image of Figure 145 relatively to the image of Figure 130, were 10.13 dB and 0.39, respectively.

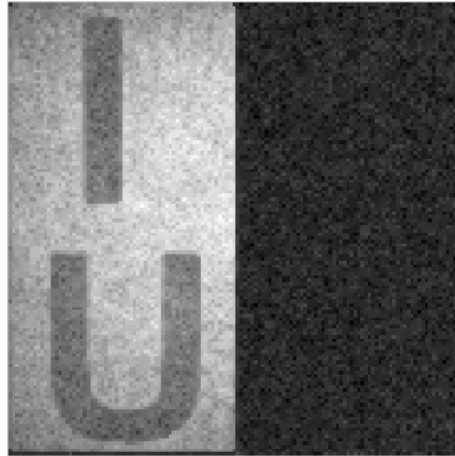


Figure 144 – 128×128 pixels image obtained with long equivalent exposure time and with a mask totally blocking the right half part, using the passive illumination HDRCI system.



Figure 145 – 128×128 pixels high dynamic range image resulting from the combination of the images acquired with different equivalent exposure times of Figure 143 and Figure 144. Tone mapping has been used to display the image with 8 bits.

Following these experiments, we pursued the acquisition of HDR images with the passive illumination compressive imaging system by means of intensity control. In a similar manner to that employed with the active illumination HDRCI system, an attenuation mask has been defined to the brighter part of the image in order to improve the contrast in its darker part. The image initially acquired without any attenuation mask was the same as that of Figure 143. Then, a mask capable of reducing the radiance of the right half of the scene by 50% has been multiplied by the compressive codes and the resulting image is displayed in Figure 146 (a). This amount of attenuation has been chosen because it was the one found to be capable of providing a reconstructed image with an almost uniform background both in the darker region and in the brighter region, thus indicating how much the radiance level varied from one region to the other.

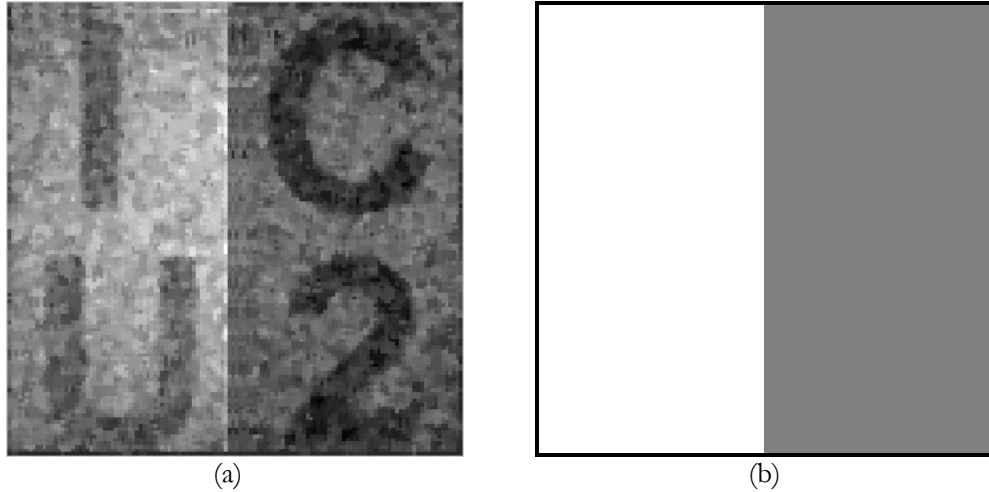


Figure 146 – (a) 128×128 pixels image reconstructed with the passive illumination HDRCI system when the mask displayed in (b) was used. The mask reduced 50% the radiance of the right half of scene.

The image in Figure 146 (a) has been divided by the mask in Figure 146 (b), in order to produce a HDR image (see Figure 147). Calculating the PSNR and the maximum of the normalized cross-correlation of the image of Figure 147 relatively to the image of Figure 130 the obtained values were 11.2 dB and 0.59, respectively. Comparing these results to those obtained for the image of Figure 145, one could be lead to conclude that the quality of the image of Figure 147 was better, what would be contrary to the opinion held by human observers.

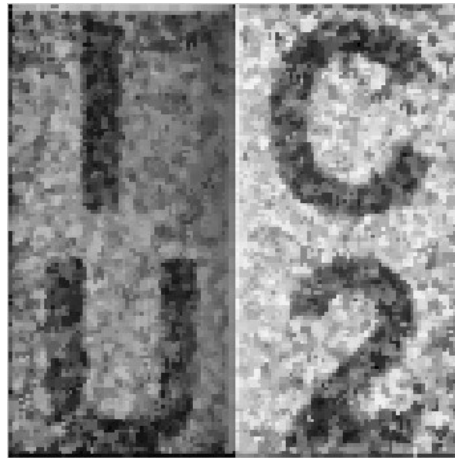


Figure 147 – 128×128 pixels high dynamic range image resulting from the division of the image in Figure 146 (a) by the mask displayed in Figure 146 (b). Tone mapping has been used to display the image with 8 bits.

If the active and passive illumination HDRCI systems are compared for the case where HDR images resulted from the combination of images acquired with different equivalent exposure times, it can be stated that both performed well, although the passive illumination system seemed to be the one which have yielded less noisy images. Even though this conclusion is true based on the

evaluation performed by human observers, it was not confirmed by the values obtained with the metrics. This can be due to the fact that the output voltage generated by the amplified photodiode circuit for the light coming from the DMD does not exhibit any ripple, opposed to that verified when the LCD of the video projector are used as spatial light modulators (see Figure 55). Despite this fact, that ripple did not compromise the results obtained with the active illumination HDRCI system because the output voltage exhibited a good dynamic range (up to 10 V) and the averaging of the collected samples minimized its effect.

Perhaps surprisingly, the performance of the passive illumination HDRCI system for the case where HDR images were obtained by means of intensity control was not that satisfactory and it was considerably worse when compared to that of the active illumination HDRCI system. This has been investigated and it is believed that it greatly depends on the fact that light intensities from the DMD are produced by pulse width modulating the mirrors, thus causing the perceived gray scale to be proportional to the percentage of time the mirror is “ON”. The human visual system effectively integrates the pulsed light to create the perception of the desired intensity [98]. For the sake of clarification, let's consider the diagrams in Figure 148. In the binary PWM pixel representation in Figure 148, a pixel's LSB consumes $1/(2^n-1)$ of the total refresh period, where n is the number of bits used to define the several intensities. The LSB+1 bit consumes double the LSB time. This pattern continues for all the bits of the given pixel. In practice, the LightCommander uses 8 bits and if the refresh rate is set to 60 Hz, which is the maximum accepted value, the bit times are as follows:

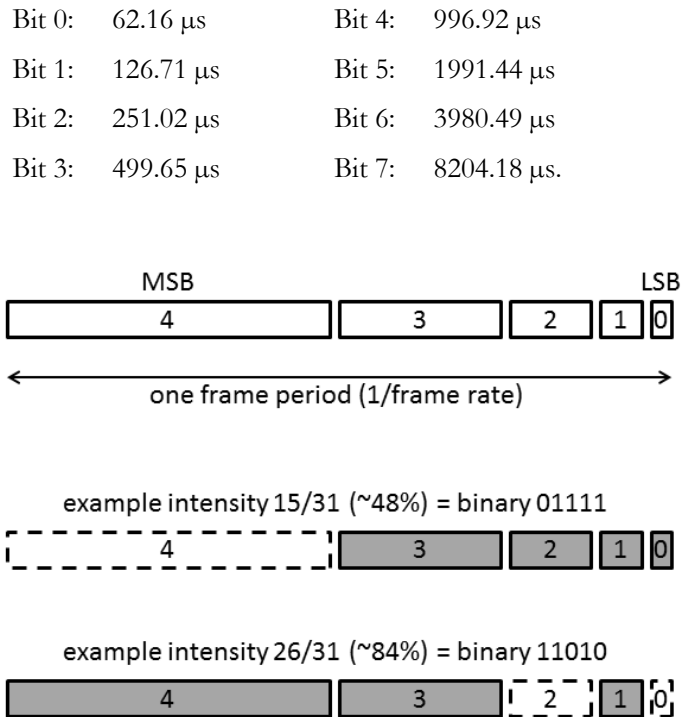


Figure 148 – Binary PWM sequence pattern with two examples of how intensity values are generated with 5 bits.

To confirm this, light was launched into the LightCommander's tunnel and the DMD mirrors were all set to represent different gray levels. The modulated light was then projected by the LightCommander and was measured by the amplified photodiode circuit. The plots of the measured signals are presented in Figure 149 for different gray levels. These signals were acquired using a sampling frequency of 250 kSamples/s.

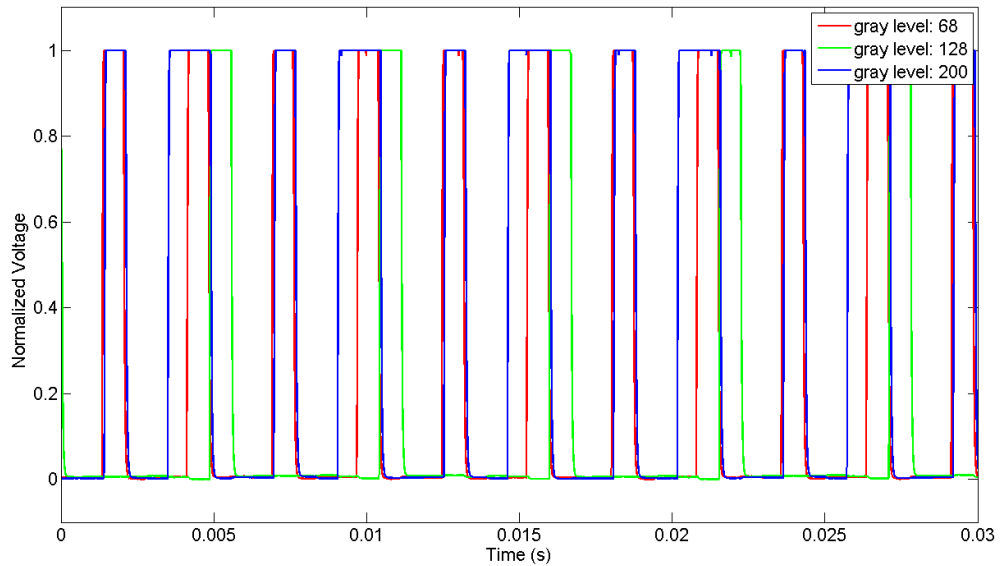


Figure 149 – Plots of the measured PWM signals when different gray levels were being assigned to the DMD pixels.

As it can be seen in the plots of Figure 149, the time patterns exhibited by the modulated light directly depend on the gray level assigned to the DMD pixels, thus corroborating the explanation given with the support of the diagrams in Figure 148. Additionally, PWM methods can result in the display of visual artifacts that the viewer can perceive (as we were told by the Texas Instruments technical staff) and, therefore, there was the need to develop techniques to mitigate these effects. For that, in the case of the LightCommander, each bit segment is divided and shown at multiple occasions, still ensuring the sum of all sub-segments equals to the whole allocated bit-time.

In this imaging setup, the increase in dynamic range of the image is limited by the dynamic range of the DMD. The same procedure which has been followed for the active illumination system with the Epson® projector (see Figure 139), was used to quantify the intensity range of the passive illumination system with the DMD and the results are shown in Figure 150. Despite exhibiting a dynamic range of ≈ 472.94 , which is ≈ 26.75 dB and 5.47 dB higher than in the passive illumination homologous case, the average intensity of the light output varies in an irregular fashion with the change of the gray level set on the DMD. Again, this is justified by the PWM used for the definition of the different gray levels.

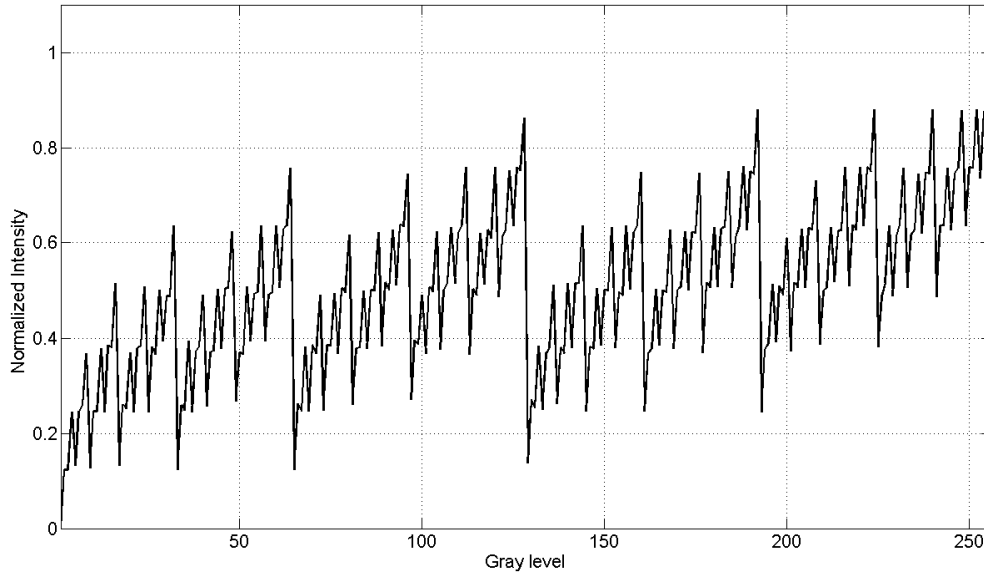


Figure 150 – Normalized intensity measured by the photodiode as a function of the gray level $[0, 255]$ of the image projected with the LightCommander.

Observing the plot of Figure 150 it is possible to emphasize the existence of a pattern-like structure occurring every 8 peaks, being the only difference the offset which seems to be increasing. This repeatability may be another indication of the effect of the PWM employed to define the 256 gray levels using 8 bits.

However, as expected, the gray levels corresponding to black (0) and white (255) correspond to the minimum and maximum output on the photodiode amplification circuit, respectively. This happens because for these extreme values all the mirrors are either off or on, therefore producing a flat output signal.

4.5.3 Concluding remarks

The content presented in these sections dealt with a problem that is in the basis of the need for high dynamic range imaging techniques. In other words, when one is in face of a scene with a broad range of intensities, usually, it is required to employ techniques for the extension of the dynamic range of the acquired images in order to encompass the brightest and darkest areas there existing, which is not possible using standard digital imaging or photographic techniques.

In particular, the principal goal was to conceive and demonstrate HDRI systems which could also benefit from compressive imaging techniques. For that, initially, a preliminary imaging system that used an LCD as a spatial light modulator, to adaptively control the intensity of a scene, and changed the exposure time of the camera in an adequate manner was described. Although the results obtained were useful to demonstrate its potential, they also served to draw the attention to some of its limitations, such as the dependence on the dynamic range of the SLM and on the

lighting conditions, for instance. Despite this, it constituted a solid starting point to the development of high dynamic range compressive imaging systems.

In that aim, two techniques have been explored: one which combines images acquired with different exposure values and another which controls the radiance of the scene being acquired. These techniques have been indifferently employed in both active and passive illumination configurations and, among all the combinations, the implementation of the technique for radiance control with the active illumination system was the one that yielded best overall results. This was supported both by the results obtained with the metrics and by the opinion of human observers. Regarding the technique that combines images acquired with different exposures into a HDR image, based on human opinion, it can be said that the passive illumination system was the one that produced best results, although the results obtained with the active illumination system were also satisfactory and the results of the metrics were better for this system.

The PWM applied to the DMD to produce different gray levels strongly compromised the performance of the passive illumination system when it was being used to control the radiance of the scene. Maybe, an interesting solution would be to modify the binary random compressive codes so that the density of white pixels and black pixels in the codes would be higher, respectively, in the regions that appear darker and brighter in the reconstructed images. With that change of density in the black and white pixels the randomness of the codes would be reduced and could eventually limit the reconstruction of the images. Consequently, this solution could only be used as long as the modified codes could guarantee the reconstruction of the images.

One common advantage to all the HDRCI systems here demonstrated is that there is no need for geometrical calibration since they require a detector with a single pixel. Depending on the scenarios where these systems can be used, it may be necessary to develop automatic procedures to define the pixels/regions to which the high dynamic range compressive imaging techniques are applied.

4.6 CMOS Based Compressive Imaging Sensor

In this section, an algorithm that was implemented for the generation of compressive codes to be used within a CMOS based imaging sensor will be presented. The development of this imaging sensor lies outside of the scope of the present work, but the algorithm here presented can be seen as an additional functionality.

4.6.1 Overall architecture and operation

This imaging sensor is based on a Single Instruction Multiple Data (SIMD) analog processor (see Figure 151). Each pixel has a photosensor, a set of analog memories and a multiplier. The

operations are done in parallel in all pixels. Each photosensor converts the light intensity into a current and its value is stored in an analog memory.

The write line (WL) and read line (RL) control if a pixel is written or read, respectively: if both vertical WL (WLV) and horizontal WL (WLH) are active, the corresponding pixel is written; the same logic happens for RL. The value to be written or read is sent to/from a bus that is connected to all pixels. The boundary line (BL) breaks the connection between pixels: the vertical BL breaks the vertical connections and the horizontal BL breaks the horizontal connections. This way, operations defined by WL and RL can be done in sections defined by BL. For instance, if BL is defined to connect adjacent horizontal pixels two-by-two ($BLV = [1\ 1\ 1\ 1\ \dots]$ and $BLH = [1\ 0\ 1\ 0\ 1\ 0\ \dots]$), the WL and RL can be set to patterns $WLH = [0\ 1\ 0\ 1\ \dots]$ and $RLH = [1\ 0\ 1\ 0\ \dots]$ to copy each left column to the right column within each section.

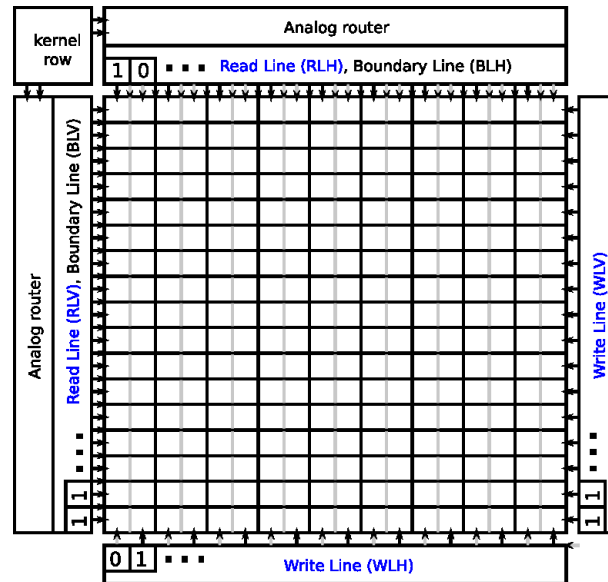


Figure 151 – Architecture of the CMOS based imaging sensor.

Using the aforementioned lines, it is possible to implement operations such as upsizing and downsizing of images. The upsizing and downsizing are performed in one dimension at a time. Initially, the horizontal dimension is collapsed or expanded by transferring each column at a time. Then, the vertical dimension is collapsed or expanded by transferring each row in the same manner. Convolution is another operation exhibited by the imaging sensor and it makes use of the multiplier in each pixel. The coefficients of each kernel row are provided by the Kernel Row component and redirected by the Analog Router component to the pixels. The Kernel Row can supply up to 32 coefficients and the Analog Router repeats the kernel sequence throughout the pixel array. By setting WL, RL and BL in a proper sequence, convolutions can be performed with an order of complexity $O(n^2)$, where n is the width of the kernel. After, the values to be transmitted off-chip are stored in the analog memories of each pixel. RL can control the pixels that are read and the

current from each pixel that is being read is added to a global bus (by Kirchhoff's Current Law) and read externally. The main specifications of the imaging sensor integrated circuit (IC) are as follows:

- $51 \times 51 \mu\text{m}^2$ pixel size;
- 38×38 pixels;
- $3.3 \times 3.3 \text{ mm}^2$;
- Austria Microsystems 0.35 μm OPTO technology,

and it is expected the following performance:

- $60 \mu\text{W}$ / pixel @ 3.3V;
- + 500 fps @ 1 MHz – operating as a conventional imaging sensor;
- 2.88 GOPS (Giga-Operations Per Second);
- Power efficiency: 28.88 GOPS/W;
- Area efficiency: 265 MOPS/ mm^2 .

Figure 152 contains the layout of the IC for the CMOS based imaging sensor.

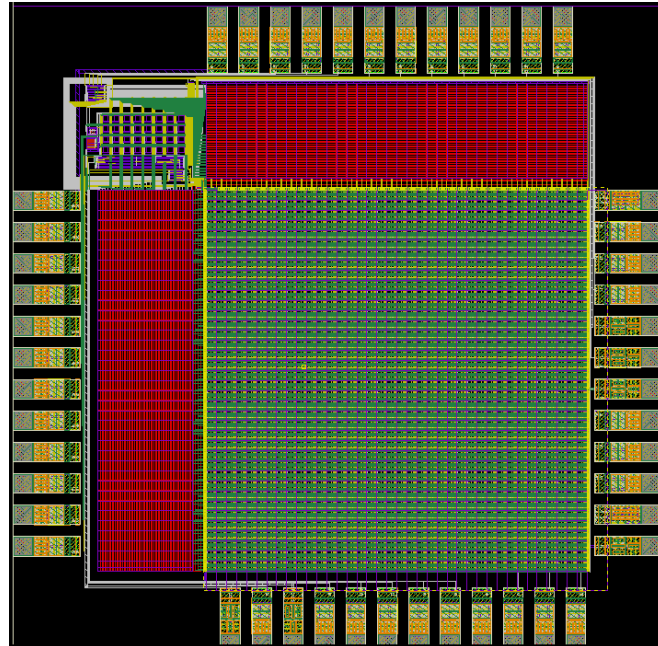


Figure 152 – Layout of the integrated circuit of the imaging sensor.

4.6.2 Compressive sensing based mode of operation

The proposed architecture and main functionalities of the imaging sensor were explored in order to implement a process for the generation of compressive codes that could be used to provide measurements towards compression and reconstruction of images. So, the idea was to randomly initialize the read lines (RL) with two arrays that would define which pixels would be read or not. The intent of this random selection of pixels was to produce the same result as that depicted in

Figure 46, i.e., do the dot-product of a binary random matrix by the values of the pixels in the sensor. The next steps consist in summing the current of all the selected pixels and register the result as the measurement corresponding to that code. In the end of each step, the RL arrays are circularly shifted to produce another compressive code for the next measurement. This process is repeated until the desired number of measurements, defined by the chosen amount of compression, is achieved. The shifts of the RL arrays are not executed simultaneously, otherwise one would not be able to produce as many codes as those required to acquire an image without compression. To better illustrate this description, the following example is presented, assuming that the sensor has 4×4 pixels, for the sake of simplicity.

If one considers the following arrays for the initial state of the vertical and horizontal read lines, respectively:

$$RLV = \begin{bmatrix} 1 \\ 1 \\ 0 \\ 1 \end{bmatrix} \qquad RLH = [1 \quad 0 \quad 1 \quad 0]$$

the result of their multiplication becomes:

$$RLV \times RLH = \begin{bmatrix} 1 & 0 & 1 & 0 \\ 1 & 0 & 1 & 0 \\ 0 & 0 & 0 & 0 \\ 1 & 0 & 1 & 0 \end{bmatrix}.$$

Then, if the horizontal read line array (RLH) is circularly shifted it assumes the following representation:

$$RLH = [0 \quad 1 \quad 0 \quad 1]$$

and the following result is obtained for the multiplication of the two random arrays. This result represents the new and succeeding compressive code.

$$RLV \times RLH = \begin{bmatrix} 0 & 1 & 0 & 1 \\ 0 & 1 & 0 & 1 \\ 0 & 0 & 0 & 0 \\ 0 & 1 & 0 & 1 \end{bmatrix}$$

This methodology has then been used to perform simulations and evaluate its feasibility. For that it was used the 32×32 pixels image of Figure 153, containing several geometric shapes and different gray levels.

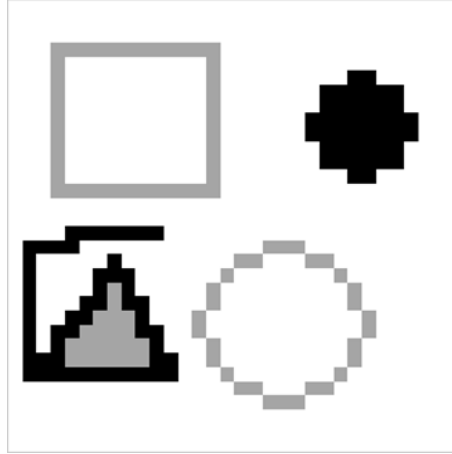


Figure 153 – 32×32 pixels image with several geometric shapes and different gray levels used in the simulations performed to study the feasibility of the algorithm created to generate binary random compressive codes to be used by the CMOS based imaging sensor.

Figure 154 presents the results of the reconstruction of the image of Figure 153 for different amounts of compression. There it can be seen images reconstructed with 10% and 50% of the total number of measurements and the respective PSNR values calculated relatively to the original image of Figure 153.

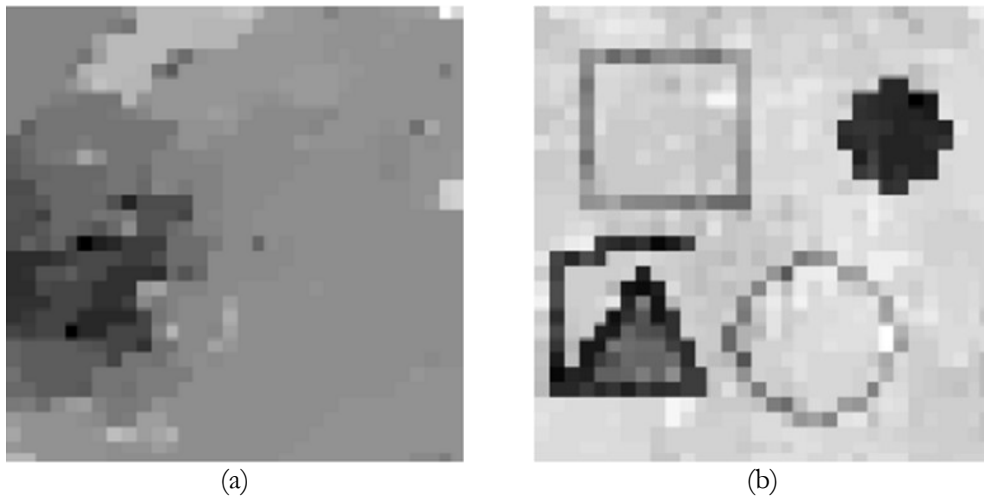


Figure 154 – 32×32 pixels reconstructions of the image in Figure 153. The reconstructions were performed using: (a) 10% (PSNR = 5.32 dB); (b) 50% (PSNR = 12.51 dB), of the total number of measurements (1024). The PSNR were calculated relatively to the image of Figure 153.

4.6.3 Concluding remarks

This work enabled the successful demonstration of the feasibility of the developed algorithm to generate binary random codes that can be used by the CMOS based imaging sensor to effectively compress and allow the reconstruction of the images from a subset of the measurements in a compressive sensing based manner.

Its use opens the possibility to reduce the consumed power since many of the components can be deactivated. Once it is possible to reconstruct an image using fewer measurements than the total number of pixels, it is possible to increase the frame rate when the imaging sensor is operating in the compressive sensing based mode.

The capabilities of the imager to sense in a reconfigurable way and process data in the analog domain provide a versatile platform for compressive sensing operations. Therefore, supported by the outcomes of this work, it has been fabricated an IC with compressive sensing based capabilities. Such IC will be in the basis of a low powered, compact and fast imager based on compressive sensing. Besides the compressive sensing based imaging capabilities, the presented architecture is also capable of executing operations such as upsizing, downsizing and convolution.

Following this work, it should be mentioned that a Provisional Patent Request has been submitted for an imager with compressive imaging capability.

Chapter 5. Applications

This section illustrates three applications of compressive sensing based single-pixel imaging systems. A passive illumination single-pixel monochrome imaging system has been used in two different scenarios. It has been assembled on a stereo microscope to acquire microscopic images and it has also been combined with pattern recognition and machine learning mechanisms to perform face detection without explicit image reconstruction. A passive illumination single-pixel hyperspectral imaging system has been used to acquire hyperspectral images of grapes, which contain important spectroscopic information useful for the analysis of their physicochemical properties.

5.1 Microscopic imaging using a passive illumination single-pixel monochrome imaging system

For these experiments, the LightCommander has been assembled on a Leica stereo microscope (Leica S6D) using adaptor optics to form an image of the scene under observation on the DMD. The optical adaptation was achieved using a 1.0x lens (Leica – reference 10445930) and a 2.5x adaptor tube (Leica – reference 10446175) connected with a T2 adaptor ring, as can be seen in Figure 155. There, it is also observable the Thorlabs PDA100A-EC amplified photodiode that was positioned on the output of the LightCommander's light tunnel and a 12V-35W halogen bulb that has been used to illuminate the scene. The scene consisted of a piece of text printed in black on standard white paper with the characters “ste” which was being illuminated in transmission. The microscope was set to its lowest magnification (0.63x) and Figure 156 shows 128×128 pixels images acquired with the single-pixel camera and with a conventional camera, for comparison purposes. The dimensions of the scene under observance corresponded to a square with 5.4 mm which yielded a spatial resolution of approximately $42.19 \mu\text{m}/\text{pixel}$ for an image with 128×128 pixels. Despite the noise evident in the image acquired with the single-pixel camera, it can be stated that both images are manifestly similar, attesting the feasibility of the single-pixel imaging system to be used in such application. As the amount of light collected by the microscope optics was rather reduced, the main difficulty was related with the establishment of good dynamic range for the compressive measurements which strongly depended on the sample and on the intensity of the illumination. It should be noted that this system also had the potential to be used for the acquisition of color and multispectral images, for instance, once the adequate spectral filtering or illumination would have been used, respectively.



Figure 155 – Photo of the LightCommander with the photodiode in front of the light tunnel assembled on a Leica microscope.

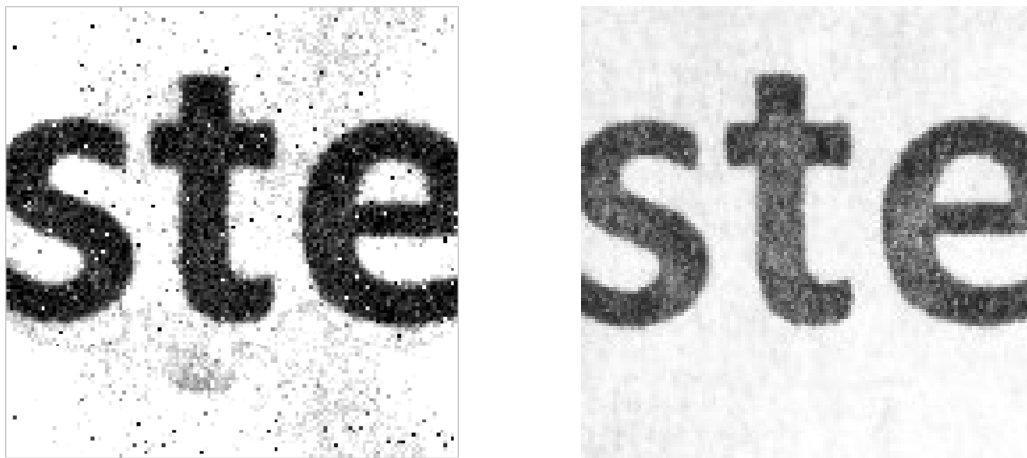


Figure 156 – 128×128 pixels result images acquired with: (left) the compressive single-pixel imaging system; (right) a conventional camera; assembled on the microscope, for a scene consisting of the characters “ste” printed in black on standard white paper.

5.2 Face detection without explicit image reconstruction

As demonstrated by Duarte *et al.* [99], compressive sensing can be further extended to statistical inference related tasks, such as detection, classification and recognition since the signal reconstruction is not explicitly required, but only the relevant statistics for the problem at hand. Face detection which nowadays has become a widespread tool due to the proliferation of mobile devices and social networks could eventually represent another application of compressive sensing

within this context. Following this idea, it was envisioned and analyzed, in a preliminary manner, the possibility of detecting faces in images without explicit reconstruction. So, for this, the main idea was to acquire incoherent projections of images, of faces and different objects, with Hadamard based codes and, then, use those projections to train a classifier. Therefore, the problem consisted of classifying if the content of a specific image corresponded either to a face or to an object. For that, two sets of images were created, one containing 200 images of faces in an upright frontal position, with 2 images per person, and other containing 50 images of different objects/animals, with 2 images per object/animal. The faces' images were obtained from the "FEI Face Database" [100] and the objects/animals' images were obtained from the "Caltech 101" database [101]. The images have been cropped and resized to 256×256 pixels (see Figure 157).



Figure 157 – Examples of images belonging to the created sets. (Top) Images of faces of three persons in upright frontal positions, with two examples for the same person. (Bottom) Images of three different objects/animals, with two examples for the same object.

Then, for each image, a vector comprising the incoherent projections, produced with the Hadamard based compressive codes in a manner similar to that exposed in Figure 46, was created. The only difference relied in the fact that this time the compressive codes were not permuted. Each incoherent projection or measurement was obtained with a different code and corresponded to the sum of the pixel values of the image resulting from that product. As the images exhibited different intensities, each of the vectors was posteriorly normalized to values between 0 and 1. To reduce the computational complexity, the used images and codes were scaled down to 32×32 pixels, therefore, producing vectors with 1024 elements. Figure 158 shows the plot of two vectors, one obtained with an image of a face and another with an image of an object/animal.

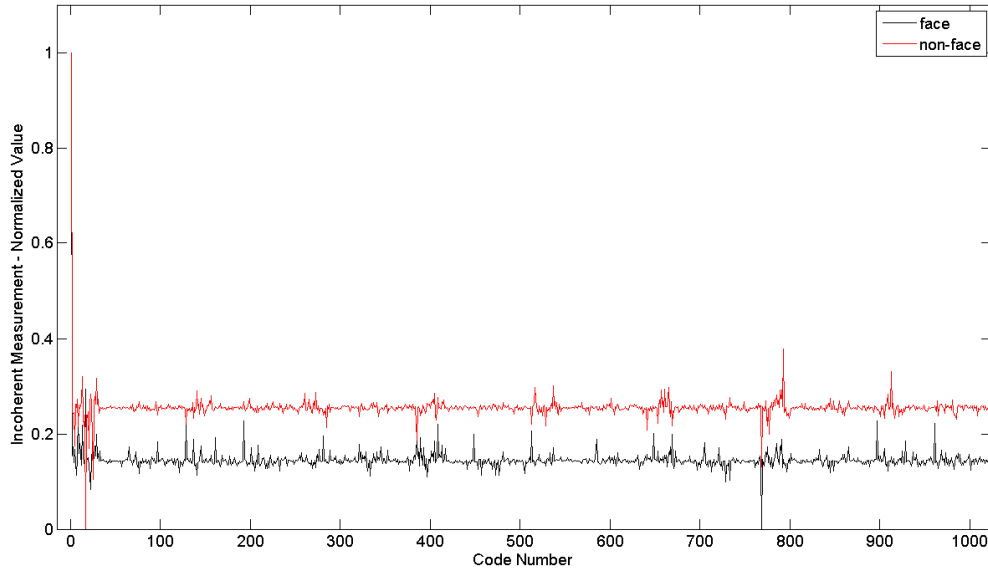


Figure 158 – Plot of vectors with the 1024 incoherent measurements obtained with an image of a face and with an image of an object/animal.

For the discrimination task we used a Support Vector Machine (SVM), which is a popular machine learning mechanism [102]. In the simplest form, a SVM uses a linear separating hyperplane to create a binary classifier with a maximal margin. In cases where data cannot be linearly separable, data are transformed to a higher dimension than the original feature space. Such is done by choosing a given kernel function, representing the inner product in some implicit higher dimension space. In our case, this transformation was made with a radial basis function (RBF).

The sets of vectors containing the incoherent measurements were split into training and test sets to be used by the classifier. The training has been performed with 20%, 40% and 60% of the data, being the respective remainder used as testing data. The splitting of the data into training and test sets was repeated 10 times in order to assess the variability of the obtained performances. The best parameterization of each model was found by a ‘grid-search’ based on a 5-fold cross validation scheme conducted on the training set.

Nowadays, it is relatively easy to solve problems with millions of instances, each of them with a reasonable number of features. However, it is common to have access to datasets with significantly higher number of features than instances leading to the well-known problem of the “curse of dimensionality”. Feature selection (FS) techniques provide the means to overcome this issue by identifying the most valuable features so that good and simple class discrimination models can be obtained. There are three types of feature selection algorithms: filter, wrapper and embedded. The former is independent of the classifier being usually done before the learning phase. Wrapper algorithms iteratively select subsets of features and assess the performance of the learning models to determine how useful those subsets are. Embedded algorithms automatically select features during the model construction [103]. Figure 159 succinctly depicts the three approaches.

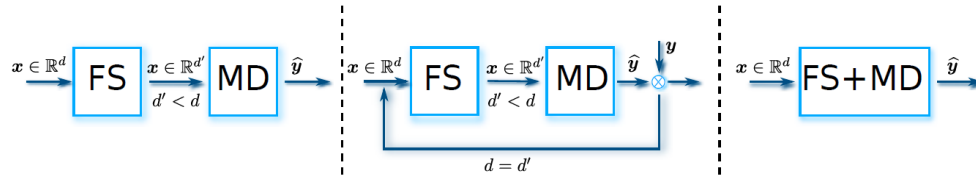


Figure 159 – Three different standard approaches for feature selection: (left) depicts the filter feature selection (FS) approach done before the model design (MD); (center) the wrapper consists on an iterative approach where features are removed step by step until a desirable performance of the model is achieved; and (right) embedded method is designed jointly with the learning model algorithm.

An FS problem can be described as a two-fold problem. First, one tries to eliminate the similar variables (redundancy) and secondly, to capture how correlated each feature is with the class (relevance). In [103] it was proposed a new way of performing FS using quadratic programming. There, the authors proposed a single mathematical formulation that was capable of simultaneously address the previously exposed redundancy and relevance requirements.

FS algorithms, as those described above, can be coupled with any learning model. For this study, we have opted for the wrapper approach applied to SVM. The performance obtained with this approach has been compared to that obtained with a random choice of features and the results are presented below. It should be referred that in this study the features correspond to the measurements obtained with a specific code. In Figure 160 one can observe the performance of the SVM classifier with random feature selection and different amounts of training data. In Figure 161 the performance of the SVM classifier with optimized feature selection (according to the method presented in [103]) and different amounts of training data is shown.

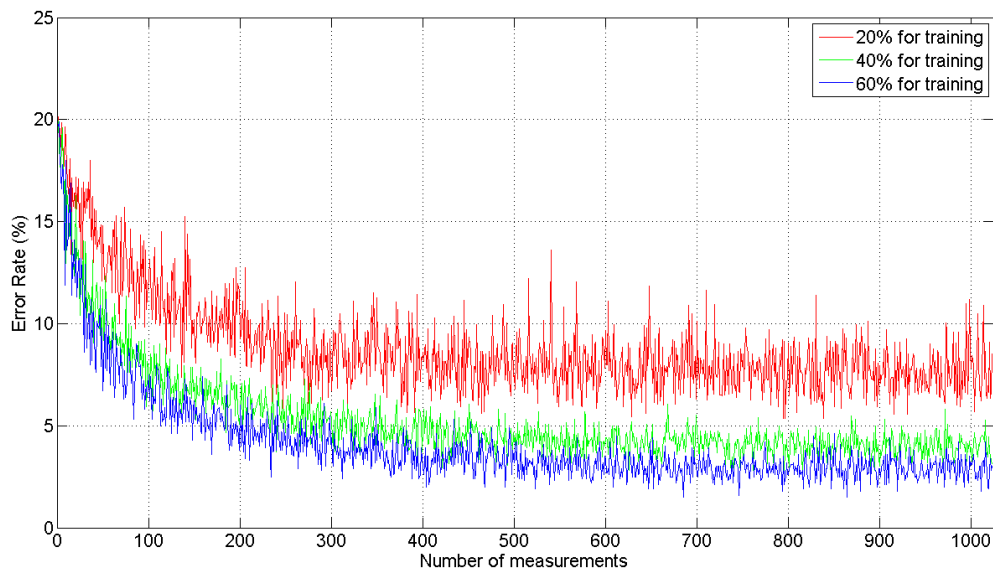


Figure 160 – Performance of the SVM classifier trained with different amounts of data and with random feature selection.

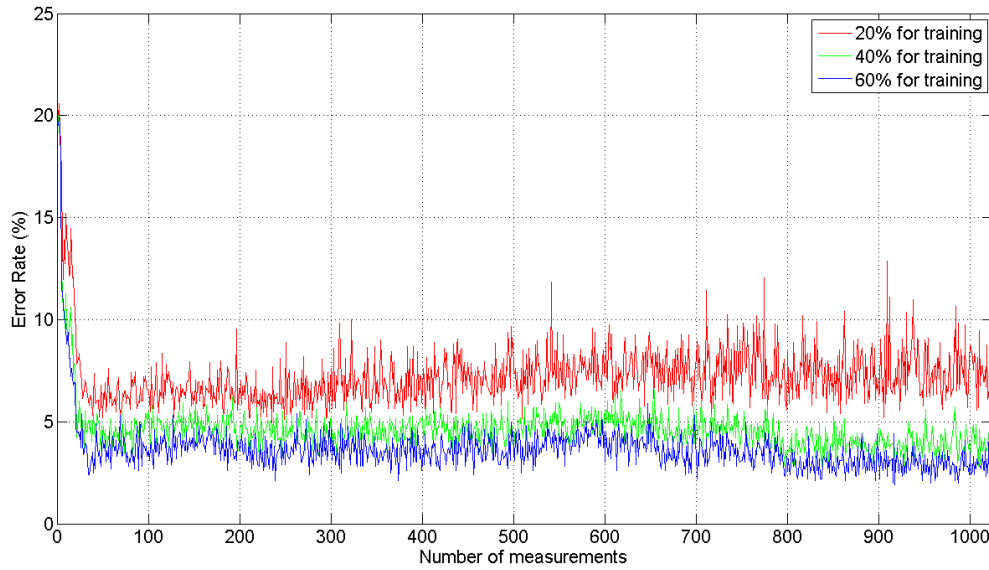


Figure 161 – Performance of the SVM classifier trained with different amounts of data and with optimized feature selection.

From the results presented in Figure 160 and Figure 161 it is obvious the increased performance of the classifier with optimized feature selection. Using 60% of data for training, with optimized feature selection the classifier was able to provide an error rate close to 3% with only 29 measurements, while the same performance was reached only after the use of 370 measurements for the case of random feature selection. The stabilization of the error rate for the case of the optimized feature selection evidences its capacity to discriminate the relevance and redundancy of the involved features at an early stage. As a reference, the performance of the SVM classifier when all the 1024 measurements have been used was also obtained. As before, the training phase was conducted with sets comprising 20%, 40% and 60% of the data. The obtained error rates were 5.15%, 3.00% and 3.10%, respectively. With these results, it can be said that using feature selection methods it was possible to obtain a competitive performance, translated by a smaller error rate, with far less features.

In this study, it was also evaluated which features typically provided the best results. Knowing that information, it could then be combined with compressive sensing theory to design a face detection system that could simultaneously minimize the amount of required measurements and maximize the amount of meaningful information. Evaluating the data, it was then possible to infer that the 16th, 28th, 408th, 512th, 768th and 784th measurements (generated with the corresponding Hadamard based compressive codes) were the most common ones when a performance of 97% was obtained. In terms of computational effort, this fact can be extremely appealing once only a reduced and predefined set of Hadamard codes has to be computed to detect a human face with such a significant performance.

For comparison purposes, another face detection system was implemented using the information obtained from the Scale Invariant Feature Transform (SIFT) descriptors as inputs to the classifier. SIFT is a well-known technique for feature detection and description with a wide number of applications, inclusively, face detection and recognition [104-107]. SIFT descriptors are built upon the measurements of the gradient in 8 different orientations in image patches of size 4×4 centered in interest points. These interest points are detected by common operators, such as Laplacian of Gaussian or Difference of Gaussian, for example, having the latter been used in these experiments. As a result, for each image patch, a feature vector of size 128 was obtained. The vocabulary for representation of the datasets was constructed with an unsupervised technique (K-means [108]) and concluded with the creation of a sparse histogram using a bag-of-words technique [109, 110]. The implemented system was then trained with 60% of the data and a performance of 80% was obtained. Figure 162 shows examples of images from the datasets with over imposed blobs representing the SIFT descriptors.

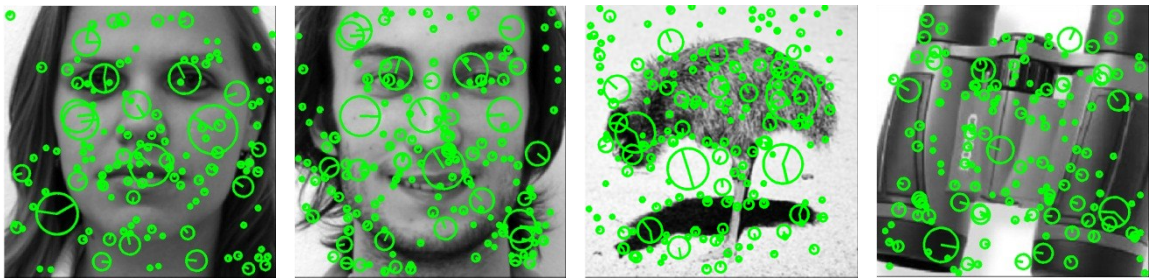


Figure 162 – Examples of images belonging to the created sets with over imposed blobs representing the SIFT descriptors.

Despite the early stage of the prospective study here presented, in face of the results obtained, it is strongly believed that the CS based framework has potential to be further developed in the future and that it would be interesting to apply it to video surveillance, for instance.

It should be said that in this study the tasks associated with the SIFT descriptors, feature selection and training/testing of the classifier were performed in collaboration with a colleague post-doc researcher.

After executing these experiments and evaluating the feasibility of detecting faces without explicit reconstruction of the images, the passive illumination single-pixel monochrome imaging system was used to assess the performance of the face detection system under real-world conditions. For that, two images, one of a face and another of an object, have been printed in white paper and placed in front of the imaging system so that the corresponding compressive measurements could be acquired (see Figure 163). The printed size of the images was $55 \text{ mm} \times 55 \text{ mm}$. The electronic circuit board, observable on the top left corner of the photo in Figure 163, contained a 10×10 matrix of white light LED and was used for illumination of the scene.

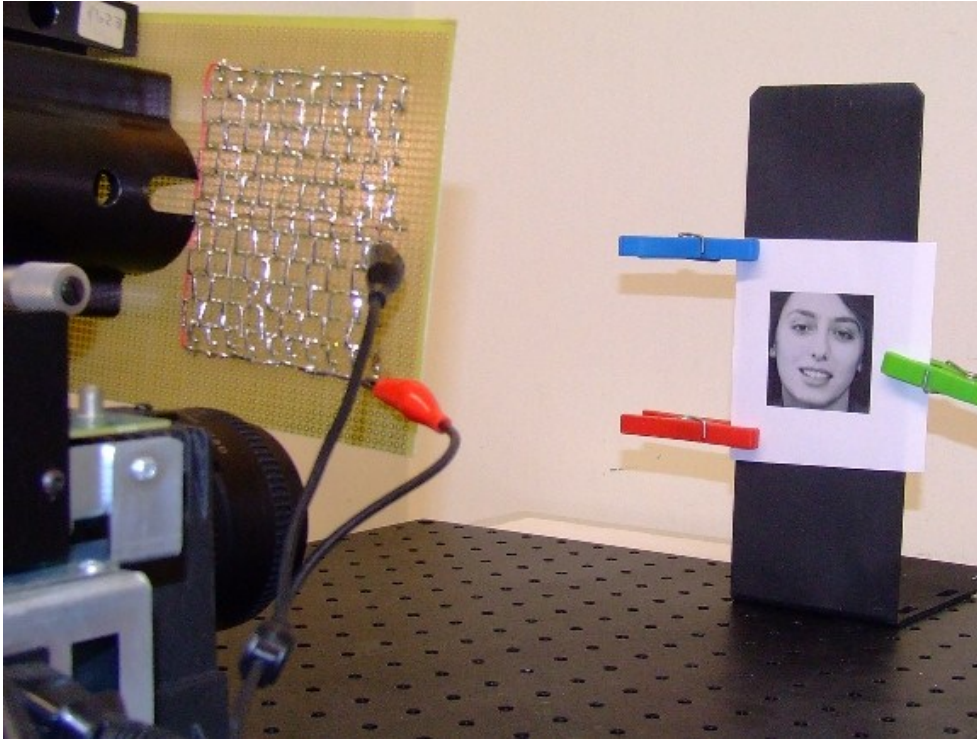


Figure 163 – Photo of the arrangement used to acquire the measurements for face detection with the passive illumination single-pixel imaging system.

The images that have been used are presented in Figure 164.

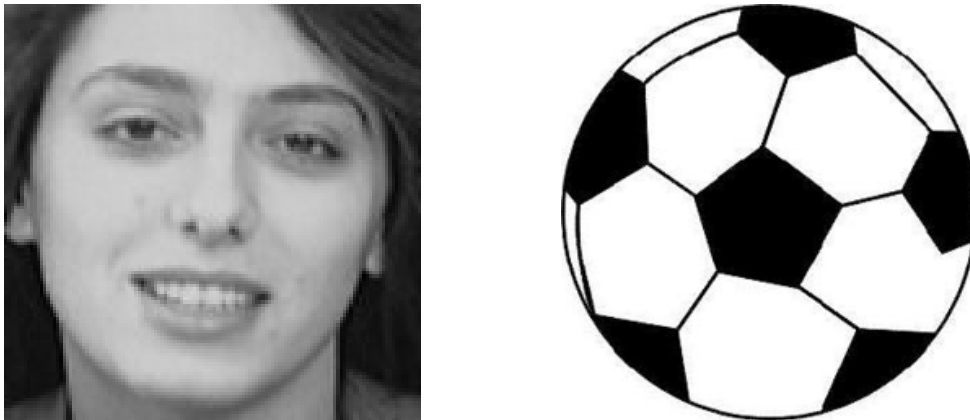


Figure 164 – Images of a face (128×128 pixels) and of an object (256×256 pixels) that have been used to assess the performance of the face detection system under real-world conditions with the passive illumination single-pixel monochrome imaging system.

The images of Figure 164 have been scaled down to 32×32 pixels and are presented in Figure 165. After, these images were used as the reference images in the calculation of the PSNR values of the reconstructed images.

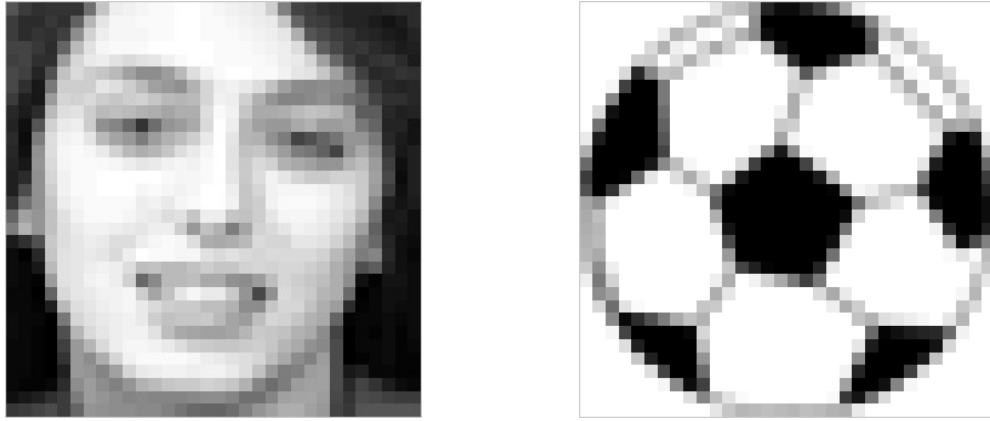


Figure 165 – Images of Figure 164 resized to 32×32 pixels.

After the data have been acquired, the corresponding vectors were input to the classifier and both examples were correctly classified when all the 1024 measurements have been used. This performance held true down to 1018 measurements. Using only 50 measurements the classifier performance decreased to 50%, failing to correctly classify the input data corresponding to the image of a face. This difference of performance, comparatively to the results previously obtained, may be supported by the following facts. During the measurement process, inevitably, there was noise involved which naturally affected the purity of the information or, by other words, masked the variability imposed by features within the images. The illumination of the images was not constant all over, mainly, because the alignment between the light source and the scene and between the scene and the imaging system was not along the same axis. The training of the classifier was performed with data that did not reflect these issues and, for that reason, the previously obtained model was not optimized for the conditions under test.

Figure 166 contains the images of Figure 164 that have been acquired with the passive illumination single-pixel monochrome imaging system. These images have 32×32 pixels and were reconstructed using all the 1024 measurements.

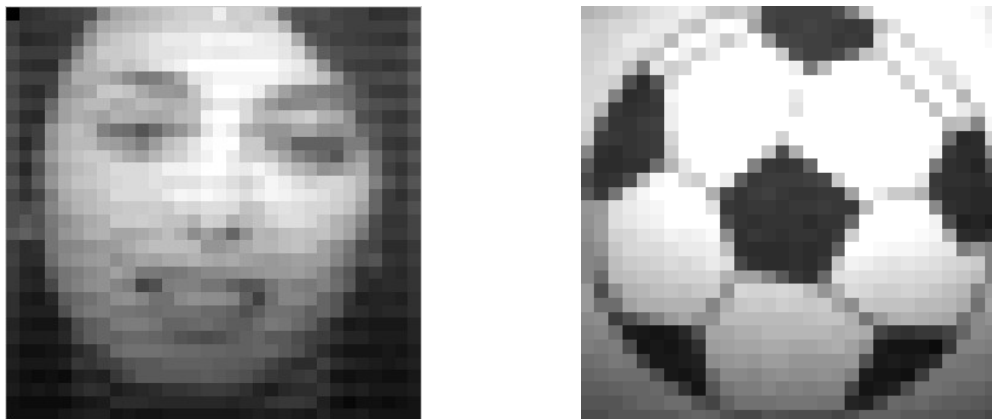


Figure 166 – Images of a face (PSNR = 12.41 dB) and of an object (PSNR = 9.86 dB) with 32×32 pixels reconstructed using 1024 measurements acquired with the passive illumination single-pixel monochrome imaging system. The PSNR values were calculated using the homologous images of Figure 165 as references.

Next, in Figure 167, the images of the same face and object of Figure 164 are presented for the case in which the measurements were obtained multiplying the image to be reconstructed by the Hadamard based random binary codes, as depicted in Figure 46. Relying on those images, it is possible to evidence the effect that the non-uniform illumination and the noise in the measurements had in the reconstructions presented in Figure 166.

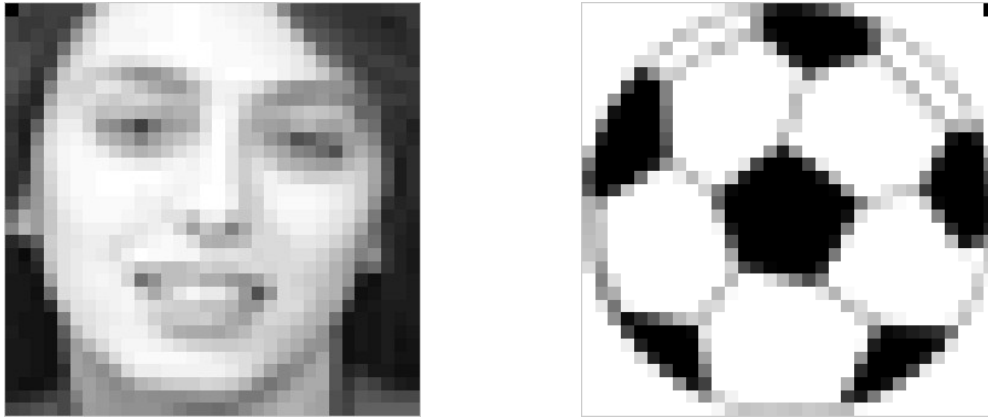


Figure 167 – Images of a face (PSNR = 24.84 dB) and of an object (PSNR = 22.93 dB) with 32×32 pixels reconstructed using 1024 measurements obtained multiplying the image to be reconstructed by the Hadamard random binary codes. The PSNR values were calculated using the homologous images of Figure 165 as references.

The higher PSNR values obtained with the images of Figure 167 reflect the improved visual quality of those images relatively to those of Figure 166 and their similarity relatively to the reference images of Figure 165.

Even though in a real-world scenario it may be difficult or even impossible to control the illumination of a scene, one way of improving the results obtained in these experiments with the passive illumination single-pixel imaging system could be to improve the uniformity of the illumination on the scene. Another aspect that could benefit the face detection system under real-world conditions would be to train the classifier with data which had incorporated the variability found under such circumstances.

A system such as the one presented here can be on the basis of the development of compact single-pixel cameras that can be optimized to detect specific targets. These cameras may have particular interest, for instance, in military, defense and surveillance scenarios.

5.3 Physicochemical analysis of grapes based on hyperspectral images

Another application that has been explored was related with the use of a passive illumination single-pixel hyperspectral imaging system for the acquisition of hyperspectral images of grapes. These experiments were conducted in collaboration with the Centre of Molecular and Environmental Biology at the University of Minho which has strong expertise in the analysis of spectroscopic data from grapes. In particular, this center holds a patent entitled “Method and Device for Monitoring the Production of Grapes with UV-VIS-SWNIR Spectroscopy” [111] (UV-VIS-SWNIR stands for ultraviolet/visible/short-wave near infrared) which, besides describing a method for monitoring the production of grapes, also exposes how to obtain and process information on the physicochemical characteristics of the grape from spectroscopic data. This knowledge is of utmost importance for the quality of wine production since it may be used, for instance, to monitor the development and maturation of the grapes; to follow the development of existing metabolite profiles in the grapes; to detect specific or anomalous features.

Therefore, our intent was to acquire hyperspectral images of grapes and subsequently perform the spectroscopic analysis of the grapes on a pixel-wise manner. Doing that, one would be able to map, for instance, the distribution of glucose on the grapes, or to quantify how many seeds existed. These are key aspects to the final flavor of the wine.

So, for these experiments, three grapes with different maturation levels were chosen. The maturation level was determined by the sugar concentration that has been quantified with a digital refractometer for sugar analysis from Hanna Instruments – model HI 96801. Brix percentage (%Bx) is directly related with the sugar content of an aqueous solution and is traditionally used in several industries, such as those for wine, fruit juice and honey production. A higher value of Brix percentage means a higher content of sugar in a solution. The three chosen grapes were measured to have 13.7 %Bx, 16.8 %Bx and 20.8 %Bx.

In order to acquire the hyperspectral images of the grapes, the setup of Figure 168 was implemented. To increase the contrast between the grape and the background in the acquired images, a piece of black plastic with an opening was used to define the area to be illuminated. The grapes were, then, placed in front of that opening. The light source was a 12V-35W halogen bulb which was placed behind the opening of the plastic piece and would illuminate the grapes in transmission, relatively to the imaging system.

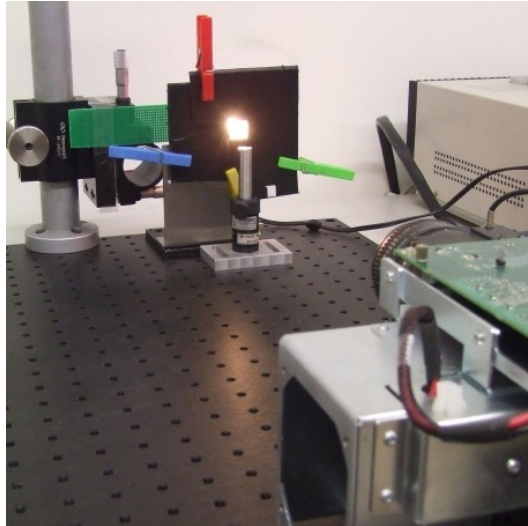


Figure 168 – Setup used to acquire hyperspectral images of grapes with the passive illumination single-pixel hyperspectral imaging system.

Figure 169 depicts three photos of the used grapes being illuminated in transmission, acquired with a conventional camera.



Figure 169 – Photos of the three grapes with different maturation levels illuminated in transmission. These photos were acquired with a conventional camera. From left to right, the grapes had 13.7 %Bx, 16.8 %Bx and 20.8 %Bx.

The passive illumination single-pixel hyperspectral imaging system used a QE65000 Ocean Optics spectrometer as the light detection device. This spectrometer was used instead of the USB2000 because of its reduced dark noise, higher SNR ratio and higher dynamic range. As the luminous intensities in these experiments were lower than before, these aspects proved essential for the quality of the measurements. The spectral range of the grating (HC-1) was 780 nm and the detector (Hamamatsu S7031-1006), which is responsive from 200 nm up to 1100 nm, had 1044 pixels ($24\text{ }\mu\text{m} \times 24\text{ }\mu\text{m}$ each). This results in a dispersion of approximately 0.75 nm/pixel. Using a $10\text{ }\mu\text{m}$ slit the pixel resolution is listed, by the manufacturer, as ~ 2.2 pixels, which results in a spectral resolution of $0.75\text{ nm/pixel} \times 2.2\text{ pixels} = 1.65\text{ nm}$.

Then, the single-pixel hyperspectral imaging system was used to construct a datacube for each of the grapes and, as an example, in Figure 170 a 32×32 pixels image of the grape with 20.8 %Bx obtained at 671.02 nm is presented. Besides the shape of the grape, two seeds are also discernible in that image. For clarification, the seeds are highlighted with a red contour in the image presented on the right side of Figure 170.

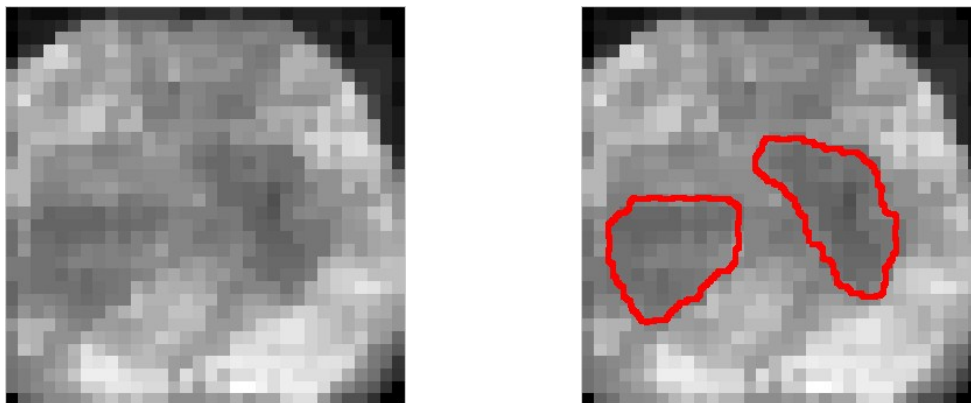


Figure 170 – (left) 32×32 pixels image of the grape with 20.8 %Bx acquired at 671.02 nm with the passive illumination hyperspectral imaging system. (right) The seeds observable in the image on the left were highlighted with a red contour.

A datacube representing the halogen bulb behind the opening on the black plastic piece was also acquired and an image of it acquired at 645.10 nm is presented in Figure 171.

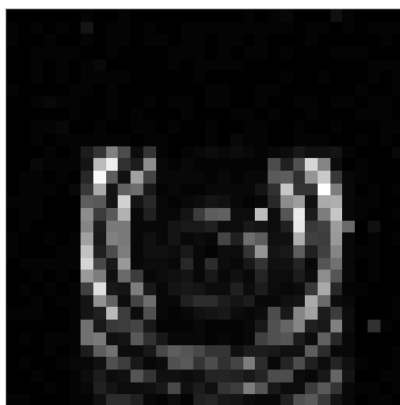


Figure 171 – 32×32 pixels image of the halogen bulb behind the opening on the black plastic piece at 645.10 nm acquired with the passive illumination hyperspectral imaging system.

As it has already been referred on this thesis, it is possible to obtain the spectrum at a spatial position along the datacube and obtain, in that way, the spectral signature of a specific pixel. For the halogen bulb it was found that depending on the spatial position, the spectrum obtained along the corresponding datacube would vary not only in intensity but also in terms of spectral density. To better illustrate this situation, three spectra were obtained along the datacube in three distinct spatial positions on the image. These positions correspond to the pixels marked in red, green and blue in Figure 172.

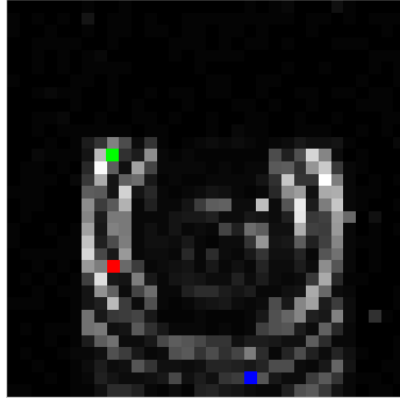


Figure 172 – 32×32 pixels image of the halogen bulb with three points marked in red, green and blue to indicate the positions where the spectra were obtained along the datacube.

The spectra obtained for the three distinct spatial positions can be observed below in Figure 173. The color of each spectrum indicates the position in the image to which each one corresponds.

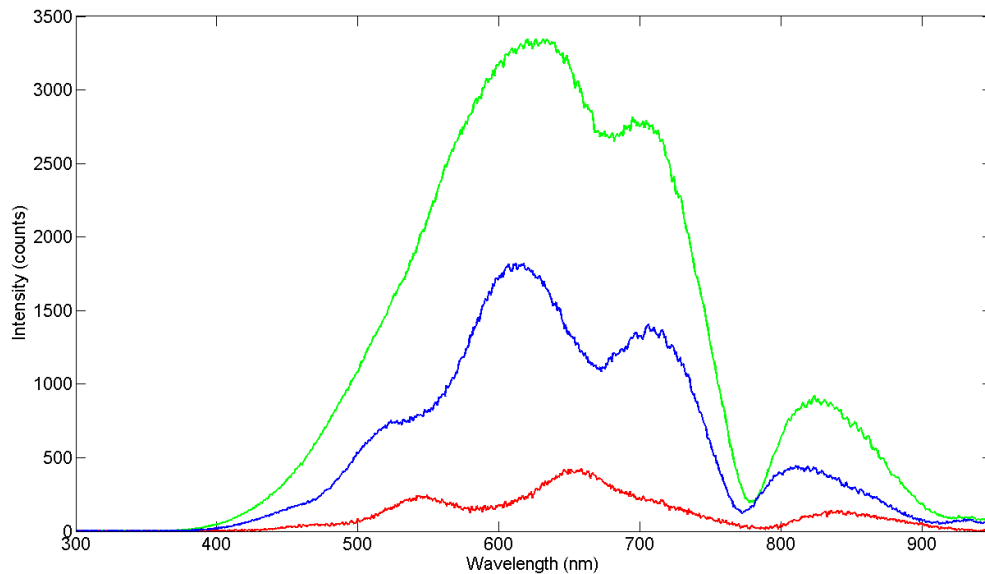


Figure 173 – Spectra obtained along the halogen bulb datacube in the positions marked by the red, green and blue pixels in the image of Figure 172.

Inspecting the spectra in Figure 173, one can perceive the different spectral densities exhibited. These differences may be justified by the dispersion, refraction and diffraction suffered by the light emitted by the bulb. These phenomena may be caused by the reflective surface located inside the bulb, by the glass of the bulb and by the grating-like and angular nature of the DMD. Additionally, the curved surface of the bulb certainly also caused the measured spectral densities to be different because the reflectance spectrum of a surface can be defined as a function of the angle of incidence. The non-uniform temperature distribution along the filament of the bulb may also have had an impact in the measured spectra.

However, despite the spatial dependency of the spectra obtained along the datacube, if the intensity of all the pixels in an image is summed for each of the datacube's spectral bins, we end up with a vector that contains the spectral signature of the ensemble of light emitted by the lamp. That vector has a length equal to the spectral depth of the datacube and the only difference is on the intensity which derives from the use of a multiplicative factor by the reconstruction algorithm. The normalized spectrum obtained with this procedure is presented in Figure 174 with a thin red line, while the normalized spectrum measured by the system when all the DMD mirrors were "ON" is traced with a thick black line. In addition, the difference between the two spectra of Figure 174 is exactly zero all over its representation, thus confirming their equivalence.

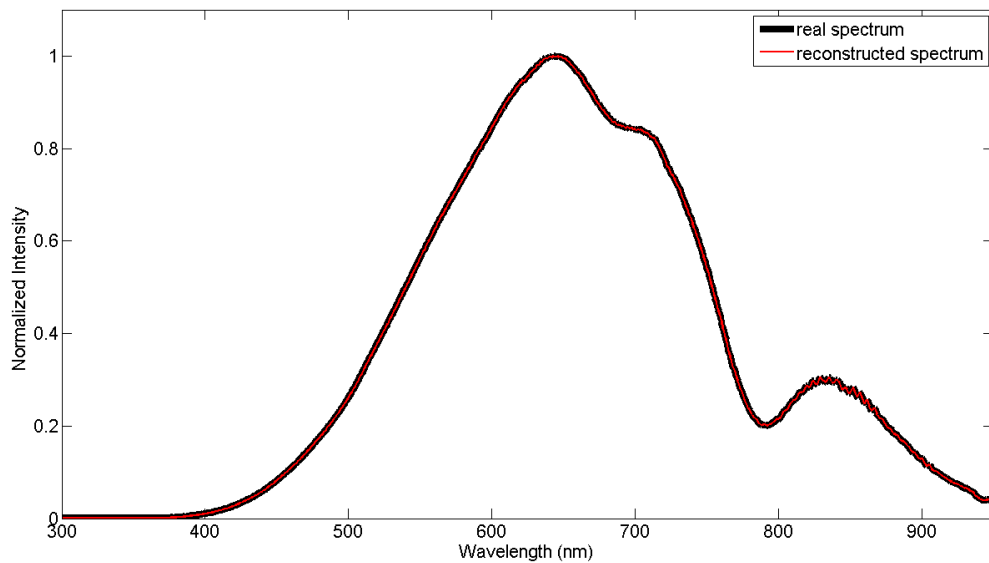


Figure 174 – Spectra of the halogen bulb. The normalized real spectrum is represented with a thick black trace while the normalized integrated spectrum, obtained from the reconstructed datacube, is represented with a thin red trace.

Similarly to the case of the halogen bulb, three spectra were also obtained from the datacube of the grape with 20.8 %Bx (see Figure 175). These spectra were obtained in the same positions of those plotted in Figure 173, indicated by the coordinates of the colored pixels in the image of Figure 172.

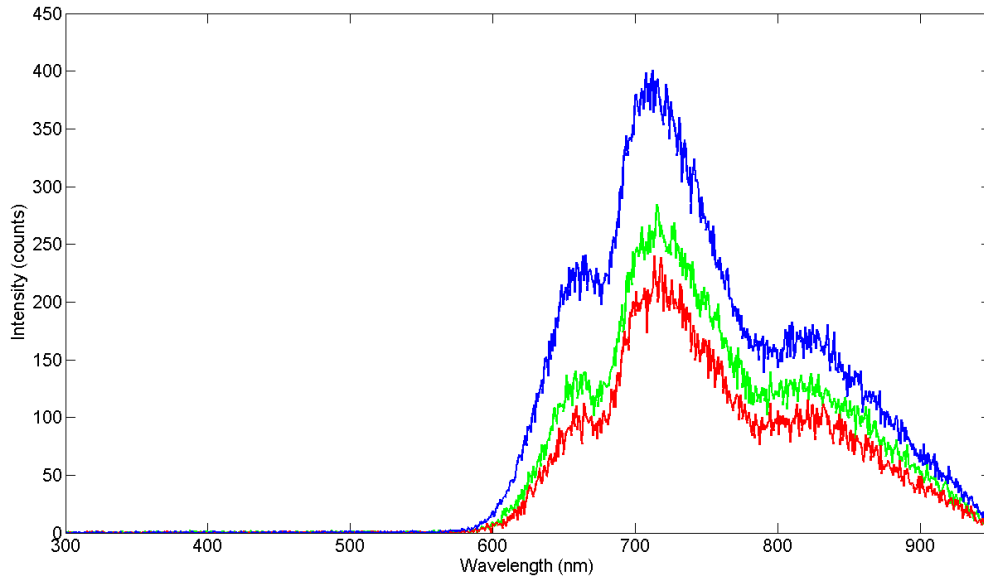


Figure 175 – Transmission spectra obtained from the datacube of the grape with 20.8 %Bx in the positions marked by the red, green and blue pixels in the image of Figure 172.

Due to the opacity of the used grape and its reddish color, the overall intensities of these spectra are much lower than the intensities of the spectra in Figure 173, and, in particular, the portions of the light corresponding to wavelengths below 600 nm have been completely absorbed. This was verified even though the spectrometer's integration time and the luminous intensity of the halogen bulb have been augmented, in order to maximize the dynamic range of the measured signals. Notwithstanding the fact that the amplitude of the noise in the spectra of Figure 175 is similar to that of Figure 173, in the former case its relative intensity is higher. The fact that the reconstructed spectra exhibited lower intensities than the spectra obtained during the measurement process, with each of the random compressive codes, also derived from the partitioning that the reconstruction algorithm made to the ensemble intensity, gathered from the entire scene, by all the pixels in each image.

However, contrarily to the case of Figure 173, the spectral densities of the spectra of Figure 175 are very similar to each other. This may have arisen from the non-uniformity of the grape, which caused the light to be scattered and become spatially uniform. By other words, the grape acted as a diffuser.

As in the case of the halogen bulb (see Figure 174), the integrated spectral signature of the grape with 20.8 %Bx was obtained from the corresponding datacube and the resulting normalized spectrum perfectly matched the normalized real spectrum (see Figure 176), obtained when all the DMD mirrors were “ON”.

The normalized integrated spectral signatures of the other two grapes were also obtained and are presented in Figure 177 along with the normalized integrated spectral signature of the grape with 20.8 %Bx. As it can be seen, the three grapes exhibit different spectral signatures, deriving from their different ripeness levels and different physicochemical compositions. This spectral

information is on the basis of the spectroscopic analysis performed by the group from the Centre of Molecular and Environmental Biology at the University of Minho. It is then expected that with the data provided by these experiments it will be possible to quantify, in a pixel-wise manner, the concentration of certain compounds such as glucose, fructose, malic acid and tartaric acid, which are fundamental for wine production and taste.

Even though in these experiments only individual grapes were imaged, this system could be adapted to image entirely a grape cluster, a vine or even a vineyard, demonstrating in that manner its true potential.

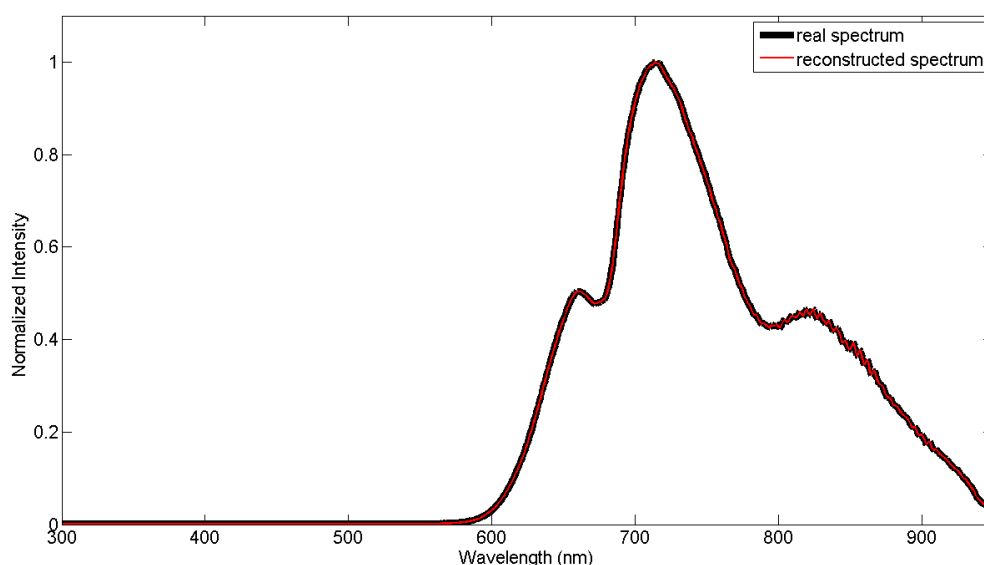


Figure 176 – Transmission spectra of the grape with 20.8 %Bx. The normalized real spectrum is represented with a thick black trace while the normalized integrated spectrum, obtained from the reconstructed datacube, is represented with a thin red trace.

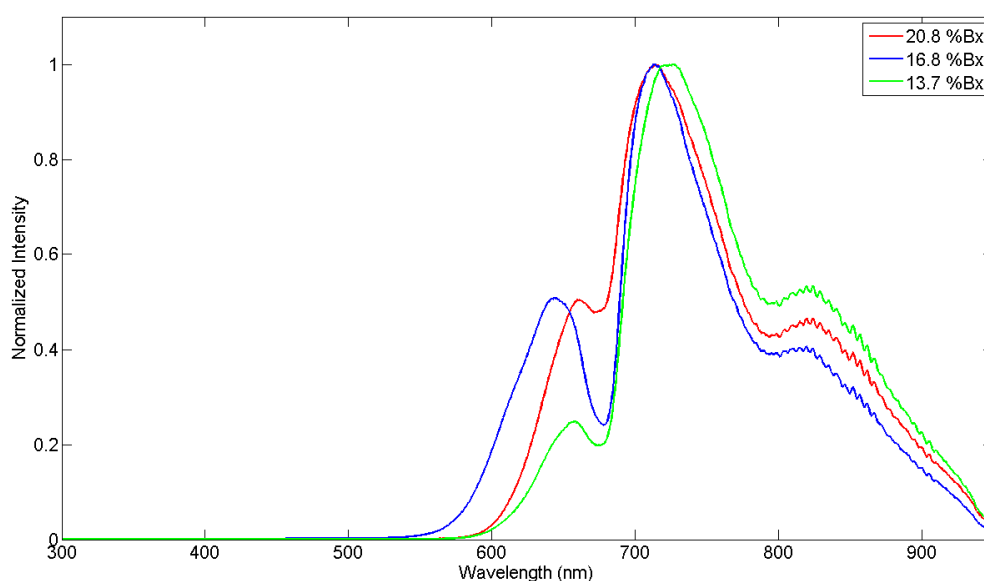


Figure 177 – Normalized integrated transmission spectra of the three grapes, obtained from each of the respective datacubes.

Besides the possibility of obtaining spectroscopic information in a pixel-wise manner without scanning of the scene or movement of the imaging system, which constitutes an inherent advantage of the used hyperspectral imaging system comparatively to the commonly used methods, this combined system of hyperspectral imaging and spectroscopic analysis has strong potential to become a choice of election. In particular, it represents a non-destructive method of analysis that is relatively cheaper and has strong potential to operate much faster. It does not require the intervention of highly qualified human resources and can be applied to the analysis of different analytes, such as olive oil, for the detection of counterfeits, fruit juices, for quality inspection, and water, for the detection of pollutants, for example. It can easily address different spectral ranges, suiting the needs of the different applications. It can also be assembled in a compact and light form to, consequently, enable its use outside of the lab and be applied, for instance, in remote sensing, which may find various applications in mineralogy, biology, defense, agriculture and environmental measurements. Agro-food industry has also recognized the potential of using hyperspectral imaging techniques and could also benefit from a system such as the one presented here [112].

Chapter 6. Future Work

The aim of this section is to trace ideas of improvement and further development of the studies related to compressive sensing based imaging systems presented in this thesis.

One improvement that is crucial, if one wants to attract the interest of potential end-users to this technology, is to reduce the time of the measurement process. This limitation can be effectively overcome by taking advantage of very fast DMD boards available on the market. For the time being, we were mainly limited by the available resources and this issue did not affect in any manner the accomplishment of the intended results.

In the following section, one prospective work directed towards the aerospace industry, for the development of a CS based imaging LIDAR system, will be suggested and presented.

6.1 Single-Pixel Imaging LIDAR System Based on Compressive Sensing

LIDAR is an optical sensing technology that, basically, measures distances through the time light takes to travel from the source to the target. It is widely used in various applications such as agriculture, meteorology and military, for instance.

In this section, a prospective work for the development of a compressive sensing based single-pixel imaging LIDAR system to be used in Space missions is presented.

Mars and the Moon are envisaged as crucial destinations of Space exploration in the upcoming decades. Therefore, several strategic missions are included as milestones in terms of development of new technologies, demonstration of key capabilities, and delivering on high priority scientific objectives. In this context, Imaging LIDAR is seen as one key enabling technology that can be extremely relevant in Guidance, Navigation and Control (GNC) tasks, which require very accurate, wide range, high-resolution distance measurement systems. In particular, crucial stages of Space missions, such as descent and selection of a safe landing site, rendezvous and docking maneuvers, or robotic surface navigation and exploration operations, can be largely supported by Imaging LIDAR Systems (ILS) [113]. Although ILS have been commercially available and used for a long time in diverse metrology and ranging applications, their size, mass and power consumption are still far from being suitable and attractive for planetary exploratory missions. So, efforts are being driven towards the achievement of technological breakthroughs that can significantly reduce these drawbacks. Therefore, we propose the development of a single-pixel ILS based on compressive sensing, which has great potential for miniaturization; to increase spatial resolution; to eliminate the need for scanning; relying on a simple and robust configuration.

The principle of operation of the proposed ILS is depicted in Figure 178. It can be seen that a pulsed laser source is used to illuminate the target scene, whose image is formed on the DMD array. Optical filtering is incorporated into the optical path to eliminate the influence from

background illumination. Depending on the random binary measurement codes applied to the DMD, the amount of light reflected towards the photon detection device will vary, thus, compressing the spatial information. Then, for each measurement code, a correlator is used to provide a timing histogram, thus compressing the distance information. At the end of the measurement process, a set of the collected timing histograms is used to reconstruct the images referring to the range-find distance.

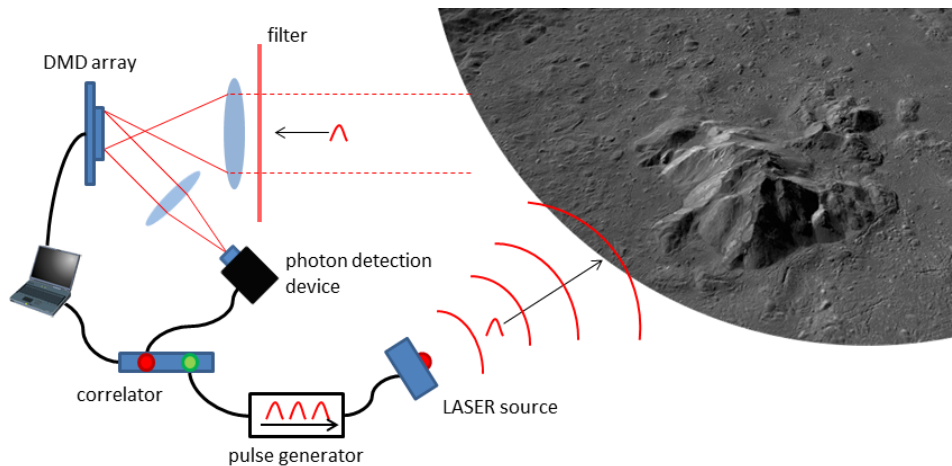


Figure 178 – Scheme illustrating the principle of operation of the single-pixel imaging LIDAR system based on compressive sensing.

When compared to passive sensors, current ILS are bigger, heavier and consume too much power. However, miniaturization is becoming real, due to recent developments in MOEMS (micro-optical-electrical-mechanical systems) and focal plane detector arrays, turning those into excellent candidates to be included into ILS to be used in Space missions. Combining these aspects with the advantages of a photon-counting compressive imaging LIDAR system, as discussed on section 3.12, turns a single-pixel ILS into a significant solution that does not suffer from the aforesaid disadvantages [13]. The proposed system does not perform any scanning, therefore it does not involve moving parts, being advantageous for Space operation. This causes the optical engine arrangement to become simpler, efficient, easier to align, lighter and more compact. In addition to the fact that a single-pixel ILS, such as the proposed one, can be more immune to dark noise and read-out noise, since it can gather more photons than an average pixel sensor, if one or more measurements are lost, this will not corrupt the entire reconstruction. This is extremely relevant in a high error prone scenario such as the one evinced in Space missions. When arrays are used there is no way of recovering the info lost by dead pixels. Fortunately, that is not the case with single-pixel configurations, which enable the implementation of redundant setups at much lower cost, occupying less space, weighting less and consuming less power. Still, if one or more mirrors of the DMD become damaged, with CS it is still possible to fully reconstruct the images. Parallel sensing can also be employed to reconstruct images constituted by parts that were reconstructed at lower

resolutions (e.g. build a 64 x 64 pixels image with four contiguous 32 x 32 pixels images), in shorter periods of time. The proposed implementation can also be extended to work in spectral regions currently inaccessible to conventional imaging arrays. It is also believed that the proposed single-pixel ILS may benefit with the incorporation of the previously demonstrated high dynamic range compressive imaging techniques.

It is anticipated that the single-pixel ILS system may be useful in diverse scenarios of Space missions. During the landing phase of a Space mission, several sub-phases need to be accomplished, namely the detection of a safe landing site. Until touchdown, ILS can be used as altimeter/velocimeter and provide assistance to the GNC tasks, to better map and retarget the descent trajectory in order to minimize fuel consumption. A rendezvous in Mars orbit between a sample container (SC) launched from the Mars surface, and the orbiter that will perform the return to Earth is foreseen in the aim of the Mars Sample Return mission. The SC is supposed to be a highly reflective sphere with 20 cm diameter and the ILS is expected to intervene in the terminal sequence of the rendezvous process. When rovers are used to explore planet surface, the capability to detect and avoid obstacles is also crucial. Stereo vision systems can provide real-time range images over significant FOV, but lack from range resolution over large measurement ranges and the environment illumination and target contrast strongly affect their performance. For rover navigation, one can further define three operational modes: regional navigation (from 10 m to 100 m); mid-range navigation (from 4 m up to 10 m) and local navigation (from rover up to 4 m), each one with its specific requirements and difficulties.

As a final point, it should be noted that the development of such an imaging LIDAR system has been proposed to the European Space Agency (ESA) and has been accepted for funding in the aim of the Innovation Triangle Initiative (ITI) program. The opportunity to collaborate with a partner so demanding and prestigious as ESA should be seen as a valuable tool to further reinforce the competencies and knowledge of the Optoelectronics and Electronic Systems Unit at INESC TEC in this area of research.

Chapter 7. General Conclusions

Despite the wide range of subjects presented in this thesis, it can be easily recognized the existence of a common conducting path to all the work: the development and study of compressive sensing based single-pixel imaging systems.

Compressive sensing based imaging, or simply compressive imaging, presented itself as an enabling new paradigm that dramatically pushed forward the frontiers of imaging and opened the doors to many promising applications.

More in detail, one of the advantages of the presented single-pixel imaging systems is the ability to operate under very low light intensities, much lower than those required by conventional cameras. This is due to the fact that usually a single photodiode exhibits much higher sensitivity than the pixels of a conventional image sensor. Additionally, one can even incorporate photomultiplier tubes or photon-counters, for instance, to further improve the system's sensitivity.

Another advantage relies on the fact that the information is acquired in an already compressed form. This avoids the waste of information often verified along the use of conventional imaging systems, which gather huge amounts of information that is then discarded through the application of compression standards.

Since data are compressed from the beginning of the process, an efficient encryption method is brought into light, once the apparently random measurements will resemble noise and have no meaning for an observer that has no knowledge about their seed.

With compressive single-pixel cameras, most of the burden is placed on the reconstruction process, reducing the complexity of the hardware and acquisition phase. This constitutes another advantage since the required computational resources are widely available and with increasing tendency to perform better without significant increase of their cost.

As it was stated in this thesis, under very specific requirements, compressive imaging systems can be the choice of election in detriment of conventional imaging systems. More, in certain situations they are currently the only available solution.

This thesis presented an encircling study of compressive sensing based single-pixel imaging systems. In general terms, the developed systems were capable of acquiring monochrome, color, multispectral, hyperspectral and high dynamic range images, operating either in a passive or in an active illumination mode. Comparing analogous systems operating with different illumination configurations, it has been possible to determine the superior quality of the results obtained with the systems operating with passive illumination, when compared to those obtained with the systems operating with active illumination. This could be explained by the ripple existent in the illumination, which in the case of active illumination could mask the effective variation caused by the random compressive codes in the signal perceived by the photodiode and, then, represent noise in the measurements. The lower contrast provided by the LCD makes the variation caused by the random

compressive codes to be fainter than that provided by the DMD, which results in a lower SNR for the measurements and, in turn, in reconstructions that reflect more that noise.

It has also been implemented for the first time a transmissive compressive single-pixel imaging system that used an LCD as the spatial light modulator. This system has been used to acquire microscopic images and provided key insights for the comparison of LCD with DMD as spatial light modulators for compressive single-pixel cameras, from which the DMD have been elected as the best option.

From the development and study of the color and multispectral imaging systems it was possible to conclude that the fidelity with which the colors of a scene are acquired and represented is directly related with the width of the spectral regions utilized to define the color components. Furthermore, in order to obtain the best results, those spectral regions shall be as sharp and narrow as possible and the overlap should be minimum. For the case of the developed hyperspectral imaging systems these issues did not find representation because the illumination was discrete, very sharp and narrow, in the case of the active illumination system, or the light detection was performed with high spectral resolution, in the case of the passive illumination system. In particular, for the first time, a passive illumination compressive single-pixel hyperspectral imaging system with 10 pm of spectral resolution has been implemented and demonstrated. This represented an improvement of two orders of magnitude relatively to the best commercially available systems.

High dynamic range imaging has been combined with compressive imaging yielding a novel imaging modality which has been designated as high dynamic range compressive imaging. This new imaging modality has been implemented using two different techniques, having both been able to provide images with extended dynamic range. However, as it has already been referred and analyzed, the technique that produces HDR images through intensity control is not adequate to be implemented in a passive illumination configuration, since DMD use PWM to define gray levels, which compromises the quality of the measurements.

Although the importance of using metrics to compare the results obtained with the developed imaging systems has been recognized, it was not possible to obtain a reliable output from their use. Two metrics have been employed but none consistently reflected the tendency obtained with the visual assessment of the quality held by human observers. For that reason, this issue shall be considered in the future towards the development of more adequate metrics that do not preclude judgments to be made based on their results.

The simulation results obtained with the algorithm developed to generate the compressive codes for the CMOS imager were also very promising. Its use is expected to provide the CMOS imager with a compressive imaging mode capable of achieving increased frame rates with reduced power consumption and higher SNR.

Two of the developed compressive single-pixel imaging systems have been explored in three distinct applications. Specifically, the passive illumination single-pixel monochrome imaging system

has been mounted on a microscope and has been used to acquire 128×128 pixels images, yielding a spatial resolution of $42.19 \mu\text{m} / \text{pixel}$. We have also presented the results of a study that was conducted to evaluate the possibility of combining compressive sensing with machine learning and pattern recognition mechanisms to develop a face detection system that would disregard the need for explicit image reconstruction. Despite being still in an early phase of development, the preliminary results obtained for this novel idea were already very good, having yielded a detection error rate as low as 3% using only 3% of the compressive measurements. This performance has even been comparatively better than the one obtained with a state-of-the-art feature detector and descriptor. The passive illumination single-pixel monochrome imaging system has been used in this context to acquire real-world data and test the implemented system. Even though the result of this test was also successful, more measurements were required to correctly classify the test samples.

The passive illumination single-pixel hyperspectral imaging system has been used to gather spectroscopic data of grapes from hyperspectral images. These data can be used to infer about the physicochemical properties of the grapes and constitute a relevant resource to ensure their quality and, consequently, the quality of wine production.

For the future exploitation of the know-how developed throughout this thesis, a proposal for the development of a compressive single-pixel imaging LIDAR system has been accepted by the European Space Agency. Establishing this partnership with a worldwide renowned institution as the European Space Agency constituted a fact of extreme encouragement and served as a proof of recognition in the developed technology. It is believed that this collaboration will be essential to further establish this line of work inside the Optoelectronics and Electronic Systems Unit at INESC TEC and consolidate the knowledge that has been gathered so far.

To finalize, it shall be said that it is believed that compressive sensing will continue to constitute a major opportunity for research and development for the scientific and technologic communities, as there are fascinating theoretical and practical research problems, promising substantial improvements in the imaging domain, as well as in others.

References

1. Candès, E.J. and M.B. Wakin, *An Introduction To Compressive Sampling*. Signal Processing Magazine, IEEE, 2008. **25**(2): p. 21-30.
2. Kirk, L.K., *Rethinking signal processing*. Commun. ACM, 2009. **52**(5): p. 13-15.
3. Claerbout, J.F. and F. Muir, *Robust modeling with erratic data*. Geophysics, 1973. **38**(5): p. 826-844.
4. Santosa, F. and W.W. Symes, *Linear Inversion of Band-Limited Reflection Seismograms*. SIAM Journal on Scientific and Statistical Computing, 1986. **7**(4): p. 1307-1330.
5. Candès, E.J., J. Romberg, and T. Tao, *Robust uncertainty principles: exact signal reconstruction from highly incomplete frequency information*. Information Theory, IEEE Transactions on, 2006. **52**(2): p. 489-509.
6. Candès, E., J. Romberg, and T. Tao, *Stable signal recovery from incomplete and inaccurate measurements*. Communications on Pure and Applied Mathematics, 2006. **59**(8): p. 1207-1223.
7. Chambolle, A., *An Algorithm for Total Variation Minimization and Applications*. J. Math. Imaging Vis., 2004. **20**(1-2): p. 89-97.
8. Robucci, R., et al. *Compressive sensing on a CMOS separable transform image sensor*. in *Acoustics, Speech and Signal Processing, 2008. ICASSP 2008. IEEE International Conference on*. 2008.
9. D. Baron, et al., *Distributed Compressive Sensing [preprint]*. 2005.
10. Golbabaee, M. and P. Vandergheynst, *Distributed Compressed Sensing for Sensor Networks, Using p -thresholding*, 2009, HAL - CCSD.
11. Haupt, J. and R. Nowak, *Signal Reconstruction From Noisy Random Projections*. Information Theory, IEEE Transactions on, 2006. **52**(9): p. 4036-4048.
12. Howland, G.A., et al. *Compressive sensing LIDAR for 3D imaging*. in *Lasers and Electro-Optics (CLEO), 2011 Conference on*. 2011.
13. Howland, G.A., P.B. Dixon, and J.C. Howell, *Photon-counting compressive sensing laser radar for 3D imaging*. Appl. Opt., 2011. **50**(31): p. 5917-5920.
14. M. Lustig, D. L. Donoho, and J.M. Pauly. *Rapid MR imaging with compressed sensing and randomly under-sampled 3DFT trajectories*. in *14th Ann. Meeting ISMRM*. 2006. Seattle.
15. Takhar, D., et al. *A new compressive imaging camera architecture using optical-domain compression*. in *Computational Imaging IV*. 2006. San Jose, CA, USA: SPIE.

16. Candès, E.J. and T. Tao, *Near-Optimal Signal Recovery From Random Projections: Universal Encoding Strategies?* Information Theory, IEEE Transactions on, 2006. **52**(12): p. 5406-5425.
17. Candès, E.J. and T. Tao, *Decoding by Linear Programming*. IEEE Transactions on Information Theory, 2005. **51**(12): p. 4203-4215.
18. Candès, E.J., *Compressive sampling*, in *Int. Cong. Mathematicians* 2006: Madrid, Spain. p. 1433-1452.
19. Baraniuk, R.G., *Compressive Sensing [Lecture Notes]*. Signal Processing Magazine, IEEE, 2007. **24**(4): p. 118-121.
20. Candès, E.J. and J. Romberg, *Sparsity and incoherence in compressive sampling*. Inverse Problems, 2007. **23**(3): p. 969-985.
21. Chen, S., D. Donoho, and M. Saunders, *Atomic Decomposition by Basis Pursuit*. SIAM Review, 2001. **43**(1): p. 129-159.
22. Tropp, J.A. and A.C. Gilbert, *Signal Recovery From Random Measurements Via Orthogonal Matching Pursuit*. Information Theory, IEEE Transactions on, 2007. **53**(12): p. 4655-4666.
23. Duarte, M.F., et al., *Single-Pixel Imaging via Compressive Sampling*. Signal Processing Magazine, IEEE, 2008. **25**(2): p. 83-91.
24. Wakin, M.B., et al. *Recovery of Jointly Sparse Signals from Few Random Projections*. in *Proceedings of the Workshop on Neural Information Processing Systems (NIPS)*. 2005. Vancouver, Canada.
25. Pitsianis, N.P., D.J. Brady, and X. Sun. *The Quantized Cosine Transform for Sensor-Layer Image Compression*. in *Adaptive Optics: Analysis and Methods/Computational Optical Sensing and Imaging/Information Photonics/Signal Recovery and Synthesis Topical Meetings on CD-ROM*. 2005. Optical Society of America.
26. Neifeld, M.A. and P. Shankar, *Feature-Specific Imaging*. Appl. Opt., 2003. **42**(17): p. 3379-3389.
27. Pal, H. and M. Neifeld, *Multispectral principal component imaging*. Opt. Express, 2003. **11**(18): p. 2118-2125.
28. Lai, S. and M.A. Neifeld, *Digital wavefront reconstruction and its application to image encryption*. Optics Communications, 2000. **178**(4-6): p. 283-289.
29. Qinfen, Z., S.Z. Der, and H.I. Mahmoud, *Model-based target recognition in pulsed ladar imagery*. Image Processing, IEEE Transactions on, 2001. **10**(4): p. 565-572.
30. Salvi, J., J. Pagès, and J. Batlle, *Pattern codification strategies in structured light systems*. Pattern Recognition, 2004. **37**(4): p. 827-849.

31. Baheti, P.K. and M.A. Neifeld, *Feature-specific structured imaging*. Appl. Opt., 2006. **45**(28): p. 7382-7391.
32. Baheti, P.K. and M.A. Neifeld, *Random projections based feature-specific structured imaging*. Opt. Express, 2008. **16**(3): p. 1764-1776.
33. Figueiredo, M.A.T., R.D. Nowak, and S.J. Wright, *Gradient Projection for Sparse Reconstruction: Application to Compressed Sensing and Other Inverse Problems*. Selected Topics in Signal Processing, IEEE Journal of, 2007. **1**(4): p. 586-597.
34. Lustig, M., D. Donoho, and J.M. Pauly, *Sparse MRI: The application of compressed sensing for rapid MR imaging*. Magnetic Resonance in Medicine, 2007. **58**(6): p. 1182-1195.
35. Taubman, A.D.S., E.M.W. Marcellin, and R.M. Rabbani, *JPEG2000: Image Compression Fundamentals, Standards and Practice*. Journal of Electronic Imaging, 2002. **11**(2): p. 286-287.
36. Lustig, M., et al., *Compressed Sensing MRI*. Signal Processing Magazine, IEEE, 2008. **25**(2): p. 72-82.
37. Chan, W.L., et al., *Terahertz imaging with compressed sensing and phase retrieval*. Opt. Lett., 2008. **33**(9): p. 974-976.
38. Chan, W.L., et al., *A single-pixel terahertz imaging system based on compressed sensing*. Applied Physics Letters, 2008. **93**(12): p. 121105-121105-3.
39. Gu, J., et al., *Compressive Structured Light for Recovering Inhomogeneous Participating Media*, in *Computer Vision – ECCV 2008*, Springer Berlin / Heidelberg. p. 845-858.
40. Gehm, M.E., et al., *Single-shot compressive spectral imaging with a dual-disperser architecture*. Opt. Express, 2007. **15**(21): p. 14013-14027.
41. Wagadarikar, A., et al., *Single disperser design for coded aperture snapshot spectral imaging*. Appl. Opt., 2008. **47**(10): p. B44-B51.
42. Sun, T. and K. Kelly. *Compressive Sensing Hyperspectral Imager*. in *Computational Optical Sensing and Imaging*. 2009. Optical Society of America.
43. Katz, O., Y. Bromberg, and Y. Silberberg, *Compressive ghost imaging*. Applied Physics Letters, 2009. **95**(13): p. 131110.
44. Erkmen, B.I. and J.H. Shapiro, *Signal-to-noise ratio of Gaussian-state ghost imaging*. Physical Review A, 2009. **79**(2): p. 023833.
45. Jacques, L., et al., *CMOS compressed imaging by Random Convolution*, in *Proceedings of the 2009 IEEE International Conference on Acoustics, Speech and Signal Processing* 2009, IEEE Computer Society.

46. Majidzadeh, V., et al. *A (256 × 256) pixel 76.7mW CMOS imager/ compressor based on real-time In-pixel compressive sensing*. in *Circuits and Systems (ISCAS), Proceedings of 2010 IEEE International Symposium on*. 2010.
47. Romberg, J. *Sensing by Random Convolution*. in *Computational Advances in Multi-Sensor Adaptive Processing, 2007. CAMPSAP 2007. 2nd IEEE International Workshop on*. 2007.
48. Wu, Y., et al., *Experimental demonstration of an Optical-Sectioning Compressive Sensing Microscope (CSM)*. Opt. Express, 2010. **18**(24): p. 24565-24578.
49. Ye, P., et al., *Compressive confocal microscopy*, in *Proceedings of the 2009 IEEE International Conference on Acoustics, Speech and Signal Processing 2009*, IEEE Computer Society.
50. Ye, P., et al., *Compressive confocal microscopy: 3D reconstruction algorithms*, J.H. Larry and R.D. Michael, Editors. 2009, SPIE. p. 72100G.
51. Marim, M.M., et al., *Compressed sensing with off-axis frequency-shifting holography*. Opt. Lett., 2010. **35**(6): p. 871-873.
52. Leitgeb, R., C. Hitzenberger, and A. Fercher, *Performance of fourier domain vs. time domain optical coherence tomography*. Optics Express, 2003. **11**(8): p. 889-894.
53. Liu, X. and J.U. Kang, *Compressive SD-OCT: the application of compressed sensing in spectral domain optical coherence tomography*. Opt. Express, 2010. **18**(21): p. 22010-22019.
54. Young, M., et al., *Real-time high-speed volumetric imaging using compressive sampling optical coherence tomography*. Biomed. Opt. Express, 2011. **2**(9): p. 2690-2697.
55. Lebed, E., et al., *Rapid Volumetric OCT Image Acquisition Using Compressive Sampling*. Opt. Express, 2010. **18**(20): p. 21003-21012.
56. Daubechies, I., M. Defrise, and C. De Mol, *An iterative thresholding algorithm for linear inverse problems with a sparsity constraint*. Communications on Pure and Applied Mathematics, 2004. **57**(11): p. 1413-1457.
57. Itzler, M.A., et al., *Geiger-mode avalanche photodiode focal plane arrays for three-dimensional imaging LADAR*. in Proc. of SPIE. Infrared Remote Sensing and Instrumentation XVIII, 2010. **7808**.
58. Coffey, V.C., *Seeing in the Dark: Defense Applications of IR imaging*. Opt. Photon. News, 2011. **22**(4): p. 26-31.
59. Smith, G.M., et al. *Reliable large format arrays of Geiger-mode avalanche photodiodes*. in *Indium Phosphide and Related Materials, 2008. IPRM 2008. 20th International Conference on*. 2008.

60. McIntosh, A. *Arrays of Gieger-Mode Avalanche Photodiodes for Ladar and Laser Communications*. in *Applications of Lasers for Sensing and Free Space Communications*. 2010. Optical Society of America.
61. Richard M. Marino and J. William R. Davis, *Jigsaw: A Foliage-Penetrating 3D Imaging Laser Radar System*. Lincoln Laboratory Journal, 2005. **15**(1): p. 23-36.
62. Gopalsami, N., et al., *Compressive sampling in passive millimeter-wave imaging*. 2011: p. 80220I-80220I.
63. Gopalsami, N., et al., *Passive millimeter-wave imaging with compressive sensing*. Optical Engineering, 2012. **51**(9): p. 091614-1.
64. Durán, V., et al., *Single-pixel polarimetric imaging*. Opt. Lett., 2012. **37**(5): p. 824-826.
65. Durán, V., et al. *Stokes imaging polarimetry with a single-pixel detector*. in *8th EOS Topical Meeting on Diffractive Optics*. 2012. Delft, Netherlands.
66. Becker, S., J. Bobin, and E.J. Candes, *NESTA: A Fast and Accurate First-Order Method for Sparse Recovery*. SIAM Journal on Imaging Sciences, 2011. **4**(1): p. 1-39.
67. Candès, E. and J. Romberg. *L1-magic : Recovery of Sparse Signals via Convex Programming*. 2005 [cited 2012 25th May]; Available from: <http://users.ece.gatech.edu/~justin/l1magic/>.
68. Park, S.C., M.K. Park, and M.G. Kang, *Super-resolution image reconstruction: a technical overview*. Signal Processing Magazine, IEEE, 2003. **20**(3): p. 21-36.
69. Glasner, D., S. Bagon, and M. Irani. *Super-resolution from a single image*. in *Computer Vision, 2009 IEEE 12th International Conference on*. 2009.
70. *Driving LCD Displays* 2012 [cited 2012 5th of June]; Available from: http://www.goldenviewdisplay.com/driving_LCD_display.html.
71. Mada, H. and K. Osajima, *Time response of a nematic liquid-crystal cell in a switched dc electric field*. Journal of Applied Physics, 1986. **60**(9): p. 3111-3113.
72. Lewis, J.P., *Fast Normalized Cross-Correlation*. Industrial Light & Magic, 1995.
73. R. W. G. Hunt and M.R. Pointer, *Measuring Colour*. 4th ed2011: John Wiley & Sons, Ltd.
74. Goetz, A.F.H., et al., *Imaging Spectrometry for Earth Remote Sensing*. Science, 1985. **228**(4704): p. 1147-1153.
75. He, K.S., et al., *Benefits of hyperspectral remote sensing for tracking plant invasions*. Diversity and Distributions, 2011. **17**(3): p. 381-392.
76. Hege, E.K., et al., *Hyperspectral imaging for astronomy and space surveillance*, S.S. Sylvia and E.L. Paul, Editors. 2003, SPIE. p. 380-391.

77. Gowen, A.A., et al., *Hyperspectral imaging - an emerging process analytical tool for food quality and safety control*. Trends in Food Science & Technology, 2007. **18**(12): p. 590-598.
78. Skala, M.C., et al., *Combined hyperspectral and spectral domain optical coherence tomography microscope for noninvasive hemodynamic imaging*. Opt. Lett., 2009. **34**(3): p. 289-291.
79. Roggo, Y., et al., *Infrared hyperspectral imaging for qualitative analysis of pharmaceutical solid forms*. Analytica Chimica Acta, 2005. **535**(1-2): p. 79-87.
80. Descour, M.R., et al., *Demonstration of a computed-tomography imaging spectrometer using a computer-generated hologram disperser*. Appl. Opt., 1997. **36**(16): p. 3694-3698.
81. Mooney, J.M., et al., *High-throughput hyperspectral infrared camera*. J. Opt. Soc. Am. A, 1997. **14**(11): p. 2951-2961.
82. Gehm, M.E. and D.J. Brady. *High-throughput hyperspectral microscopy*. in *Three-Dimensional and Multidimensional Microscopy: Image Acquisition and Processing XIII*. 2006. San Jose, CA, USA: SPIE.
83. Mather, J. *Spectral and XYZ Color Functions*. 2010 [cited 2012 4th of August]; Available from: <http://www.mathworks.com/matlabcentral/fileexchange/7021-spectral-and-xyz-color-functions>.
84. U.C.L., C.V.R.L.-. *Colour Matching Functions*. [cited 2012 4th of August]; Available from: <http://cvrl.ioo.ucl.ac.uk/cmfs.htm>.
85. I.E.C., *IEC 61966-2-1 ed1.0 - Multimedia systems and equipment - Colour measurement and management - Default RGB colour space - sRGB*, 1999. p. 51.
86. Debevec, P.E. and J. Malik, *Recovering high dynamic range radiance maps from photographs*, in *Proceedings of the 24th annual conference on Computer graphics and interactive techniques* 1997, ACM Press/Addison-Wesley Publishing Co. p. 369-378.
87. Erik Reinhard, et al., *High Dynamic Range Imaging: Acquisition, Display, and Image-Based Lighting (The Morgan Kaufmann Series in Computer Graphics)* 2005, San Francisco, CA: Morgan Kaufmann.
88. Mann, S. *Compositing multiple pictures of the same scene*. in *Proceedings of the 46th Annual Imaging Science and Technology Conference*. 1993. Springfield, VA: Society for Imaging Science and Technology (imaging.org).
89. Steve Mann and R.W. Picard. *On being 'undigital' with digital cameras: extending dynamic range by combining differently exposed pictures*. in *Proceedings of the 46th Annual Imaging Science and Technology Conference*. 1995. Springfield, VA: Society for Imaging Science and Technology (imaging.org).

90. Madden, B.C., *Extended Intensity Range Imaging*, 1993, University of Pennsylvania - Department of Computer and Information Science - GRASP Laboratory. p. 21.
91. Moriwaki, K., *Adaptive exposure image input system for obtaining high-quality color information*. Systems and Computers in Japan, 1994. **25**(8): p. 51-60.
92. Mitsunaga, T. and S.K. Nayar. *Radiometric self calibration*. in *Computer Vision and Pattern Recognition, 1999. IEEE Computer Society Conference on*. 1999.
93. Nayar, S.K. and T. Mitsunaga. *High dynamic range imaging: spatially varying pixel exposures*. in *Computer Vision and Pattern Recognition, 2000. Proceedings. IEEE Conference on*. 2000.
94. Mannami, H., et al. *High Dynamic Range Camera using Reflective Liquid Crystal*. in *Computer Vision, 2007. ICCV 2007. IEEE 11th International Conference on*. 2007.
95. Adeyemi, A.A., N. Barakat, and T.E. Darcie, *Applications of digital micro-mirror devices to digital optical microscope dynamic range enhancement*. Opt. Express, 2009. **17**(3): p. 1831-1843.
96. Fujifilm. *FinePix F550EXR*. [cited 2012 August 13th]; Available from: http://www.fujifilm.com/products/digital_cameras/f/finepix_f550exr/features/.
97. Ntziachristos, V., C. Bremer, and R. Weissleder, *Fluorescence imaging with near-infrared light: new technological advances that enable in vivo molecular imaging*. European Radiology, 2003. **13**(1): p. 195-208.
98. Dudley, D., W.M. Duncan, and J. Slaughter. *Emerging digital micromirror device (DMD) applications*. in *Proc. SPIE 4985, 14 - MOEMS Display and Imaging Systems*. 2003. San Jose, CA, USA: SPIE.
99. Duarte, M.F., et al. *Sparse Signal Detection from Incoherent Projections*. in *Acoustics, Speech and Signal Processing, 2006. ICASSP 2006 Proceedings. 2006 IEEE International Conference on*. 2006.
100. Junior, L.L.d.O. and C.E. Thomaz. *FEI Face Database*. 2006; Available from: <http://fei.edu.br/~cet/facedatabase.html>.
101. L. Fei-Fei, R. Fergus, and P. Perona. *Learning generative visual models from few training examples: an incremental Bayesian approach tested on 101 object categories*. in *IEEE CVPR 2004 - Workshop on Generative-Model Based Vision*. 2004. Washington, DC (USA).
102. Marti, A.H., *Support Vector Machines*. IEEE Intelligent Systems, 1998. **13**(4): p. 18-28.
103. Rodriguez-Lujan, I., et al., *Quadratic Programming Feature Selection*. J. Mach. Learn. Res., 2010. **11**: p. 1491-1516.
104. Bicego, M., et al. *On the Use of SIFT Features for Face Authentication*. in *Computer Vision and Pattern Recognition Workshop, 2006. CVPRW '06. Conference on*. 2006.

105. Jun, L., et al. *Person-Specific SIFT Features for Face Recognition*. in *Acoustics, Speech and Signal Processing, 2007. ICASSP 2007. IEEE International Conference on*. 2007.
106. Cong, G. and J. Xudong. *Face recognition using sift features*. in *Image Processing (ICIP), 2009 16th IEEE International Conference on*. 2009.
107. Stein, S. and G.A. Fink. *A new method for combined face detection and identification using interest point descriptors*. in *Automatic Face & Gesture Recognition and Workshops (FG 2011), 2011 IEEE International Conference on*. 2011.
108. Jain, A.K., *Data clustering: 50 years beyond K-means*. Pattern Recogn. Lett., 2010. **31**(8): p. 651-666.
109. Csurka, G., et al., *Visual categorization with bags of keypoints*, in *Workshop on Statistical Learning in Computer Vision, ECCV 2004: Prague, Czech Republic*. p. 1-22.
110. Yang, J., et al., *Evaluating bag-of-visual-words representations in scene classification*, in *Proceedings of the international workshop on Workshop on multimedia information retrieval 2007*, ACM: Augsburg, Bavaria, Germany. p. 197-206.
111. Ferreira, A.C.S., V.V. Lopes, and R.C. Martins, *Method and Device for Monitoring the Production of Grapes with UV-VIS-SWNIR Spectroscopy*, W.I.P. Organization, Editor 2010, WO/2010/131197.
112. Bannan, D. and C.V. Veen, *Hyperspectral Imaging Gets Stamp of Approval for Food Processing*. Photonics Spectra, 2012(June 2012): p. 44-49.
113. Pereira do Carmo, J., et al., *Imaging lidars for space applications*. Novel Optical Systems Design and Optimization XI, 2008. **7061**(70610J).